

UNIVERSITY OF THE WESTERN
CAPE

Disentangling star formation and
AGN activity in the GAMA (G23)
region

by

Harris Yao Fortune Marc

A thesis submitted in partial fulfillment for the
degree of Doctor of Philosophy

in the

Faculty of Science

Department of Physics and Astronomy



UNIVERSITY *of the*
WESTERN CAPE

June 2021


Supervisor: [A/Prof. Michelle Cluver](#)

Co-supervisors: [Prof. Tom Jarrett](#), [Prof. Mario Santos](#)

Declaration of Authorship

I, Marc Harris Yao Fortune, declare that this thesis, titled 'Disentangling Star formation and AGN activity in the GAMA (G23) region' and the work presented in it are my own. I confirm that:

- This work was done wholly or mainly while in candidature for a research degree at this University.
- Where any part of this thesis has previously been submitted for a degree or any other qualification at this University or any other institution, this has been clearly stated.
- Where I have consulted the published work of others, this is always clearly attributed.
- Where I have quoted from the work of others, the source is always given. With the exception of such quotations, this thesis is entirely my own work.
- I have acknowledged all main sources of help.
- Where the thesis is based on work done by myself jointly with others, I have made clear exactly what was done by others and what I have contributed myself.

Signed:  _____

Date: 23/06/2021 _____

“Learn avidly, question it repeatedly. Analyse it carefully. Then put what you have learned into practice intelligently.”

Confucius



UNIVERSITY *of the*
WESTERN CAPE

UNIVERSITY OF THE WESTERN
CAPE

Abstract

Faculty of Science
Department of Physics and Astronomy

Doctor of Philosophy

by Harris Yao Fortune Marc

Observations of galaxies at different wavelengths have shaped our understanding of their formation and evolution through time. The commonly derived parameters, such as stellar mass and star formation rate (SFR), rely on the assumption that the radiation received is exclusively generated by the stars within the galaxy. This assumption is true for pure star-forming (SF) galaxies, but not in the presence of an active galactic nucleus (AGN). AGNs are structures that also radiate in the full electromagnetic spectrum, inducing additional flux to that emitted by stars. Their small sizes in comparison to the host galaxy ($\ll 1\%$) generally make them invisible in galaxy images. AGNs come in many variations making the most powerful (e.g., quasi-stellar objects) easily identifiable, whereas others with much weaker signatures can be hidden in the total emission from the host. Therefore it is imperative to find accurate methods to separate and study the properties of AGNs versus pure SF galaxies.

This project aims to combine data from multiple wavelengths (optical GAMA G23, infrared *WISE*, and MeerKAT radio data) to shed new light on the existing AGN/SF separation methods. The study requires high-quality data, which was obtained by creating the first Wide-field Infrared Survey Explorer (*WISE*) catalogue containing carefully measured photometry for the resolved sources in the area of study. The Baldwin, Phillips and Terlevich (BPT) diagram used in the optical wavelengths for galaxy classification was compared to the *WISE* colour-colour diagram. We found good agreement of the two methods on the classification of SF galaxies. Misclassifications were mostly seen among the AGNs owing to their complex structures. We created a hybrid optical-infrared diagram with an improved classification capability. The

radio emission associated with the optical-infrared data revealed more hidden AGNs whose activity are not detected in optical and/or infrared diagrams. The estimation of SFR using the radio luminosity appears to be systematically high in comparison to the commonly used infrared SFR. We thus derived a new radio SFR relation calibrated using the infrared (*WISE*, $12\ \mu\text{m}$).

We find that the infrared/radio luminosity ratio (q_{TIR}) can identify up to 70% more AGNs not visible in the optical and/or the infrared wavelengths. The q_{TIR} is an excellent detector of massive galaxies with AGNs emitting most of their power in radio (e.g., galaxy M87). However, it becomes inefficient and will miss AGNs with infrared emission as strong as the radio emission. With the advent of larges radio surveys such as the SKA, the q_{TIR} will be an essential tool to be combined with the *WISE* colour-colour diagram or other galaxy classification techniques.



UNIVERSITY *of the*
WESTERN CAPE

Acknowledgements

The biggest thanks go to my supervisors, Prof. Michelle Cluver, Prof. Tom Jarrett, and Prof. Mario Santos. Thank you, Michelle, for your support and guidance since my master's degree. Tom, I have been learning a lot from you during this Ph.D. You both are such great supervisors! I wonder how you manage to be always available to discuss my work. I remember our late Skype meeting during the pandemic outbreak. I thank you, Prof. Mario, for your financial support, without which this project wouldn't have been possible.

Big thanks to Michelle Gabler and Nicky Walker who have been real guides since my first year in South Africa. I also owe special thanks to all my officemates and fellow students. Shean Jolicoeur, Amidou Sorgho, and Marie Korsaga, you as my closest friends deserve the best for always being there for me. Thank you for your support and our useful discussions. I also thank the Physics and Astronomy departments at the Universities of the Western Cape and Cape Town for all your support. This Ph.D. is fully funded by the South African Square Kilometre Array Project through the Centre for Radio Cosmology.

Grand merci à vous père et mère, à la grande famille et à ma tante Rosine Yao spécialement. Je n'aurai pas pu finir ce doctorat sans votre soutien et votre amour. Spécial merci à ma bien aimée Sylvie Kokora. Tu as toujours été à mes cotés durant toutes ces années. Merci pour ton amour, ton soutien et ta patience. Merci à vous mes encadreurs de la Côte d'Ivoire particulièrement au Prof. Arsene Koba, Prof. Olivier Obrou et Dr. Zaka. A toi mon ami Ahoua, je te suis vraiment reconnaissant de m'avoir informé du program NASSP pour la toute première fois.

Finally, thanks be to God Almighty for guiding and inspiring me throughout this Ph.D. Thank you for making it happen.

Contents

Declaration of Authorship	i
Abstract	iii
Acknowledgements	v
List of Figures	ix
List of Tables	xiv
Abbreviations	xv
1 Introduction	1
2 Background and Literature Review	5
2.1 Structures in the Universe	5
2.2 Galaxies	7
2.2.1 Radio Continuum Emission from Galaxies	7
2.2.2 Star-forming Galaxies	9
2.2.3 Star-forming Main Sequence	11
2.2.4 Active Galactic Nuclei	13
2.2.4.1 The Unification Theory	14
2.2.4.2 Luminous Infrared and Ultraluminous Infrared Galaxies	17
2.2.4.3 QSOs	17
2.2.4.4 LINERs	17
2.2.4.5 Seyferts	18
2.2.4.6 High Excitation Radio Galaxies and Low Excitation Radio Galaxies	19
2.3 AGN Identification	20
2.3.1 X-ray Selection of AGN	20
2.3.2 Optically Selected AGN	21
2.3.3 AGN in the Mid-infrared wavelengths	22
2.3.4 Radio-selected AGN	24
2.4 Multiwavelength Selection of AGN	25
2.4.1 Spectral Energy Distribution Fitting	25

2.4.2	Infrared-to-Radio Luminosity Ratio: q_{TIR}	27
2.5	Most Recent Works on AGN	28
3	Data and Data Reduction	30
3.1	Optical: The GAMA Survey	30
3.1.1	The GAMA G23 Region	31
3.1.1.1	Spectral Line Measurement	32
3.2	Optical: KiDS Imaging	34
3.3	Mid-Infrared: The <i>WISE</i> Survey	34
3.3.1	<i>WISE</i> Image Reconstruction	34
3.3.2	Catalogue of <i>WISE</i> Galaxies in G23	35
3.3.2.1	Extraction and Cleaning Method	36
3.3.2.2	Rest-frame Correction	38
3.4	Radio: The SKA Pathfinder MeerKAT	39
3.4.1	The MeerHOGS Survey	41
3.4.2	Observations and Data Reduction	42
4	Source Extraction	44
4.1	<i>ProFound</i> : Concept and Parameters	44
4.1.1	Extraction Method	45
4.1.2	Functions in <i>ProFound</i>	46
4.1.3	Photometry Multiband (Colour Me Happy)	47
4.2	Testing <i>ProFound</i> on <i>WISE</i> Photometry	47
4.2.1	<i>WISE</i> Cross-matched to <i>ProFound</i> 's Detections	48
4.2.2	Point-source Magnitudes in <i>WISE</i> and <i>ProFound</i>	51
4.2.2.1	Comparison between <i>WISE</i> and <i>ProFound</i> 's Magnitudes	51
4.3	Photometry of Resolved Sources in the standard pipeline and <i>ProFound</i>	59
4.3.1	Magnitude Difference between the standard pipeline and <i>ProFound</i> for Resolved Sources	59
4.4	MeerKAT Source Extraction with <i>ProFound</i>	63
4.4.1	Conclusions	66
5	Separating AGN and SF Galaxies with Optical and Mid-IR Data	68
5.1	Data	69
5.1.1	Property of the GAMA- <i>WISE</i> Galaxies	69
5.1.2	The Study Sample	71
5.2	AGN Classification	74
5.2.1	Optical Emission Line Diagnostics: BPT Diagrams	74
5.2.2	Classifications Derived from the Combination of Mid-IR and Optical Line Properties	77
5.2.3	Galaxy Properties in Different Activity Classifications	82
5.3	Case Studies	86
5.3.1	Optical- and IR-classified SF Galaxies	88
5.3.2	Optical-IR AGNs	89
5.3.3	Optical AGNs, IR Non-AGNs	89
5.3.4	Optical Non-AGNs, IR AGNs	91
5.4	The New Diagnostic: $[W1-W2]$ vs $[N\text{ II}]/H\alpha$	101
5.5	Discussion	104

5.6	Conclusion	107
6	Expanding the Analysis: Radio Continuum from MeerKAT	115
6.1	Assessing the Photometric and Astrometric Quality	115
6.2	Radio Catalogue	118
6.2.1	Resolved Sources in the Field	118
6.2.2	MeerHOGS Cross-matched with the <i>WISE</i> -GAMA Sample	124
6.3	Optical–IR–Radio Study of AGN vs SF	125
6.3.1	The Infrared-to-Radio Luminosity Ratio: q_{TIR}	126
6.3.2	Evolution of some Parameters with the Radio Power	127
6.3.3	Relationship between the q_{TIR} and <i>WISE</i> Colours	133
6.3.4	HERGs and LERGs	138
6.3.5	Relation between $\text{SFR}_{\text{radio}}$ and Stellar Mass	139
6.4	Discussion	143
6.5	Conclusion	145
7	Concluding Remarks	152
7.1	Optical and Mid-IR View	154
7.2	Folding in the Radio Continuum	154
7.3	Future Prospects	155



UNIVERSITY of the
WESTERN CAPE

List of Figures

2.1	Cosmic web built based on subhalo/galaxy catalogues by Countinho et al. (2016)	6
2.2	Synchrotron emission processes and the standard spectrum.	8
2.3	Star-forming spiral galaxy in the GAMA G23 field	10
2.4	Star-forming galaxy main sequence	12
2.5	Schematic figure showing the AGN unification theory.	15
2.6	VLA image at 1.4 GHz of Cygnus A. It is one of the strongest radio galaxies and among the first to be discovered (in 1939 by Grote Reber). In the image, the wide span of the radio lobes is shown by the red arrows.	16
2.7	Image of NGC1068. A well-known Seyfert and starburst galaxy. It is a relatively close (14.4 Mpc away) bright AGN, which has been extensively studied and was one of the first galaxies to be classified as a Seyfert. Image credit: NASA, ESA and A. van der Hoeven.	19
2.8	Calibrated optical spectrum from GAMA (CATAID: 5252110) of a galaxy classified as AGN in optical and in WISE wavelength regimes.	21
2.9	Optical emission line BPT diagrams. (a): The $[O III]5007/H\beta$ vs. $[N II]6583/H\alpha$ classification diagram.	22
2.10	<i>WISE</i> W1[3.4 μ m] - W2[4.6 μ m] vs W2[4.6 μ m]- W3[12 μ m] colours (colour-colour diagram)	23
2.11	Ratio between radio and optical flux density versus absolute magnitude. Image reproduced from Kellermann et al. (1989). Galaxies with $R \geq 10$ and $R < 10$ are classified as RL and RQ, respectively. The arrows indicate the upper limit objects not detected as radio sources above 0.25 mJy.	24
2.12	A schematic representation of an AGN spectral energy distribution based on observed SEDs of non-jetted quasars (e.g., Elvis et al. 1994; Richards et al. 2006).	26
3.1	The five GAMA fields (white rectangles) equatorially projected on the sky. One can see the overlapping with other major surveys but only the three equatorial fields have SDSS data available	32
3.2	The <i>WISE</i> 50 deg ² view of the G23 field. In the zoomed area (14 \times 11 arcmin) the reddish extended galaxies are easily distinguishable from foreground stars (blue in general)	35
3.3	Image showing the resolved galaxies cleaning process. On the first row of each panel are the 4-colour image, and the images in W1, W2, W3 and W4, respectively.	37

3.4	Example of SEDs for an early type galaxy in (a) and a SF spiral in (b). A typical AGN and a QSO are represented in (c) and (d), respectively. The SEDs are constructed using the templates presented in this section. The best fit template is indicated on the y axis. The GAMA identification and the spectroscopic redshift of the galaxies are provided on top of each image.	39
3.5	Image of the MeerKAT dishes located in the Karoo desert in South Africa. We can see the Gregorian design characterised by the offset of the secondary reflector. This configuration maximises the collecting area, as it does not block the aperture. At the heart of each dish is a receiver tuned to the L-band (900- 1670 MHz) with 4 096 channels, which are some of the most sensitive arrays ever created. Image taken from the MeerKAT webpage. . .	41
3.6	The MeerHOGS survey	42
4.1	Diagram showing the different steps in <i>ProFound</i> 's data processing.	45
4.2	<i>WISE</i> total number of resolved sources in area 3 in black squares (962 galaxies) and <i>WISE</i> cross-matched <i>ProFound</i> in yellow circles (901 galaxies) for a cross-matched radius of $3''$	49
4.3	Galaxies among the sample with cross-matched radius between $3''$ and $5''$ in area 3	50
4.4	Histogram of the total number of <i>ProFound</i> 's detected point-source galaxies (green) and resolved sources (red) in W1 after cross-matching with the G23 catalogue in area 3	52
4.5	Magnitude difference diagram for area 3 (point source detections. <i>WISE</i> (mpro) - <i>ProFound</i> (mag) vs <i>WISE</i> (mpro) for respectively W1 (left panel) and W2 (right panel)	54
4.6	Magnitude difference diagram for area 3 detections in W1 band. <i>WISE</i> (W1mpro) - <i>ProFound</i> (W1) vs <i>WISE</i> (W1mpro)	55
4.7	Magnitude difference diagram for area 3 detections in W2 band. <i>WISE</i> (W2mpro) - <i>ProFound</i> (W2) vs <i>WISE</i> (W2mpro)	56
4.8	Magnitude difference diagram for area 3 detections in W3 band. <i>WISE</i> (W3mpro) - <i>ProFound</i> (W3) vs <i>WISE</i> (W3mpro)	57
4.9	Magnitude difference diagram for area 3 detections in W4 band. <i>WISE</i> (W4mpro) - <i>ProFound</i> (W4) vs <i>WISE</i> (W4mpro)	57
4.10	Summary plot showing the magnitude differences between the G23 catalogue and <i>ProFound</i>	58
4.11	Magnitude difference diagram for area 3 detections. Left panel: <i>WISE</i> (best) - <i>ProFound</i> (mag) vs <i>WISE</i> (mag) for respectively W1, W2, W3 and W4 . .	61
4.12	The selected outliers from Figure 4.11. The left and right panels show the <i>WISE</i> 3-colours image before and after cleaning.	62
4.13	<i>ProFound</i> compared to commonly used source extraction software such as AEGEAN and pyBDSF	64
4.14	Distribution of integrated 1.4 GHz flux densities of all sources. The number of sources peaks around a flux density ~ 0.1 mJy. The two galaxies at the brightest end (300–400 mJy) are respectively MH17 and MH37 presented in Table 6.1.	65
4.15	MeerHOGS vs NVSS continuum flux	65

5.1	The number distribution as a function of the redshift. All <i>WISE</i> -GAMA G23 galaxies ($\sim 41\,000$ galaxies with GAMA redshifts) represented by the solid pink line, of which more than 75 % have redshifts < 0.3	69
5.2	Differential W1 ($3.4\ \mu\text{m}$) source counts in the G23 region with magnitudes in the Vega system	70
5.3	The <i>WISE</i> k-corrected colour-colour plane, W1-W2 vs W2-W3 (magnitudes are in the Vega system).	71
5.4	The distribution of stellar masses for the galaxies in the study sample. The sample contains very few low-mass galaxies with $< 2\%$ having $\log(M_{\text{stellar}}/M_{\odot}) < 9$	72
5.5	The BPT diagram OIII(5007)/H β vs. SII(6716, 6731)/H α with all the required lines in emission.	75
5.6	The BPT diagram OIII(5007)/H β vs NII(6583)/H α with all the required lines in emission.	75
5.7	Comparison of the two optical classifications. About 85 % (998/1 173) of the galaxies represented in Figure 5.6 respect the conditions applied in Figure 5.5	76
5.8	The BPT OIII(5007)/H β vs. NII(6583)/H α classified galaxies from Figure 5.6 plotted in the <i>WISE</i> colour-colour diagram.	79
5.9	Summary of the classification combining both the optical BPT and the <i>WISE</i> mid-IR colour-colour diagrams.	81
5.10	Combined optical-IR BPT diagram, showing the different classes of galaxies.	81
5.11	Left panel: (a) distribution of the $\text{SFR}_{12\mu\text{m}}$ as a function of stellar mass for the galaxies classified as non-AGNs in both optical and mid-IR	84
5.12	The redshift distribution (fraction of galaxies per redshift bin; the BLAGNs are included in a different AGN category as presented in Table 5.2	87
5.13	Classification of the galaxy (GAMA ID: 5241095) based on its optical (GAMA) and mid-IR (<i>WISE</i>) properties.	92
5.14	Galaxy 5240983. Classified as SF (blue). See also Figure 5.13, the companion galaxy.	93
5.15	Galaxy 5306682. Classified as SF (blue).	93
5.16	Galaxy 5205726. Classified as composite (green).	94
5.17	Galaxy 5339805. A BLAGN classified as oAGN (mAGN).	94
5.18	Galaxy 5151978. A BLAGN classified as oAGN (mAGN).	95
5.19	Galaxy 5347780. A BLAGN classified as oAGN (mWarm).	95
5.20	Galaxy 5294374. A BLAGN classified as oAGN (mWarm).	96
5.21	Galaxy 5249547. Classified as oAGN (mSF) (yellow, an example of a discordant classification).	96
5.22	Galaxy 5155115. Classified as oAGN (mSF) (yellow).	97
5.23	Galaxy 5200866. Classified as non-oAGN (mAGN) (orange, example of a discordant classification).	97
5.24	Galaxy 5158890. Classified as non-oAGN (mAGN) (orange).	98
5.25	Galaxy 5275222. A BLAGN classified as non-oAGN (mAGN). Note the [N II] line cannot be distinguished from H α	98
5.26	Galaxy 5241310. A broad-line AGN classified as a non-oAGN (mAGN).	99
5.27	Galaxy 5204947. Classified as non-oAGN (mWarm) (orange). Blended system seen as a single in <i>WISE</i> 3-band colour.	99
5.28	Galaxy 5135645. Classified as SF (blue). Extreme colours in <i>WISE</i>	100

5.29 Individual KiDS r-band images of the galaxies selected from Figures 5.13 to 5.28. The GAMA names are in the upper left corner. All panels are 2 by 2 arcminutes.	100
5.29 continued.	101
5.30 Optical–IR SF-AGN diagnostic plot. The new method used to classify galaxies based on both the optical BPT and the (<i>WISE</i>) colour-colour diagrams.	103
5.31 The <i>WISE</i> colour-colour representation of the galaxies classified in Figure 5.30b using the same key. The AGNs are well delimited by the 2σ offset	104
6.1 Average position offset between MeerHOGS and <i>WISE</i>	116
6.2 Offsets of the 1.4 GHz MeerHOGS positions from the <i>WISE</i> positions for sources detected in both surveys.	117
6.3 List of some resolved representative galaxies in MeerHOGS (the central images). Each stamp is 5×5 arcmin except MH17, which is 7×7 arcmin, and the beam size is 13.5 arcsecs. See Table 6.1 for measurements. MH17 is a known giant radio galaxy (GRG), which will be discussed in the text.	119
6.3 continued.	120
6.3 continued.	121
6.4 The variation of flux in the different components (East lobe, Core, West lobe) of MH17 (PKS 2250–351) as presented in Table 6.2	123
6.5 The redshift distribution of the radio galaxies in MeerHOGS	125
6.6 q_{TIR} versus <i>WISE</i> colours for the entire MeerHOGS– <i>WISE</i> –GAMA sample	126
6.7 Radio flux as a function of radio luminosity for the total sample (a). The different categories of galaxies using the new classification diagram are represented in (b). The obscured AGNs as defined by Jarrett et al. 2011 are also represented along with the radio bright galaxies	128
6.8 Radio luminosity as a function of $\text{SFR}_{12\mu\text{m}}$ and q_{TIR} for SF galaxies	129
6.9 Radio luminosity as a function of q_{TIR} for SF galaxies	130
6.10 Figure 6.8 is reproduced adding the remaining group of galaxies as classified using our new diagram. The blue, green, and red points are SFs, composites, and AGNs, respectively	131
6.11 Figure 6.9 is reproduced adding the remaining group of galaxies as classified using our new diagram. The blue, green, and red points are SF, composites, and AGN, respectively	132
6.12 q_{TIR} versus <i>WISE</i> colours. It is similar to Figure 6.6 with the different galaxy groups represented. The q_{TIR} range for SF galaxies is from 2 to 3.4, but more typical values of 2.5 ± 0.22 , and the radio bright AGNs are found for q_{TIR} values < 2 . The yellow circles represent the galaxies classified as oAGN(mSF) in Chapter 5 (see Figure 5.9) with a radio counterpart. They show similar radio properties ($2 \leq q_{\text{TIR}} \leq 3$) to normal SF galaxies.	134
6.13 Relationship between the q_{TIR} , the W1-W2 colour and the stellar mass	135
6.14 The <i>WISE</i> colour-colour diagram colour-coded by the q_{TIR} and the stellar mass.	136
6.15 Variation of the q_{TIR} as a function of stellar mass	137
6.16 The <i>WISE</i> colour-colour diagram colour-coded as a function of q_{TIR} . There is no clear dichotomy between HERGs and LERGs.	138
6.17 $\text{SFR}_{12\mu\text{m}}$ vs stellar mass (a) and $\text{SFR}_{\text{radio}}$ vs stellar mass (b). The $\text{SFR}_{\text{radio}}$ is derived using the equation derived in Figure 6.9	141

6.18	SFR _{12μm} vs stellar mass (a) and SFR _{radio} vs stellar mass (b) similar to Figure 6.17. The total sample is shown in black. The non-classified galaxies (the visible black points in the background) did not meet the requirement to be classified using the new diagram ([N II] and H α in absorption, lines with S/N >3... see Section 5.4 for more details about the new classification diagram). The SF and composite galaxies are also presented. Both samples have the same distributions.	142
6.19	SFR _{12μm} vs stellar mass (a) and SFR _{radio} vs stellar mass (b) similar to Figure 6.17. Here only the galaxies with AGN activity are represented. One can see the radio bright galaxies (cyan) below the main sequence in (a), while their SFRs are estimated to be high in radio (b). The radio cannot be reliably used to estimate the SFR of these galaxies, since the flux observed is coming mostly from the central AGN. All the galaxies selected as examples are represented (SFs and AGNs).	142
6.20	SFR _{12μm} vs stellar mass (a) and SFR _{radio} vs stellar mass (b). Here only the radio bright galaxies are represented and colour-coded as a function of q _{TIR} . The galaxies with the lowest q _{TIR} deviate more from the stellar mass SFR relation. This is not very surprising, as it was shown earlier that the AGNs with the lowest q _{TIR} are massive galaxies with very low SFR _{12μm} (see Figures 6.13 and 6.14). We also represented all the galaxies selected as examples (SFs and AGNs).	143
6.21	Evolution of the q _{TIR} with redshift colour-coded as a function of radio luminosity.	144
6.22	The <i>WISE</i> image and the physical properties of the galaxies selected as example cases. Their general parameters (stellar mass, SFR, <i>WISE</i> colours, etc.) are presented	147
6.23	MHGS006 (radio image presented in Figure 6.3, MH17) is a giant radio galaxy (PKS 2250–351 in Abell 3936, Seymour et al. 2020) classified as SF in <i>WISE</i> with a radio flux of 0.318 Jy.	148
6.24	For comparison purposes, here is the massive Fornax Cluster galaxy, Fornax A (NGC1316), NGC1316 is classified as spheroid in <i>WISE</i> with a radio flux of 125 Jy.	149
6.25	For comparison purposes, here is the massive Virgo Cluster galaxy, Virgo A (M87), M87 is classified as spheroid in <i>WISE</i> with a radio flux of 138.487 Jy. It has a supermassive black hole at the centre, which was pictured as the first ever real image of a black hole.	150
6.26	For comparison purposes, here is the nearby grand design spiral galaxy, M101, is classified as SF in <i>WISE</i> with a radio flux of 0.75 Jy.	151

List of Tables

3.1	The <i>WISE</i> G23 Catalogue created using reconstructed images (enhanced resolution).	36
3.2	Observation details of the MeerHOGS Survey	43
4.1	<i>ProFound</i> 's photometry tools (from the online description)	46
4.2	<i>ProFound</i> extracted Sources and the G23 Catalogue (W1 Band) in area 3	48
4.3	Statistical diagnostic by <i>ProFound</i> of point sources galaxies in area 3 (3'' cross-match radius). AW and P represent <i>ALLWISE</i> and <i>ProFound</i> , respectively.	55
4.4	Magnitudes correction for <i>ProFound</i>	56
4.5	Statistical diagnostic by <i>ProFound</i> of resolved galaxies in area 3 . S P stands for standard pipeline.	59
4.6	Resolved galaxy outliers	63
5.1	Table showing the number of galaxies for different constraints applied.	71
5.2	Subgroups and their different constraints applied to the Sample.	85
5.3	Measured properties of a representative sample of the galaxies from each activity group	109
5.4	Derived properties of a representative sample of the galaxies from each activity group	113
6.1	Radio flux densities of the components of the resolved galaxies selected in Fig 6.3 It is an ensemble of interesting single and multicomponent radio emitters found in the observed area.	122
6.2	Radio flux densities of the components of MH17 (PKS 2250–351). Some of the measurements compiled by Seymour et al. (2020) are presented along with our own measurements using MeerKAT (64 dishes).	123

Abbreviations

Acronym	What (it) Stands For
AAO	Anglo-Australian Telescope
AGN	Active Galactic Nuclei
ASKAP	Australian Square Kilometre Array Pathfinder
ATCA	Australia Telescope Compact Array
EMU	Evolutionary Map of the Universe
GAMA	Galaxy And Mass Assembly
GLASS	GAMA Legacy ATCA Southern Survey
KiDS	Kilo Degree Survey
MeerHOGS	MeerKAT Habitat Of Galaxies Survey
MeerKAT	Meer Karoo Array Telescope
MIGHTEE	MeerKAT International GHz Tiered Extragalactic Exploration
MOST	Molonglo Observatory Synthesis Telescope
SKA	Square Kilometre Array
SUMSS	Sydney University Molonglo Sky Survey
uGMRT	upgraded Giant Metrewave Radio Telescope
VLA	Very Large Array
WISE	Wide-field Infrared Survey Explorer

Chapter 1

Introduction

The Milky Way has been one of the sources of fascination for humanity for thousands of years. The name referring to milk has been used since antiquity and has been translated from one civilisation to the other. It is no doubt related to its appearance of a white band. It was not until 1610 that Galileo put an end to the mystery by resolving the band of light into individual stars with his telescope (see “Sidereus Nuncius” by Galileo). It was, therefore, a common belief that the entirety of stars in the universe was contained in the Milky Way. It took three more centuries for the next breakthrough when Edwin Hubble (1920) showed that the Milky Way was just one galaxy among many that compose the universe and that the Milky Way is the galaxy in which our solar system is located. Furthermore, in 1929 (Edwin Hubble 1929) discovered that the galaxies were accelerating away from one another. By studying external galaxies we have the advantage of seeing them as a whole and looking at their evolution over time. Indeed, since the speed of light is finite, the further away one looks, the younger the galaxies are.

Another great discovery is that of Zwicky (1933). By studying the rotation curve of galaxies he discovered the existence of dark matter (DM). Combining the discovery of the accelerating universe and the existence of DM, one of the greatest theories about the formation of the universe was born, namely the Λ CDM theory, which can be explained as follows. The acceleration of the universe implies that it had a beginning where it all started with a bang, in fact, a “big bang”. DM was first nearly homogeneously distributed in the universe, with only small perturbations. These perturbations grew in response to the force of gravity. The DM started to concentrate into filamentary structures, then DM halos were formed. Gas was attracted in these halos, leading to the birth of the first stars.

Gas clouds that were large enough formed galaxies. Following the DM distribution, the galaxies were also organised in filaments, groups, and eventually clusters and superclusters. Clustering has also been demonstrated in simulations and in observations. As one would expect, galaxies grow by forming new stars. On the other hand, several observations have shown galaxy-galaxy interactions. Here are the open questions: How do galaxies interact in these different environments and what is the impact on their evolution? What regulates star formation, the conversion of gas to stars?

The discovery of AGN (Matthews 1963; Oke 1963) activity resulting from the presence of supermassive black holes (SMBH) at the centre of galaxies raises new questions such as:

- How are galaxies that host AGN different from normal star-forming (SF) galaxies and what is their role in galaxy evolution?
- How reliably can we separate AGN activity from that of star formation in galaxies?

The answer to the last two questions is the focus of the present thesis.

Indeed studies over the last four decades have proven processes like AGN feedback (Croton et al. 2006), starvation of the gas supply (Larson, Tinsley & Cadwell 1980) and ram-pressure stripping (Gunn & Gott 1972) to have an influence on galaxies' key parameters such as the star formation rate (SFR), stellar mass, colour and metallicity, which make imperative the need to better understand AGN vs star formation dominated activity within galaxies.

Knowing that the universe is evolving as a whole, and up to 50% of the galaxies in the universe ($z \sim 0$) reside in groups (Eke et al. 2004; Robotham et al. 2011), probing large and contiguous areas with a diversity of environments appears to be more promising compared to studies of isolated groups or filaments. These environments provide both a statistically significant number and variety of galaxy types.

Moreover, unlike past decades where astronomy was divided into different branches from X-ray to radio astronomy, the power is now in multiwavelength astronomy. This approach is more efficient for offering a follow-up of a given process in different wavebands. This gives a wider view and better understanding of the phenomenon at work. In this regard, substantial efforts have already been made by our team. Indeed, following the location of the three equatorial fields of the galaxy and mass assembly (GAMA), cleaned catalogues of resolved galaxies in the Wide-field Survey Explorer (*WISE*) have been created and used for several multiwavelength studies (see Cluver et al. 2014; Jarrett et al. 2017 for more details). One has to be aware that the *WISE* mission, which is a widely used all-sky survey

in the mid-infrared waveband was optimised for point source galaxies. The large (resolved) sources were automatically treated as agglomerations of point sources. Therefore, any work based on nearby and extended galaxies requires preliminary treatment of the archival images in order to carefully extract the photometric and shape characteristics of resolved galaxies (see Jarrett et al. 2013, for details; the extraction and cleaning process will be also discussed in the current work). These cleaned *WISE* resolved and point source catalogues are published and serve as references for nearby IR studies.

With MeerKAT in operation now and the imminent arrival of Square Kilometre Array (SKA) phase 1, we undertook to create another cleaned *WISE* resolved and point-sources catalogue in the GAMA (G23) region which is located in the southern sky and therefore easily accessible by MeerKAT. The spectroscopic depth and broad wavelength data coverage available through GAMA allows the derivation of luminosities and the 3-D mapping of galaxies in the area (G23). This catalogue will be the first of its kind in the south.

The aim of the present project is to use the G23 galaxy catalogue (to be created), combined with the GAMA multiwavelength and redshifts, followed by MeerKAT early science data to study AGN versus star formation activity.

An outline of this thesis:

- Chapter 2 gives the background and presents the literature review.
- Chapter 3 discusses data processing. It describes how the *WISE* 's archive images are reprocessed to enhance the spatial resolution in order to extract the resolved galaxies. It shows the details of the creation of the *WISE* resolved and point-source catalogues. It also describes the derivation of parameters (photometry, redshift, etc.) in GAMA. The high-resolution Kilo-Degree Survey (KiDS) *r*-band is available for detailed visualisation.
- Chapter 4. In this chapter the researcher tests a newly created software (*ProFound*) based on a novel source extraction approach against one widely used to extract sources and their photometry in all big surveys such as *WISE*, SDSS, etc. The purpose is to use *ProFound* as an alternative for future studies.
- Chapter 5. This chapter combines the author's carefully derived *WISE* (mid-IR) catalogue with the high-quality data from GAMA (optical) to compare the widely used optical AGN selection to the mid-IR selection methods.

- Chapter 6: The analysis is expanded to the radio wavelength. We associate our continuum data using MeerKAT to the optical and IR data looking for new ways to identify hidden AGNs.
- Chapter 7 presents the conclusions. It summarises all the key findings of the project. It also discusses future work, which will require a larger area of study and ultimately the addition of X-ray analysis as a final touch to this multiwavelength study of AGNs.



UNIVERSITY *of the*
WESTERN CAPE

Chapter 2

Background and Literature Review

As introduced in the previous section, AGN and star formation play a key role in understanding the evolution of galaxies and the formation of structures in our Universe. This is a key consideration in both observational studies, as well as theoretical modelling of galaxy formation and evolution. In this section, we will describe both AGN and star formation dominated galaxies and consider how they are identified and studied, as well as methods used to separate their relative contributions.

2.1 Structures in the Universe

On large scales, galaxies are distributed in a network known as the cosmic web (Figure 2.1). It shows large empty spaces called voids and connections of galaxies in filaments, walls, and knots. The structures are the result of fluctuations in matter density in the early Universe (Bond et al. 1996; Van de Weygeart & Bond 2008). The cosmic web has a wide variety of applications to cosmology and astrophysics. In cosmology, the filaments are used to understand the missing baryons (Bouchet et al. 1992; Buchert et al. 1994), voids to study the baryon acoustic oscillations (BAO; Bouchet et al. 1995; Betancort-Rijo et al. 2000) and redshift space distortion (Kitaura et al. 2012; Hahn et al. 2015). Cosmological models based on the observed large-scale structure show that most of the baryonic matter in the Universe is hiding in the warm plasma that connects galaxies. The BAO, which represents the maximum distance that the acoustic waves could travel in the early Universe, is measured based on the galaxy distribution observed by large surveys. These

measurements are important to understand the acceleration of the expanding Universe. Recent studies have shown that galaxies inside filaments are more massive (Postman & Geller 1984), redder, and are forming fewer stars than those outside filaments (Kuutma et al. 2017; Kraljic et al. 2018). They also have an influence on the orientation of galaxies. Other studies (Tempel & Libeskind 2013; Pahwa et al. 2016; Rong & Zhang 2013; Hirv et al. 2017) have demonstrated that the spin axis of spiral and major axis of elliptical

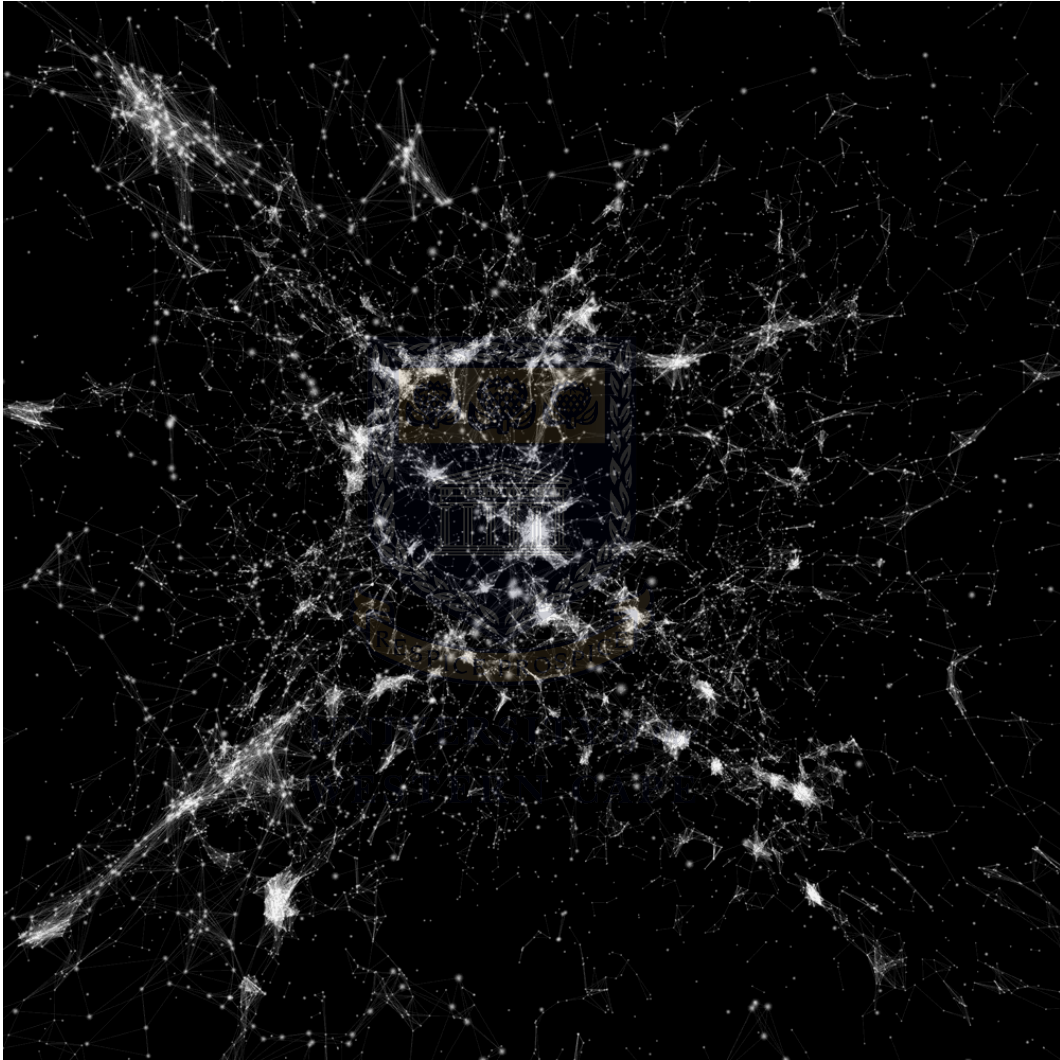


Figure 2.1: Cosmic web built based on subhalo/galaxy catalogues by astronomer Bruno Coutinho and colleagues. The model used (M1) links two nodes with a link if the distance between them is smaller than a predefined length (<http://cosmicweb.kimalbrecht.com/>; see Coutinho et al. (2016) for more details about the simulation.

galaxies are preferentially aligned with filaments. Recent simulation by Song et al. (2021) using the DisPerSE code found high-mass galaxies to be located closer to filaments. On the contrary, the SFR seems to be quenched at the edge of filaments. The authors think that the efficiency of the gas transfer inside the haloes where galaxies reside (see Lim &

Mo 2019 for more information) is reduced by the high angular momentum at the edge of filaments. We can see that the structures in the cosmic web such as filaments, clusters, etc. have an environmental influence on galaxy evolution.

This work is focused on the individual galaxies and their properties. We look at their interactions with close neighbours where it is relevant (see Section 5.3), but we do not extend to the environmental effect of the large-scale structures.

2.2 Galaxies

Galaxies are an agglomeration of celestial objects bound by gravity. They are mostly made up of DM (see Trimble 1987), stars (and planetary systems), interstellar gas, and dust. Galaxies exhibit a wide variety of morphological types and physical properties. This section describes the AGN and star formation activities within galaxies and their associated physical processes. Different categories of galaxies and their properties are also presented.

2.2.1 Radio Continuum Emission from Galaxies

In investigating the radio properties of the earth atmosphere and ionosphere for telecommunication purpose, Karl Jansky (the unit of the radio flux density “Jy” is named after him) first discovered the radio emission (at 20.5 MHz) from the centre of the Milky Way in 1931. This discovery marked the humble beginning of radio astronomy. Since then, systematic scans of the sky at radio wavelengths have been conducted, leading to great discoveries through a variety of radio emissions from almost all celestial bodies (interstellar medium, planets, galaxies, etc.).

The major source of radio emission in galaxies is synchrotron radiation. It is non-thermal radiation caused by charged particles interacting with a magnetic field. The charged particles in the presence of a magnetic field accelerate in a spiral path around the magnetic lines of force. At relativistic speed (nearly the speed of light) the emission from these particles (mostly cosmic rays) is known as synchrotron radiation (see Figure 2.2 middle panel). Another process that generates radio emission is free-free emission from HII regions. It happens when the trajectory of a fast-moving ion particle is deflected by a heavier particle (see Figure 2.2 upper panel). However, the free-free component of the radio emission is negligible and becomes significant only in the frequency windows from

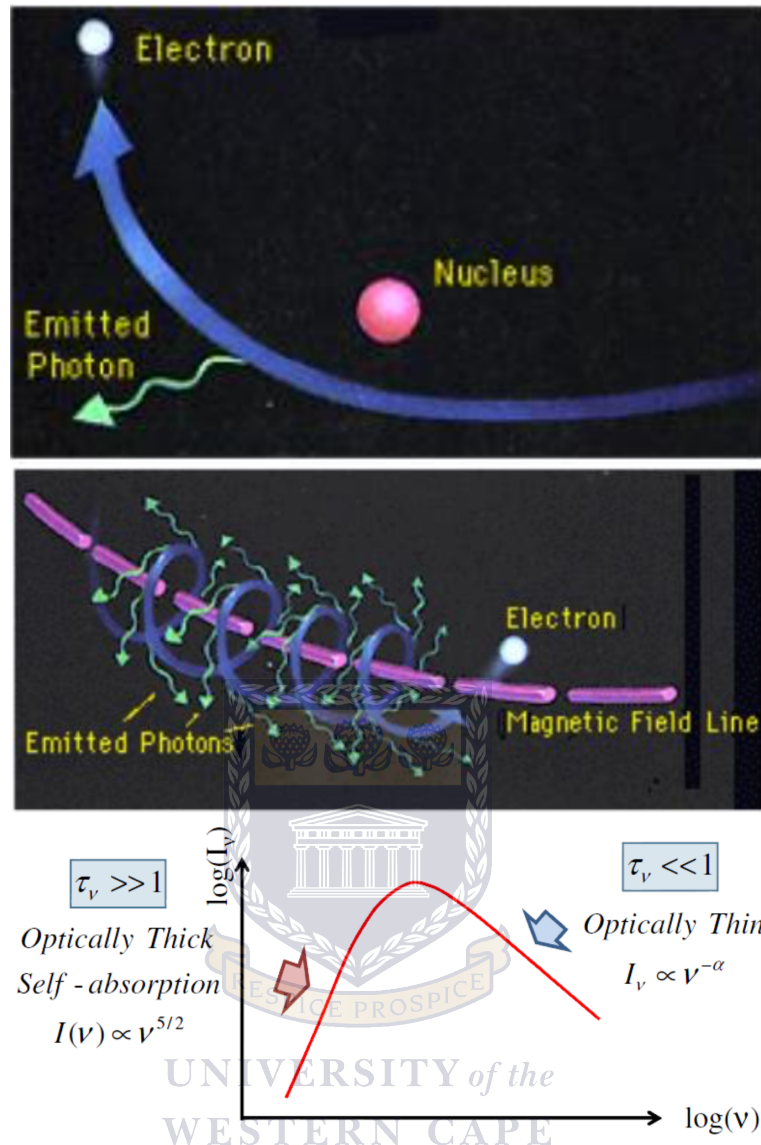


Figure 2.2: Synchrotron emission processes and the schematic spectrum. The upper panel shows a free-free emission process in which a free charged (and relativistic) particle moving around a heavier particle releases a photon and goes free afterward (image credit: NCRA-TIFR). It generally happens in the HII regions within the galaxy. In the middle panel, we have synchrotron emission (image credit: OER, Free Education Resource Online). It happens when relativistic charged particles (cosmic rays, e.g., electrons, protons, and heavier nuclei) interact with interstellar magnetic fields. The schematic synchrotron power spectrum is presented in the lower panel (image credit: astro.caltech.edu). In the optically thick part (left side) both the free-free and synchrotron emission are drastically reduced and the spectrum is dominated by self-absorption. The emission on the right side (optically thin) is a combination of synchrotron and free-free emission. However, the synchrotron largely dominates from ~ 1 GHz up to 30 GHz. The contribution from the free-free emission becomes important in the window from 30-200 GHz. The spectrum will rise again with the thermal emission beyond 200 GHz (a good description of the radio power spectrum is given in Condon 1992).

30-200 GHz. These two processes require a strong magnetic field, which is generated in SF regions by supernova remnants. In AGNs, the magnetic field is thought to be generated by high-energy jets.

The cosmic rays are very energetic particles (photons and atomic ions) with energies that can reach $\sim 10^{20}$ eV (millions of times the energy attainable in accelerators such as the Large Hadron Collider), and up to 90% are simple protons (e. g., hydrogen nuclei). It is believed that AGNs and pulsars have rotating magnetospheres capable of forcing the particles into centrifugal acceleration driving them to ultra-high energies. Also, during supernova explosions, the material (ejecta) from the star expands at very high speed (thousands of km s^{-1}), creating numerous shocks in the interstellar medium. The particles scattering during these shocks gain energy (see Bell 1978; Blandford & Ostriker 1978) through the process called “diffusive shock acceleration”.

The synchrotron emission behaves like a power law, which is represented on the optically thin part (see Figure 2.2 lower panel) by the Equation 2.1.

$$S_\nu \propto \nu^{-\alpha}, \quad (2.1)$$

where S_ν is the flux density, ν the frequency, and α the spectral index. Generally, α has a value between 0.7 and 0.8 (e.g., Condon 1992; Intema et al. 2017; Smolcic et al. 2017a). In AGNs the turn-over of the flux density is around $\nu \sim 1$ GHz. Often below this frequency, the HII regions start to become optically thick. In this case, both the free-free and synchrotron flux densities are reduced and the source is a power law whose index α is 5/2.

UNIVERSITY of the
WESTERN CAPE

2.2.2 Star-forming Galaxies

When studying galaxies, one of the most important questions is to know whether they are inactive, actively forming stars, and/or have AGN activity. The life of galaxies can be described as an early stage dominated by active star formation. The galaxies still have immense reservoirs of cold gas and are building up stellar mass (these galaxies are referred to as SF galaxies). As they grow through mergers and the formation of new stars, they show AGN activity via the infall of material into the central SMBH. Finally, when their gas content is exhausted, they become inactive (quenched). Elliptical (early-type) galaxies generally have very low SFR, while spirals (late-type) are active star formers. Knowing the rate at which new stars are being formed is important to understand the evolution stage of the galaxy. We should note that although galaxies dominated by AGN activity have a

different classification from SF galaxies, most of them are still actively forming stars.

It is well known that stars are formed from the interstellar gas that collapses when

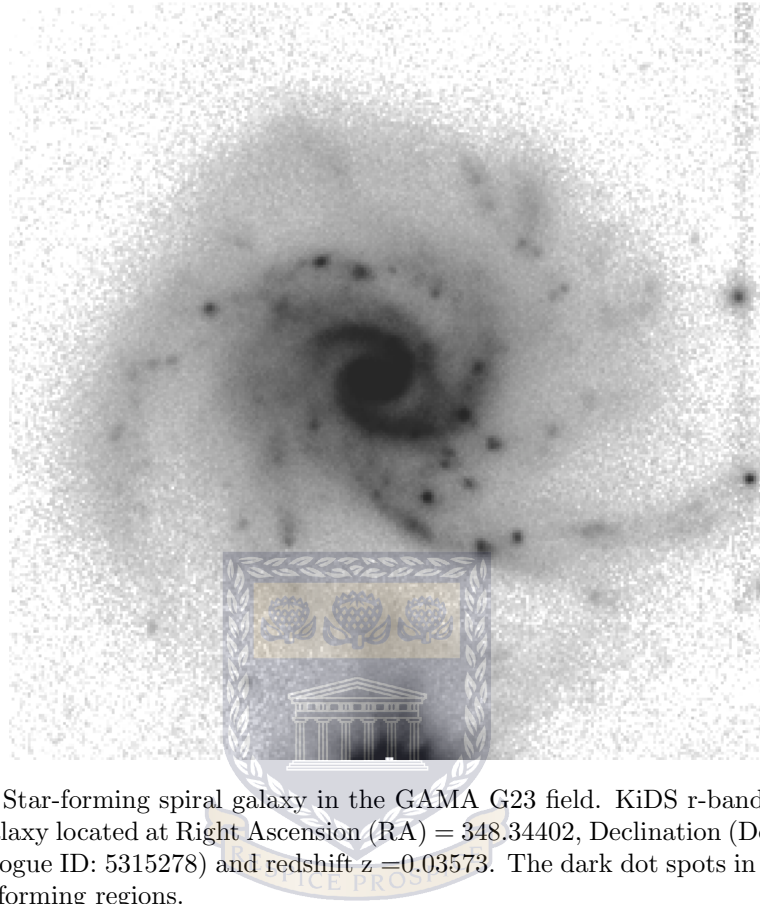


Figure 2.3: Star-forming spiral galaxy in the GAMA G23 field. KiDS r-band image (56×56 arcsec) of a galaxy located at Right Ascension (RA) = 348.34402, Declination (Dec) = -34.15076 (GAMA catalogue ID: 5315278) and redshift $z = 0.03573$. The dark dot spots in the spiral arms are high star-forming regions.

reaching a certain density threshold. The SFR is the estimation of newly forming stars as opposed to the old stellar population, reflected in a galaxy's stellar mass. Figure 2.3 is the KiDS r-band image (a high-resolution image) of a galaxy with high SFR visible throughout the disk. Schmidt (1959) proposed a relationship between SFR and gas density. Later, observations by Kennicutt (1998a, 1998b) found a strong relationship between star formation surface density and the surface density of cold gas, leading to the so-called Kennicutt-Schmidt (K-S) law that is widely used in theoretical models of galaxy evolution. Studies of nearby galaxies (Chen et al. 2015; Tan et al. 2018) using gas tracers such as HCN, HCO⁺ show that only the denser parts of the molecular clouds are directly linked to star formation activity.

The ultraviolet (UV) continuum is dominated by the emission from young stars, making it a very good proxy for star formation. However, as the UV flux is not completely free from old stars emission, model synthesis (initial mass function, IMF; see review by Kennicutt et al. 1998a) is used to convert the flux into SFR. Here the accuracy of the SFR depends

on the choice of the IMF. An IMF that is not adapted to the galaxy population of interest can lead to significant errors (up to $> 50\%$ errors; Leitherer et al. 1995). Also, the UV is heavily extinct by the dust surrounding stars (Murphy et al. 2011; Reddy et al. 2012) and therefore requires corrections to get the true flux. The ionised gas surrounding young stars is responsible for optical emission lines such as $H\alpha$ (Anders & Fritze-v. Alvensleben 2003; Reines et al. 2010) present in the spectra of SF galaxies. It makes the $H\alpha$ line another good tracer of SFR (Casasola et al. 2015), but also subject to extinction due to dust. On the other hand, spectroscopical surveys are time-consuming and very scarce, making the IR spectrum with all-sky survey such as IRAS, Spitzer, and *WISE* a more accessible way to determine SFR for galaxies in large scale studies. The $11.3 \mu\text{m}$ PAHs (polycyclic aromatic hydrocarbon) are large molecules excited by ultraviolet radiation from young stars, as well as radiation from older, evolved stars (see, for example, Kaneda et al. 2008). The $7.7 \mu\text{m}$ PAHs are more related to the current star formation and generally invisible in passive disks. They ($7.7 \mu\text{m}$ and $11.3 \mu\text{m}$ PAHs) are detected in the broad W3 ($12 \mu\text{m}$) band. Thus, W3 appears to be a reliable SFR measure as much as the optical $H\alpha$ in the absence of strong silicate absorption common in compact, dust-embedded starbursts, and powerful AGNs (see Cluver et al. 2014; Cluver et al. 2017).

2.2.3 Star-forming Main Sequence

Several studies have shown a tight relation between the SFR and the stellar mass in SF galaxies (known as the main sequence; MS) up to a redshift of ~ 4 (Elbaz et al. 2007; Noeske et al. 2007; Kashino et al. 2013; Kurczynski et al. 2016; Pearson et al. 2018). More recent work by Cluver et al. (2020), using a sample of relatively isolated SF galaxies in the GAMA Galaxy Group Catalog (G^3C), is presented in Figure 2.4a, with the best fit given by Equation 2.2. The SFR- M_{stellar} relation appears to be one of the most important in constraining galaxy formation and evolution models.

$$\log \text{SFR}(M_{\odot}\text{yr}^{-1}) = 0.93 \times \log M_{\text{stellar}}(M_{\odot}) - 9.08 \quad (2.2)$$

It seems to be driven by the rate of gas flow (Bouche et al. 2010; Scoville et al. 2017). The galaxies below the main sequence (located on the right side of the dashed line) are generally passive galaxies, whereas starbursts lie above (Leslie et al. 2016; Tacchella et al. 2016).

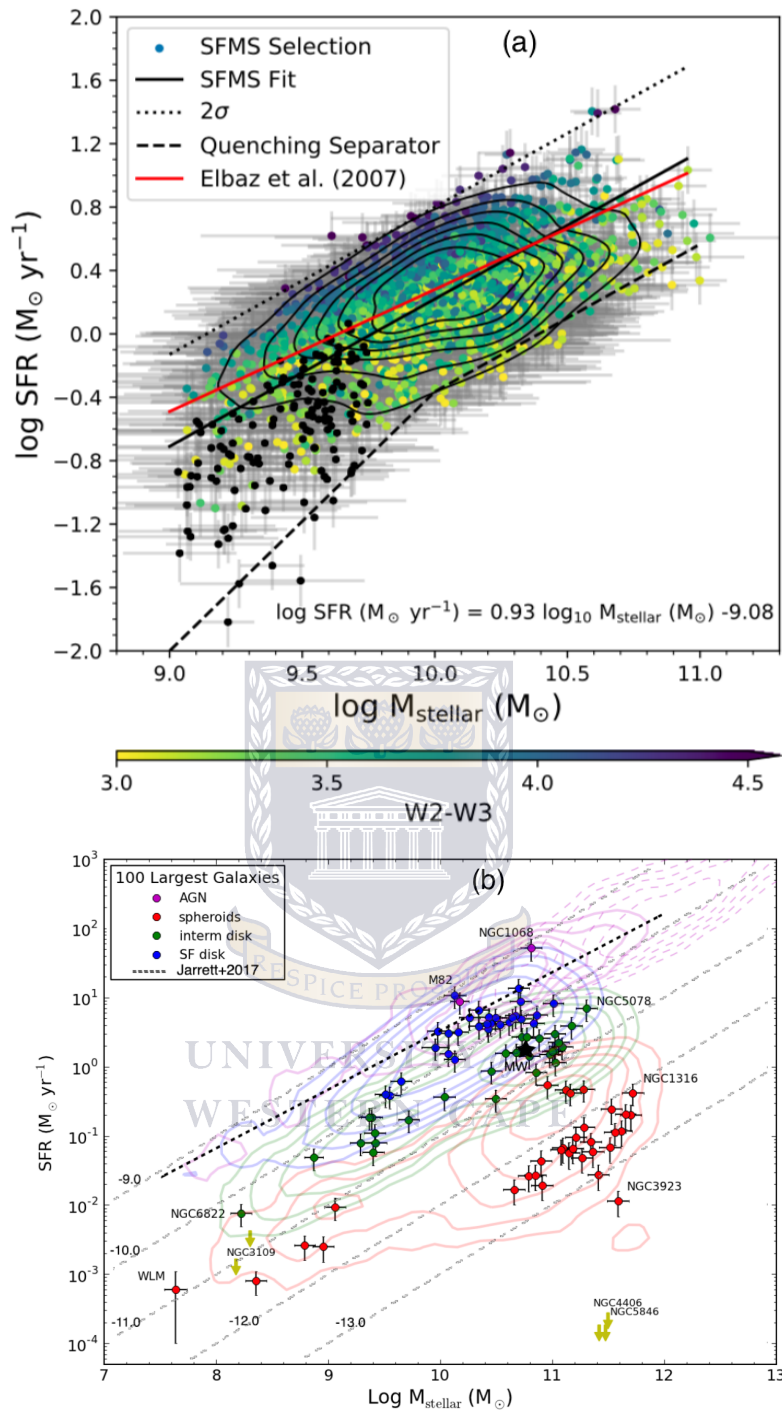


Figure 2.4: Star-forming galaxy main sequence. (a): main sequence from Cluver et al. (2020). The sample is represented by the coloured points. Some low mass galaxies with high S/N are added for comparison. Below the dashed line lie the quenched galaxies (they are no longer forming new stars or have very low SFR). (b): galaxy main sequence from Jarrett et al. (2019) using the 100 largest galaxies in WISE (extended sources). The extraction of the WISE extended sources is described in Section 3.3.2. The contours represent the different groups of galaxies and the faint dashed lines are lines of constant $\text{Log sSFR} = -13, -12, -11, -10$ and -9.0 yr^{-1} .

Several works in literature have shown that SFR density decreases by a factor of 10 since $z = 1$ (Madau et al. 1996; Lilly et al. 1996; Perez-Gonzalez et al. 2005). However, this knowledge does not give any information about how individual galaxies are contributing to the recent SFR. The star formation rate per unit galaxy stellar mass or specific star formation rate (sSFR; e.g, Brinchmann & Ellis 2000) shows how the SF contributes to galaxy growth for galaxies of different masses at different times in the history of the universe.

In the figure (Figure 2.4a), the passive or quenched galaxies would be found at high stellar mass ($\log M_{\text{stellar}} > 10 M_{\odot}$) and relatively low SFR. Their gas content is probably getting depleted such that they are forming new stars at a very low rate. The high SFR found in the starbursts is typically related to major mergers of galaxies or starburst events (Whitaker et al. 2012; Silverman et al. 2018). Some galaxies with extreme SFR exceeding $10^3 M_{\odot}\text{yr}^{-1}$ are very dusty and referred to as dusty SF galaxies (DSFG). However, not all the DSFG seem to be the result of major mergers. Indeed, the gas accretion could be a driving factor in some cases, as shown in recent works (Michalowski et al. 2017).

The galaxies above the main sequence with high specific star formation rates (sSFR) are less clustered than those below the main sequence showing lower sSFR at fixed stellar mass (Berti et al. 2021). This relates the scatter seen in the main sequence to the environment in which the galaxies reside.

Figure 2.4b shows the main sequence from Jarrett et al. (2019) for the 100 largest galaxies in *WISE*. In addition to the SF galaxies, populations of spheroids, AGNs, and intermediate disk galaxies are overplotted. As can be seen, the AGNs share the same space with the SF galaxies at the highest SFR limit. But, as we will see later in Chapters 5 and 6, the SFR and M_{stellar} of AGNs are overestimated. It is, therefore, clear that the sample of galaxies used to determine the galaxy main sequence is very important. Proper removal of the AGNs is needed because their inclusion will lead to an inaccurately steeper SF main sequence relation. This is one of the many reasons why it is imperative to find better ways to separate AGNs from SF galaxies.

2.2.4 Active Galactic Nuclei

Observations by Edward Fath (1909) in the early 1900 showed spectroscopic emission lines in the nuclei of NGC1068 and M81, and later the radio jet in M87 was discovered (Heber Curtis 1918). The idea of AGN started with the work of Carl Seyfert (1943), which showed some galaxies with unusually broad emission lines and became effective when Baade and

Minkowski (1954) found similar emission lines in the galaxy associated with the Cygnus A radio source. Since then AGNs have been discovered in various wavelength regimes, each one providing different physics. We introduce here the AGN activity and the diverse groups based mostly on the viewing angle often described as the unification theory.

2.2.4.1 The Unification Theory

According to the unification model of AGN, all the different classes of AGN are just the same physical object observed under different orientation conditions (Antonucci 1993). Figure 2.5 presents diverse nomenclatures of AGN that can be related to the viewing angle of the observer. At the centre of galaxies lie SMBH surrounded by an accretion disk made by diffuse materials in rotation. The central engine is believed to be obscured by a toroidal structure (the torus; coplanar to the accretion disk), which is not yet well understood. In the perpendicular direction to the disk, the region within the torus height is the broad-line (BL) region. Close enough to the SMBH, the temperature, speed, and gas density are appropriate for the formation of broad optical lines (e.g., broad $H\alpha$). Beyond this zone (still in the perpendicular direction) lies the narrow-line region where optical lines such as $[O III]$ are produced. In SF galaxies the $[O III]$ lines are very narrow, while those related to AGN activity are broad with line widths that can range from 50 to 500 km s^{-1} (see Boroson 2005; Liu et al. 2013).

At first, Figure 2.5 can be divided into two parts separated by the horizontal grey dashed line. The lower side without the jet represents the radio-quiet AGNs. The observer pointing directly at the central black hole sees a Seyfert 1. It becomes a Seyfert 2 when the viewing angle is inclined, passing slightly through the torus. Seyferts have an intensively bright core with strong emission lines, but their host galaxies are still visible, unlike in quasars (see description of quasi-stellar objects [QSOs] in the next section).

The upper sides with the jet represent the radio-loud AGNs. The radio-loud AGNs have powerful jets that contribute significantly to the total luminosity of the galaxies. They are generally associated with elliptical galaxies that have been through a recent merger. The radio-quiet AGNs, on the other hand, with weaker radio emission, are mostly found in spiral galaxies. The difference between these two classes is thought to be related to the spin of the black hole (see Wilson & Colbert 1995 for more details). The Fanaroff and J.M. Riley (FR; Fanaroff & Riley 1974) types FRI and FRII are low- and high-power radio-loud AGNs respectively. The jet in BL Lacertae (BL Lac) and flat-spectrum radio

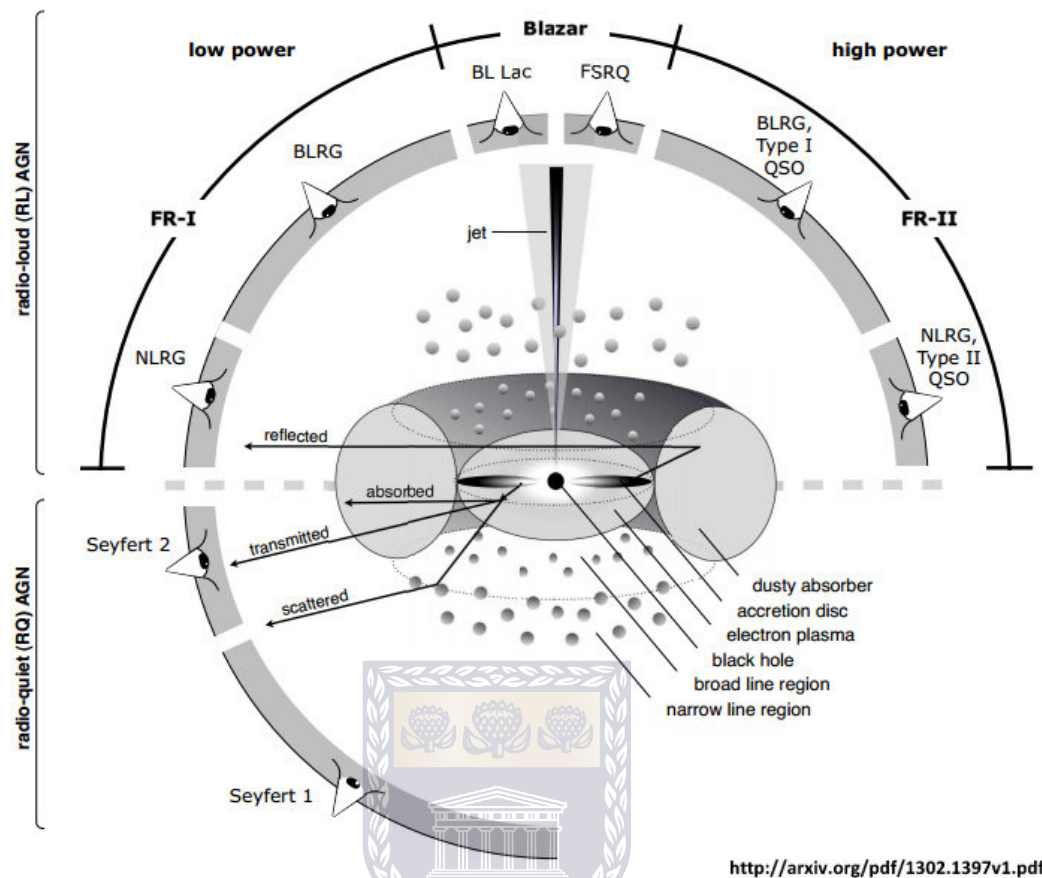


Figure 2.5: Schematic figure showing the AGN unification theory. The different components of AGN activity are presented. The viewing angles most likely to explain most of the categories of AGN are also highlighted. Image reproduced from Beckmann et al. (2012).

quasars points directly at the observer or has a very small inclination angle. Their fluxes vary significantly over a short time scale (hours or days), similar to variable stars. Unlike other blazars, BL Lacertae (BL Lac) have a spectrum dominated by continuum emission with almost no emission or absorption lines. Powerful jets, seen at higher viewing angles but where the central engine is still visible, are type I QSOs. Type II QSOs are observed through a much higher viewing angle, which is obscured by the torus. The light seen comes from the reflecting area of the torus.

Although the viewing angle can explain the difference between several classes of AGNs, some of them have characteristics that cannot be justified by only a simple orientation effect. For example, the spectra of many radio-loud AGNs lack optical excitation lines, which are the major ingredients for the classification of optical AGNs (Laing et al. 1994), and others seem not to have a torus (Ogle et al. 2006) and/or an accretion disk (Hardcastle et al. 2006). Galaxies with an accretion disk and torus radiate efficiently across the whole electromagnetic spectrum while the ones lacking these structures (disk and dusty torus)

emit most of their energy as powerful radio jets (Merloni & Heinz 2007; Hardcastle et al. 2009).

Figure 2.6 is the very large array (VLA) image of Cygnus A observed at 1.4 GHz. It

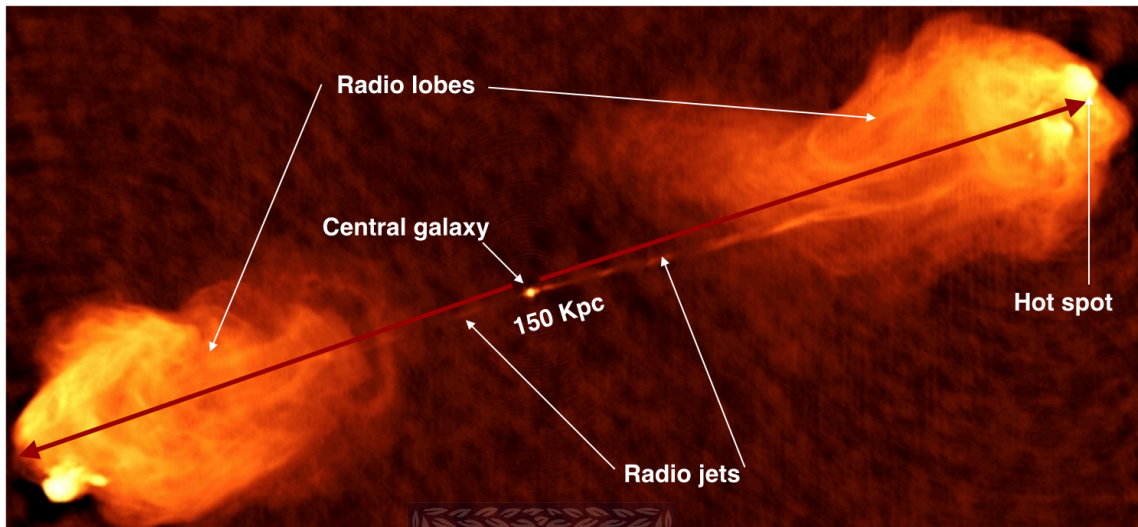


Figure 2.6: VLA image at 1.4 GHz of Cygnus A. It is one of the strongest radio galaxy and among the first to be discovered (in 1939 by Grote Reber). In the image, the wide span of the radio lobes is shown by the red arrows. The source in the middle (between the two arrows) is the central galaxy. The temperature increases from the red to the white colour. The white represents the hot spots located at the front of the jets in both directions. Image credit: NRAO/AU

has two massive lobes expanding ~ 150 Kpc with hotspots at each edge. Hotspots are believed to be products of the shock between the jet and the interstellar medium. During this interaction, the kinetic energy is probably converted into relativistic particles.

Radio jets are ionised materials from the accretion disk that are ejected along the rotation axis of the black hole (at velocities close to the speed of light) when in contact with the strong magnetic field around the black hole (Sadowski et al. 2013; Pu et al. 2015). The continuum radio emission is believed to be due to synchrotron emission by the relativistic electrons that rotate in the magnetic field carried by the jets. When jets are visible on both sides of the galaxy and brighter toward the edge of the lobes, they are referred to as FR II. On the contrary, we have FR I when the brightness decreases toward the edge of the jets. About 10% of the AGNs release their energy in form of powerful jets (see Netzer 2015; Hada et al. 2018), which interact with the interstellar medium therefore influencing the evolution of the galaxy (see Fabian 2012; Hardcastle & Croston 2020).

Moving from the central part (more energetic) to the outer shells of an AGN (less energetic) some identification methods exist across the diverse wavebands and will be described in the next subsections.

2.2.4.2 Luminous Infrared and Ultraluminous Infrared Galaxies

Luminous IR galaxies (LIRGs; Sanders & Mirabel 1996) are very bright galaxies with infrared luminosity $> 10^{11}L_{\odot}$. Most of their energy is emitted in the IR waveband owing to their high star formation, but could also be generated by a AGN activity at the centre of the galaxy. The star formation and the AGN activities generate (both) enormous amounts of dust, which absorb the visible light and reemit it in the IR.

At higher luminosity ($> 10^{12}L_{\odot}$), we have the ultraluminous IR galaxies (ULIRGs). The LIRGs and ULIRGs are generally seen among interacting galaxies, which could be a boosting factor for star formation. It is believed that they are products of an evolutionary merger scenario where LIRGs are found in systems at the beginning of the merging process and evolve into ULIRGs at a later stage.

2.2.4.3 QSOs

Quasi-stellar radio sources contracted as quasars (also known as quasi-stellar objects; or QSO) are a type of AGN with supermassive black holes reaching billions of stellar masses (Wu et al. 2015). The core with extreme power density can be up to 100 times brighter than the host making them look like stars (they are among the most luminous objects in the Universe). Although they were first discovered in the radio waveband and subsequently identified as high-redshift objects with anomalous emission lines, only 10% are radio-loud. Galaxies with radio luminosity $> 10^{23} \text{ W Hz}^{-1}$ at 1.4 GHz are commonly classified as radio-loud (see Best et al. 2005). Quasars can be classified into different groups, such as radio-loud or radio-quiet quasars, according to their radio properties. The radio-loud quasars for which the jet is directed toward the observer are known as optically violent variable quasars. Type II quasars are higher luminosity Seyfert 2. Their accretion disks are generally highly obscured by dust.

2.2.4.4 LINERs

The low-ionisation nuclear emission-line regions (LINER) are common galaxies in the nearby Universe (Heckman 1980; Ho et al. 1997). They are found in a wide variety of galaxies (ellipticals, lenticulars, and early-type spirals), but very rare among irregular

galaxies (Ho et al. 1997). LINERs have stronger low ionisation forbidden lines ($[\text{N II}]$, $[\text{S II}]$, $[\text{O II}]$, $[\text{O I}]$) compared to $\text{H}\beta$, $\text{H}\alpha$ and also $[\text{O III}]$ lines.

There have been scientific debates about the source of the low-ionisation emission-lines region (LIER). Believed to be caused by AGN activity at the centre of the galaxy, recent studies are pointing at other potential origins. Belfiore et al. (2016) showed that the low-ionisation emission-line region seen in LINERs are more probably coming from hot evolved (post-asymptotic giant branch) stars disseminated throughout the galaxy rather than a central source (the AGN). Likewise, Yan and Blanton (2012) reject AGN as the primary source of the LIER in LINERs. A more reconciling view is that LINERs are associated with low accretion rate AGNs. In this case, the central AGN does not have enough power to ionise on large scale as usually seen in LINERs. Several studies (Dopita et al. 1996, 1997; Molina et al. 2018) therefore present shocks between the jets or outflows (powerful wind generated in the vicinity of the AGN) with their immediate environment as an additional source of ionisation. Molina et al. (2018) propose a scenario where a low-power AGN can photoionise the gas within ~ 20 pc and ionisation by shock on a larger scale. The true nature of LINERs is not well understood.

2.2.4.5 Seyferts

Seyferts are AGNs with the closest brightness to that of quasars, but whose hosts are clearly visible, unlike quasars. Viewed in the optical wavelength they generally look like normal spiral galaxies (Adams 1977) with the core as bright as the entire population of stars within the host (Seyfert 1943). They have a very compact core (< 100 pc) and are classified as Seyfert 1 and Seyfert 2 according to the width of their optical spectral lines, with intermediate classification in between these two main groups (Osterbrock & Koski 1976). The type 1 Seyfert shows a combination of broad allowed and narrow forbidden lines, whereas both allowed and forbidden lines are narrow in Seyfert 2 (see the viewing angle for type 1 and 2 Seyfert in figure 2.5). Figure 2.7 shows NGC1068, a well-known Seyfert with an extremely bright nucleus emitting broad emission lines. One can observe regions of active star formation (represented in red colour) throughout the spiral arms.

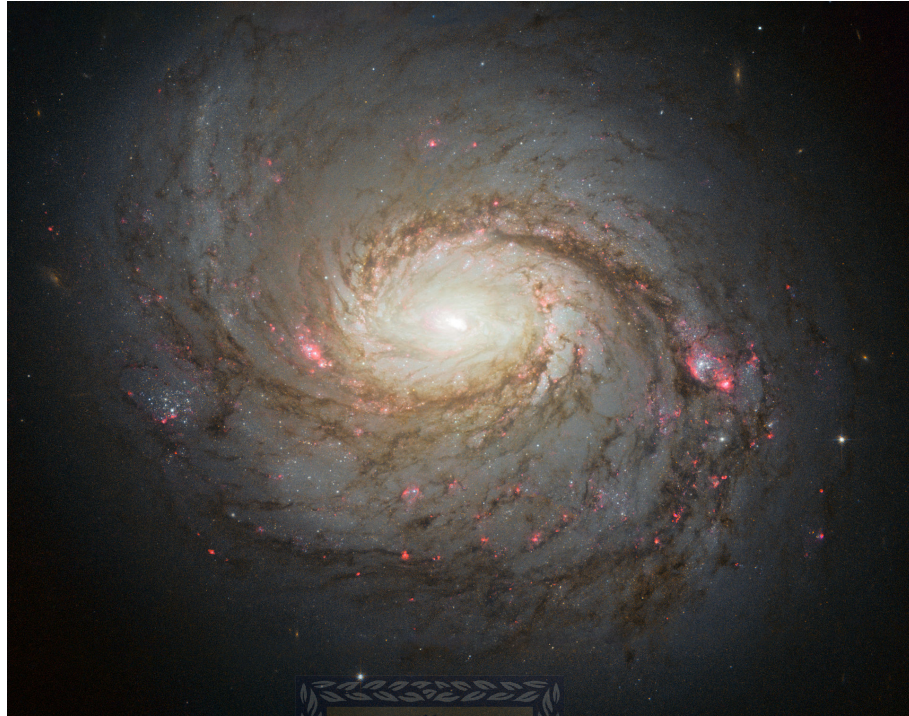


Figure 2.7: Image of NGC1068. A well-known Seyfert and starburst galaxy. It is a relatively close (14.4 Mpc away) bright AGN, which has been extensively studied and was one of the first galaxies to be classified as a Seyfert. Image credit: NASA, ESA and A. van der Hoeven.

2.2.4.6 High Excitation Radio Galaxies and Low Excitation Radio Galaxies

Radio-loud AGNs seem to be fundamentally divided into two groups based on their accretion mode. One is made up of galaxies having a dusty torus that radiates in the mid-IR spectrum and an accretion disk causing excitation lines detectible in the optical spectrum, these are referred to as high excitation radio galaxies (or ‘quasar-mode’; HERGs). They are generally found in low mass galaxies and accrete the cold gas (cold accretion mode) within the host galaxy into the central black hole through a thin disk (Shakura and Sunyaev 1973).

The galaxies from the second group (low excitation radio galaxies-LERGs) seem to lack both a torus and an accretion disk. They do not present the optical lines seen in the previous group and are thus referred to as LERG (radio-mode). The HERGs have mostly accretion rates between 1 and 10% of Eddington, while LERGs accrete at a lower rate $< 1\%$ Eddington (Best & Heckman 2012). For a SMBH, the Eddington accretion rate represents the accretion rate at which it radiates the maximum luminosity. LERGs are predominantly found in big galaxies at the centre of groups and clusters (Burns 1990; Best et al. 2007). They have an older stellar population compared to HERGs (Miraghaei & Best 2017; Ching et al. 2017) and accrete the gas from their hot environment into the central black hole (hot

accretion mode). In the infrared waveband HERGs and LERGs are distributed all over the *WISE* colour-colour diagram, but the spheroid region in this diagram is mostly populated by LERGs (see Jarrett et al. 2017). We will briefly discuss their radio properties in Section 6.3.4.

2.3 AGN Identification

The AGN activity involves radiations over a wide range of wavelengths. This enables a large number of classifications through observations at different electromagnetic bands. Each one of these observations provides additional information about the physics of the AGN's substructures. In this section we describe the AGN selection methods, the physics we can learn from them, and the strengths and shortcomings of each selection method.

2.3.1 X-ray Selection of AGN

AGNs generate a tremendous amount of energy owing to the accretion material falling into the supermassive black hole. All the classification methods try to relate physical processes to this energy that is much higher than that generated by the star formation within galaxies. The temperatures generated are inversely proportional to the distance from the SMBH. Hard X-ray ($> 2\text{KeV}$) radiation is the result of Compton scattering from the accretion disk photons in the corona (Haardt & Maraschi 1993) close to the SMBH, while the UV, optical, and IR radiations are from the outer region (Kubota & Done 2018). This makes the X-ray the most direct detection of AGN activity. The hard X-ray emissions have the advantage of being powerful enough even to see through obscured AGNs. It can penetrate high hydrogen column densities (Xue 2017) and dust over a wide range of temperatures.

In comparison, the optical identification method (see below) only sees the most luminous and unobscured AGNs. It becomes less reliable at high redshift with increasing misclassification between AGN and SF galaxies (Dickey et al. 2016). In the IR it is sometimes difficult to disentangle the emission of the dusty torus from that generated by the SF-heated interstellar medium (ISM) in the host galaxy.

The X-ray, although the best classification method is not without limits. Indeed, the X-ray is unable to identify Compton-thick AGNs (Li et al. 2019) and the rare population

of intrinsically X-ray weak AGNs (Teng et al. 2014; Luo et al. 2014). There is also limited capacity with space-borne X-ray telescopes.

2.3.2 Optically Selected AGN

From observational and simulation works, [Ne v] λ 3426, [O II] λ 3727, [He II] λ 4686, H β λ 4861, [O III] λ 5007, [O I] λ 6300, H α λ 6563, and [N II] λ 6584 were proposed as potentially useful lines for discriminating between different excitation mechanisms (see Baldwin, Phillips & Terlevich 1981). Figure 2.8 presents a spectrum (black line) from the GAMA catalogue. The pics (vertical dash lines) represent the optical lines with the names written on top. The green line is the 1 sigma error and the blue is the sky (where available), smoothed by five pixels.

Baldwin, phillips and Terlevich (1981), combining some specific optical line ratios

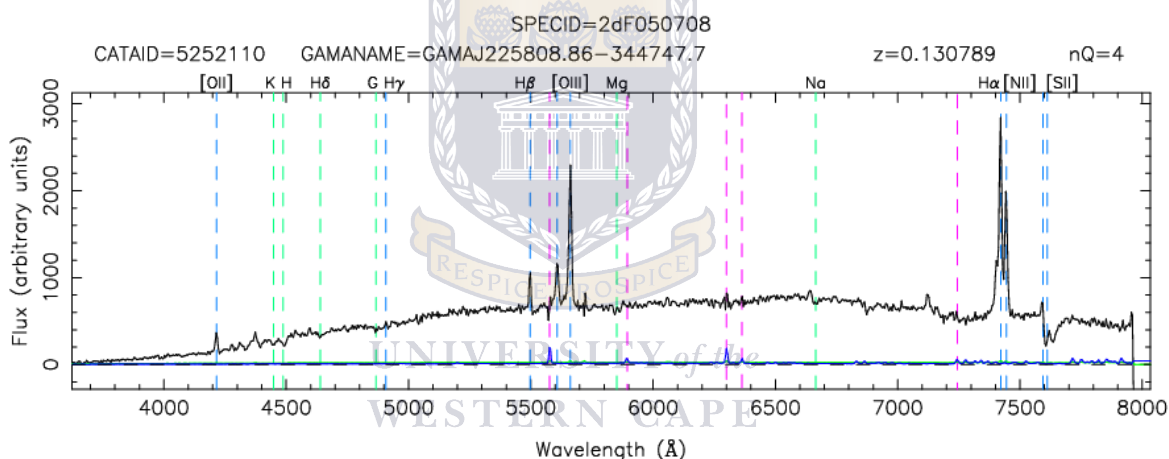


Figure 2.8: Calibrated optical spectrum from GAMA (CATAID: 5252110) of a galaxy classified as AGN in optical and in WISE wavelength regimes (see classification in Table 5.3). Most of the optical lines can be clearly seen, except for [Ne v] λ 3426 and [He II] λ 4686, which are not represented on GAMA spectra.

([O III]/H β vs [N II]/H α ; [O III]/H β vs [S II]/H α ; [O III]/H β vs [O I]/H α), were able to put a hard limit between pure optical AGNs and non-AGNs. The different planes are often referred to as *Baldwin, phillips & Terlevich (BPT)* diagrams. According to their studies, these line ratios are sensitive to the hardness of the ionising extreme ultraviolet radiation, such that they can provide an important constraint on the shape of the extreme ultraviolet spectrum, and may also be used to estimate the mean ionisation parameter and metallicity of the galaxies. AGNs have a much harder ionising spectrum than hot stars, they can thus be differentiated from starburst galaxies in many cases, notably when optical lines are

present. As galaxy surveys became much larger with better data, the BPT diagram was also improved (see Veilleux et al. 1987; Kewley et al. 2001; Kauffmann et al. 2003; Kewley et al. 2006). The most frequently used version of the BPT (also used in the current study, see Chapter 5) is presented in Kewley et al. (2006).

Taking into account the complementary work of Kauffmann et al. (2003), they (Kewley et al. (2006) selected AGN and SF galaxies, leaving an intermediate group in between the two samples, which is presumably a mixture of AGN and SF galaxies. Figure 2.9 (a) shows the AGNs above the red line; below the dashed-blue line lie the SF galaxies and the composites are located between the two groups. In Figure 2.9 (b) and (c), the thick blue line (an error gap delimited by the two lighter lines) can differentiate between Seyferts and LINERs. However, the BPT classifications are only limited to the galaxies with emission lines, leaving the ones with absorption lines unclassified. In addition, one should be particularly cautious while using the version in Figure 2.9 (a). The classification of the low-mass AGNs can be inaccurate owing to their low metallicity, which would affect the $[\text{N II}]$ line (see Section 5.2.1 for more details about low-mass AGNs' classification).

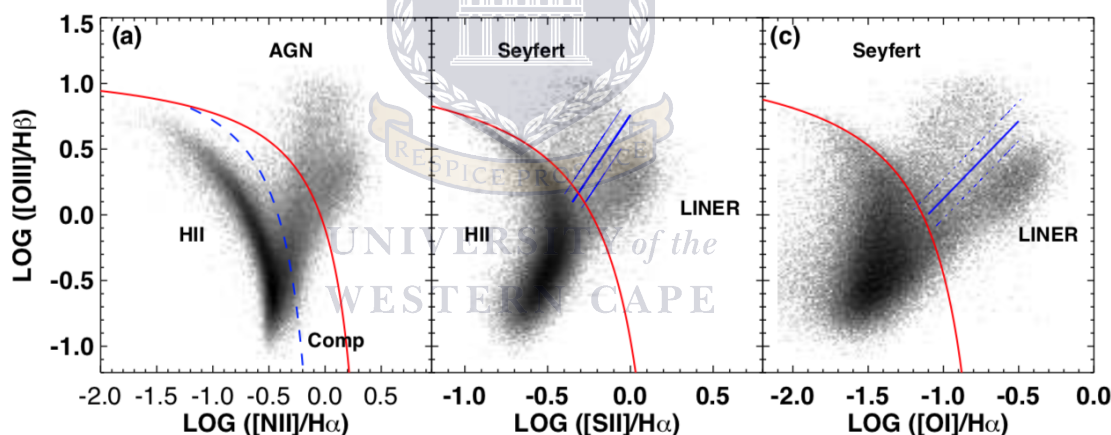


Figure 2.9: Optical emission line BPT diagrams. (a): The $[\text{O III}]5007/\text{H}\beta$ vs. $[\text{N II}]6583/\text{H}\alpha$ classification diagram. The red line represents the limit between AGN and Not AGN galaxies (Kewley et al. 2006) and the Kauffmann et al. (2003) pure star formation line (blue dashed). (b): $[\text{O III}]5007/\text{H}\beta$ vs. $[\text{S II}]6716,6731/\text{H}\alpha$. The extreme starburst classification line (red) and the Seyfert-LINER separation line (thick solid blue) by Kewley et al. (2006). Above the red line lie the AGNs (Seyferts or LINERs) and below the galaxies that are not AGN. (c) is similar to (b) with the $[\text{S II}]6716,6731/\text{H}\alpha$ ratio replaced by $[\text{S I}]6364/\text{H}\alpha$. Image reproduced from Kewley et al. (2006).

2.3.3 AGN in the Mid-infrared wavelengths

The AGN activity is mostly related to cold gas and dust falling into the central supermassive black hole within the host galaxy. The radiation from the torus of dust around the SMBH,

which is heated up to its sublimation limit of ~ 1500 K (see Assef et al. 2013), can be detected in the mid-IR (refers to the IR wavelengths except clearly stated otherwise) and *WISE* appears to be well equipped for this task. Launched in December 2009, *WISE* surveyed the entire sky in four mid-IR bands: $3.4 \mu\text{m}$, $4.6 \mu\text{m}$, $12 \mu\text{m}$, and $22 \mu\text{m}$ respectively, W1, W2, W3 and W4 (Jarrett et al. 2017).

While W1 and W2 are both sensitive to the continuum emission from evolved stars,

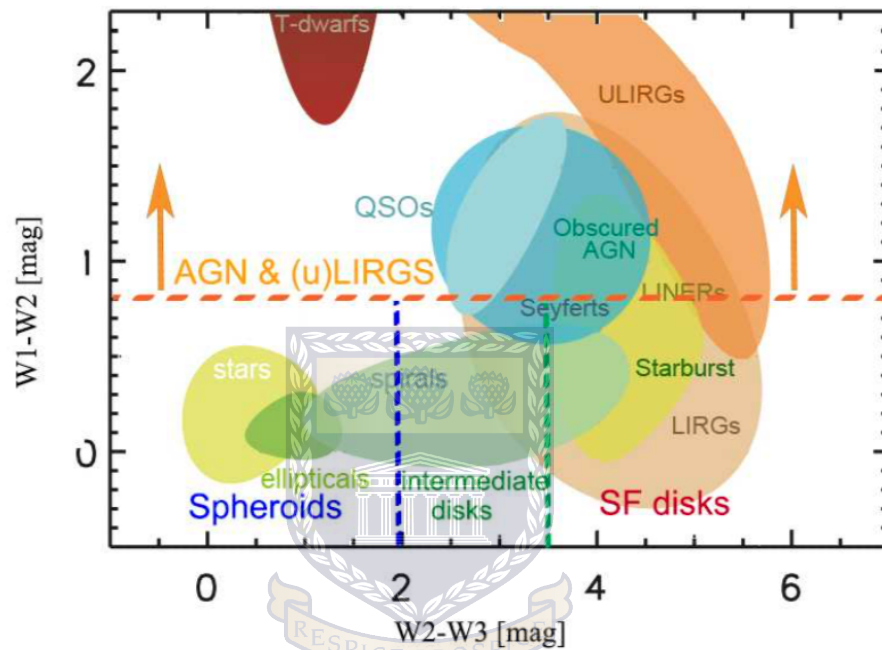


Figure 2.10: *WISE* W1[$3.4 \mu\text{m}$] - W2[$4.6 \mu\text{m}$] vs W2[$4.6 \mu\text{m}$] - W3[$12 \mu\text{m}$] colours (colour-colour diagram). The location of the different classes of galaxies are represented. Stars and ellipticals are low in colours while ULIRGs and obscured AGN are high in both colours. The T-dwarfs are the brightest in W1-W2 colours. Image reproduced from Jarrett et al. (2017).

the W2 band is additionally sensitive to hot dust; hence, this makes the $3.4 \mu\text{m} - 4.6 \mu\text{m}$ colour a good diagnostic to identify galaxies dominated globally by AGN emission (see e.g., Jarrett et al. 2011; Stern et al. 2012). The technique entails projecting the galaxy colours W1 - W2 vs W2 - W3, known as the colour-colour diagram (Figure 2.10). Figure 2.10 from Jarrett et al. (2017) is a perfect illustration of how different classes of objects are distributed in the *WISE* colour-colour diagram based on how colours change with redshift. Stars and early-type galaxies have colours near zero, while brown dwarfs are very red in W1-W2, and ULIRGs tend to be red in both colours. The galaxies dominated by an AGN have a W1-W2 colour roughly above 0.5. Subsequent works (Jarrett et al. 2011; Stern et al. 2012; Assef et al. 2013) improved the technique and proved *WISE* colour to be an excellent AGN selection tool. In our recent study presented in this thesis (Yao et al. 2020, see

Chapter 5) we combined the BPT and the *WISE* colour-colour (a hybrid diagram) capable of classifying more galaxies with better accuracy than using these classification diagrams separately.

2.3.4 Radio-selected AGN

In the radio band, the dominant radiation process is the synchrotron emission, which is the radiation produced by charged particles spiralling at relativistic velocities through a mag-

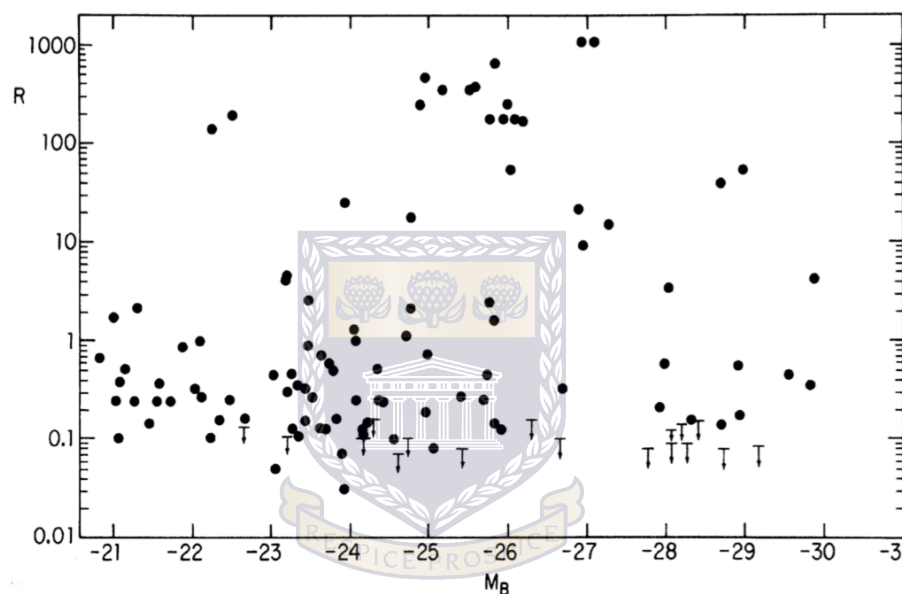


Figure 2.11: Ratio between radio and optical flux density versus absolute magnitude. Image reproduced from Kellermann et al. (1989). Galaxies with $R \geq 10$ and $R < 10$ are classified as RL and RQ, respectively. The arrows indicate the upper limit objects not detected as radio sources above 0.25 mJy.

netic field. Most of the bright radio sources represent synchrotron emission from AGNs, while the fainter population comes from synchrotron emission in the disks of galaxies that are powered by the normal SF process (Miley et al. 1980; Condon et al. 1992). Radio galaxies can be classified into radio-loud (RL) and radio-quiet (RQ) galaxies. The distinction between RL AGN and RQ AGN was initially related to either the radio luminosity or the ratio of radio to optical flux density (e.g., Schmidt 1970). Figure 2.11 shows the radio to IR flux ratio R versus the absolute magnitude, where $R = f_{5\text{GHz}}/f_{4400\text{\AA}}$. In this diagram, galaxies with $R \geq 10$ and $R < 10$ are classified as RL and RQ, respectively (see Kellermann et al. 1989). About 10 - 20% of AGNs are RL and often display a powerful jet. These simple classifications, which are only valid for type 1 AGNs (Padovani et al. 2011; Bonzini et al. 2013), have since evolved in the literature (see Baloković et al. 2012; Padovani et al.

2016, 2017). Radio galaxies can also be classified as HERG and LERG using their optical lines (see Best & Heckman 2012; Whittam et al. 2020). HERG and LERG have already been presented in Section 2.2.4.6. In their recent work, Whittam et al. (2020) found HERG to be hosted by galaxies with lower masses and younger stellar populations than LERG.

2.4 Multiwavelength Selection of AGN

Knowing that the energy coming from the central engine of AGNs is radiated across the electromagnetic spectrum, the ideal would be to combine all this information for more efficient identification. However, this approach is costly. Indeed, X-rays and spectroscopic surveys are still very scarce, time-consuming, and expensive. Optical radio surveys are mostly available in the northern sky. Fortunately, the advent of the SKA in the southern hemisphere is about to change the situation for the radio spectrum. It is worth mentioning that integral field spectroscopy (see Allington-Smith 2006) is progressively making spectroscopic surveys more efficient as they allow a 3-D view of large objects (galaxies, nebulae) at a cheaper cost. Some effective multiwavelength diagnostics of SF and AGN-dominated hosts are presented below.

2.4.1 Spectral Energy Distribution Fitting

The spectral energy distributions are one of the main sources of information about galaxies, especially for the point sources for which detailed studies are very difficult (because of their compressed size). The multiple physical processes that take place in galaxies radiate at specific wavelengths (or wavebands), which combined give the full shape of the spectrum. The ideal, therefore, would be to observe a galaxy at all wavelengths to understand the full extent of its properties as opposed to looking for a single feature at a given wavelength (e. g., measuring the $H\alpha$ $\lambda 6563$ to derive the SFR).

Obscured AGNs are generally not seen in UV, optical, and soft X-rays observations (Alexander et al. 2001; Richard et al. 2003). The emission from their dusty torus can be detected in the IR as well as the emission from the ISM due to star formation activity. In the IR, SF galaxies emit from the warm dust and polycyclic aromatic hydrocarbon molecules (PAH; used as a tracer of SFR) at 3.3, 6.2, 7.7, 8.6, and 11.3 μm while the AGNs have a power law spectrum from black body radiation. This is why IR colours can be used

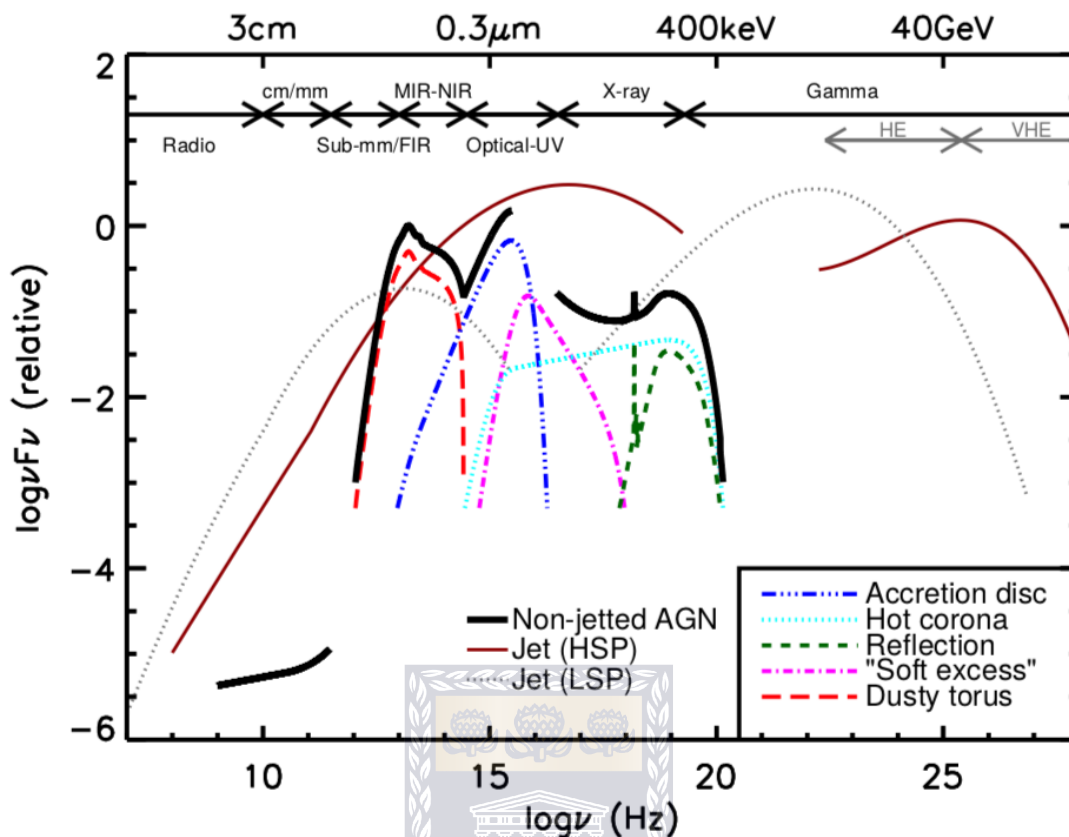


Figure 2.12: A schematic representation of an AGN spectral energy distribution based on observed SEDs of non-jetted quasars (e.g., Elvis et al. 1994; Richards et al. 2006). The total emission is represented by the black solid curve and the coloured curves (shifted down for clarity) are for the individual components. The intrinsic shape of the SED in the mm-far IR (FIR) regime is uncertain; however, it is widely believed to make a minimal contribution (to an overall galaxy SED) compared to star formation, except in the most intrinsically luminous quasars and powerful jetted AGN. The primary emission from the AGN accretion disk peaks in the UV region. The jet SED is also shown for a high synchrotron peaked blazar (HSP, based on the SED of Mrk 421) and a low synchrotron peaked blazar (LSP, based on the SED of 3C 454.3). Figure reproduced from Padovani et al. (2017). Image credit: Harrison (2014). Some SEDs derived from our real data are presented in Figure 3.4.

to separate AGNs from SF galaxies (Stern et al. 2005; Jarrett et al. 2011). However, typical IR surveys such as *WISE* or IRAC are limited to four bands each. The combination of several emission bands (in the form of an SED) reveals the features of AGN and SF galaxies more accurately. SED templates of known AGN and SF galaxies exist in the literature (eg., Polletta et al. 2007; Brown et al. 2014, 2019). The templates of Brown et al. (2014, 2019) were used for our SED fitting and k-correction presented in Section 3.3.2.2. Fitting codes (eg., LePhare Code; Arnouts et al. 1999) are used to compare the SEDs to the existing templates. The type of galaxy is determined at the end of the process according to the best-fitting model.

The emission in IR from the AGN comes from its dusty torus. Figure 2.12 (reproduced

from Padovani et al. (2017) shows a schematic representation of an AGN's SED. The different components of an AGN are represented with the respective frequency regimes in which they radiated and the associated observation windows. For example, the emission from the torus seems to be confined to the frequency range from 10^{12} to 10^{14} Hz and is most observable in the IR window. On the other hand, the emission from the jet spans a wider frequency range, observable from radio to Gamma rays. Based on this information, appropriate models (SED templates) can be used to separate the AGN's contribution to the SED from that of the star formation in galaxies where the host dominates the AGN emission.

2.4.2 Infrared-to-Radio Luminosity Ratio: q_{TIR}

In the 1970s, a correlation was found between mid-IR and radio luminosities for Seyfert galaxies (Van der Kruit 1971). A tight correlation was later established between the FIR and the non-thermal radio flux density (at 1.4 GHz) for spiral galaxies (Helou et al. 1985). The FIR flux and the FIR/radio luminosity ratio (q_{TIR}) are given by Equations 2.3 and 2.4, respectively; starting with the total IR flux:

$$\text{FIR} = 1.26 \cdot 10^{-14} \times 2.58 f_{\nu}(60 \mu\text{m}) + f_{\nu}(100 \mu\text{m}) \quad (2.3)$$

In this equation, the FIR is estimated using 60 and 100 μm . f_{ν} are the flux densities in Jy, and FIR is in W m^{-2} . Here the IRAS bands of 60 and 100 μm are used as a proxy to estimate the total infrared flux. This assumes a particular dust temperature and emissivity.

$$q_{\text{TIR}} = \log\left(\frac{L_{\text{TIR}}}{3.75 \times 10^{12} \text{ Hz}}\right) - \log\left(\frac{L_{1.4\text{GHz}}}{\text{W Hz}}\right), \quad (2.4)$$

where 3.75×10^{12} Hz is the frequency at 80 μm representing the centre of the IRAS bandwidth.

The FIR emission comes from the re-emission of the UV and optical light (from young massive stars) absorbed by the dust, while the radio flux is mainly due to synchrotron emission when the cosmic ray electrons interact with the magnetic fields of supernova remnants formed after the death of these massive stars (Voelk 1989; Lacki & Thompson

2010).

This strong relationship has been very useful in many studies, such as estimating the SFR in dusty nuclear starburst galaxies (Condon 1992). In this way, the q_{TIR} can show excess either in FIR or radio luminosities. It helps in classifying the galaxy as SF or AGN, respectively. This property of the q_{TIR} will be used later in the radio study to identify the AGNs from our sample missed in the IR and the optical (see Chapter 6).

Recent investigations have shown the evolution of the q_{TIR} parameter with redshift (Ivison et al. 2010; Calistro Rivera et al. 2017). However, the samples used at high redshift could be biased toward radio bright galaxies. Moreover, the spectral indices needed in this case to correct the radio luminosity are not well constrained (see Murphy 2013; Kaiser 2006). In my study, presented in Chapter 6, we are limited to a redshift range < 0.3 , and hence the q_{TIR} is relevant to the local Universe.

2.5 Most Recent Works on AGN

The energy radiated by AGNs is produced by materials falling into the SMBH at the centre of the galaxy through the accretion disk. This flow of material (mainly cold gas) starts from galactic scales beyond 100 pc to the sub-parsec environment. New studies are revealing that the radiative pressure generated by the AGN during the process unbinds a large amount of gas, which is expelled via a radiative-pressure-driven wind (Hönig et al. 2019; Leftley et al. 2019). The work by Sarangi et al. (2019) demonstrates that this wind creates the condition enabling dust formation in the galaxy. They also found that the resultant distribution of the dense dusty gas resembles a toroidal shape, with high column density, which is consistent with the definition of the torus as presented by the AGN unification theory. The AGN classification technique used in the IR relies on the dust reprocessed by the torus and this toroidal structure has generally been thought to be smooth. However, recent simulations using clumpy torus models appear to reproduce the X-ray observations better (Tanimoto et al. 2019; Ogawa et al. 2020).

In optical spectra, the relative intensity of strong emission lines is used to estimate the chemical abundance and the physical properties of the galaxies. Photoionisation models exist to derive O and N abundances (Dors et al. 2017), while a combination of some of these emission lines is the basis for optical classification methods (e.g., the BPT). Several works based on photoionisation models of the narrow-line region (NLR) have been used to estimate

the metallicity of AGN host galaxies (Castro et al. 2017; Mignoli et al. 2019). High-level photoionisation is supposed to be caused by radiation from the central AGN. However, current works are pointing at shocks due to gas outflows as another source (Contini 2019; Riffel et al. 2021). Strong [O III] emission lines are expected to be related to AGN activity and represent a proxy for AGN strength. Therefore, if they have a shock-ionisation origin, using the optical BPT classification model could lead to misclassifications, as will be seen later in some case study examples in Section 5.3.

Now with more powerful instruments we see a higher fraction of galaxies where both AGN activity and star formation activity coexist. The challenge is to be able to measure crucial parameters such as the SFR accurately. While many calibrations exist to determine the SFR for SF galaxies, they cannot be used directly for galaxies with AGN because in this case part of the gas is ionised by the AGN, as well as the dust emission arising from the torus and not star formation. The spectral synthesis of the stellar population using the SED is the way forward. It simultaneously fits different composite or simple stellar population templates and can help to differentiate the AGN's contribution from that of pure star formation in a given spectrum (Baldwin et al. 2018; Salim et al. 2018; Peterken et al. 2020; Riffel et al. 2020).

The aim of this section is not to give an exhaustive list of all the active areas and new findings in AGNs studies. Instead, we highlight a few difficulties encountered in the present work and how alternative solutions are being found. For example, knowing the structure of the torus is needed to explain why some galaxies show no AGN signature in the IR but are classified as AGN in the optical (refers to the optical spectrum except clearly stated otherwise). Also, the source of photoionisation is important for the optical classification of galaxies and the derivation of SFR in galaxies having both AGN and star formation activities. We can see in Chapter 5 and Chapter 6 how the SFR and stellar mass could be overestimated for AGNs if the AGN's contribution to the total flux is not properly accounted for. In this current thesis, our aim is to identify galaxies that may have significant AGN emission contribution to the total emission coming from the galaxy. These galaxies should then be treated accordingly when studying their physical properties.

The next chapter will be dedicated to data and data reduction.

Chapter 3

Data and Data Reduction

In this chapter we describe the data used in this thesis starting from the GAMA survey and its optical line measurements. The high-resolution images from the KiDS are briefly described. They will be used mostly to study details within the galaxies and their nearby environment. The high resolution helps to see whether the galaxies are isolated or closely interacting systems. We present the *WISE* galaxy catalogue, including the resolved sources. The focus is on the resolved galaxies, which require special treatment, as they are not well measured (see explanations in the Section 3.3.2.1) in the *ALLWISE* data available online. The images from the survey (*WISE*) are reprocessed to enhance the spatial resolution and the photometry of the resolved sources is subsequently measured. The last data set presented is the radio continuum data from MeerKAT. These are some of the earliest data from the survey obtained through the first call for proposal in 2019. It will be used in combination with *WISE* as part of our AGN investigation through multiwavelength analysis (see Chapter 6).

3.1 Optical: The GAMA Survey

The GAMA is an optical and spectroscopic galaxy survey (Driver et al. 2009; 2011) of $\sim 300\,000$ galaxies over an overall area of about 286 deg^2 . The survey is divided into five fields, with three (G09, G12, and G15) in the equatorial region and two (G02, G23) in the southern hemisphere (see Liske et al. 2015). The main scientific goals of the survey are to use the large-scale distribution of galaxies as a test for the cold DM theory, and

also to study the galaxies and their evolution. GAMA has a lot of ancillary data ranging from UV to radio (see Driver et al. 2009). The equatorial fields have been extensively studied (Cluver et al. 2014; Jarrett et al. 2017) as opposed to the south, where, generally, multiwavelength data and spectroscopic redshifts are scarce. For example, the Sloan Digital Sky Survey (SDSS), which is one of the largest optical surveys to this day, located in the northern hemisphere, does not cover G02 and G23 (Figure 3.1). However, things are about to change with the unprecedented data from the MeerKat (see Jonas & MeerKAT Team 2016) and the upcoming SKA. It is the motivation for choosing the G23 field for the current study.

3.1.1 The GAMA G23 Region

Located between the right ascension (RA) from 339° to 351° and the Declination (Dec) from -35° to -30° (see Figure 3.1), G23 is the largest of the two GAMA southern fields (G23, G02). The main surface area after accounting for lost areas due to bright stars is about 50 deg^2 . The optical spectra were obtained primarily with the 2dF instrument mounted on the 3.9m Anglo-Australian Telescope at Siding Spring Observatory (Australia), which feeds the AAOmega spectrograph. Additional 2dF data were extracted from the 2dFGRS (Colless et al. 2001), and also from the 6dF Galaxy Survey (6dFGS, Jones et al. 2010), which used the 1.2m UK Schmidt Telescope, also at Siding Spring Observatory. More details about the GAMA survey strategy and spectroscopic data products can be found in Baldry et al. (2010), Baldry et al. (2018), Robotham et al. (2010), Hopkins et al. (2013), Gunawardhana et al. (2013), and Liske et al. (2015). The spectroscopic redshifts used in this study are obtained from G23TilingCatv11.

Redshifts are associated with a quality number from 0 to 4. Zero (0) represents a failure of the data reduction, 1 means no redshift is found, and 4 is the highest certainty with an associated probability ≥ 0.95 (Driver et al. 2011). We require quality greater than 3 for this thesis project. The raw data from the GAMA survey are processed using the software developed at AAO called 2DFDR (Sharp & Birchall 2010). The spectral output obtained from the 2DFDR is spectroscopically calibrated following the idlspec2d pipeline used for the SDSS DR6 (Adelman-McCarthy et al. 2008). Checking the calibrated data for the galaxies observed by both GAMA and SDSS shows good agreement, as presented in Hopkins et al. (2013).

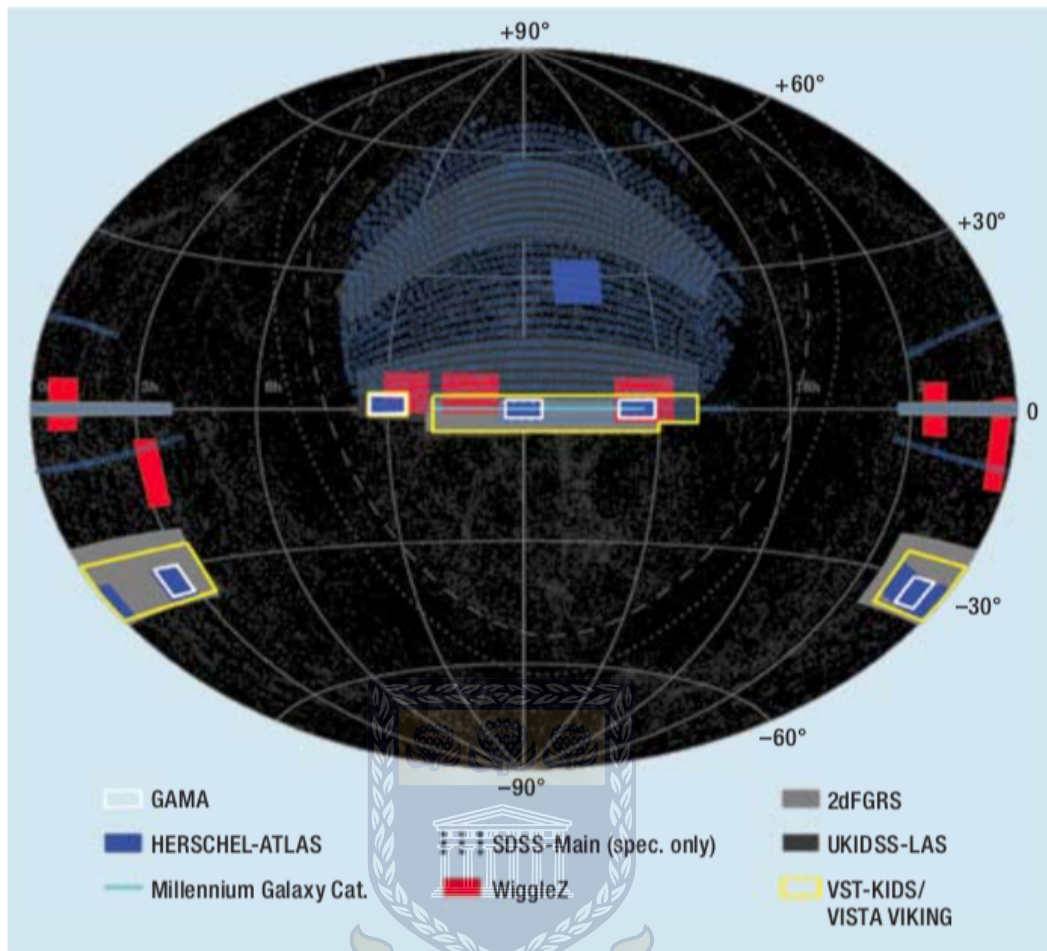


Figure 3.1: The five GAMA fields (white rectangles) equatorially projected on the sky. One can see the overlap with other major surveys but only the three equatorial fields have SDSS data available. The G23 on the lower right has optical data from KiDS. Image reproduced from Driver et al. (2009).

UNIVERSITY of the
WESTERN CAPE

3.1.1.1 Spectral Line Measurement

The optical line fluxes of the galaxies are extracted from the G23 GAMA II catalogue (“GaussFitSimplev05” from within the SpecLineSFR DMU; Gordon et al. 2017) with redshifts > 0.002 and a magnitude limit of $i < 19.2$ mag. The data has a mean resolution of $R \sim 1300$, with an observed wavelength range of 3750–8850 Å. The spectra are fitted with the IDL code “mpfitfun” (Markwardt 2009), which uses Levenberg–Marquardt non-linear least squares minimisation to identify the best-fitting parameters for the model, given the data and its associated uncertainties.

Among the lines available in the catalogue, we use $H\beta$ $\lambda 4861$, $[O\text{ III}]$ $\lambda 4959$, $[O\text{ III}]$ $\lambda 5007$, $[N\text{ II}]$ $\lambda 6548$, $H\alpha$ $\lambda 6563$, $[N\text{ II}]$ $\lambda 6583$, $[S\text{ II}]$ $\lambda 6716$, and $[S\text{ II}]$ $\lambda 6731$. For lines that are always expected to be narrow, such as $[S\text{ II}]$, the fitting can either be a straight line (in the case of

non-detection. The width of the Gaussian fit is by default 0 where no detection, which sets the flux to be 0) or a Gaussian shape. Fitting the H β and H α in combination with their associated lines [O III] λ 4959/ λ 5007 and [N II] λ 6548/ λ 6583, respectively, can have more levels of complexity above the continuum. For example, fitting H α + [N II] λ 6548/ λ 6583 can increase in complexity as follows:

- no emission or absorption, just continuum,
- H α in absorption and no [N II] λ 6548/ λ 6583 emission,
- [N II] λ 6548 + H α + [N II] λ 6583 all with narrow emission,
- [N II] λ 6548 + [N II] λ 6583 in emission + H α in absorption,
- [N II] λ 6548 + [N II] λ 6583 in emission + H α in emission and absorption,
- [N II] λ 6548 + [N II] λ 6583 in emission + H α in narrow plus broad emission,

Each of the above fits are performed on the data and a single global score is given based on whether a more complicated model should be chosen versus a simpler one and vice versa. For models with the same number of fitted parameters, the model with the lowest χ^2 value is chosen. The following limits are applied to the fitting model: the line position is maintained within 200 km s $^{-1}$ (to give a freedom of movement to the fit based on GAMA's spectrograph resolution) of the expected position. The width of the Gaussian (σ) for the narrow emission lines is constrained by $0.75 \sigma_{\text{inst}} < \sigma < \sqrt{500^2 + \sigma_{\text{inst}}^2}$, where σ_{inst} is the resolution of the spectrum in km s $^{-1}$. The preceding constraints are made larger for broad emission lines, $\sqrt{500^2 + \sigma_{\text{inst}}^2} < \sigma < \sqrt{5000^2 + \sigma_{\text{inst}}^2}$, and the position of the line is maintained within 400 km s $^{-1}$. Only the AAOmega spectra are flux-calibrated (unlike the 2dF spectra) and can be used as individual line fluxes, while uncalibrated fluxes may be used for line ratios. For the doublets such as [O III] λ 4959/ λ 5007, [N II] λ 6548/ λ 6583, and [S II] λ 6716/ λ 6731, the line with the longest wavelength is generally the strongest (e.g., [O III] λ 5007 can be up to three times stronger than [O III] λ 4959) and is used to estimate the H α /[O III] line ratio.

3.2 Optical: KiDS Imaging

The KiDS is an optical survey of $\approx 1500 \text{ deg}^2$ (de Jong et al. 2013; Bilicki et al. 2018) using OmegaCAM inside the field imager on the VLT survey telescope. With its 268 megapixel wide-field camera that provides a $1^\circ \times 1^\circ$ field of view (with a pixel scale of $0.214 \text{ arcseconds pixel}^{-1}$), the exposure time is selected such that it can reach a median redshift of $z = 0.7$ which is well beyond the redshift limit used for the present study ($z < 0.3$). The median seeing is about $0.''7$, and the observations are done in four bands (u, g, r, i), with the r-band being the deepest, reaching a depth of 25.4 mag (AB system). The resolution of the images is subarcsecond; it is, therefore, a valuable data set to visualise details within the galaxies, usually not visible using *WISE* images ($\sim 6''$ resolution). KiDS has several data releases, starting from KiDS-ESO-DR1. The release used in this study is KiDS-ESO-DR4 (see Kuijken et al. 2019 for more details).

3.3 Mid-Infrared: The *WISE* Survey

Launched in December 2009, *WISE* surveyed the entire sky in four mid-IR bands: $3.4 \mu\text{m}$, $4.6 \mu\text{m}$, $12 \mu\text{m}$, and $22 \mu\text{m}$ respectively, W1, W2, W3 and W4 (Wright et al. 2010). While W1 and W2 are both sensitive to the continuum emission from evolved stars, the W2 band is additionally sensitive to hot dust; hence, this makes the $3.4 \mu\text{m} - 4.6 \mu\text{m}$ colour a good diagnostic to identify galaxies dominated globally by AGN emission (see e.g., Jarrett et al. 2011; Stern et al. 2012).

3.3.1 *WISE* Image Reconstruction

The *WISE* image mosaics for G23 are reconstructed using the “drizzle” resampling technique (Jarrett et al. 2012; Masci 2013). The final images with $1 \text{ pixel}''$, have a native resolution of $5.''9$, $6.''5$, $7.''0$, and $12.''4$ in W1, W2, W3, and W4, respectively, as opposed to $8.''1$, $8.''8$, $11.''0$, and $17.''5$ given by the *WISE* all-sky ‘Atlas’ imaging. For more information about the archival data, see Cutri et al. (2012). The source measurement, characterisation, and extraction processes are amply described in Cluver et al. (2014) and Jarrett et al. (2013, 2017).

Figure 3.2 is the four-band combination of all the mosaics in the G23 field ($\sim 50 \text{ deg}^2$).

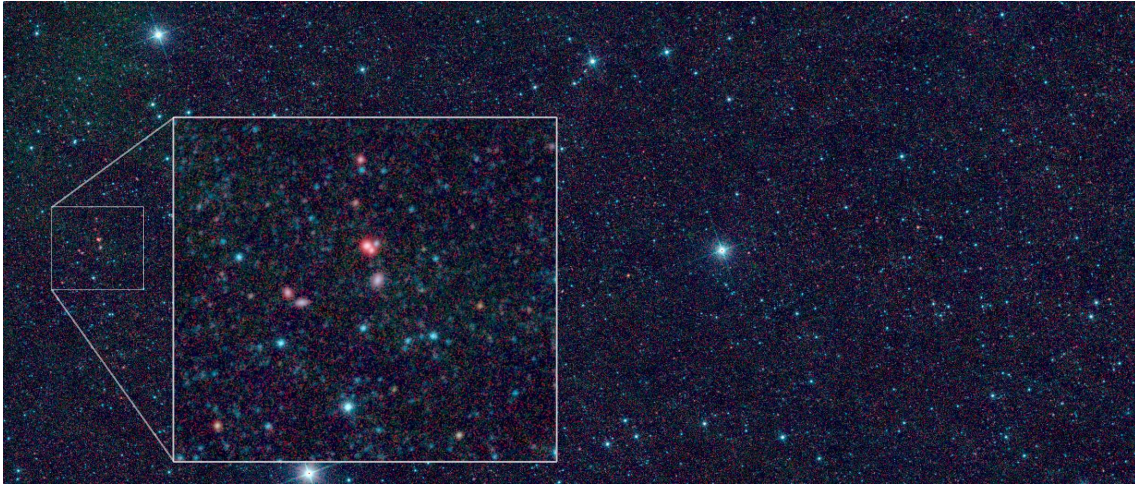


Figure 3.2: The *WISE* 50 deg² view of the G23 field. In the zoomed area (14×11 arcmin) the reddish extended galaxies are easily distinguishable from foreground stars (blue in general). The image was created combining the four *WISE* colours: 3.4 μm (blue), 4.6 μm (green), 12 μm (orange) and 22 μm (red). The 50 deg² area contains about 700 000 *WISE* sources (galaxies + stars).

Stars have not yet been removed and are typically blue ¹. Extragalactic sources are usually blue (little star formation) or red (copious star formation). Some red extended galaxies can easily be identified by sight in the zoomed area.

3.3.2 Catalogue of *WISE* Galaxies in G23

A positional cross-match between *WISE* sources from the *ALLWISE* catalogue and galaxies with known redshifts in the GAMA G23 region was performed using a 3'' cone radius, as suggested by Cluver et al. (2014) and was similarly used in the Jarrett et al. (2017) GAMA G12 study. Table 3.1 shows the number of galaxies classified as resolved based on W1 photometry, the point sources, and their cross-match with GAMA in G23. This cross-match radius is motivated by the fact that the PSF fitting of the *ALLWISE* pipeline can affect the resulting accuracy of the source's position, particularly for resolved sources. This produces a catalogue of 40 843 *WISE*-GAMA galaxies.

We next briefly describe the extraction and cleaning method used to create our final catalogue of *WISE* galaxies (W1 resolved and point-like sources) in the GAMA G23 region, and the sample used for the current study. This is the fourth catalogue of its kind (after the GAMA G12, G09, and G15 fields), and the full procedure is described in Cluver et al. (2014) and Jarrett et al. (2017).

¹because the W1 band (blue) dominates the mid-IR for cool stars, and the Rayleigh-Jeans tail of their emission is much lower in W2 (green) and W3 (red) bands

Table 3.1: The *WISE* G23 Catalogue created using reconstructed images (enhanced resolution).

Groups	Total
<i>WISE</i> resolved in G23	2,979
<i>WISE</i> point source in G23	528,054
<i>WISE</i> resolved \times GAMA (G23)	2,696
<i>WISE</i> point source \times GAMA (G23)	38,147

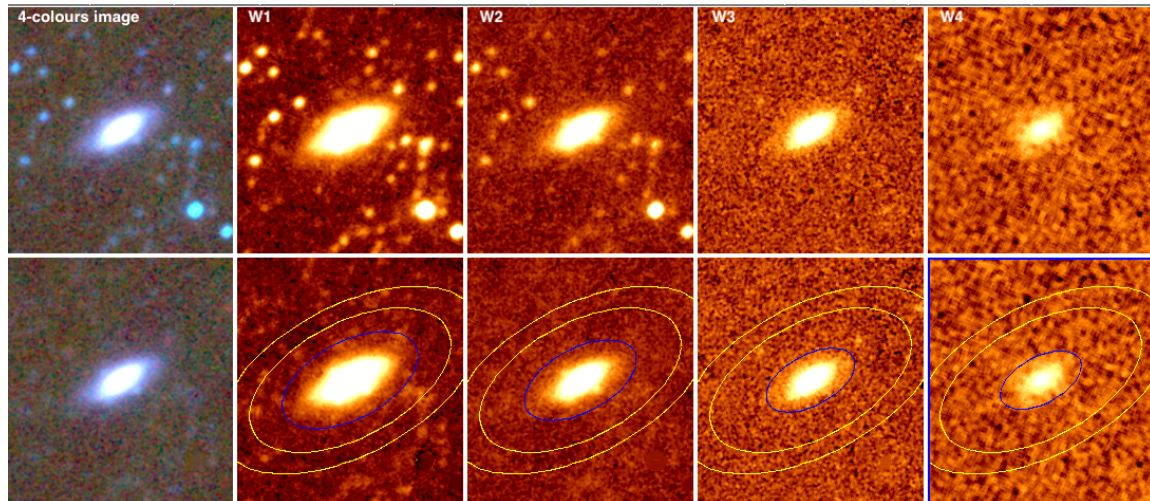
3.3.2.1 Extraction and Cleaning Method

The whole process of extracting the *WISE*-resolved sources arises from the fact that the *WISE* survey was optimised for the detection of point-source. Hence, we make the effort to identify and characterise resolved sources, notably discrete galaxies. Potentially resolved galaxies based on the W1 ($3.4\ \mu\text{m}$) band are selected from the *ALLWISE* catalogue using the PSF goodness-of-fit metric, `w1rchi2`. We search for values of `w1rchi2` > 2 , remeasure them with our special resolved source pipeline that characterises the global and surface brightness emission, revealing sources that are extended beyond the PSF. These candidates are then characterised using the resolved-galaxy pipeline. In other words, it is necessary to measure a galaxy before one can confirm that it is, in fact, resolved.

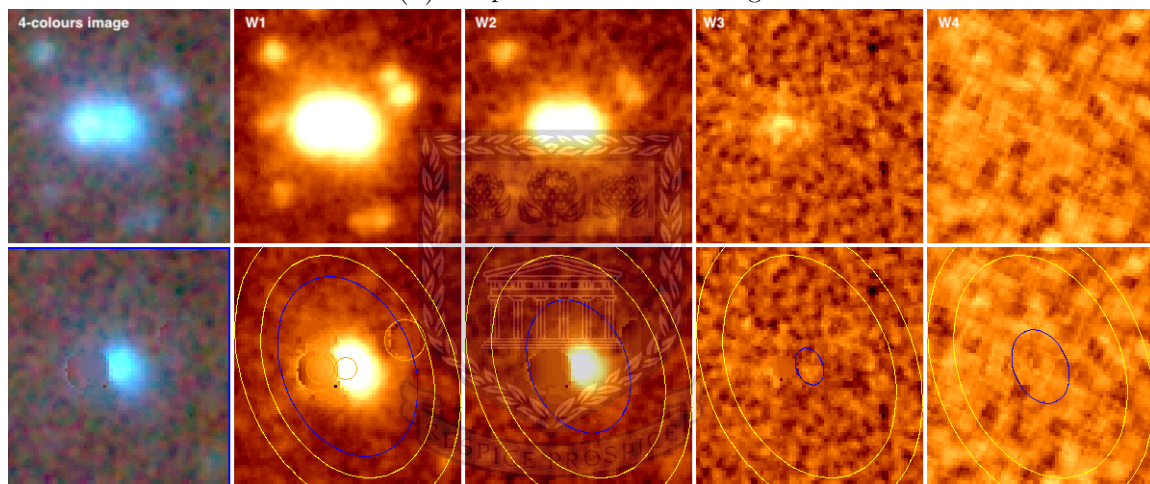
Using the reprocessed *WISE* imaging described above, the photometry can be remeasured as appropriate for a resolved source. The different steps are taken via custom software, which adapted tools developed for 2MASS extended sources (Jarrett et al. 2000) and the *WISE* pipeline (Jarrett et al. 2011, 2013; Cutri et al. 2012). Henceforth, we will refer to this pipeline as “standard” for resolved sources in *WISE*. The process is semi-automated such that each level can be visually inspected and corrected if necessary. The details are as follows:

(i) The point sources are removed by a combination of PSF subtraction and pixel masking. The bright stars and their artifacts in the vicinity are also masked out for better estimation of the background. The shape of the galaxy is determined based on the 3σ isophote (of the background rms), which is considered to be constant at all isophotes. The first set of photometry is derived at the 1σ isophote, which already encloses more than 90% of the light (Jarrett et al. 2019). A double-Sérsic fit (Sersic 1968) is used to estimate the light beyond the 1σ isophote and to compute the curve of growth asymptotic fluxes extending down to convergence.

Previously extracted resolved sources are then removed from the images using their smoothed light distribution.



(a) Simple automated cleaning.



(b) Tough blending which requires a human intervention.

Figure 3.3: Image showing the resolved galaxies cleaning process. On the first row of each panel are the 4-colour image, and the images in W1, W2, W3 and W4, respectively. On the second, the nearby and foreground contaminations have been removed. The concentric ellipses are the 1 sigma photometric aperture (blue), and the annulus (yellow) within which the local background is estimated. (a): is simple foreground cleaning that can automatically be done by our pipeline (see Jarrett et al. 2013). (b): an extreme blending case that requires human intervention.

(ii) The process is repeated until all the sources have been extracted.

(iii) The Rfuzzy parameter (see Cluver et al. 2014) is the second-order intensity-weighted moment that allows a separation between faint, resolved, and unresolved systems. Each type of object has a characteristic Rfuzzy value that is systematically smaller than that of the resolved galaxies. This step is important in order to select our final sample of resolved galaxies.

The final step is the visual inspection to validate and identify blends and other complex

scenarios. The whole area of study is divided into smaller areas centred on galaxies identified as resolved and processed by the pipeline. Each of the galaxies was visualised (by myself and cross-checked by Tom Jarrett) to make sure that it is definitely not a star or unresolved galaxy, that the deblending has been well-performed (mostly for close proximity blend cases), and the apertures and position angles follow the 2D light profile well. The standard pipeline does well (see Figure 3.3 a) when the background is smooth and the signal-to-noise ratio (S/N) is high (10% or higher). It needs human assistance in dense and low-S/N environments, and with closely blended pairs (see Figure 3.3 b). The parameters and source contamination can be interactively adjusted (see Jarrett et al. 2017).

3.3.2.2 Rest-frame Correction

To account for the redshifted emission across the optical and IR bands, we applied a “k-correction” to the magnitudes based on SED fitting before the derivation of any physical value. The SEDs are built by combining flux densities spanning the optical, the near-IR spectra, and *WISE* mid-IR; for the optical and near-IR data, we used photometry available in the GAMA G23 region (see Bellstedt et al. 2020). The spectra are fitted to empirical templates of well-studied galaxies from Brown et al. (2014, 2019) and Spitzer-SWIRE/GRASIL (Silva et al. 1998; Polletta et al. 2006, 2007). From the rest-frame-corrected catalogue, key parameters such as stellar mass were derived using the W1 in-band luminosity and the mass-to-light ratio (M/L; Meidt et al. 2012; Cluver et al. 2014; Querejeta et al. 2015; Kettlety et al. 2018). The SFR ($\text{SFR}_{12\mu\text{m}}$) and the specific SFR (sSFR) are estimated using $\nu L\nu$ luminosities and the mid-IR to total-IR calibration from Cluver et al. (2017). The SEDs permit, to some extent, the differentiation of the AGNs from normal SF galaxies and generally follow the *WISE* colour-colour classification. The data available for the SED fitting in this case allow a good k-correction of the data. But, the accuracy of the SED classification depends on the variety of data and templates available and should be normally better (where sufficient data and templates exist) than that optical or WISE. Examples of SEDs are presented in Figure 3.4.

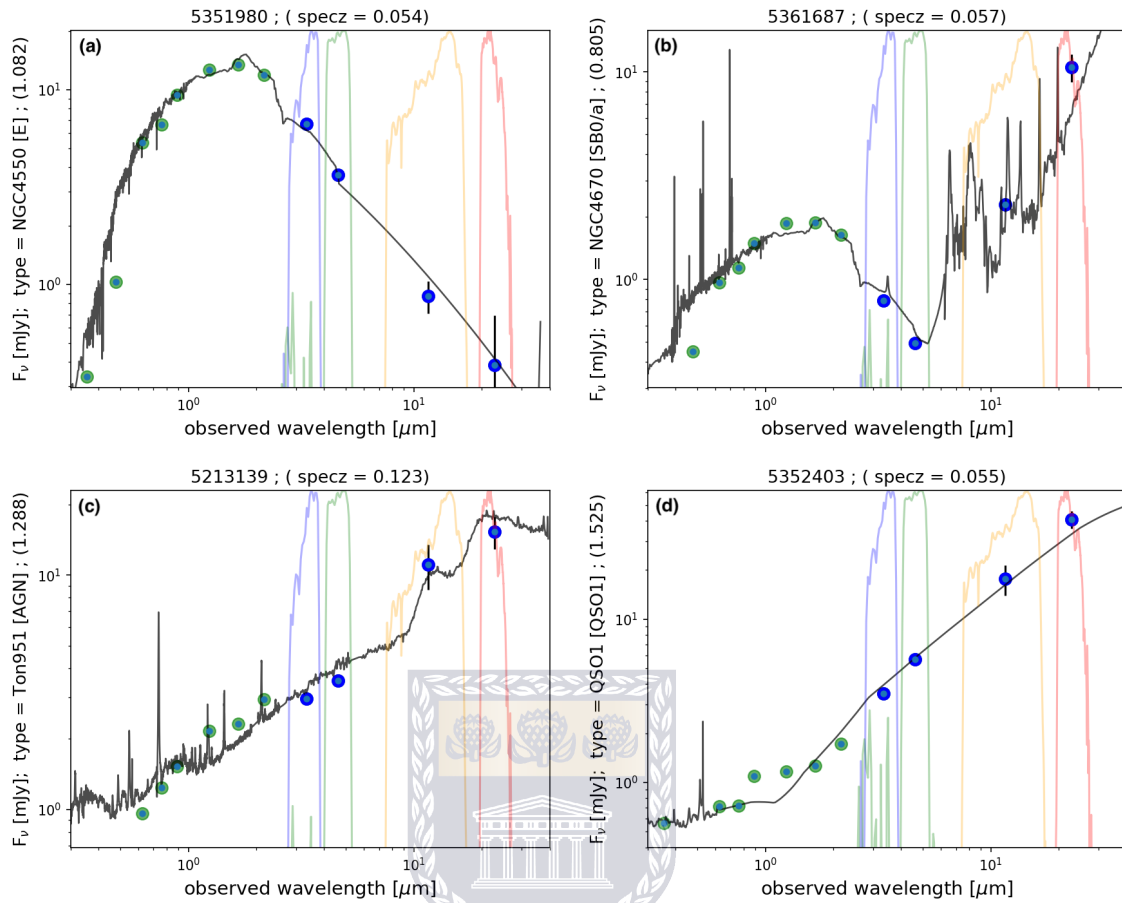


Figure 3.4: Example of SEDs for an early type galaxy in (a) and a SF spiral in (b). A typical AGN and a QSO are represented in (c) and (d), respectively. The SEDs are constructed using the templates presented in this section. The best fit template is indicated on the y axis. The GAMA identification and the spectroscopic redshift of the galaxies are provided on top of each image.

UNIVERSITY of the

WESTERN CAPE

3.4 Radio: The SKA Pathfinder MeerKAT

Because of the atmospheric opacity, ground-based astronomical observations are limited to the optical, near-IR, and the radio wavelengths. Radio astronomy is the study of emission from celestial bodies in the frequency window from 10 MHz to 1 THz, equivalent to wavelength $30 \text{ m} > \lambda > 0.3 \text{ mm}$ (which includes the mm-wave band). This radio frequency range is much larger (in logarithmic scale) compared to the optical range confined between 400 nm and 700 nm. The broad radio band allows the observation of many more celestial objects through a variety of emission processes (free-free, thermal, synchrotron emissions, etc.). The advent of radio astronomy helped to discover a new sky, different from what was known in the optical wavelengths. Among other discoveries were the cosmic microwave background, interstellar molecular clouds, pulsars, quasars, radio galaxies, etc.

Radio observation is done in either single-dish or interferometry mode. Radio observation with a single dish is able to capture much of the emission of the source, depending on the receiver, but has poor resolution owing to the long radio wavelengths. Resolution scales with the diameter of the telescope as presented by Equation 3.1 such that arcsec resolution will require a dish of diameter in orders of km. This is not practical for engineering or observation because in this case the telescope will be in a fixed position, impossible to move around (too massive). Even the largest single-dish radio telescope, FAST (Nan et al. 2011) with its 500 m diameter, has a resolution of 1.′5 at 1.4 GHz.

$$\theta_{res} \sim \frac{\lambda}{D} \sim \frac{c}{\nu D}, \quad (3.1)$$

where θ_{res} is the angular resolution, λ is the wavelength, c is the speed of light, and the aperture diameter is D .

An alternative to the resolution issue with single-dish observation is interferometry, which combines multiple antennas into a single “synthetic” telescope. The resolution is now determined by the maximum baseline (B ; the longest distance between two antennas in the array) rather than the diameter (D) in Equation 3.1. In this way antennas kilometres apart can achieve arcsec resolution. However, there is a caveat: while the long wavelengths increase the angular resolution, the information at larger angular scales is lost. The solution is to have both very short and long baselines, such that we can still see on a large scale at high resolution, and more baselines mean more sensitivity. The SKA (SKA; <https://www.skatelescope.org/>), with its short baselines (the compact core will have thousands of dishes in a region 5 km in diameter) will be able to observe large-scale structures and the very long baselines (~ 3000 km) will ensure arcsec resolutions.

The SKA is a project that aims to build the world’s largest radio telescope (interferometry) with 1 km^2 of collecting area. It is an international collaboration that will build thousands of radio telescopes across Africa and Australia. This telescope is a revolutionary instrument that will observe large areas of the sky much faster than any other telescope, with a high-resolution factor of 50 times that of the Hubble Space Telescope. The SKA project has two pathfinders. The Australian SKA Pathfinder (ASKAP²) has 36 antennas, now operational in the Western Australian desert. The precursor in South Africa is the Meer Karoo Array Telescope (MeerKAT; Jonas & MeerKAT Team 2016), with its 64 dishes

²<https://www.atnf.csiro.au/projects/askap/index.html>



Figure 3.5: Image of the MeerKAT dishes located in the Karoo desert in South Africa. We can see the Gregorian design characterised by the offset of the secondary reflector. This configuration maximises the collecting area, as it does not block the aperture. At the heart of each dish is a receiver tuned to the L-band (900-1670 MHz) with 4096 channels, which are some of the most sensitive arrays ever created. Image taken from the MeerKAT webpage.

located in the Karoo desert. The diameter of each dish is 13.5 m and the array is distributed across an area of 8 km in diameter (the minimum baseline is 29 m). Figure 3.5 is an image showing the MeerKAT array. The dishes have an offset Gregorian configuration design, which yields a better performance for image quality and also facilitates the installation of multiple receiver systems. The telescope was inaugurated in July 2018 and the first call for proposal started in December 2018.

3.4.1 The MeerHOGS Survey

The MeerHOGS project was part of the first MeerKAT call for observation in early 2019. We recall that our main project is to decipher how AGN and SF galaxies separate, combining multiwavelength data. Chapter 5 will focus on the optical and the IR wavebands, and Chapter 6 on the radio continuum. As a follow-up study, MeerHOGS targeted a filamentary structure including a dense galaxy group. Although covering only a fraction of the G23 field ($\sim 10 \text{ deg}^2$), the quality of the MeerKAT survey makes it a highly valuable radio continuum

data set. Details are provided in Chapter 6.

Figure 3.6 shows the footprint of MeerHOGS (grey shade) and GAMA G23 delimited

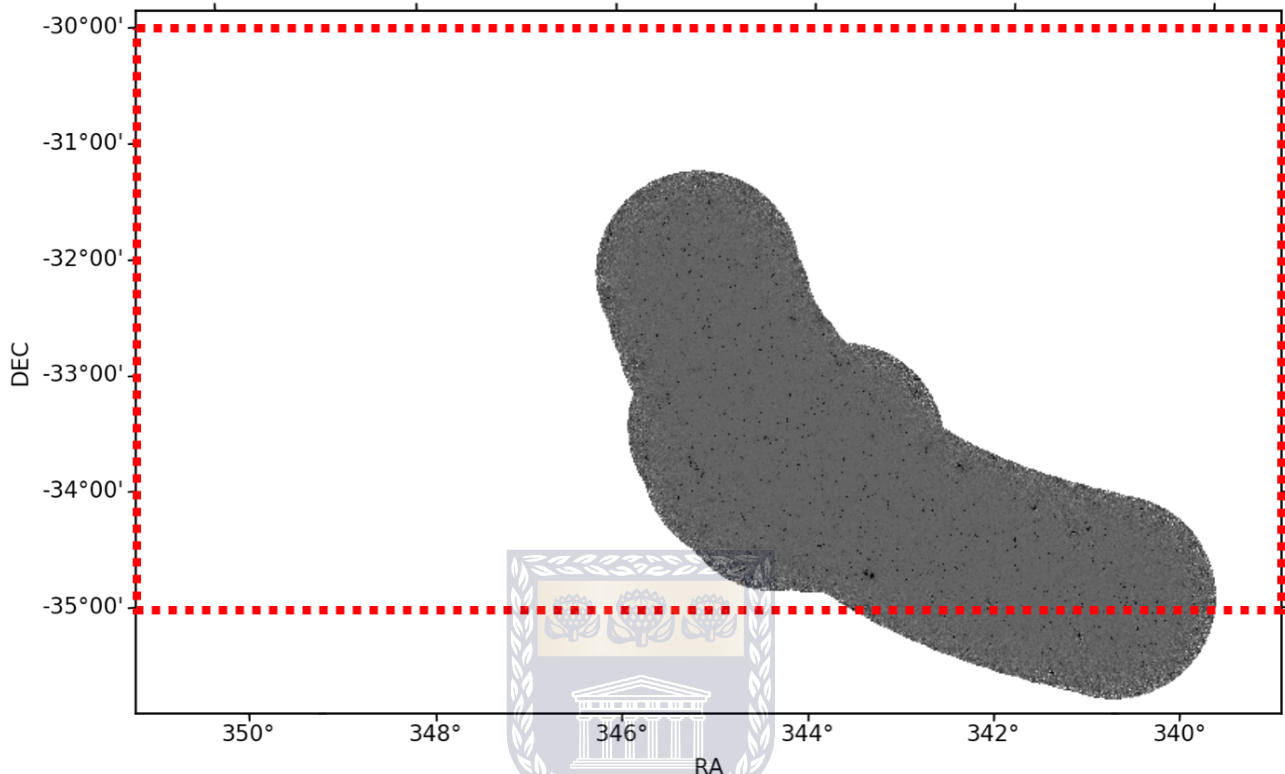


Figure 3.6: The MeerHOGS survey. The grey scale represents a continuum observation at 1.4 GHz with the MeerKAT (64 dishes) located in the GAMA G23 region. The red-dashed square is the footprint of the G23 region. The observation targeted a filamentary structure between $0.025 < z < 0.034$ with a dense galaxy group at its centre.

by the dashed-red contour. It was carefully selected to follow a filamentary structure at $z = 0.03$ that crosses the G23 field. An over-density was targeted with additional observations to increase sensitivity and coverage. The MeerHOGS survey is mostly within the G23 region, except for the small portion at declinations $< -35^\circ$. The MeerHOGS area to be crossmatched with G23 is therefore reduced to $\sim 8 \text{ deg}^2$ after accounting for the few galaxies lost at the edge of the survey.

3.4.2 Observations and Data Reduction

The total observation time was 16.5 hours (with 13.2 h spent on source) over $\sim 10 \text{ deg}^2$ using MeerKAT at 1.4 GHz. With 25 pointing in total (20 on the filament and an extra five in the dense galaxy group area), the survey reached an average rms of $18 \pm 2 \text{ mJy beam}^{-1}$ and a spatial resolution of $13.''5 \times 13.''5$. The total observation time for each pointing was \sim

30 min. During each observation epoch, J2302-3718 was observed (2 min) for the purpose of gain calibration. PKS 1934-63 was also observed (three times 10 min) for bandpass and flux calibrations (see the observation details in Table 3.2). The available frequencies range from 900 - 1670 MHz, but only a reduced interval from 1319.8 to 1517.1 MHz (limited to redshifts < 0.1) was used during the data reduction to minimise the data volume and mitigate the RFI contamination.

The data were reduced with the CARACal pipeline (Józsa et al. 2020). CARACal

Table 3.2: Observation details of the MeerHOGS Survey

Date	Number of antennas used	Duration
17-03-2019	58	4.5 h
24-03-2019	58	4 h
26-03-2019	64	4 h
31-03-2019	58	4 h

uses the Stimela Python framework, which can combine several versions of data reduction software in a system of containers (see Chapter 4 of Makhathini, S. 2018 and references therein). The reduction process required 36 cores with a total memory of 300 GB.

AOFlagger (Offringa 2010) was run to flag for shadowing and RFI. PKS 1934-63 (primary calibrator) was first used for the bandpass and gain calibration. Then, the result was transferred to the second calibrator for combined gain and flux calibration. The calibration tables obtained were finally applied to the observation and the continuum imaging was done using WSClean (Offringa et al. 2014). During the imaging process, the source-finding software SoFiA (Serra et al. 2015) was used to generate a CLEAN mask using a threshold of $\sim 4\sigma$ and following self-calibration with CUBICAL (Kenyon et al. 2018). The final image resulted in a synthesised beam of $13.''5 \times 13.''5$ and an rms noise of $\sigma_{\text{rms}} = 18 \pm 2 \mu\text{Jy}$.

Chapter 4

Source Extraction

Detecting and carefully measuring *WISE* resolved sources is challenging and time-consuming, and generally not designed for semi-interactive methods, such as those developed for well-resolved nearby galaxies (e.g., Jarrett et al. 2013, 2019). In this chapter we therefore investigate a new, more automated method for source finding and extraction software. The first aim is to see if it can reliably replace our existing pipeline and help to speed up the process. Secondly, we plan to use this new software, of which the features seem to be well adapted for extended radio flux extraction on our radio data.

As presented below, we find that *ProFound* does poorly with *WISE* imaging, relative to our pipelines, both in the sense of photometric accuracy and systematics, but seems to do adequately well with detection and characterisation of radio fluxes from MeerKAT synthesised imaging.

4.1 *ProFound* : Concept and Parameters

ProFound is a source finding and image extraction package created by Robotham et al. (2018). A 2D galaxy profile fitting tool named ProFit (Robotham et al. 2017) was developed earlier and required reasonable guesses as initial input parameters. Among others, the most important input parameters for ProFit are the pixel matched sigma map, the segmentation map, and a good sky subtraction. *ProFound* is thus a kind of complementary software package developed to provide the initial input need for ProFit. It nonetheless seems to be a powerful source extraction package with a few innovative features. It firstly differs

from preceding source finding and extraction software packages in the way the flux of the different sources is measured. *ProFound* uses non-symmetric segments that follow the flux of the source rather than applying a circular or elliptical aperture to fit the light profile. It also attempts to deblend the blended sources automatically.

This *WISE* analysis is based on the earlier version (2018) of *ProFound*. New versions have been developed since then, with various improvements. The radio data used in Chapter 6 are extracted with the newest version of *ProFound*.

4.1.1 Extraction Method

ProFound uses an initial image FITS file, where almost all the required inputs are directly collected from the image header except for the magnitude zero point, which has to be placed manually. Once the image is given, the steps listed below (Figure 4.1) are executed to extract the photometric information of the source.

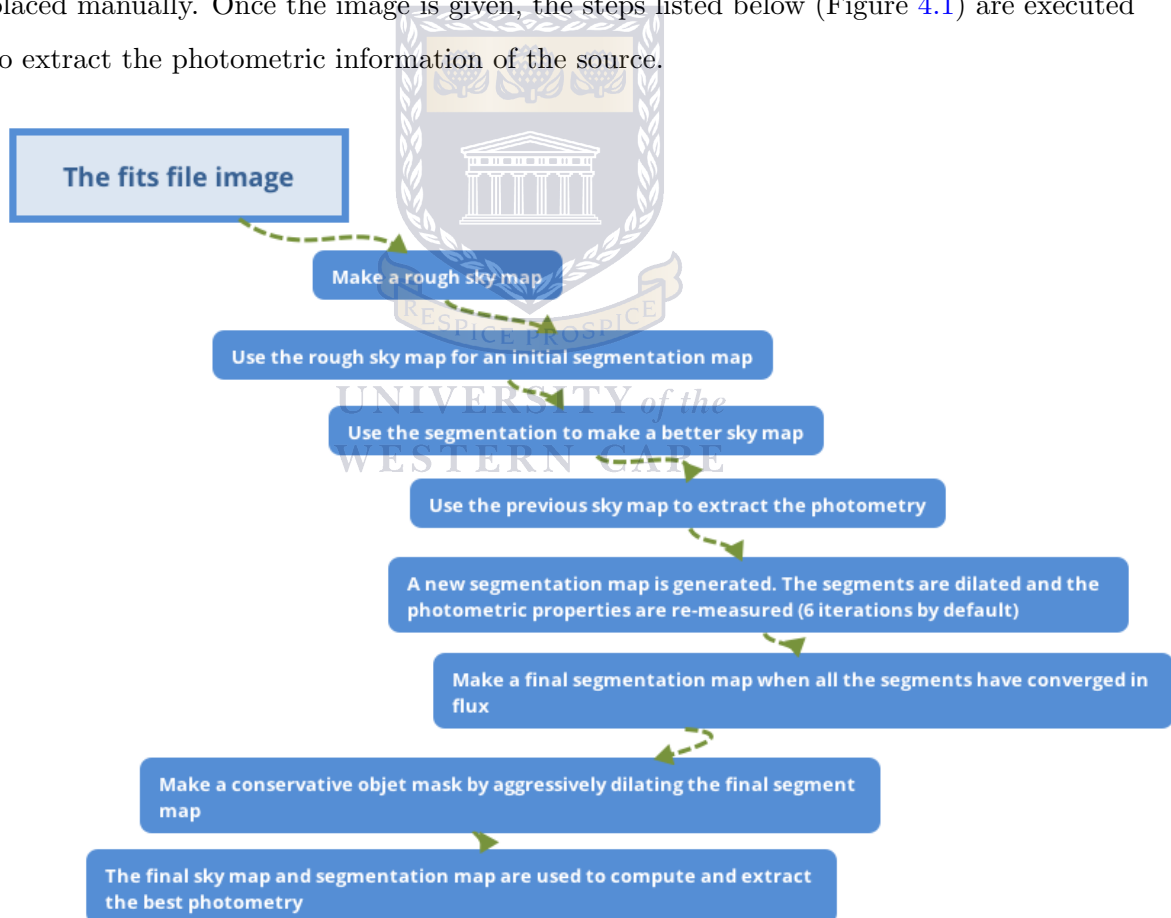


Figure 4.1: Diagram showing the different steps in *ProFound*'s data processing. Each level involves a specific sub-function. See Robotham et al. (2018) for more details.

Figure 4.1 briefly presents the different stages to extract the photometry using “*profoundProFound*”, which is the highest source extraction function in *ProFound*. Mid-level functions are used at each stage. The photometric properties in terms of RA, Dec, flux, magnitude, etc., and the different maps, such as the segmentation map that shows the different sources and the segments enclosing their flux, the sky map, etc. are also available if requested by the user.

4.1.2 Functions in *ProFound*

The main function used is *profoundProFound* for the source finding and extraction. It uses different tools at a given stage of the photometry determination process. For instance, following the sequence in Figure 4.1, the tool called “MakeSkyMap” will be used to estimate the sky, followed by “MakeSegim” for the segmentation map. The segments will be dilated with “MakeSegimExpand” ... in the end, the output in terms of segmentation statistic is given by “segimInfo”. Some of these functions are listed in Table 4.1.

profoundProFound has several arguments that can be tuned to optimise the quality of

Table 4.1: *ProFound*’s photometry tools (from the online description)

Name	Description
MakeSkyMap	Calculate the sky map
MakeSegim	Watershed image segmentation map
MakeSegimExpand	Segmentation map expansion and dilation
MakeSegimMerge	Merge the segmentation map
MakeSigma	Make a sigma map
segimInfo	Image segmentation statistics
Skycut	The lowest threshold to make on the image in units of the skyRMS

both the source detection and extraction. Most of the parameters are adapted to any kind of photometry, except for a few that may largely affect the final result if not appropriately adjusted. According to Robotham et al. (2018), the first in this order is the “tolerance”, which sets up the level of deblending between nearby sources. The lower the tolerance is, the more deblended the sources are. Next comes the smoothing parameter “sigma”. It is the standard deviation of the blur used to smooth the data. The maximum value is 4; high values lead to smoother data. Furthermore, the searching radius for nearby pixels belonging to other objects “ext” plays a key role so that small objects are smoothed out for high “ext” values.

After some trials, informal discussions with other users of *ProFound* and readings enabled us to determine the adapted values for our data. The tolerance value, the sigma

and the skycut were therefore respectively reset to 1, 1.5, and 2.5. Trying a few different values of “box size”, “ext” etc. yielded no significant changes. *ProFound*’s default settings were used for all the other parameters. Below is a snippet of the different arguments in *profoundProFound*. These are default parameters subject to modification depending on the data set used. As it can be seen the skycut used in this study is 2.5 not the default parameter of 1 presented in the snippet etc.

```
\textit{profoundProFound}(image, segim, objects, mask, skycut=1, pixcut=3,
tolerance = 4, ext = 2, sigma = 1, smooth = TRUE, SBlim, size = 5, shape = "disc",
iters = 6, threshold = 1.05, converge = 'flux', magzero = 0, gain = NULL,
pixscale = 1, sky, skyRMS, redosky = TRUE, redoskysize = 21, box = c(100,100),
grid = box, type = "bilinear", skytype = "median", etc.)
```

4.1.3 Photometry Multiband (*Colour Me Happy*)

Multiband photometry is a way of measuring the flux of sources in a given area in different bands. In this study, we use the four *WISE* bands (W1, W2, W3, and W4), with W1 being the brightest with the highest image quality. Usually, the most sensitive band (here W1) is used for the source detections. The sources will therefore be extracted in all the bands based on the positions and apertures given by W1. *Colour Me Happy* is typically *profoundProFound* with a few added tools to render the interplay between the different bands easier. The multiband photometry requires the same pixel scale in all the bands. If this is not the case, *ProFound* offers a way to correct the issue by calling a pixel warping function “magwarp”. It changes the image characteristics of the other bands (pixel scale etc.) to match the chosen one. All our four *WISE* bands in this case have the same pixel scale.

4.2 Testing *ProFound* on *WISE* Photometry

In this section, we used the early version of *ProFound* (Robotham et al. 2018) just after the release in 2018 to test our *WISE* source characterisation pipeline as presented in Jarrett et al. (2013; hereafter referred to as the standard pipeline). The two pipelines are source finding and image analysis packages. Their major difference comes from the extraction

method. While the standard pipeline uses elliptical apertures to fit the morphology of the sources, *ProFound* is based on dilated segment maps that follow the shape of the sources. The two pipelines were run using the same enhanced images in a 15 deg^2 area within the GAMA G23 region. The photometry multiband task inside *ProFound*, called “Colour me Happy” was mostly run in the default mode, except for a few parameters such as the Skycut, the tolerance, and sigma, respectively reset to 2.5, 1, and 1.5.

4.2.1 *WISE* Cross-matched to *ProFound*’s Detections

We selected a *WISE* tile (named tile 1370) in G23 covering an area of roughly 7.14 deg^2 . Similarly, a second overlapping tile (tile 1268) of 7.84 deg^2 was selected. The two tiles combined are referred to as **area 3** (total area of $\sim 15 \text{ deg}^2$) throughout this chapter. After running *profoundProFound*, using the skycut, the tolerance and sigma of respectively 2.5, 1, and 1.5 in **area 3**, we detected 195 618 sources, which were position cross-matched with our galaxy catalogue. The results are reflected in Table 4.2. The percentages were derived by dividing the number of galaxies by the respective total of 962 and 157 458 for resolved and point source galaxies (based on our original catalogue).

Table 4.2: *ProFound* extracted Sources and the G23 Catalogue (W1 Band) in **area 3**

Right ascension (tile 1370 in G23)	341.9587 to 345.5773
Declination (tile 1370 in G23)	-35.616 to -32.6270
Right ascension (tile 1268 in G23)	341.6160 to 345.1163
Declination (tile 1268 in G23)	-32.6218 to -29.9985
Surface area in deg square	$\approx 15 \text{ deg}^2$
Total <i>ALLWISE</i> sources	218 208
Total <i>ProFound</i> extracted sources	195 618
Total <i>WISE</i> galaxies	158 420
<i>WISE</i> point sources galaxies	157 458
<i>WISE</i> resolved sources galaxies	962
<i>WISE</i> point sources cross-matched <i>ProFound</i> (1'')	46 250 (29.37 %)
<i>WISE</i> point sources cross-matched <i>ProFound</i> (3'')	115 039 (73.06 %)
<i>WISE</i> point sources cross-matched <i>ProFound</i> (5'')	131 397 (83.44 %)
<i>WISE</i> resolved sources cross-matched <i>ProFound</i> (1'')	431 (44.80 %)
<i>WISE</i> resolved sources cross-matched <i>ProFound</i> (3'')	901 (93.65%)
<i>WISE</i> resolved sources cross-matched <i>ProFound</i> (5'')	955 (99.27 %)

In Figure 4.2 we show the location of the resolved sources in **area 3**. The resolved sources from our catalogue are in black squares. We cross-matched them respectively with *ProFound*’s extracted sources in a radius of 3'' (yellow circles) and a radius between 3'' and

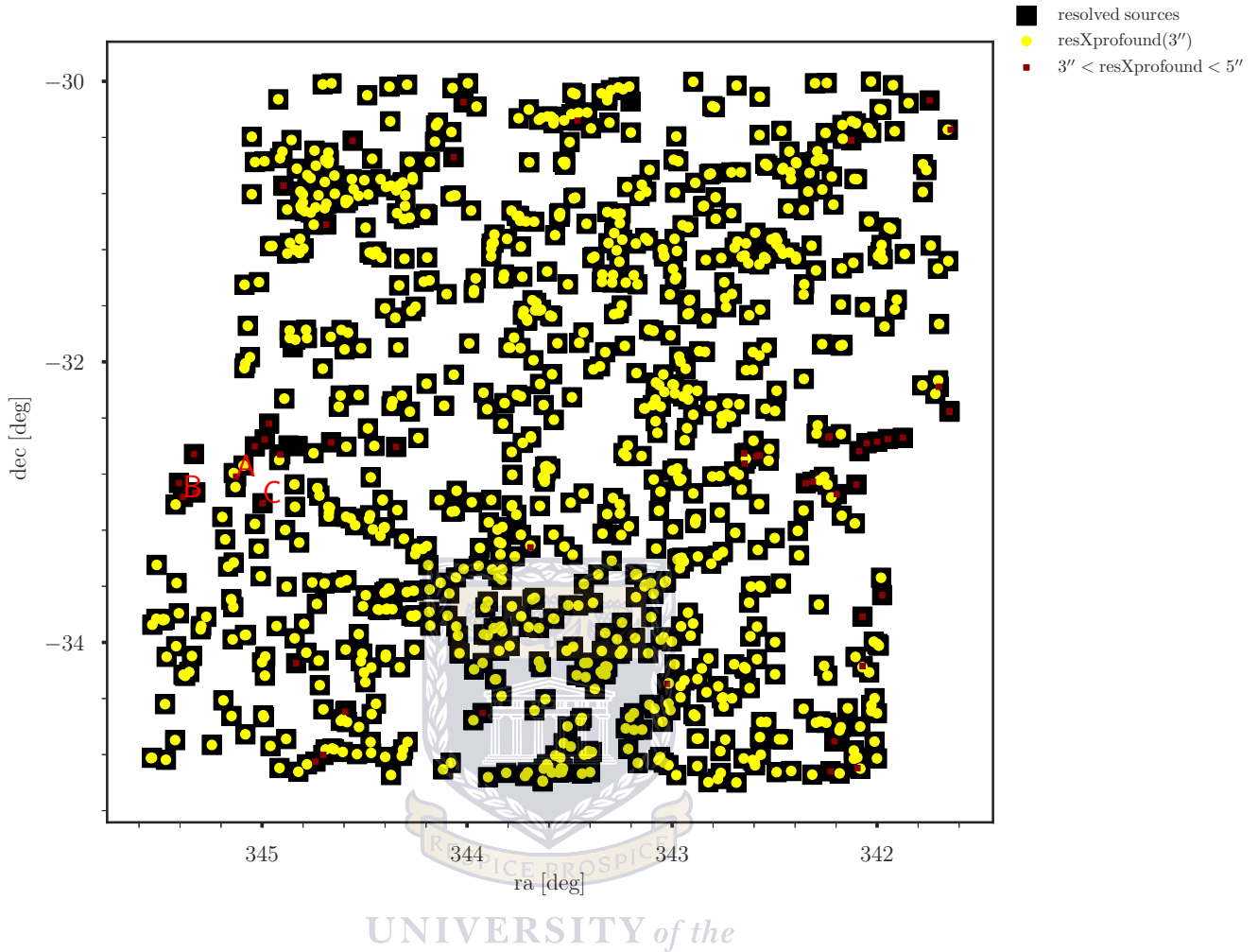


Figure 4.2: *WISE* total number of resolved sources in **area 3** in black squares (962 galaxies) and *WISE* cross-matched *ProFound* in yellow circles (901 galaxies) for a cross-matched radius of $3''$. The red squares (54) represent *ProFound* cross-matched with *WISE* for a radius (r) between $3''$ and $5''$. A, B and C are randomly selected galaxies with $3'' < r < 5''$ for further investigation (see Figure 4.3). Seven *WISE* detected resolved galaxies do not have a match in *ProFound* within a $5''$ search radius.

$5''$ (red squares). The quasi-totality of the resolved galaxies is found within a cross-matched radius $r = 5''$. Only seven galaxies detected with the standard pipeline do not have a match in *ProFound* for a search radius of less than $5''$. More than 90% of the galaxies are found at $r < 3''$ and respectively 44% and 81% at $r < 1''$ and at $r < 2''$.

A diagnostic of the galaxies with the cross-matched radius between $3''$ and $5''$ (red inside the black squares) revealed mostly blended galaxies that required manual intervention (using the standard pipeline) for the deblending and also to recentre the aperture. The process may have added slight errors in the positions of the centres between *WISE* and *ProFound*. Indeed, the elliptical apertures used in *WISE* can overlap for close sources,

while the segments in *ProFound* are not allowed to overlap. The deblending in *ProFound* is automatically made across saddle points in flux (see Robotham et al. 2018). Several galaxies that match at high searching radius are located at the edge of the tiles where deleterious artifacts may occur.

Figure 4.3 presents the three galaxies previously selected for investigation in Figure 4.2

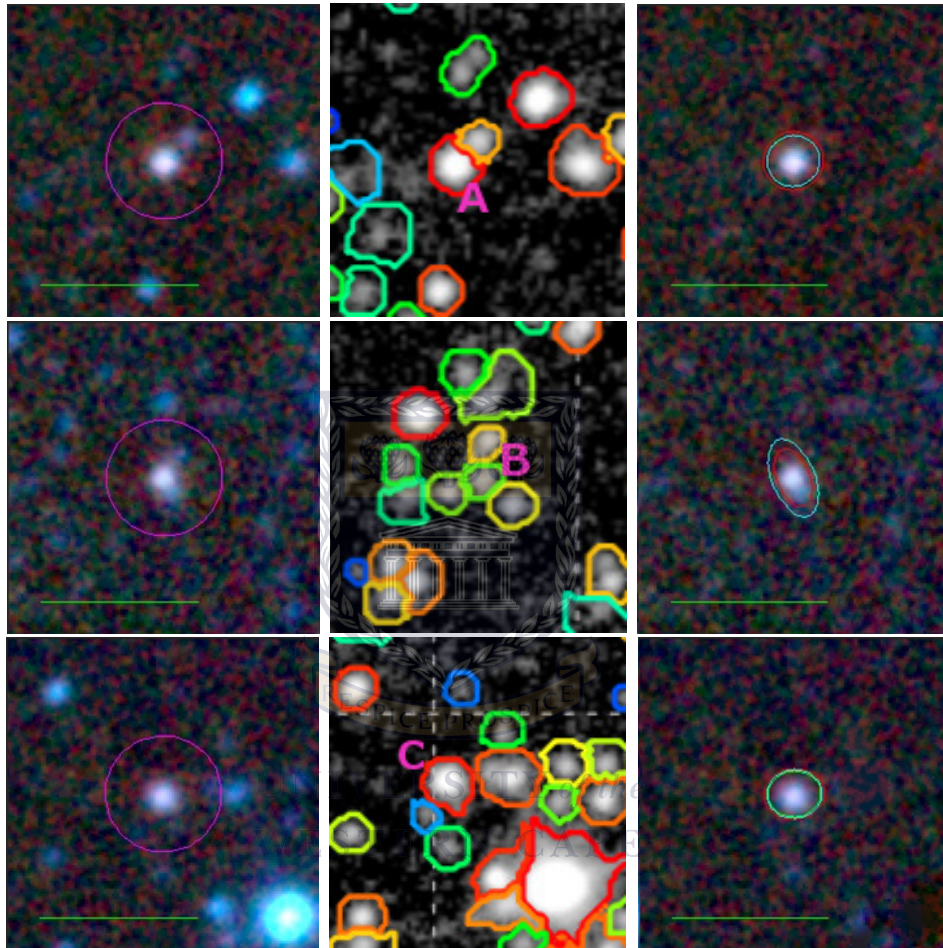


Figure 4.3: Galaxies among the sample with cross-matched radius between $3''$ and $5''$ in **area 3**. The green scale bar represents 1 arcmin. TJ23003022-3249048.0, TJ23013253-3257462.0 and TJ225959.29-330027.4 are respectively in the top panel (A), the centre panel (B) and the bottom panel (C). The three galaxies are blended cases from our G23 catalogue and correspond to A, B and C in Figure 4.1. Left: *WISE* tri-colour images showing the detected galaxy. The foreground stars are still visible and the aperture has not been removed. Centre: *ProFound* segmentation maps on W1. Right: Similar to the left with the foreground stars removed and the aperture fixed. The elliptical contours show the extent of the light distribution in W1 (blue), W2 (green), W3 (orange), and W4 (red), respectively. The targeted galaxy in the centre is to be compared with the one on the right side. W1 and W2 can have the same aperture. Likewise for W3 and W4. In this cases only two colours will be visible in the right column. All four apertures can be identical sometimes.

(see A, B and C in red in the image). The galaxies (A) and (C) were perfectly deblended in the standard pipeline while galaxy (B) still has a foreground star, which probably escaped

the visual inspection.

The segment of the galaxy (A) in *ProFound* suggests an elliptical shape with a position angle perpendicular to the line between the two centres of the galaxies, while in *WISE* we have something roughly circular. These are faint little galaxies, probably unresolved in W3 and notably in W4; hence, they will be point sources (with no shape at all) in W3 and W4. Also, the separation of the two galaxies (A) and (B) in *ProFound* appears somewhat problematic. The deblending of galaxy (C) looks quite similar in both *ProFound* and the standard pipeline. The deblending is an issue for both the standard pipeline and *ProFound*, which can extract either more or less light from each galaxy. This could not only compromise the position of the centre, but also affect the magnitude.

The galaxies' distribution as a function of the cross-matched radius is presented in Figure 4.4. The resolved and point source galaxies are respectively in red and blue colours. Each histogram has been normalised to unity. Both distributions show the maximum fraction of galaxies around $1''$, followed by a decrease for greater radii. More than 90% of the resolved and point sources galaxies are within a separation radius of $3''$. Both samples show perfectly similar distributions.

4.2.2 Point-source Magnitudes in *WISE* and *ProFound*

In this section, we are testing for effects of confusion and false-matches.

4.2.2.1 Comparison between *WISE* and *ProFound*'s Magnitudes

Figure 4.5 examines the difference between the profile-fit (*ALLWISE* *wmpro*) point-source magnitudes in the G23 catalogue and their counterpart in *ProFound* for a given galaxy as a function of *wmpro*. The number of galaxies, the mean difference, the 25 percentiles, and the 75 percentiles are given on each frame. The first column (from Figure 4.5-a to 4.5-e) and the second column (from Figure 4.5-f to 4.5-j) represent respectively the W1 and W2 bands. The separation radius interval is given in the top left-hand corner of each frame. For the interval $[0'' - 1'']$ that contains the most reliable cross-match results, we have an average difference close to 0 (≈ 0.004 mag), which is expected for comparable photometries between our catalogue and *ProFound*. The mean difference increases with the separation radius reaching 0.4 mag for $4'' < r < 5''$. There is perfect symmetry around the mean value in W2 compared to W1, which has a slight offset. We suspect that the S/N limit

of two not being strong enough for W1, which is the brightest band. As we can see, the number of galaxies in W1 is twice that in W2 for the first interval and at least 40% larger in the second interval. An increase in the S/N up to $S/N = 10$ still shows the initial offset for the W1 band. There is more scatter at higher radius, showing probable contamination by false matches and blending confusion. Based on the above analysis, we will adopt a cross-match radius of $3''$ throughout all the following sections.

We further applied the cross-matched radius of $3''$ to the sample and investigated the general behaviour of the magnitude difference (see Figure 4.6, 4.7, 4.8 and 4.9). A $S/N > 2$ was applied to both the G23 catalogue and *ProFound's* data (see Table 4.3). The statistics of each sample are in blue, with the blue dashed and the magenta dot-dashed lines representing respectively the mean and the 0 magnitude difference. We applied a 2σ

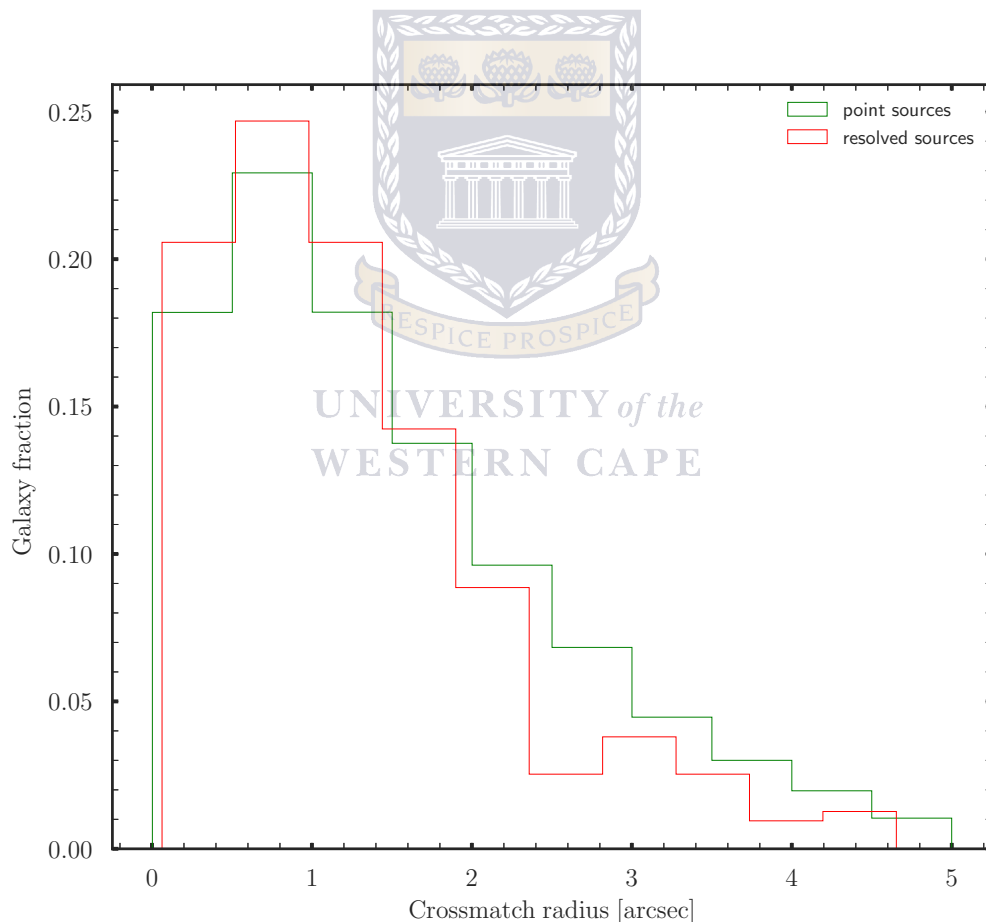
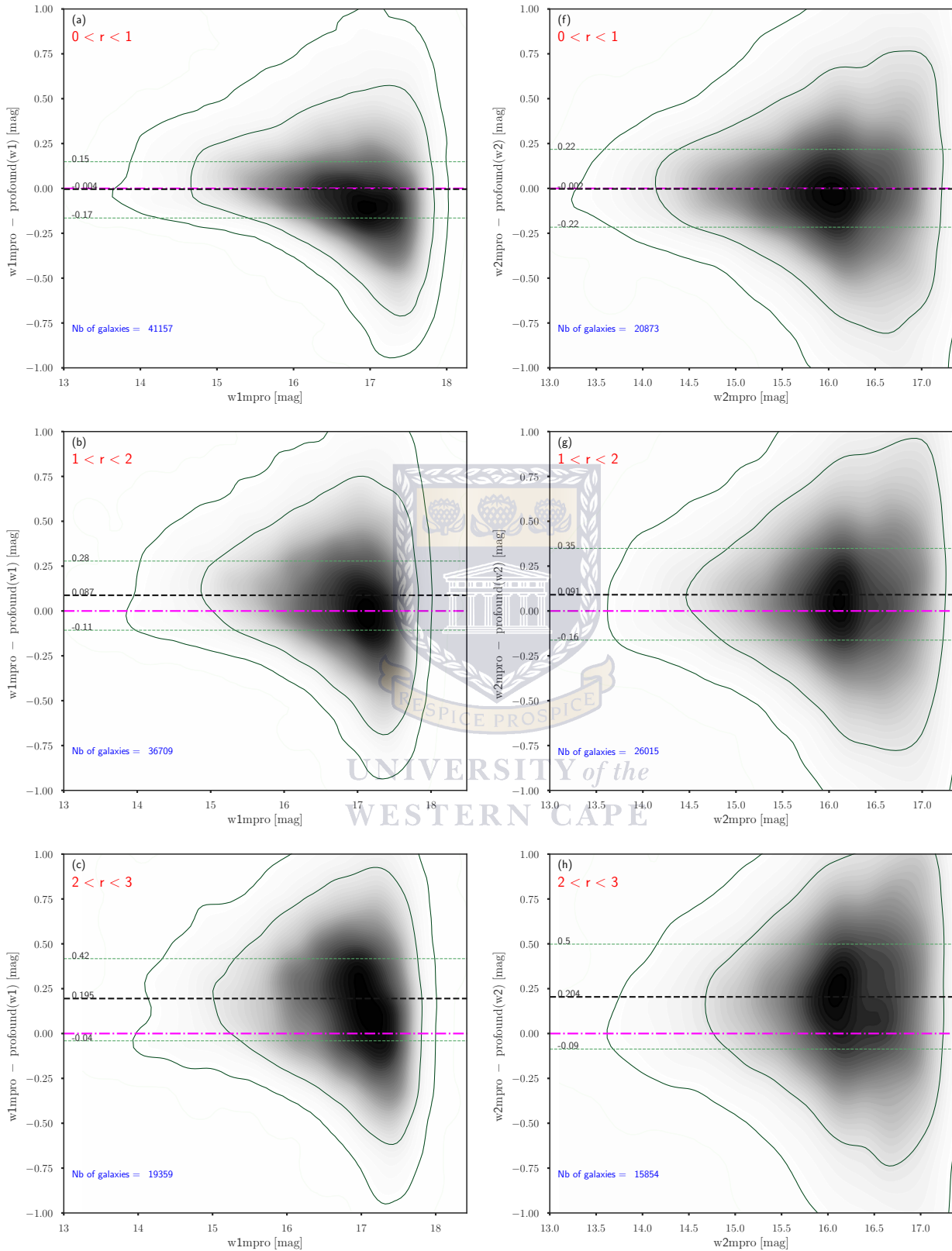


Figure 4.4: Histogram of the total number of *ProFound's* detected point-source galaxies (green) and resolved sources (red) in W1 after cross-matching with the G23 catalogue in **area 3** (it is the total area of study that combines the two tiles 1268 and 1370 presented in Section 4.2.1). The total number of resolved and point-sources galaxies are respectively 955 and 13 1397. The two samples show similar distributions.

rejection for a robust statistic (in red). The rejections were applied to the subsets of the



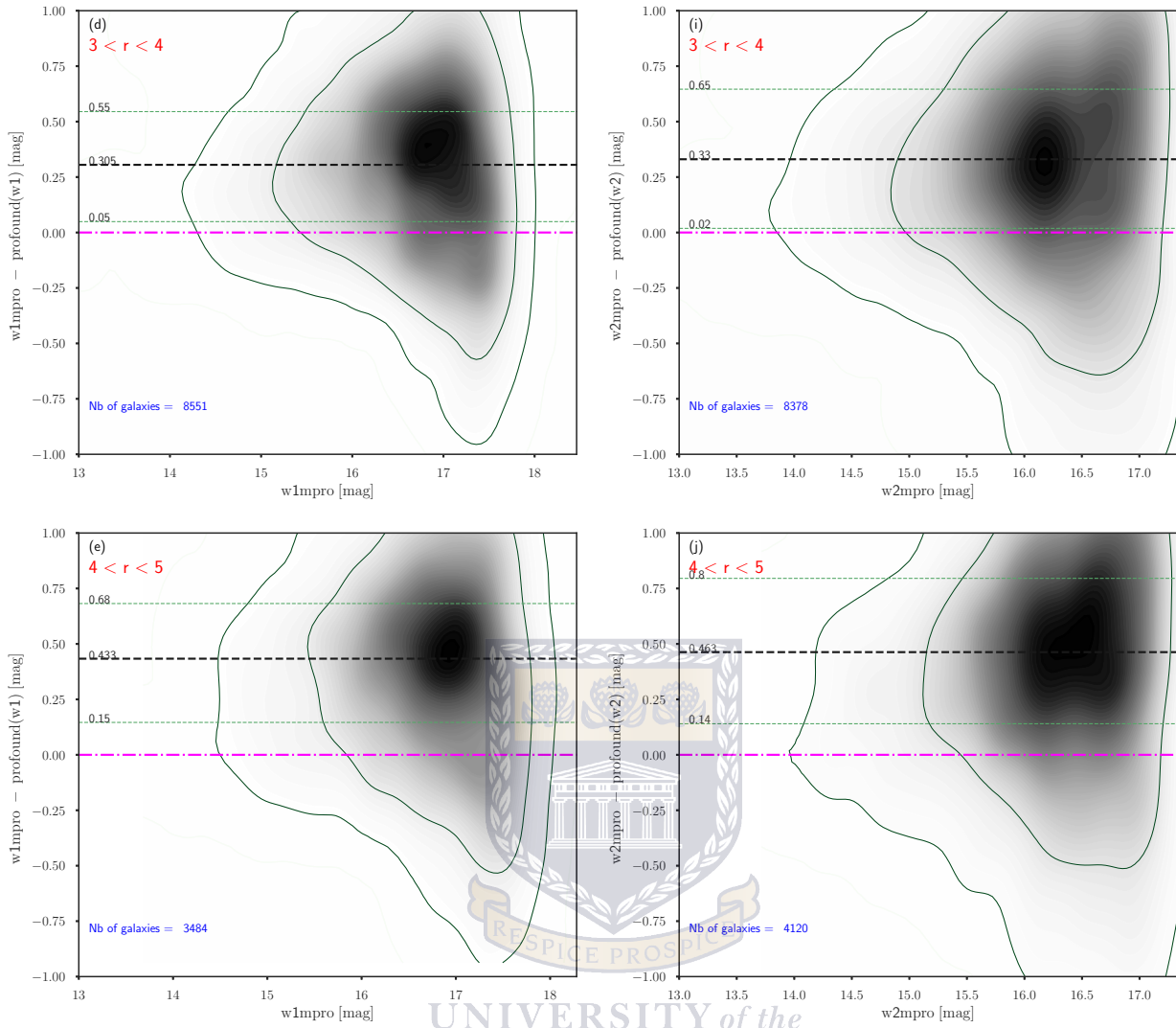


Figure 4.5: Magnitude difference diagram for **area 3** detections. *WISE*(mpro) - *ProFound*(mag) vs *WISE*(mpro) for respectively W1 (left panel) and W2 (right panel). On each panel we have different cases for the cross-match radius (r) varying between 0 and $5''$. The dark dashed lines represent the mean and the green dashed lines are the 25 percentile and 75 percentile. The density plot represents point sources and the green density contours are added for more clarity. The total number of galaxies for each case is given in the lower left corner. The gap between the mean and the 0 mag line (dot-dashed magenta) shows the systematic deviation of *ProFound* magnitude from our *ALLWISE* point source catalogue.

real samples in each band using only the brightest galaxies. The magnitude thresholds used are respectively 16.5, 15.6, 12, and 8.4 in W1, W2, W3, and W4. There is symmetry around the mean in all the bands except for W1, which has a slight offset. W1 and W2 have an overall magnitude difference mean between 5% to 10%, while bands representing the longer wavelengths, W3 and W4, respectively have mean of ≈ -0.21 and ≈ -0.59 . Therefore the red galaxies are looking brighter in the G23 catalogue compared to *ProFound*.

Table 4.3: Statistical diagnostic by *ProFound* of point sources galaxies in **area 3** ($3''$ cross-match radius). AW and P represent *ALLWISE* and *ProFound*, respectively.

bands	Total	only S/N > 2 applied to both (AW and P)	only edge-excess < 1	only flag-border = "false"	all-constraint applied together
w1	115039	115039	99984	114913	97225
w2	82911	80490	65197	82806	62742
w3	13740	11826	10486	13721	8800
w4	3195	2380	2376	3191	1734

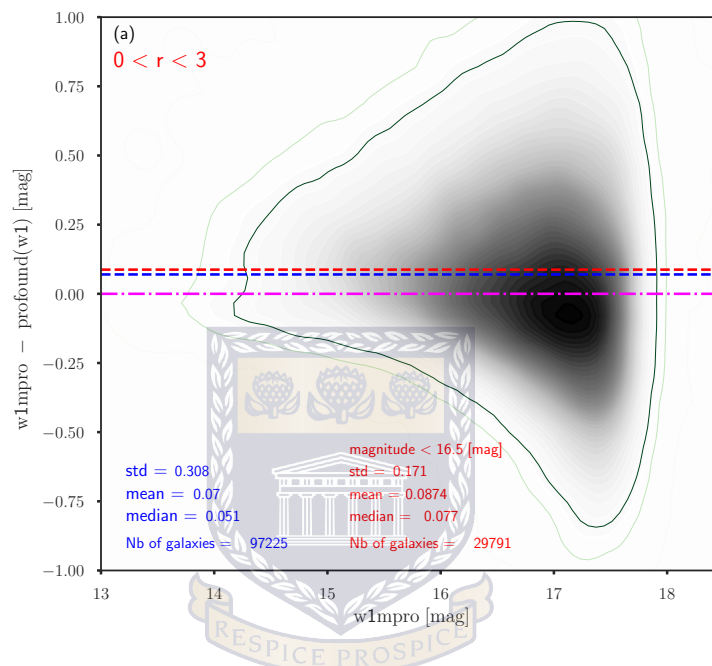


Figure 4.6: Magnitude difference diagram for **area 3** detections in W1 band. *WISE*(W1mpro) - *ProFound*(W1) vs *WISE*(W1mpro). A 2σ rejection was applied to the sample. The blue and red dashed lines represent respectively the mean value of the initial sample and the situation after applying 2σ rejection. The statistics of the two data sets are also given in respectively blue and red. The cross-match radius is $3''$. The density plot represents the point sources galaxies in the area.

This could be caused by the poor resolution of the W3 and W4 as opposed to W1 and W2 or just some simple zero offset. The automated deblending becomes more problematic as the resolution drops. Moreover, the *WISE* longer wavelength has a much lower S/N.

The comparison between the photometry of the G23 catalogue (standard pipeline) and *ProFound* revealed a mild offset in W1 and W2 but became more significant in W3 and W4. We therefore rigorously quantified these shifts after applying a strong statistic to galaxies brighter than 16.5, 15.6, 12, and 8.4 mag in W1, W2, W3, and W4, respectively. The values are displayed in Figures 4.6, 4.7, 4.8 and 4.9 (see the statistic in red). The mean difference values of 0.082, 0.064, -0.22 and -0.59 thus derived were added to *ProFound* magnitudes

respectively in W1, W2, W3, and W4 (Table 4.4). The colour differences and the colour-colour plot will be investigated later using the corrected magnitudes.

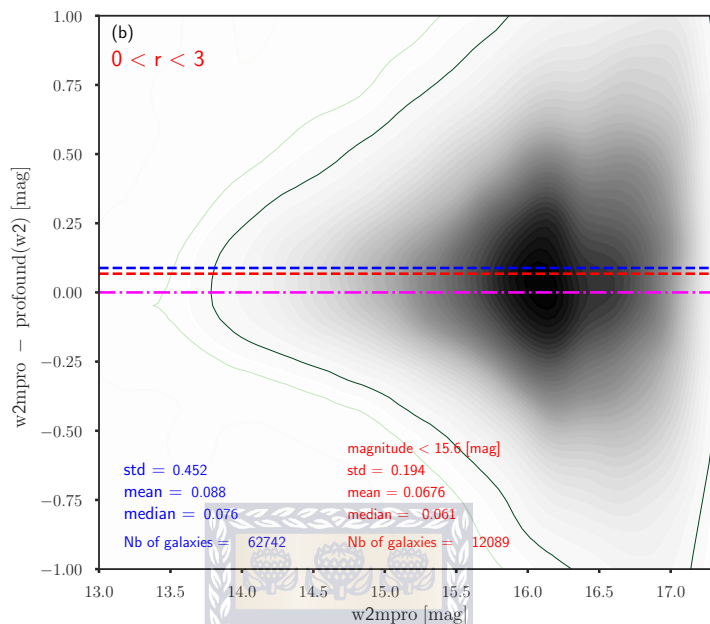


Figure 4.7: Magnitude difference diagram for **area 3** detections in W2 band. *WISE*(W2mpro) - *ProFound*(W2) vs *WISE*(W2mpro). A 2σ rejection was applied to the sample. The blue and red dashed lines represent respectively the mean value of the initial sample and the situation after applying 2σ rejection. The statistics of the two data set are also given in respectively blue and red. The cross-match radius is $3''$. The density plot represents the point sources galaxies in the area.

Table 4.4: Magnitudes correction for *ProFound*

<i>WISE</i> bands	W1	W2	W3	W4
Correction applied	0.087	0.067	-0.21	-0.59

Figure 4.10 shows the final plot of the magnitude difference for point source galaxies between our pipeline and *ProFound*. We added some binned statistics to each band. The magnitude ranges were divided into 10 bins for a given *WISE* band. The average magnitude differences and their error-bars are plotted on top of the greyscale. As expected, the mean difference shows more deviation from the zero magnitude for fainter galaxies, probably due to the large error related to the measurement at these magnitudes. The corrections helped to re-centre the magnitudes in the first three bands within an error less than 5%. The last band (W4) still shows 9% magnitude difference. This could have been caused by the low number of galaxies used for the magnitude correction and the rather larger scatter observed (see red statistic in Figure 4.9).

The error-bars are relatively low in W1 and W2, ranging from $\approx 3\%$ for the brightest

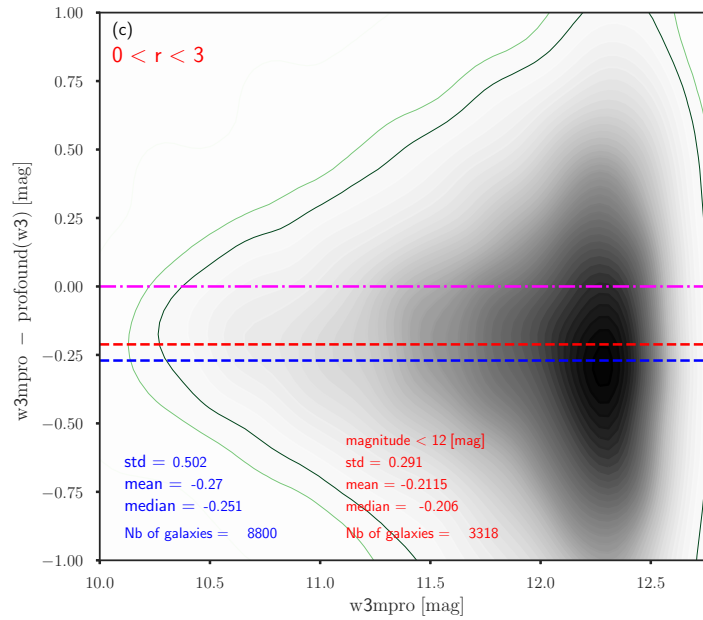


Figure 4.8: Magnitude difference diagram for **area 3** detections in W3 band. *WISE*(W3mpro) - *ProFound*(W3) vs *WISE*(W3mpro). A 2σ rejection was applied to the sample. The blue and red dashed lines represent respectively the mean value of the initial sample and the situation after applying 2σ rejection. The statistics of the two data set are also given in respectively blue and red. The cross-match radius of $3''$. The density plot represents the point sources galaxies in the area.

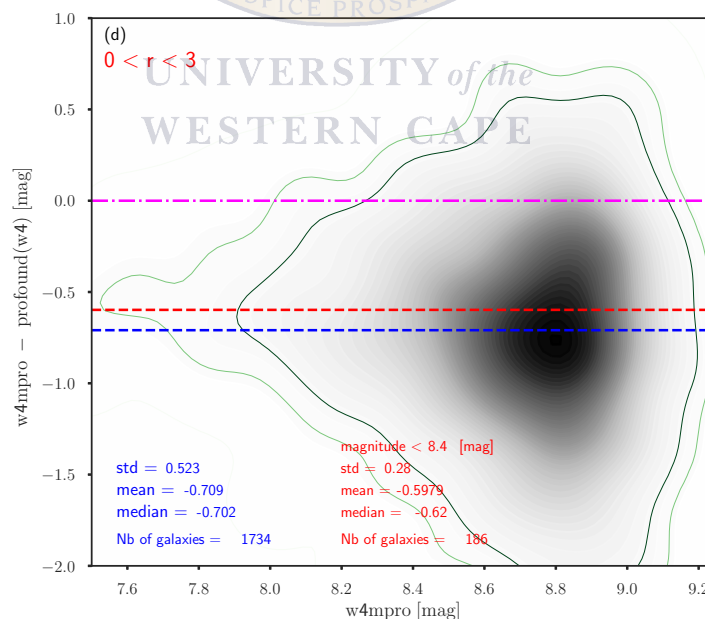


Figure 4.9: Magnitude difference diagram for **area 3** detections in W4 band. *WISE*(W4mpro) - *ProFound*(W4) vs *WISE*(W4mpro). A 2σ rejection was applied to the sample. The blue and red dashed lines represent respectively the mean value of the initial sample and after applying 2σ rejection. The statistics of the two data set are also respectively given in blue and red. The cross-match radius is $3''$. The density plot represents the point sources galaxies in the area.

galaxies up to 20 % in W1 and 30 % in W2 for the faintest. In W3, the error-bars become big, starting from magnitude = 11 mag. The W4 band exhibits much bigger error-bars than W3, both reaching $\approx 50\%$ at their faint end. This could partly explain the offset in the W3 and W4 bands. However, given that the offset in W4 is much higher (-0.59 mag) than the maximum error (± 0.495 mag), additional factors might therefore also be causing this anomaly.

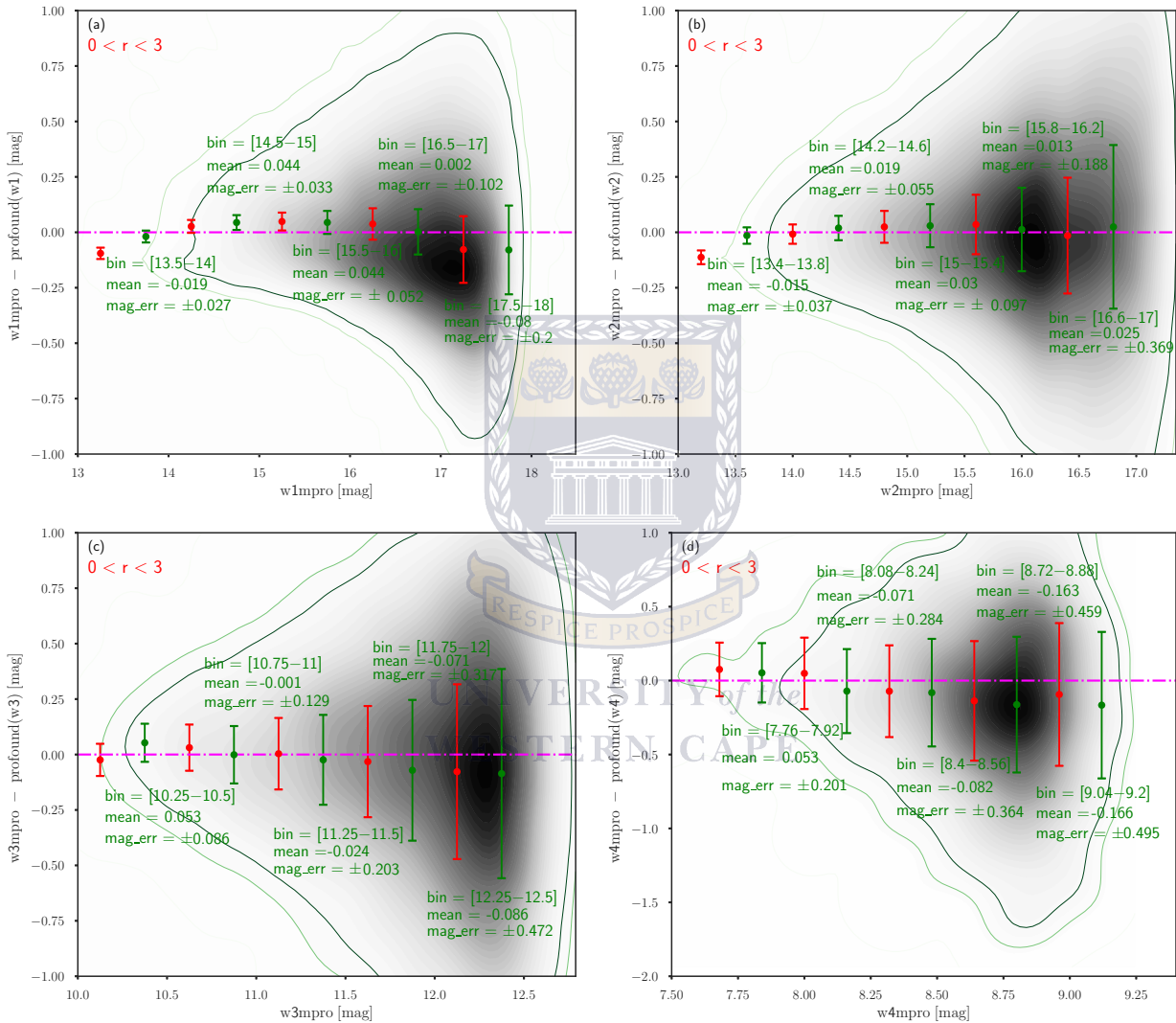


Figure 4.10: Summary plot showing the magnitude differences between the G23 catalogue and ProFound. The offsets seen in Figure 4.6, 4.7, 4.8 and 4.9 have been corrected by adding their mean magnitude difference determined rigorously in each case (Table 4.4). The mean magnitude differences (blue and red) with their error-bars per magnitude bins are plotted on top of the greyscale. The statistics of some points (blue points) are also displayed.

4.3 Photometry of Resolved Sources in the standard pipeline and *ProFound*

The standard pipeline’s photometry is compared to that of *ProFound* for the resolved galaxies in **area 3**. The IR sky is generally very crowded owing to the small aperture of our space telescopes. In this environment, resolved galaxies, much larger than the point sources, are more subject to galaxy-galaxy or galaxy-star blending. We check the performance of *ProFound* relative to the standard pipeline in this section.

4.3.1 Magnitude Difference between the standard pipeline and *ProFound* for Resolved Sources

In Figure 4.11 we compare the photometry derived with our customised software and its counterparts derived using *ProFound*. A $S/N > 2$ was applied as a limit for both extraction methods. We also made sure that all the galaxies used have reliable photometries. The restrictions are given in Table 4.5, which shows the rejection criteria applied to Figure 4.11 for a more robust statistical comparison the standard pipeline and *ProFound*. After applying all the constraints together, there is a significant decrease in the number of galaxies in all the *WISE* bands compared to the initial totals. However, we still have the same general trend as in the raw sample.

Table 4.5: Statistical diagnostic by *ProFound* of resolved galaxies in **area 3**. S P stands for standard pipeline.

Bands	Total	Only $S/N > 2$ applied in both S P and Profond	Only edge-excess < 1	Only flag-border = “false”	All-constraint applied together
w1	901	901	583	900	583
w2	897	897	502	896	502
w3	729	633	404	720	361
w4	479	296	249	445	155

The scatter plots are colour-coded as a function of the S/N from the G23 catalogue on the left panel and from *ProFound* on the right panel. More scattering is seen for fainter galaxies in all the bands, which are correlated with S/N ratio. W1 and W2 appear to be brighter in *ProFound* than our catalogue, which is shown by the averages positives Δmag . However, their Δmag varying between -0.5 and 0.5 mag with average values of respectively 0.05 mag and 0.06 mag, show consistency between the two software used for the extractions.

In contrast to W1 and W2, the W3 and W4 bands that are also the less sensitive, show much higher differences. Indeed, a negative offset is seen on the W3 distribution, resulting in a mean value of -0.28 mag, while W4 presents a difference of 0.1 mag between the two pipelines. They show also more scatter than W1 and W2.

Some galaxies among extreme outliers (outliers in at least one of the bands) have been selected and designated by letters from F to K in Figure 4.11. Details about these galaxies outside the general trend are summarised in Table 4.6. Their names (the name given in the G23 catalogue), as well as the magnitude difference between the G23 catalogue and *ProFound*, are shown for all the bands. The edge-fraction and edge-excess in W1 are also given. According to *ProFound* diagnostic, if a galaxy has an edge-excess greater than 1, then it is a sign that the segment geometry is irregular, and is probably a flag for compromised photometry. The edge fraction starts from 1 for a completely isolated galaxy and decreases up to 0 for the densest environment. “NA” shows that the galaxy was either not detected or was rejected by the constraints applied in a given band. Figure 4.12-H shows a tough blended case where more than half of the galaxy’s edge pixels are touching other galaxies. The edges of the galaxy were sharply cut in *ProFound*, as opposed to our pipeline where the three nearby sources were identified as foreground stars and removed. This led to an underestimation of the flux by *ProFound*. In “F” and “G”, the galaxies were not cleaned at all by *ProFound*. The foregrounds are probably too faint to be picked up by *ProFound*.

As a matter of fact, they were manually cleaned in the G23 catalogue because they were not automatically cleaned by standard pipeline (reminder, the standard pipeline is semi-automated, with interaction an important component). So, those foreground stars added extra flux to the galaxies in the W1 and W2, which are more sensitive to detecting stars. In W3, the galaxy “G” appears fainter because the contribution from the stars is no longer detected at this wavelength. The apertures of the galaxy “I” in *ProFound*, after the visual inspection in W3 and W4, are too wide for the visible flux in these bands. *ProFound* is probably picking up more from the background flux.

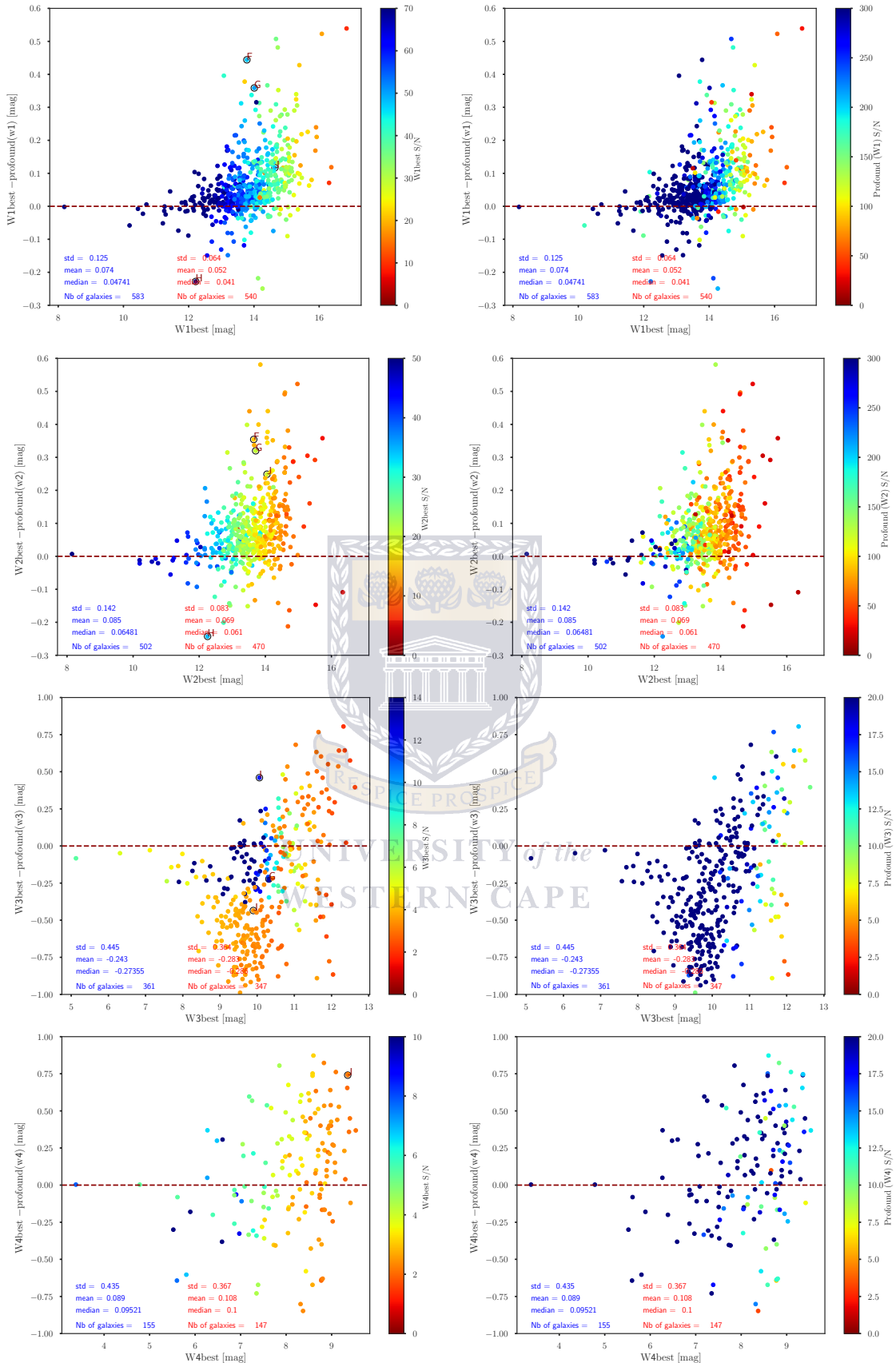


Figure 4.11: Magnitude difference diagram for **area 3** detections. Left panel: *WISE*(best) - ProFound(mag) vs *WISE*(mag) for respectively W1, W2, W3 and W4. The third dimension is colour-coded as a function of *WISE*(best) S/N. The right panel is similar to the left panel except for the third dimension which is colour coded as a function of *ProFound*'s S/N. The statistics before and after applying 2σ rejection are given respectively blue and red in the lower left-hand corner. The black dashed line represents $\Delta\text{mag} = 0$. No correction was applied to *ProFound* magnitude in the figure.

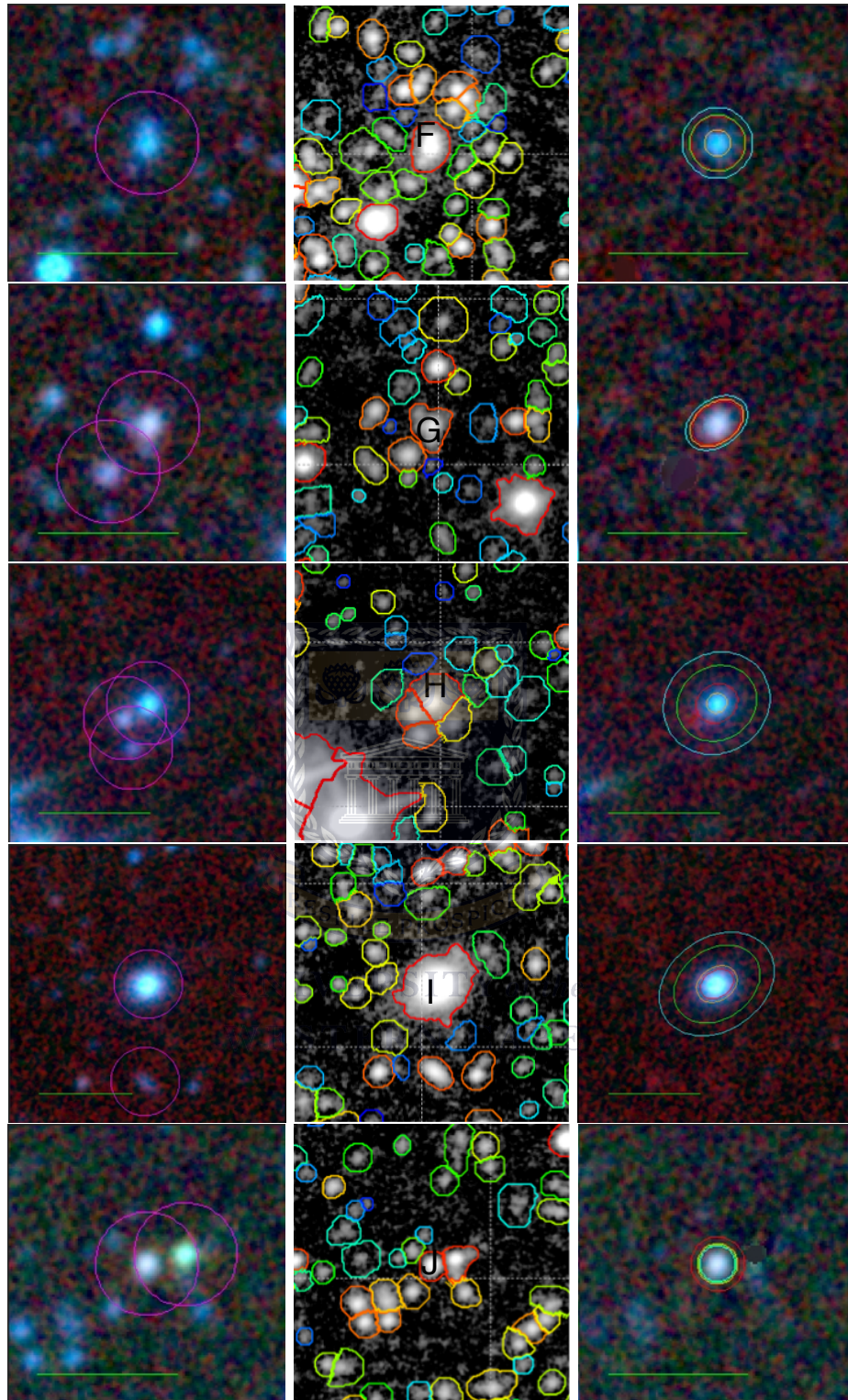


Figure 4.12: The selected outliers from Figure 4.11. The left and the right panels show the *WISE* 3-colours image before and after cleaning. The magenta circles in the first frame show that the galaxy has been picked up as a resolved galaxy. The elliptical contours in the right panel show the extent of the light distribution in W1 (blue), W2 (green), W3 (orange), and W4 (red). The middle panel shows *ProFound*'s segmentation map in W1. The foreground of the galaxies “F” and “G” have not been removed in *ProFound* (they were added to the galaxies' total fluxes). “H” is confused leading to poor deblending. “I” looks well extracted in *ProFound* for the W1 image, but the apertures in *ProFound* for W3 and W4 images (not presented here) are too wide. “J” is a blended case and the deblending might have affected the photometries.

Table 4.6: Resolved galaxy outliers

Galaxy name	Designation	Δmag (W1)	Δmag (W2)	Δmag (W3)	Δmag (W4)	ed-excess (W1)	ed-frac (W1)
J225702.40-333755.2	F	0.4440	0.3542	NA	NA	0.8969	1.000
J225100.34-342332.0	G	0.3587	0.3198	-0.2228	NA	0.9799	0.9494
J225736.45-331044.2	H	-0.2279	-0.2426	NA	NA	0.9679	0.4411
J225735.10-340515.3	I	NA	NA	0.4600	NA	NA	NA
TJ225527.27-341549.5	J	0.1171	0.2488	-0.4348	0.7407	0.9171	0.693

4.4 MeerKAT Source Extraction with *ProFound*

The Karoo Array Telescope (*MeerKAT*; Jonas, 2009; Jonas & *MeerKAT* Team, 2016) is a precursor of the SKA (see Norris et al. 2017). It consists of 64 dishes located in the Karoo, spanning an area of 8 km in diameter. The main reflector and the sub-reflector of each antenna have diameters of 13.5 and 3.8 m, respectively. It appears to be one of the best quality radio instruments in the world today when all the dishes are used in interferometry mode together, as the second SKA pathfinder (*ASKAP*, Johnston et al. 2008), located in Australia has only 36 antennas available. The 64 dishes in *MeerKAT* provide better uv coverage compare to the 32 dishes available in *ASKAP*. Larger scale flux components thus are potentially better captured in *MeerKAT*.

The major problems faced while comparing *ProFound* vs the pipeline used for *WISE* photometry were both the overcrowded environment observed by *WISE* and the blending (galaxy-galaxy or star-galaxy) that goes along with it. Indeed, the IR images obtained by the *WISE* survey are overcrowded because of the small aperture of the space telescopes in general. The radio images on the other hand, even with deep surveys such as *MeerKAT* still have less dense galaxy distribution than the mid-IR (*WISE*), which is more suitable for *ProFound*'s source extraction.

We use *ProFound* for our *MeerKAT* source extraction because the standard pipeline created for *WISE* images is not optimised for *MeerKAT* radio images. Moreover, there is some history with using *ProFound* with radio (*Evolutionary Map of the Universe - EMU*).

In Figure 4.13 Hale et al. (2019) compared *ProFound* to *AEGEAN* and *pyBDSF*. They found that *ProFound* has the ability to capture the complicated shape of the galaxies best. The others relying on the association of several Gaussian components struggle to extract the total flux as seen in the residual, although the activation of the `actrous_do` parameter in *pyBDSF* leads to an improved result.

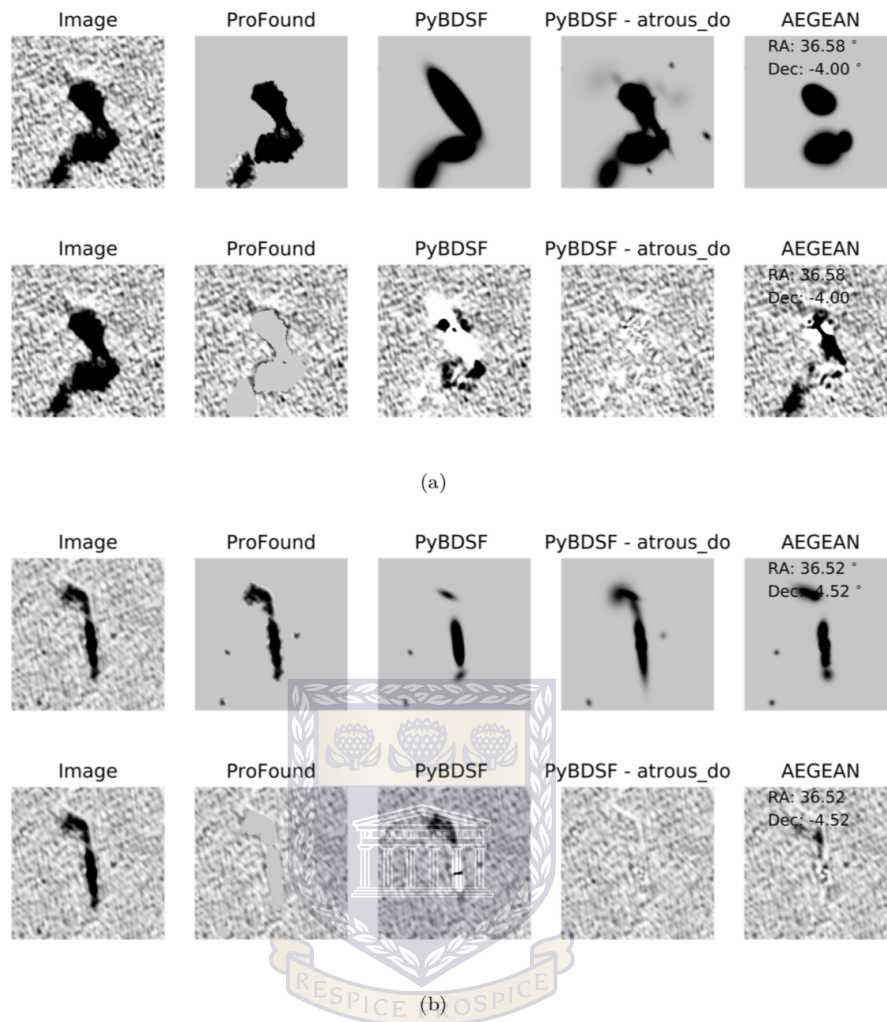


Figure 4.13: *ProFound* compared to commonly used source extraction software such as AEGEAN and pyBDSF. Here two resolved galaxies are presented to be extracted by the different types of software. One can see from the images extracted and their residuals that *ProFound* extracted the shape of the radio emission with greater fidelity than the two other types. Image reproduced from Hale et al. (2019).

The distribution of the 1.4 GHz integrated flux densities for all the sources is shown in Figure 4.14. There is a rise in the detection starting from flux density ~ 0.03 mJy up to 0.017 mJy, where it reaches about 5000 galaxies detected. It is followed by a constant (in the log) decrease in detection up to a flux density of about 0.4 Jy.

In Figure 4.15 we compare the flux measurement from the MeerHOGS data with the difference in flux between the MeerHOGS and NRAO VLA Sky Survey (NVSS; Condon et al. 1998) catalogue data. The measurements from the two surveys agree within 10% in average. MeerHOGS seems to capture about 40% more fluxes at the faint end and this tendency decreases reaching $\sim 10\%$ at 100 mJy. This could be related to the difference in sensitivity between the surveys or the source extraction method used. *ProFound*, whose

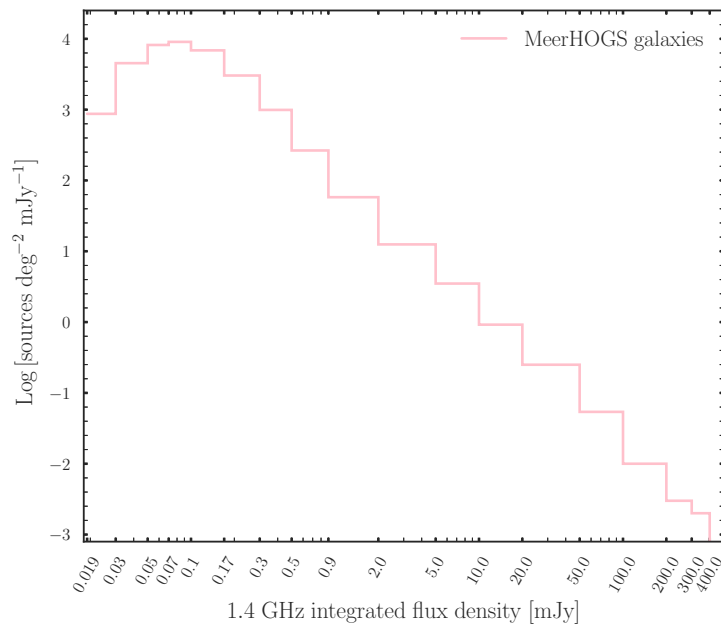


Figure 4.14: Distribution of integrated 1.4 GHz flux densities of all sources. The number of sources peaks around a flux density ~ 0.1 mJy. The two galaxies at the brightest end (300–400 mJy) are respectively MH17 and MH37 presented in Table 6.1.

algorithm follows the light distribution in the galaxy, might be collecting slightly more fluxes as opposed to the conventional extraction methods such as AEGEAN and pyBDSF used for NVSS data. We should also take into account the calibration applied to the MeerHOGS data. Indeed, the CARACal pipeline (Jozsa et al. 2020) used for the data processing is

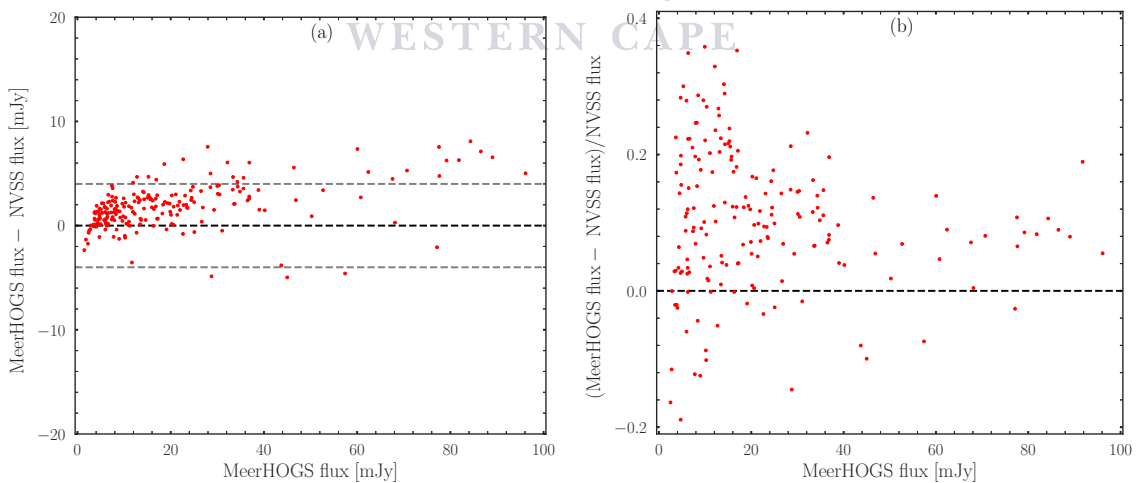


Figure 4.15: (a) MeerHOGS vs MeerHOGS - NVSS continuum flux. The mean difference is 1.77 mJy. (b) MeerHOGS vs (MeerHOGS - NVSS)/NVSS continuum flux. The two surveys agree within $\pm 40\%$ for fluxes ~ 2 mJy, which difference in flux decreases up to 10% around 100 mJy. The MeerHOGS sources extracted using *ProFound* are in average $\sim 10\%$ brighter (which is expected) than NVSS. The total number of galaxies is 213.

still in the early development phase. Overall, the data obtained appears to be of very good quality and science-ready.

4.4.1 Conclusions

We compared *ProFound* and the standard pipeline which are both source-finding and extraction software. We investigated both the detection rate and extraction by cross-matching the result of the two packages and the extraction via the comparison of photometries. After a few trials, the tolerance, the sigma, and the skycut values of respectively 1; 1.5 and 2.5 appeared to be most suitable for giving a plausible number of detections and also showing a segmentation map with fewer blended cases. However, we found the standard pipeline, more adapted for source extraction on *WISE* images. *ProFound* was used to extract the radio continuum data from MeerKAT and science results will be presented in Chapter 6, using this catalogue. As explained in 4.4, we were among the first users to test the newly created version of *ProFound* in 2018 on our *WISE* photometry and our results were sent to the team that built the pipeline.

The results found are as follows:

- *ProFound* was able to detect most of the resolved galaxies within a $3''$ cross-match radius with standard pipeline (Jarrett et al. 2013) detections. A visual check of the few remaining sources detected between $3''$ and $5''$ revealed most of the galaxies being blended with nearby stars. We remind the reader that the standard pipeline like all the traditional source-extracting pipelines, fits the light distribution with ellipses such that the centre of the galaxies corresponds to that of the ellipse. On the other hand, *ProFound* follows the random distribution of the light from which the centre of the galaxy is estimated. The centre of the galaxies determined by both versions of software may vary according to its real shape. It also depends on the capacity of the software to deblend the blended galaxies.
- Comparing coordinate positions (using a $3''$ cross-match radius), we find average RA and declination differences of $0.''07$ and $0.''06$, respectively.

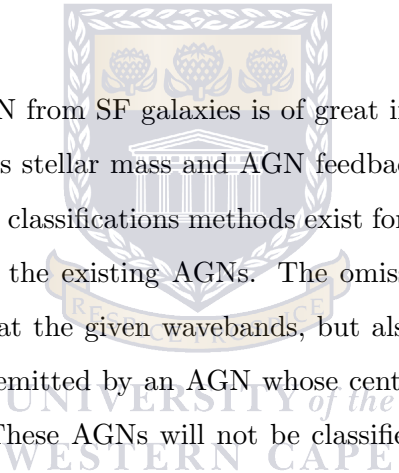
- Both pipelines reach similar magnitudes for the sources extracted in W1 and W2; however, significant differences are found in W3 and W4. This could be related to the lower resolution of W3 and W4 in comparison to the two first bands (W1 and W2).
- *ProFound* appears to be better adapted to the radio continuum data. It excels in the extraction of the extended emissions following their typical non-symmetric shapes. *ProFound* was therefore only used for the extraction of the radio data.



UNIVERSITY *of the*
WESTERN CAPE

Chapter 5

Separating AGN and SF Galaxies with Optical and Mid-IR Data



Being able to separate AGN from SF galaxies is of great interest in understanding galaxy evolution because SF builds stellar mass and AGN feedback can disrupt this process. We recall (see Section 2.3) that classification methods exist for different wavebands, with each one revealing a fraction of the existing AGNs. The omissions are thought to be related to the features observable at the given wavebands, but also to the orientation effect. For example, the optical lines emitted by an AGN whose central part is clouded by dust will be completely absorbed. These AGNs will not be classified using the optical wavelength regime or in the worst case classified as SF galaxies. They are referred to as obscured AGNs. The IR observation on the other hand relies heavily on the dusty torus, whose absence will compromise the classification at these wavebands. Based on this non-exhaustive list of issues, we decided to combine two of the most frequently used classification methods (the optical BPT and *WISE* colour- colour) with the aim of deriving an improved classification scheme.

This chapter is based on the work published in the *Astrophysical Journal* (ApJ): Yao, H. F. M., Jarrett, T. H., Cluver, M. E., et al. 2020, ApJ, 903, 91, doi:10.3847/1538-4357/abba1a

5.1 Data

The *WISE* galaxy catalogue is cross-matched with the GAMA spectroscopic data as presented in Chapter 3. The resulting catalogue is used to combine the widely used diagnostic method in the optical (the Baldwin, Phillips & Terlevich 1981 diagram, BPT diagram) and in the mid-IR (*WISE* colour-colour diagram) for a) identifying, and b) better understanding the processes at work in SF and AGN dominated galaxies.

5.1.1 Property of the GAMA-*WISE* Galaxies

Figure 5.1 presents the full *WISE*-GAMA galaxy catalogue in G23 with redshifts (40 843 galaxies). The *WISE*-resolved galaxies (total of 2 695 in G23) have been added to the point-source photometry from *ALLWISE* to create a quality-controlled catalogue, which is

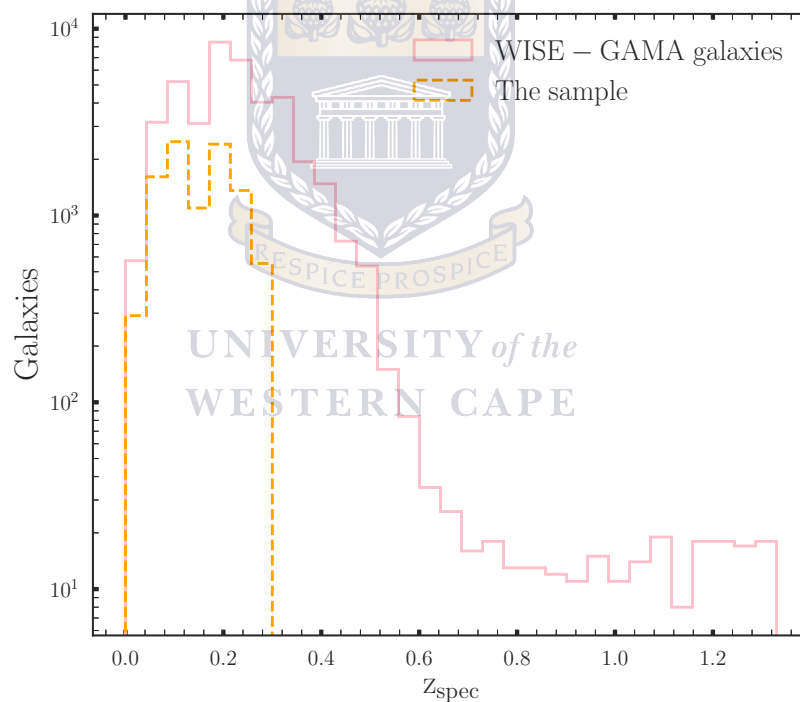


Figure 5.1: The number distribution as a function of the redshift. All *WISE*-GAMA G23 galaxies ($\sim 41\,000$ galaxies with GAMA redshifts) are represented by the solid pink line, of which more than 75% have redshifts < 0.3 . The sample (dashed orange line) has about 9 800 galaxies after applying a redshift and magnitude cuts of $z < 0.3$ and $W1 < 15.5$ mag, respectively (see Section 5.1.2).

well suited to detailed study at low redshifts. The galaxy distribution peaks around $z = 0.2$, with more than 75% located at $z < 0.3$, and most of the resolved galaxies at redshifts

less than 0.15.

The differential source counts in W1 for the different *WISE* and/or GAMA sources are shown in Figure 5.2. The galaxy source counts for the Galactic North Pole and GAMA

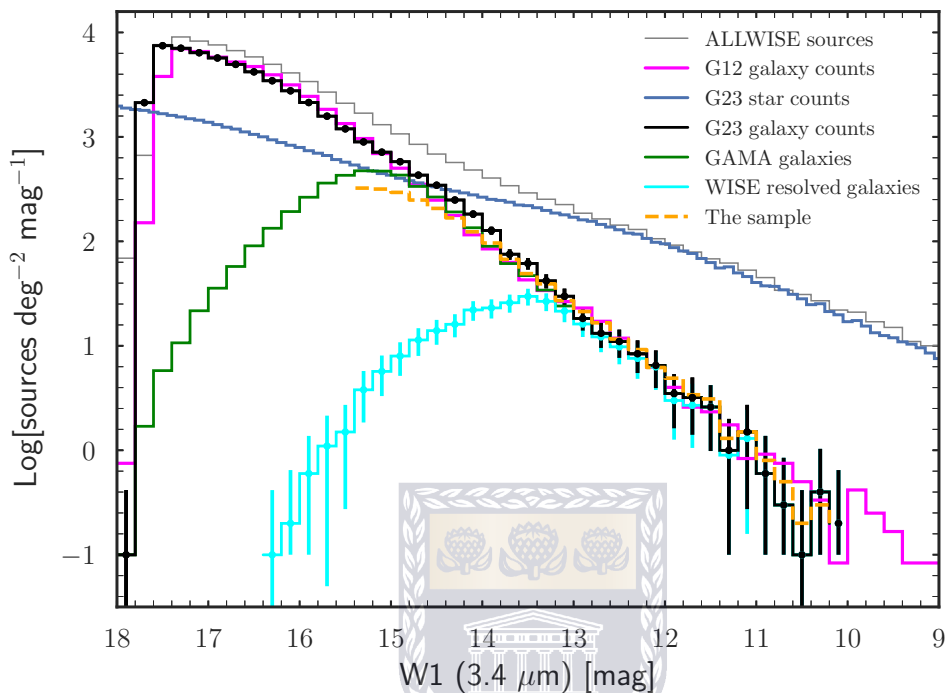


Figure 5.2: Differential W1 ($3.4 \mu\text{m}$) source counts in the G23 region with magnitudes in the Vega system. The *ALLWISE* sources are shown in solid grey. The *WISE* star and galaxy counts are the dark blue and black lines, respectively. The *WISE* cross-matched GAMA galaxies and resolved galaxies are in solid green and light blue lines, respectively. The total number of *WISE* sources is $\sim 600\,000$ (galaxies + stars) and $\sim 41\,000$ of the galaxies have GAMA redshifts. The orange dashed histogram represents our sample, which has a magnitude limit in W1 < 15.5 mag (in Vega system) and redshifts < 0.3 . The *WISE* cross-matched GAMA (G12, Jarrett et al. 2017) galaxies in magenta have been added for comparison. The vertical lines represent Poisson error bars.

G12 from Jarrett et al. (2017) have been added for comparison. The large majority of galaxies at the bright end are resolved up to a W1 magnitude of 13.5 mag (1.2 mJy), where the distribution turns over. The galaxy counts in G23 and G12 are similar all the way to the faint end (~ 17.5 mag), which may be expected because both are focused near the Galactic poles. The *WISE*-GAMA galaxy counts rise close to the *WISE* galaxy counts up to 15.5 mag, where it turns over, owing to the G23 survey redshift limit. The proximity of the two curves in Figure 5.2 (the green and the black lines, respectively) shows that a very high fraction of *WISE* sources have redshifts in GAMA up to 15.5 mag. The *ALLWISE* counts (galaxies + stars) show the domination of Galactic stars at the bright end, although we only expect minimal contamination due to our filtering and classification. The faint end,

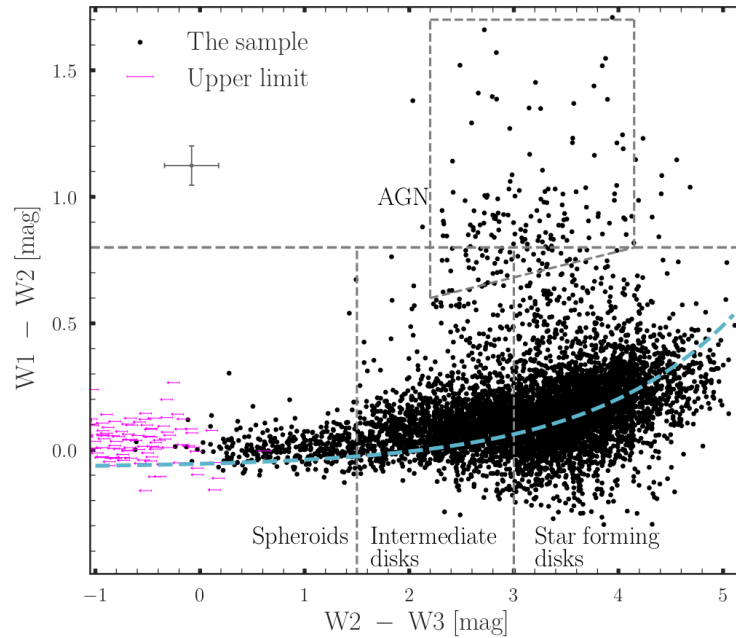


Figure 5.3: The *WISE* k-corrected colour-colour plane, $W1-W2$ vs $W2-W3$ (magnitudes are in the Vega system). The upper limits are represented by the magenta arrows and the dashed blue line is the SF sequence (Jarrett et al. 2019) seen at low $W1-W2$ (<0.5 mag) colour, typical of SF galaxies. The AGN box is from Jarrett et al. (2011) and the horizontal line from Stern et al. (2012). We also plot the mean $W1 - W2$ and $W2 - W3$ uncertainties with the error bars in the upper left corner.

which is not relevant to the study presented here, is expected to have unresolved galaxies with a higher probability of blending as the confusion limit of *WISE* is reached (Jarrett et al. 2017).

5.1.2 The Study Sample

Table 5.1: Table showing the number of galaxies for different constraints applied.

Total <i>WISE</i> -GAMA G23 catalogue (A)	41 000
A with $W1 < 15.5$ mag, $z < 0.3$ (B)	9 800
B with $S/N(W1) > 5$, $S/N(W2) > 5$, $S/N(W3) > 2$ (C)	6 493
C with $H\alpha$, $H\beta$, $[O III]$, $[N II]$ all in emission and $S/N > 3$ (D)	1 173
C with $H\alpha$, $H\beta$, $[O III]$, $[S II]$ all in emission and $S/N > 3$ (E)	1 037

Notes. The letters in brackets represent a given sample (e.g., A)

For the comparative study of *WISE* colours and the optical BPT diagrams, we have applied a magnitude and a redshift cut of $W1 < 15.5$ mag (in Vega) and $z < 0.3$, respectively, to the *WISE* catalogue of galaxies in G23 having redshifts, hereafter referred to as “the

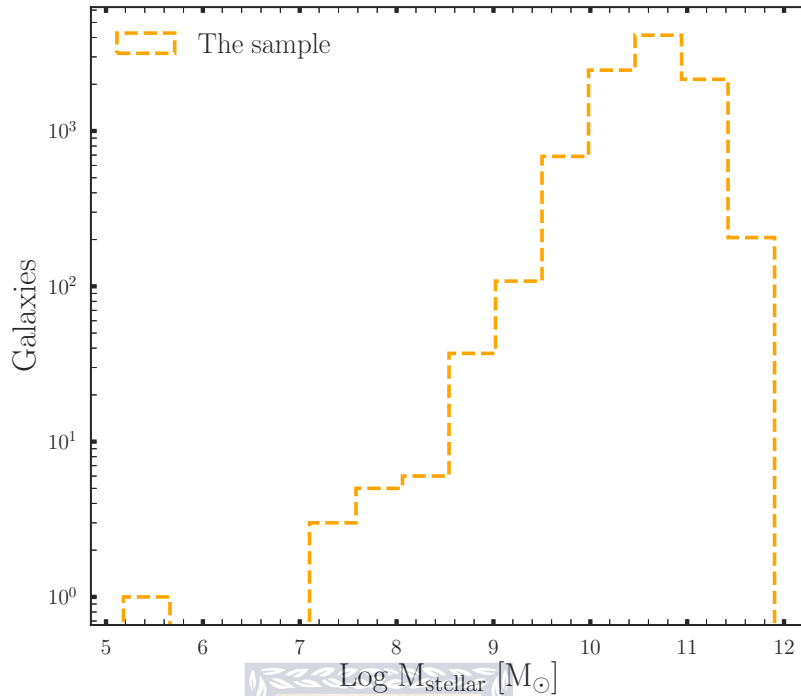


Figure 5.4: The distribution of stellar masses for the galaxies in the study sample. The sample contains very few low-mass galaxies with $< 2\%$ having $\log(M_{\text{stellar}}/M_{\odot}) < 9$.

sample”. For the resolved galaxies, this corresponds to an average $S/N \approx 30$ in W1, and corresponding lower values for the W2 and W3 bands. An S/N limit of 3 is imposed on the optical spectral line flux measurements used in the BPT. Table 5.1 shows how the number of galaxies decreases from the initial *WISE*-GAMA G23 catalogue to the final number of galaxies used for the optical and IR diagnostics. (A), (B), (C), and (D) represent each step. For example, “A” with $W1 < 15.5$ mag, $z < 0.3$ means that in the second row, a magnitude limit of $W1 < 15.5$ mag and redshift $z < 0.3$ are applied to the total *WISE*-GAMA G23 catalogue

In Figure 5.1, the sample (dashed orange) is presented along with the *WISE*-GAMA galaxy catalogue, with more than 70% of galaxies found at redshifts less than 0.2. The magnitude cut in W1 (the brightest band) ensures detections with high S/N , but also selects well-deblended sources (based on *WISE* images), hence, good photometry quality in general.

The magnitude limit (in W1) of 15.5 mag eliminates most of the low-mass galaxies, $\log(M_{\text{stellar}}/M_{\odot}) < 9$, which are often misclassified using only the *WISE* colour-colour diagram (low mass starbursts mimic the W1-W2 colour of AGNs; Hainline et al. 2016). Using a sample of 18000 nearby dwarf galaxies ($M_{*} < 3 \times 10^9 M_{\odot}$), selected from the

Sloan Digital Sky Survey, the authors found that while the *WISE* colour-colour diagram is reliable in classifying moderate- to high-mass galaxies, the W1-W2 colour alone should not be used for dwarf galaxies.

As can be seen in Figure 5.2, a cut of 15.5 mag offers the best of our carefully measured *WISE*-resolved galaxies (2 383, $\sim 90\%$ of the *WISE* resolved sample) and also the brightest unresolved sources (7 426 point-like galaxies). A brighter magnitude cut will lead to fewer galaxies, and a fainter cut will include more faint point-source galaxies with lower S/N. In this way, 15.5 mag is the best balance between completeness and mid-IR (W1, W2, and W3 bands) photometric quality, giving a final sample of 9 809 galaxies.

The W1 - W2 vs W2 - W3 colours (colour-colour diagram) of the sample, with an S/N cut of 5, 5, and 2 in W1, W2, and W3, respectively, are presented in Figure 5.3. The lower S/N for W3 is to account for the lower sensitivity in this band relative to the W1 and W2 bands, as well as taking advantage of the large dynamic range (five orders of magnitude) seen in the W2-W3 colour. The W1-W2 colour is the more critical of the two, as its lower dynamic range requires higher accuracy and is used to distinguish AGN. The AGN box (Jarrett et al. 2011) is the expected location of luminous AGNs, while the W1 - W2 = 0.8 mag is a conservative limit for AGNs; galaxies above this limit are classified as *WISE* (mid-IR) AGNs and are frequently in the QSO class (Stern et al. 2012). The dashed blue line is the fit to the sequence (Equation 5.1) seen in the colour-colour diagram for all the catalogues of *WISE*-resolved sources (Cluver et al. 2017; Jarrett et al. 2019). The relation is described by Jarrett et al. (2019) as

$$(W1-W2) = \left[0.015 \times e^{\frac{(W2-W3)}{1.38}} \right] - 0.08 \quad (5.1)$$

In Figure 5.4 less than $< 2\%$ of the galaxies in our sample have a stellar mass $\text{Log}(M_{\text{stellar}}/M_{\odot}) \leq 9$. We therefore do not expect the result in this study to be significantly affected by misclassifications related to dwarf galaxies. The misclassification here is caused by low mass starbursts having similar W1-W2 colour than AGNs (Hainline et al. 2016) or low mass AGNs (with low metallicity) being found in the extreme starburst region of the BPT diagram (Kewley et al. 2019).

5.2 AGN Classification

5.2.1 Optical Emission Line Diagnostics: BPT Diagrams

In this section we investigate the optical emission-line properties of the sample derived from our *WISE*-GAMA catalogue. Special care has been taken to derive the photometry of the resolved sources, which makes our sample a high-quality dataset for a comparative study between the optical and mid-IR diagnostics of activity. The constraints put on the magnitude and the redshift allow us to take advantage of the best photometry from *WISE* and avoid the required optical lines being shifted out of the wavelength range (often [N II] and [S II] for $z > 0.3$) of the AAOmega spectrograph used in GAMA. All the optical spectra have been visually inspected to detect any systematic fitting anomalies. To this end, GAMA has a flag for the quality of each fit corresponding to each one of the optical lines of interest, but sometimes human supervision is needed for the final decision, notably with broad-line systems. The selection criteria are that we detect the emission lines of H α , H β , and [O III] as well as [N II] or [S II] depending on the diagnostic diagram used. H α and H β are corrected for both reddening and stellar absorption using Equation (5.2), and all the lines have a S/N > 3 (note that this strict criterion eliminates a large fraction of sources from our sample). The Balmer line absorption correction is applied as follows:

$$F_{\text{corr}} = \left[\frac{\text{EW} + 2.5}{\text{EW}} \right] \times F_{\text{obs}}, \quad (5.2)$$

where EW is the equivalent width of the line of interest, F_{obs} is the observed flux and 2.5 is the approximate correction required for GAMA spectra (see Gunawardhana et al. 2011, 2013; Hopkins et al. 2013).

The BPT classification on the plane [O III]5007/H β vs. [S II]6716,6731/H α is shown in Figure 5.5. A count of 1037 out of the 9809 initial sample satisfy the S/N conditions mentioned above. Seventy-five galaxies are classified as Seyferts and five as LINERs.

The redshift (z) cut of 0.3 is only for GAMA-derived spectra, but the catalogue also contains 6dF and 2dF spectra where $z = 0.13$ and $z = 0.2$, respectively, should be used as upper limits.

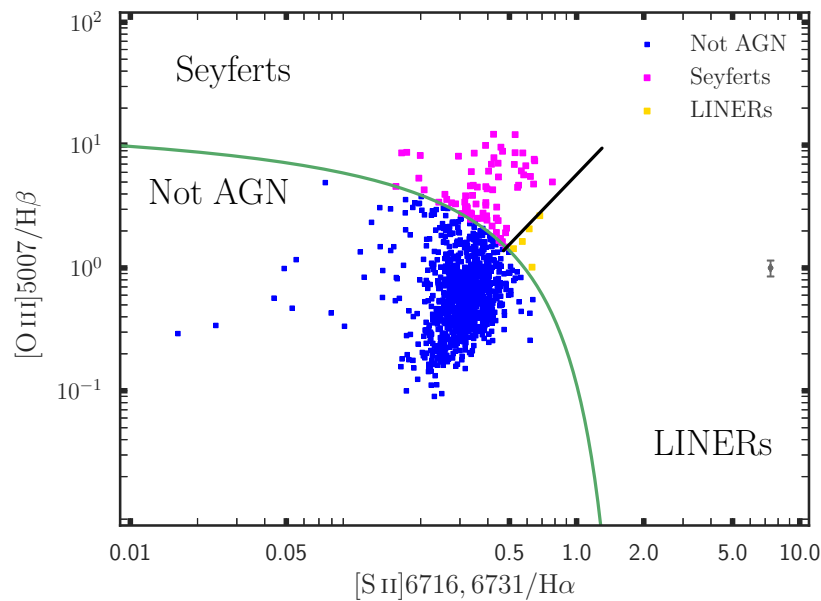


Figure 5.5: The BPT diagram ($[O\text{ III}]5007/H\beta$ vs. $[S\text{ II}]6716,6731/H\alpha$) with all the required lines in emission. The extreme starburst classification line (green solid) and the Seyfert-LINER separation line (black solid) by Kewley et al. (2006). Above the green line lie the AGNs (Seyferts or LINERs) and below it the galaxies that are not AGNs. There are very few LINERs in comparison with Seyferts. We also plot the mean $[S\text{ II}]/H\alpha$ and $[O\text{ III}]5007/H\beta$ uncertainties with the error bars (middle right).

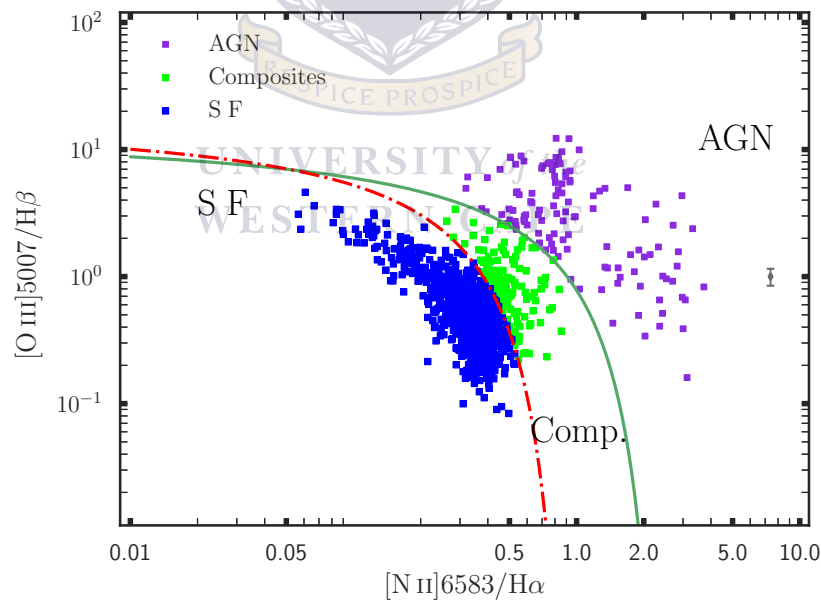


Figure 5.6: The BPT diagram ($[O\text{ III}]5007/H\beta$ vs. $[N\text{ II}]6583/H\alpha$) with all the required lines in emission. The green line represents the limit between AGN and non-AGN galaxies (Kewley et al. 2006) and the Kauffmann et al. (2003) pure star formation line (red dashed). Above the green line lie the AGNs (violet), between the two lines are the composite galaxies (green), and below the red dashed line lie the SF galaxies (blue). Note a clear separation of the AGN group into two distinct subgroups. The second subgroup (right side) tends to be BL systems. We also plot the mean $[N\text{ II}]/H\alpha$ and $[O\text{ III}]5007/H\beta$ uncertainties with the error bars (middle right).

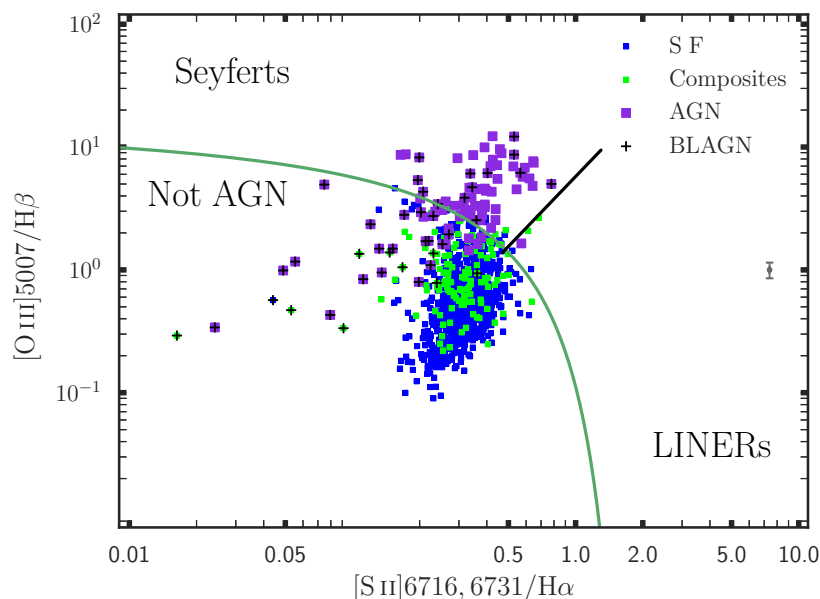


Figure 5.7: Comparison of the two optical classifications. About 85% (998/1173) of the galaxies represented in Figure 5.6 respect the conditions applied in Figure 5.5. In this figure, one can see that the two BPT diagrams agree generally on the separation of AGN and SF galaxies. In most cases, the AGNs seen as outliers are very broad-line systems for which the measurement presents challenges that will be addressed in the next sections. We also plot the mean $[S II]/H\alpha$ and $[O III]/H\beta$ uncertainties with the error bars (middle-right).

The second BPT diagnostic diagram, $[O III]5007/H\beta$ vs. $[N II]6583/H\alpha$, is shown in Figure 5.6. Similar constraints have been applied. In total, 1173 galaxies are selected; 122 are classified as AGNs, 170 as composites, and 881 as SF.

The $[N II]6583/H\alpha$ line varies as a function of metallicity, which has a correlation with stellar mass (Wu et al. 2016). Therefore, the low-metallicity AGNs could be found below the extreme starburst line presented in Kewley et al. (2019). The study by Kauffmann et al. (2003) shifted the Kewley et al. (2006) line to create a new limit for pure SF galaxies. The mixed region between the two lines, supposedly made up by galaxies exhibiting both AGN and star formation activities, is referred to as “composites” (Kewley et al. 2019). The current optical separation lines derived based on local galaxies are subject to variations with redshift and can be reliably used at redshift $z < 1$ (Kewley et al. 2013).

The redshift limit used in our study is 0.3 (relatively local universe), where low-metallicity AGNs are extremely rare (Groves et al. 2006).

This is further confirmed by comparing both optical methods in Figure 5.7. The AGNs seen as outliers in the figure have extremely broad $H\alpha$ lines that are difficult to measure accurately, as they are deeply entangled with the blended $[N II]$ lines. The BL AGNs are

specifically addressed in the current work. One more noticeable feature is the quasi-presence of the composites in the SF region, Figure 5.7, which suggests that composites might be SF dominated. Except for particular cases of BLAGNs mentioned above, the two diagrams largely agree on classifying AGN and SF galaxies. We therefore do not expect our result to be significantly affected by the misclassification of AGNs as SF caused by the variation in metallicity.

5.2.2 Classifications Derived from the Combination of Mid-IR and Optical Line Properties

The [N II] emission lines are stronger than the [S II] lines, and using the [N II] rather than the [S II] line has the added benefit of including composite galaxies in the analysis. Based on these facts, we will be using the [O III]5007/H β vs. [N II]6583/H α as the primary optical AGN diagnostic plane, which will be compared to the W1-W2 vs W2-W3 colour plane throughout this work, except where explicitly stated otherwise.

For comparison between *WISE* and BPT, the detection S/N ratio in W1, W2, and W3 are also required to be greater than 5, 5, and 2, respectively, giving a total of 1154 galaxies. We use the results from Figure 5.8, which combines and plots the optical classification from Figure 5.6 displayed in the *WISE* colour-colour diagram, keeping the same colour-coding scheme. The violet dots represent the optically selected AGNs (designated as oAGN hereafter), the blue points are the optical SF galaxies (oSf), and the green points are the composites (referred to as “composite”), which are between the two. The crosses represent galaxies identified as BL AGNs (BLAGNs). The BLAGN selection is based on the method described in Gordon et al. (2017). However, we only keep the galaxies clearly seen as BLAGNs without ambiguity after visual checking. We overplot in magenta and gold circles the galaxies classified as Seyferts and LINERs (where available in the current diagram) from Figure 5.5.

We establish a $+2\sigma$ offset from the SF colour-colour sequence (Equation 5.1) delineated by the green dashed curve in Figure 5.8, which represents photometric scatter in the SF sequence. The colour-colour diagram is divided into three zones represented by the circled numbers: 1, 2, and 3. Zone 1 (pink shade) is where the *WISE* obscured-AGNs, QSOs, LINERs, and ULIRGs are located. Zone 2 (gray shade), just below, is where the low-power Seyferts and LINERs reside – we call it the “mWarm” zone, signifying warmer W1-W2 colour due to greater nuclear activity and corresponding accretion disk emission. Zone 3

(light blue shade) contains the sequence of *WISE* SF galaxies, mostly a mixture of intermediates and SF disk galaxies having low (blue) W1-W2 colours indicative of the host galaxy aggregate stellar population.

The diagram in Figure 5.9 summarises the galaxy classification considering both their optical emission-line properties and their IR *WISE* colours indicative of the host galaxy aggregate stellar population. The galaxies displayed in Figure 5.8 are divided into different groups, taking into account both their optical line properties and their mid-IR colours in *WISE*. Galaxies classified as AGNs in Figure 5.6 (BPT), which are in colour-colour Zone 1 (see Figure 5.8b), are labelled as oAGN (mAGN). The optically classified SF or composites in Zone 1 are labelled non-oAGN (mAGN). The same applies to Zone 2 where the two groups are called respectively oAGN (mWarm) and non-oAGN (mWarm). The mWarm are the galaxies with warmer mid-IR colour than the typical SF galaxies based on the W1-W2 colour. Finally, in Zone 3, all the galaxies classified as AGNs in the optical spectrum that reside in Zone 3 are called oAGN (mSF). The optical SF and composites in Zone 3 (see Figure 5.8a) are called “SF” and “composite,” respectively.

There is a clear presence of oAGNs in the *WISE* SF zone. Some non-oAGN objects are located in both the mid-IR warm (mWarm) and the obscured-AGN zone, of which 25% in the mAGN zone are composites and 50% are BLAGNs misclassified by the BPT (Figure 5.8a). Having some optically classified composite galaxies in the mid-IR warm or AGN zone is expected, as they are a mixture of both AGN and star formation. However, the vast majority lie in the mid-IR SF zone, meaning that their host galaxies generally dominate over the AGN activity. The Seyferts are found in the mid-IR AGN zone as well as in the SF and are generally classified as oAGNs, while in most cases the LINERs (classification based on [S II] line) designate a non-oAGN (classification based on [N II] line) and are classified as SF galaxies in the *WISE* colour-colour diagram. The nature of LINERs is not well understood, and while they may be associated with SF and shocks thereof, they may also harbour low-luminosity AGNs (Flohic et al. 2006). Our data and analysis are unable to address this ongoing issue properly, and we provide no further analysis on LINERs.

Another trend is the presence of oAGNs in the *WISE* SF zone. There are even a few BLAGNs with SF colours, which is intriguing because *WISE* generally seems to be very sensitive to broad H α lines. They constitute very good specimens to be followed up in radio and X-rays.

We now reproject back into the BPT plane the new optical and mid-IR classification codes, as shown in Figure 5.10a. The figure shows a clear separation of the oAGN (mAGN)

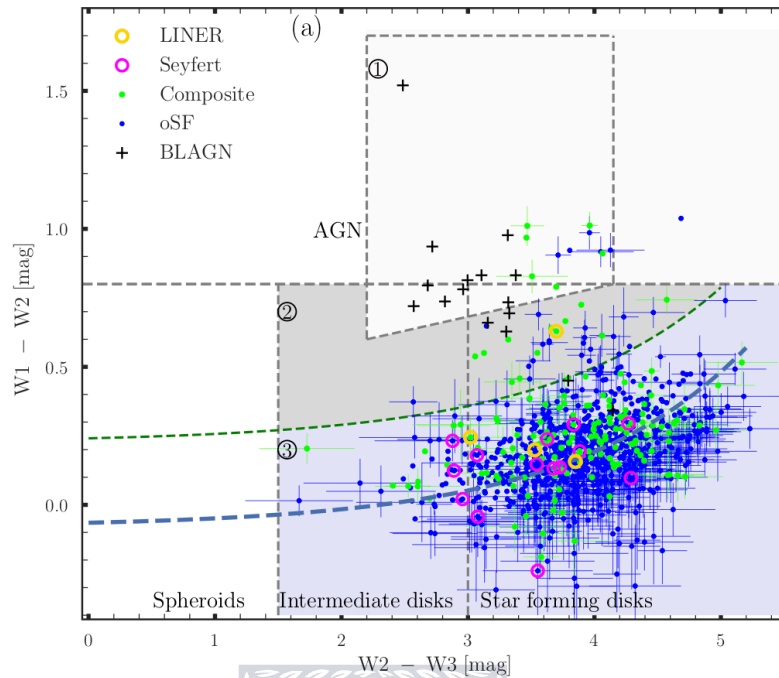
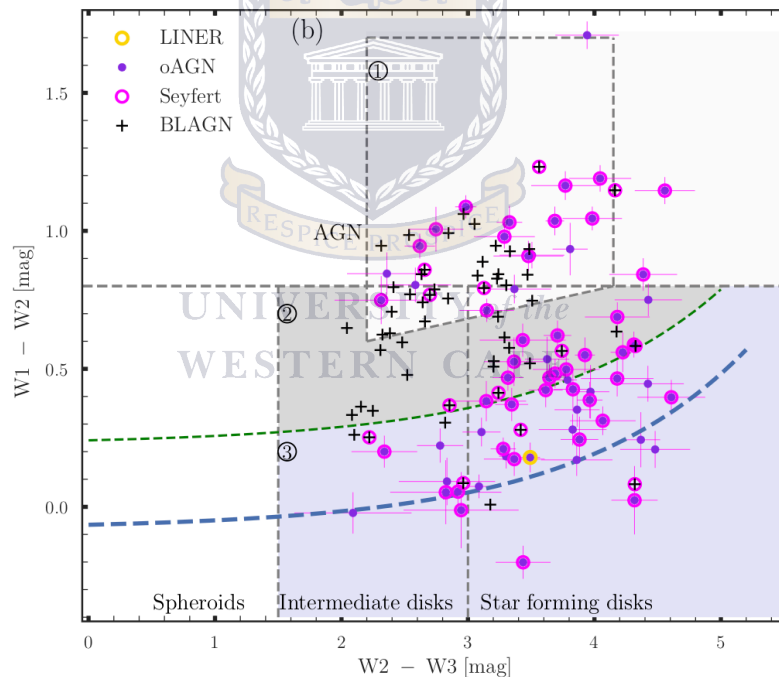
(a) *WISE* colour-colour for optical SF and composites(b) *WISE* colour-colour for optical AGNs

Figure 5.8: The BPT $[\text{O III}]\lambda 5007/\text{H}\beta$ vs. $[\text{N II}]\lambda 6583/\text{H}\alpha$ classified galaxies from Figure 5.6 plotted in the *WISE* colour-colour diagram. Those also classified as Seyferts and LINERS from Figure 5.5 are overplotted in magenta and gold circles, respectively. The dashed blue and green lines are the fit to the sequence of galaxies (Equation 5.1) seen at low $W1-W2$ colour and the 2σ RMS curve of the fit. The AGN box is from Jarrett et al. 2011). The diagram is separated into three zones: Zones 1, 2, and 3 are the respective locations of the *WISE* powerful AGNs, the low-power AGNs and finally the non-AGN zone mostly populated by SF galaxies. The majority of the galaxies classified as LINERS using $[\text{S II}]$ are classified as composites or SF based on the $[\text{N II}]$ line, while the Seyferts are generally classified as AGNs using $[\text{N II}]$. The composites (green) occupy the SF zone. The majority of the optical non-AGNs in the *WISE* AGN zone are BLs for which using the line ratio is problematic. The optical SF galaxies and composites are presented in (a) and optical AGNs in (b); they are separated for clarity.

into two subsamples. The lower-right corner above the green curve shows BLAGNs whose line ratios have been overestimated by the line-fitting algorithm in GAMA. Here it is striking to see all the galaxies with $[\text{N II}]/\text{H}\alpha$ ratio > 1 being BLs with generally overestimated $[\text{N II}]$ fluxes. A larger sample is likely to have shown a few non-BLAGNs for which $[\text{N II}]/\text{H}\alpha$ flux ratios are truly > 1 , but these cases are rare. It is sometimes extremely challenging, if not impossible, to separate $\text{H}\alpha$ and $[\text{N II}]$ when the $\text{H}\alpha$ line becomes broad. Even a reassessment of the flux, which will probably give a more reasonable ratio, lower than 1, will shift the galaxy (BLAGN) into the SF zone unless the $[\text{O III}]$ line's flux is highly elevated. Those galaxies with an underestimated flux ratio constitute 50% of our non-oAGN (mAGN) sample. The GAMA pipeline does not handle the BLs well, notably the blending of $\text{H}\alpha$ and $[\text{N II}]$. Therefore, in these cases, the BPT is not appropriate using the automated pipeline data from GAMA. We have displayed them in this diagram to show where they might correctly or incorrectly be located in the BPT diagram.

The oAGN (mSF) are generally located on the upper left-hand side of the AGN zone along with the oAGN (mAGN). Although classified as AGNs both in *WISE* and optical wavelength regimes, some of the latter galaxies are labelled as either peculiars or late-type spirals by their SED template fits. This could be explained by the fact that they share similar properties with some of the oAGN (mSF), which are also classified as non-AGN based on the SED. Among the non-oAGNs classified as mAGNs only six are oSFs. *The trend is that most of the WISE AGNs are also optical AGNs* or at least composite galaxies that need further attention using other diagnostic methods based on radio or X-ray data. Zone 2 (mWarm) seems to be a transition zone where we find the optical SF galaxies, the composites, and the BLAGNs in similar proportions.

Figure 5.10b shows the host stellar mass as a function of $[\text{O III}]$ line luminosity. In this figure, which requires the use of individual fluxes, unlike the BPT based on line ratios, only calibrated measurements are used (see Hopkins et al. 2013 for the data description). The number of galaxies, therefore, is reduced. The distribution can be separated into two regions, with optical AGNs generally having luminosity greater than 10^{41} erg s^{-1} and SF galaxies with lower values. The BLAGNs also appear to have strong $[\text{O III}]$ lines. Most of the oAGN (mSF) present strong $[\text{O III}]$ luminosity, confirming the presence of nuclear activity (if we assume that $[\text{O III}]$ lines are always related to AGN or nuclear shocks). As expected, the non-oAGN (mAGN) usually have weak $[\text{O III}]$ luminosity, like the SF and composites, with a few exceptions. *WISE* classifying them as AGNs probably has to do with other processes beyond that of a central AGN activity. Some interesting cases such as

oAGN (mSF) with high [O III] luminosity are discussed in Section 5.3.

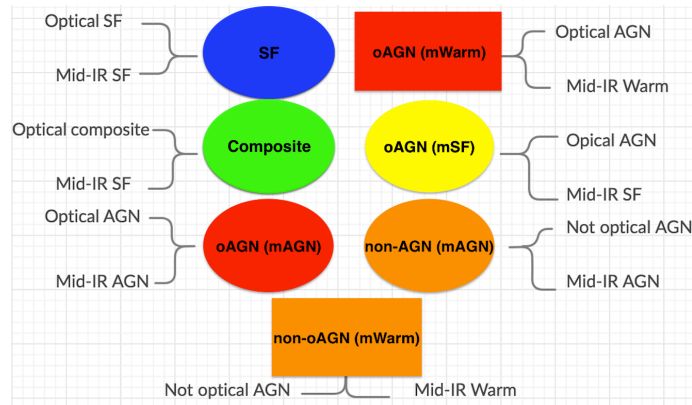


Figure 5.9: Summary of the classification combining both the optical BPT and the *WISE* mid-IR colour-colour diagrams. The ellipses, rectangles, and colours are chosen to follow the legend as presented in Figure 5.10. Blue and red represent the optical and IR classifications that agree, while yellow and orange are in counter-agreement.

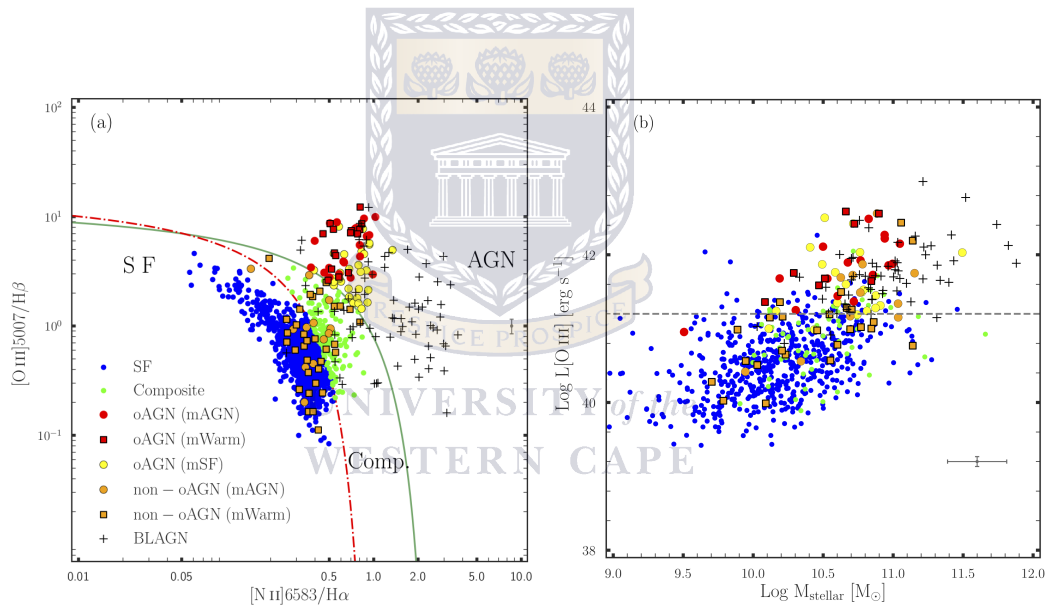


Figure 5.10: Combined optical-IR BPT diagram, showing the different classes of galaxies. (a) The galaxies classified in Figure 5.8 are displayed with different colours according to their categories. As can be seen, only six *WISE* AGNs are classified as SF in the BPT while six are composites. Both the oAGN (mAGN) and oAGN (mSF) are clearly divided into two parts. The AGNs in the lower right-hand corner are almost exclusively BLAGNs whose [N II] line fluxes were overestimated, therefore giving larger [N II]/H α ratio. The mean [N II]/H α and [O III]5007/H β uncertainties with error bars are plotted (middle right). Panel (b) shows the AGN strength represented by the [O III] line luminosity (not reddening-corrected) as a function of stellar mass. In general, there is a clear separation between the AGN and SF galaxies except for the non-oAGN (mAGN) exhibiting low [O III] luminosities. All data points, including the BLAGNs are plotted using a simple Gaussian fit. Only the [O III] luminosity derived from GAMA spectra (calibrated) are used in (b). The dashed line ($\log L[\text{O III}] = 41.2 \text{ erg s}^{-1}$) is the line above which the great majority of optical AGNs are likely to be found. We also plot the mean $\log M_{\text{stellar}}$ and $\log (L[\text{O III}])$ uncertainties with the error bars in the lower right-hand corner.

Table 5.3 contains the detailed measurements used in this study, organised by their BPT-IR classification. $W1$, $W2$, and $W3_{\text{PAH}}$ are rest-frame fluxes (using SED fitting; see Jarrett et al. 2017 for more details). The stellar emission has been subtracted in $W3$. $W1$ - $W2$ and $W2$ - $W3$ are the rest-frame colours used for the colour-colour diagram. The $[\text{O III}]/\text{H}\beta$ and $[\text{N II}]/\text{H}\alpha$ represent the optical line ratios used for the BPT diagnostic. Stellar masses and SFRs ($\text{SFR}_{12\mu\text{m}}$) are derived using the calibration by Cluver et al. (2014) and Cluver et al. (2017), respectively. The specific SFR is the ratio between the SFR and the stellar mass. The galaxies have been classified according to their different AGN groups.

Table 5.2 gives the number of galaxies and their average parameter values in the subsets for different conditions applied to the sample. The number of BLAGNs included in each subset is also shown. “Condition A” presents only the IR classification, while in “B” the optical classification is presented. Both diagnostics are combined in “C,” giving a total number of 1154 classified galaxies. “Condition D” is where we reclassify the BLAGNs based on the fact that they are clearly optical AGNs that were misclassified by the BPT diagram. Notably, the two BLAGNs found in the composite group were reclassified as oAGN (mSF), the BLAGNs (three galaxies) found in the non-oAGN (mWarm) group became oAGN (mWarm) and finally 11 non-oAGN (mAGN) became oAGN (mAGN). We consider the galaxies in the mWarm region to have AGN activity; therefore, in “D” both methods agree on the final classification of 84.4% and 8.2% of the galaxies as non-AGNs (SF + composite) and AGNs, respectively, and disagree on the classification of 7.4%. The redshift distribution of the different groups of galaxies is presented in the next section in Figure 5.12.

5.2.3 Galaxy Properties in Different Activity Classifications

In Figure 5.11 we plot the $\text{SFR}_{12\mu\text{m}}$ as a function of stellar mass and include the main sequence relation of the local galaxies from Grootes et al. (2013), Jarrett et al. (2017), Parkash et al. (2018), and Cluver et al. (2020).

The upper limits trace the galaxies with the lowest SFR corresponding to the passively evolving galaxies (also presented in Figure 5.3). All the groups share the same mass range from $10^{9.8}M_{\odot} < M_{\text{stellar}} < 10^{11.5}M_{\odot}$. The low mass end ($M_{\text{stellar}} < 10^{9.8}M_{\odot}$) is exclusively populated by SF galaxies having low levels of star formation along with a few non-oAGN (mWarm). The high mass end ($M_{\text{stellar}} > 10^{11}M_{\odot}$) is populated by galaxies with broad Balmer lines (panel b), which are classified as AGN, both in the optical and the mid-IR

wavelength regimes. The linear fit to the selection of Jarrett et al. (2017), which is similar to our sample (except that here the AGNs have been separated from the SF galaxies) follows our sequence, especially the high mass end, which is generally populated by AGN. The new sequence fit by Cluver et al. (2020), based on a sample of isolated SF galaxies, also traces our distribution with a slightly flatter slope.

Grootes et al. (2013) UV-selected a sample of nearby ($z < 0.13$) spirals in GAMA that gives a flatter SFR- M_{stellar} relation. The SF-dominated relation given in Parkash et al. (2018) traces our low-mass galaxies best and also seems to follow the background distribution of galaxies (the grey points), which likely includes absorption-line features. Our sample is limited to only bright galaxies ($W1 < 15.5$ mag); moreover it requires at least a detection in W3 (dusty), which might preferably select more massive, star-bursting systems, compared to UV or optically selected samples, as discussed in Jarrett et al. (2017). Figure 5.11c shows a flat distribution with the selected galaxies generally having specific star formation rate (sSFR) $\log \text{sSFR} > -11.4 \text{ yr}^{-1}$. The BPT is more suited for classification of galaxies that are building up their stellar disks not probing as many intermediate (so-called “green valley”) galaxies. We note that we do expect a mass (and $\text{SFR}_{12\mu\text{m}}$) overestimation in galaxies having an AGN because of the additional mid-IR flux coming from the active nucleus, rather than related to the star formation activity itself; this section is therefore intended to be illustrative.

The SF galaxies with the highest $\text{SFR}_{12\mu\text{m}}$ ($\log \text{SFR}_{12\mu\text{m}} > 1.6 M_{\odot} \text{ yr}^{-1}$) are all located at $W2 - W3 > 4.6$ mag and $0.22 \text{ mag} < W1 - W2 < 0.7$ mag. Most of them (7/9, 77%) have $W1 - W2$ well above 0.43 mag, indicating extreme activity. Also, six from a total of nine have a peculiar morphological type (by the SED template and confirmed through visual inspection). This could be a hint that the star formation has been triggered by external processes such as mergers or the tidal influence of the environment. Their masses range from $\log (M_{\text{stellar}}/M_{\odot}) = 10.6$ to 11. On the other hand, the SF galaxies with the highest stellar mass ($\log M_{\text{stellar}} > 11 M_{\odot}$) are SF disk galaxies in the *WISE* colour-colour diagram with $2.6 < W2 - W3 < 3.9$ mag. They also have very low $W1 - W2$ colour (< 0.13 mag), except for one galaxy (CATAID: 5256068, see Table 5.3), which is warmer ($W1 - W2 \sim 0.54$ mag and $W2 - W3 \sim 4.5$ mag) and hence it likely harbours an AGN. They are among the lowest sSFR with a mean $\log \text{sSFR}$ of -10.2 yr^{-1} .

We show the $\text{sSFR}_{12\mu\text{m}}$ ($\text{SFR}_{12\mu\text{m}}/\text{stellar mass}$) as a function of stellar mass in Figure 5.11c and 5.11d. The non-oAGN (mAGN) and non-oAGN (mWarm) have the highest $\log \text{sSFR}$, or building rate, on average, $\sim -9 \text{ yr}^{-1}$. In this case, the environmental influences

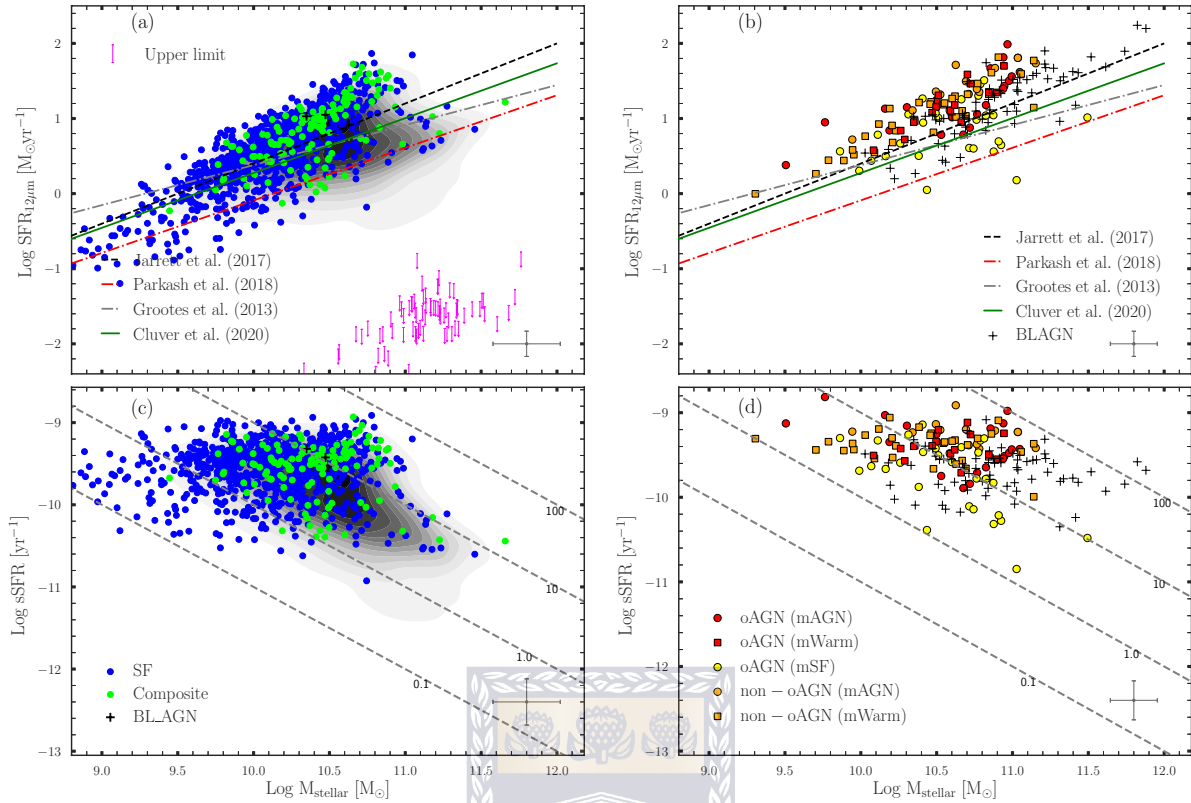


Figure 5.11: Left panel: (a) distribution of the $\text{SFR}_{12\mu\text{m}}$ as a function of stellar mass for the galaxies classified as non-AGNs in both optical and mid-IR. Panel (c) shows the sSFR as a function of stellar mass for the same non-AGN sample, with the dashed lines representing lines of constant SFR (0.1, 1, 10, 100 $\text{M}_{\odot}\text{yr}^{-1}$). The grey shade represents the total sample. The right panels are similar to the previous panels but applied to our different groups of AGNs as indicated in the legend. We expect the stellar mass and the $\text{SFR}_{12\mu\text{m}}$ to be overestimated owing to the AGN activity within the galaxies (in the right panel) thus skewing the SFR and mass estimates, notably for those in which AGNs dominate (i.e., QSOs and BLAGNs). We also plot the mean uncertainties with the error bars for each parameter in the lower right-hand corner.

such as tidal interactions or mergers could have triggered additional star formation as well as AGN emission skewing the IR metrics. They are therefore warm enough to be classified as warm-AGN in *WISE*.

Table 5.2: Subgroups and their different constraints applied to the Sample.

	Number	Broad-line AGN	Redshift	LogM _{stellar}	SFR _{12μm}	Log (sSFR)
				(M _⊙)	(M _⊙ yr ⁻¹)	(yr ⁻¹)
Groups	No. (%)	BLAGN	mean(med)	mean(med)	mean(med)	mean(med)
<i>WISE</i> /G23	Condition A ¹					
Mid-IR SF (mSF)	6133 (94.5 %)	N/A	0.14 (0.13)	10.52 ± 0.003 (10.55)	5.44 ± 0.041 (3.57)	-10.0 ± 0.004 (-9.95)
Mid-IR “warm” (mWarm)	181 (2.8 %)	N/A	0.19 (0.2)	10.52 ± 0.014 (10.6)	11.35 ± 0.425 (9.23)	-9.63 ± 0.019 (-9.61)
Mid-IR AGN (mAGN)	179 (2.8 %)	N/A	0.19 (0.2)	10.6 ± 0.012 (10.71)	23.98 ± 1.126 (13.84)	-9.49 ± 0.017 (-9.52)
Optical/G23	Condition B ²					
Optical SF (oSF)	881 (75.11 %)	1	0.11 (0.09)	N/A	N/A	N/A
Optical (composite)	170 (14.49 %)	15	0.15 (0.14)	N/A	N/A	N/A
Optical AGN (oAGN)	122 (10.4 %)	56	0.18 (0.19)	N/A	N/A	N/A
<i>WISE</i> /Optical/G23	Condition C ³					
SF	838 (72.6 %)	0	0.10 (0.09)	10.11 ± 0.01 (10.13)	06.23 ± 0.13 (03.48)	-9.58 ± 0.01 (-9.52)
Composites	138 (12.0 %)	2	0.14 (0.12)	10.39 ± 0.02 (10.41)	10.43 ± 0.48 (07.28)	-9.56 ± 0.02 (-9.48)
oAGN (mAGN)	49 (4.2 %)	30	0.20 (0.21)	10.90 ± 0.02 (10.93)	32.89 ± 2.67 (24.92)	-9.56 ± 0.03 (-9.58)
oAGN (mWarm)	33 (2.9 %)	18	0.17 (0.18)	10.61 ± 0.03 (10.62)	14.84 ± 1.25 (10.86)	-9.58 ± 0.04 (-9.55)
oAGN (mSF)	37 (3.2 %)	7	0.17 (0.18)	10.61 ± 0.03 (10.60)	09.33 ± 0.76 (08.82)	-9.78 ± 0.04 (-9.66)
Non-oAGN (mAGN)	23 (2.0 %)	11	0.21 (0.21)	10.79 ± 0.03 (10.78)	28.14 ± 2.53 (22.92)	-9.43 ± 0.04 (-9.43)
Non-oAGN (mWarm)	36 (3.1 %)	3	0.18 (0.19)	10.46 ± 0.03 (10.51)	16.79 ± 1.43 (13.11)	-9.41 ± 0.04 (-9.37)
<i>WISE</i> /Optical/G23	Condition D ⁴					
SF	838 (72.6 %)	0	0.10 (0.09)	10.11 ± 0.01 (10.13)	06.23 ± 0.13 (03.48)	-9.58 ± 0.01 (-9.52)
Composites	136 (11.8 %)	0	0.14 (0.12)	10.39 ± 0.02 (10.41)	10.42 ± 0.49 (07.02)	-9.56 ± 0.02 (-9.49)
oAGN (mAGN)	59 (5.1 %)	41	0.20 (0.21)	10.89 ± 0.02 (10.91)	30.75 ± 2.23 (23.72)	-9.57 ± 0.03 (-9.58)
oAGN (mWarm)	36 (3.1 %)	21	0.18 (0.18)	10.64 ± 0.03 (10.64)	15.82 ± 1.26 (11.81)	-9.58 ± 0.04 (-9.55)
oAGN (mSF)	39 (3.4 %)	9	0.16 (0.18)	10.60 ± 0.03 (10.59)	09.41 ± 0.73 (09.17)	-9.76 ± 0.04 (-9.66)
Non-oAGN (mAGN)	13 (1.1 %)	0	0.20 (0.20)	10.74 ± 0.04 (10.77)	34.18 ± 4.23 (24.68)	-9.29 ± 0.06 (-9.23)
Non-oAGN (mWarm)	33 (2.9 %)	0	0.17 (0.19)	10.41 ± 0.03 (10.46)	15.90 ± 1.45 (12.64)	-9.39 ± 0.04 (-9.36)

Notes. The mean and median values of some properties have been added. The Condition C was applied to Figure 5.8.

¹S/N: W1 > 5, W2 > 5 and W3 > 2, redshift < 0.3; and magnitude (W1) < 15.5 mag (in Vega).

² S/N (optical lines) > 3; redshift < 0.3; H α > 0; H β > 0; [O III]5007 > 0; [N II]6583 > 0 and magnitude (W1) < 15.5 mag (in Vega).

³ S/N (optical lines) > 3, redshift < 0.3, H α > 0, H β > 0, [O III]5007 > 0, [N II]6583 > 0. S/N: W1 > 5, W2 > 5, and W3 > 2; and magnitude (W1) < 15.5 mag (in Vega).

⁴When in “Condition C,” all the BL non-oAGNs are considered to be BL oAGNs and BL composites to be BL oAGN(mSF). Recall that the position of the BLAGNs are highly uncertain on the BPT due to errors related to the [N II]/H α flux ratio.

The non-oAGN (mAGN) group with average $\log(\text{sSFR}) = -9.29 \text{ yr}^{-1}$ can be divided into two sub-samples. The first is composed of galaxies having a very strong $\text{H}\alpha$ line compared to $[\text{N II}]$ ($\approx 60\%$ of galaxies in this group) where the $[\text{O III}]$ and $\text{H}\beta$ are almost non-existent. Galaxy 5200866, which is in the starburst zone, has one of the highest sSFRs (see Table 5.4). The second sub-group concerns BLAGN that have been misclassified by the BPT diagnostic. Indeed, in some cases of BLAGN, it is impossible to disentangle the $\text{H}\alpha$ and $[\text{N II}]$, such that their ratio is either under- or overestimated. The non-oAGN (mWarm) share similar properties as the first group. The third highest mean sSFR group is oAGN (mAGN) and the lowest sSFRs are seen among the oAGN (mSF). It looks like the AGN classified by *WISE*, with almost no/weak $[\text{O III}]$ line exhibit higher sSFR compared to the galaxies classified as AGN in the optical and SF in *WISE* with very strong $[\text{O III}]$ lines (Table 5.2 gives a brief summary of the mean values). The fact that the oAGN (mSF) galaxies have the lowest sSFR might be a hint of quenching activity (AGN feedback) occurring inside the galaxies. Once more, the trend seen could just be related to the overestimation of the IR-based parameters due to the presence of the AGN itself. An alternative way of deriving the parameters (mass, $\text{SFR}_{12\mu\text{m}}$, sSFR) is with the AGN modelled and removed from the host emission (Assef et al. 2010; Hainline et al. 2014), which should provide a more robust separation of AGN and ISM dust-emission. However this procedure is case-by-base, an expensive and time-consuming.

Figure 5.12 has been added to show the repartition of the different group of galaxies classified in the current study as a function of redshift. Our sample shows a high concentration of SF galaxies at low redshift peaking at 0.08 with large scale structure, that decreases significantly toward higher redshift. It is important to recognise that the oAGN (mSF) and the oAGN (mWarm) are equally distributed from low to high redshift as opposed to the non-oAGN (mAGN) generally found at higher redshift. Recall that the non-oAGN (mAGN) and the oAGN (mSF) groups represent galaxies for which the IR and optical classification are contradictory. Due to Malmquist Bias, the more luminous galaxies – including AGN-dominated – are preferentially seen at higher redshifts.

5.3 Case Studies

In this section, we showcase galaxies selected from the different subgroups created in Figure 5.8. Each diagram from Figure 5.13 to 5.28, presented at the end of the section, illustrates

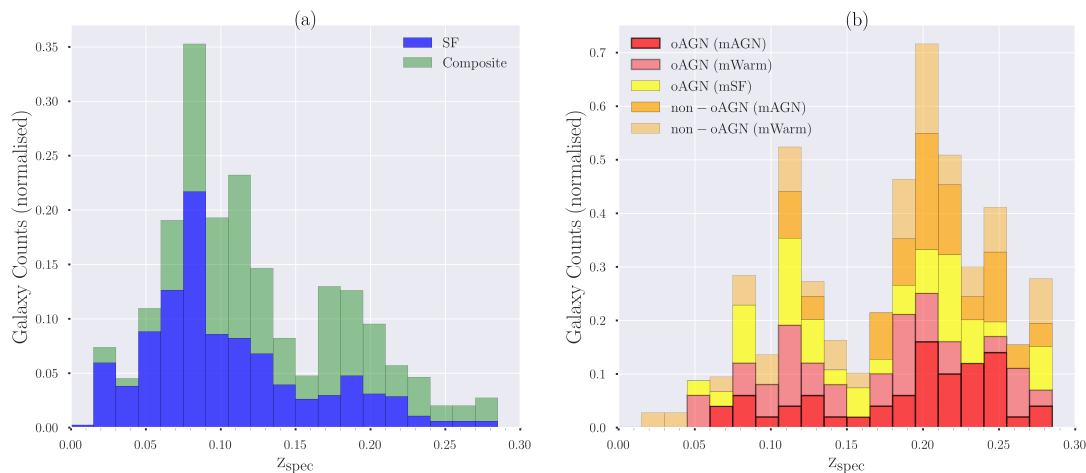


Figure 5.12: The redshift distribution (fraction of galaxies per redshift bin; the BLAGNs are included in the different AGN category as presented in Table 5.2 “Condition D”) for the SFs and composites (a) and the different groups of AGN (b). The colours and shades of the histograms have been kept consistent with Figures 5.10 and 5.11. Although the redshift distribution could be only an observation bias due to the higher brightness of AGNs compared to SFs, it is presented here to facilitate the description in this section. There are two main peaks located at redshifts of ~ 0.08 and ~ 0.2 . The SFs and the composites are concentrated at lower redshift (around $z = 0.08$), while the oAGN (mAGN), non-oAGN (mAGN), and non-oAGN (mWarm) seem to be generally located at redshift $z > 0.2$. The oAGN (mWarm) and oAGN (mSF) groups look like a middle class with as many galaxies at low as at high redshifts. An inspection of the galaxy distribution using the entire G23 catalogue reveals the depletion around $z = 0.15$ to be related to large-scale structures. The highest peaks at redshift $z \geq 0.2$ are seen among the non-oAGN (mAGN) and non-oAGN (mWarm), which also contain the majority of blended cases not visible in *WISE*.

the investigation procedure adopted for the classification of the individual galaxies. Instead of making a comparison based only on the optical and the mid-IR catalogues usually available online, we adopted a more rigorous approach in our study. For a given galaxy, a complete picture showing the BPT and mid-IR classification, the photometric SED with template fit, and the spectrum itself along with the *WISE* RGB image are presented. Finally, a deeper and more detailed picture is provided by the KiDS r-band imaging. The advantage here is that we see the photometric and physical properties while also pinpointing any issues related to the data themselves. This combination facilitates a consistency check of the data. A list of the inferred parameter values and their uncertainties can be found in Tables 5.3 and 5.4 (the selected galaxies as study cases are designated by the asterisk). In this section, we will refer to the galaxies by their GAMA catalogue ID “CATAID” or “Cat ID” (in blue colour on the diagrams). The *WISE* name and the fluxes in W1, W2, and W3 are also available on the diagrams.

5.3.1 Optical- and IR-classified SF Galaxies

Here we present the optical SF galaxies and composites, both classified as SF in the mid-IR. They are by far the most abundant type with a total (SF+composites) of $\sim 84\%$ of the classification (see Table 5.2). They have the lowest averages of the stellar mass, partly because they are young galaxies that are still in the growing process, but on the other hand, unlike the galaxies hosting AGNs whose fluxes are overestimated (as explained above), they have the most unaffected, reliable parameters (mass, $\text{SFR}_{12\mu\text{m}}$ and sSFR).

Galaxies 5241095 and 5240983 (Figure 5.13 and 5.14) are an interacting SF pair located at redshift $z = 0.027$. Both galaxies are quite similar in their spectra and location in the BPT and *WISE* colour-colour diagram. This galaxy pair is atypical in the sense that each of the galaxies shows the presence of a very high [O III] line, which is stronger than the $\text{H}\alpha$ and a quasi-absence of the [N II] line. The best-fit SED template classifies 5241095 as “Irr” and 5240983 as a normal spiral “Sc” galaxy. The KiDS image shows clear interaction between the two galaxies. It appears as though 5240983 is pulling material from 5241095, which is being ripped apart. Although the parameters here have much smaller values than the averages in their group (SF group, Table 5.2), the high values of stellar mass, $\text{SFR}_{12\mu\text{m}}$ and sSFR for 5240983 (9.14, 0.49, and -9.45) in comparison to 5241095 (9.05, 0.2, and -9.75) seem to corroborate this scenario. It could also be viewed as follows: galaxies becomes bigger over time through a series of mergers, which in turn triggers occasional AGN activity (looking at the unusually high [O III] in this pair).

Galaxy 5306682 (Figure 5.15) is the perfect candidate (typical) to represent the SF group for having a very high $\text{H}\alpha$ line flux, followed by [N II], [O III], and $\text{H}\beta$ with significantly smaller relative proportions. It is a good example that illustrates how the deep KiDS image helps to decipher and reveal the host and its environment. Figure 5.15 shows one of our closest specimens in the total sample (redshift $z = 0.005$). While in the *WISE* image, the magenta marker circle seems to enclose most of the galaxy, KiDS reveals a far larger galaxy that goes beyond the dusty part presented by *WISE* (recall that the two images have the same angular size).

Galaxy 5205726 in Figure 5.16 is presented in the KiDS image as a galaxy with clear spiral arms, a bar, and a nuclear ring. It is a large galaxy ($\log M_{\text{stellar}} = 10.51 M_{\odot}$) with $\text{sSFR} = 10^{-10.22} \text{ yr}^{-1}$. It belongs to the composite group of galaxy with a relatively high [O III] luminosity of $10^{40.29} \text{ erg s}^{-1}$.

5.3.2 Optical-IR AGNs

In this category, we have galaxies classified as AGNs both in the optical (BPT) and the *WISE* colour-colour diagram (5.1 % of the entire study sample).

The galaxy with GAMA ID 5339805 (Figure 5.17) is a typical case in the oAGN (mAGN) group. Its spectrum visually shows a broad $H\alpha$ line with a greenish colour in the *WISE* three-band image characteristic of mAGNs. The KiDS image reveals a spiral galaxy with a bulge (or pseudobulge) and a thin disk. It is also confirmed as an AGN by the SED fit.

Although close to $\sim 70\%$ of this sample is made up of BLAGNs, they are mostly located at higher redshifts with a mean value of 0.2 (see Figure 5.12) as opposed to the current galaxy, which is one of the nearest of its kind (redshift $z = 0.089$). Generally, the $[N\ II]$ is swallowed up by the broad $H\alpha$, which leads to either underestimation or overestimation of $[N\ II]/H\alpha$ line ratios. Indeed, the BPT shows a $[N\ II]/H\alpha$ line ratio > 2 , when in reality the $[N\ II]$ line is barely visible next to the $H\alpha$.

In the same group, GAMA ID 5151978, presented in Figure 5.18, is located at higher redshift with the same typical *WISE* AGN colour. We can see a very strong $[O\ III]$ line compared to $H\beta$, which places it well above the AGN dividing line in the BPT. It is located at the edge of the obscured-AGN box. The $[O\ III]$ line luminosity $> 10^{42}$ erg s $^{-1}$ makes it a potential obscured quasar according to the criteria of Jarvis et al. (2019). Intriguingly, the SED template suggests a normal late-type galaxy, not an AGN. The KiDS image provides a hint about the issue. Although the nearby source does not seem to interact with our main galaxy, it is close enough for *WISE* not to be able to disentangle both sources; they are instead treated as a single source because of the large beam of *WISE*. The main galaxy is definitely an AGN, as shown by the spectrum and also the *WISE* colour, but the presence of the second galaxy might add extra features that somehow affect the SED fitting. Overall, we classify this galaxy, as an AGN as demonstrated by the diagnostics presented in the Figure (Figure 5.18).

5.3.3 Optical AGNs, IR Non-AGNs

This category is made up of galaxies that are classified as AGN based on the optical BPT, but seen as normal SF or as just getting warmer in *WISE* colour. We call warm galaxies in *WISE*, galaxies for which $W1-W2$ is greater than a certain threshold (above 2σ of the SF sequence; see Figure 5.8), but below the AGN zone (recall Figure 5.8 for the different

zones). One has to be careful during the classification, for most of the discordant cases are found in this category. Indeed, taking into account the data quality flag in GAMA and also visually inspecting the spectra reduce the number of galaxies here by 25 % is not to mention that without a k-correction and a correction for stellar absorption, the number of false positives would have been much greater. The oAGN(mWarm) and oAGN(mSF) groups seem to belong to the same family, which evolves with redshift. The two groups have average redshifts of $z = 0.16$ and 0.18 , respectively.

The oAGN(mWarm) group appears to be dominated by BLs (21/36), which unlike the general trend, are unable to raise W1-W2 above the threshold required to be classified as IR AGNs or QSOs. Indeed, *WISE* is very sensitive to the BL systems, and in most cases, such galaxies are classified as AGNs. Maybe a parallel process is at work in the host, making it difficult for *WISE* to have a clear view of the ongoing AGN activity. Galaxy 5347780 in Figure 5.19 reveals broad H α and H β lines, associated with a prominent [O III] line, all strong indications of AGN activity. However, W1-W2 is barely close to 0.6 mag, which falls in the “warm” AGN zone. The explanation for this behaviour might lie in the SED characteristic of a SF galaxy (i.e. the host dominates the observed emission). Nevertheless, this warm colour is well offset from that seen for SF galaxies, and hence it stands out. This is clear evidence for AGN activity.

Galaxy 5294374 in Figure 5.20 tells a slightly different story. Here, in addition to the spectrum, the SED also presents the galaxy as an AGN, while the *WISE* colour stills fall below the strong AGN threshold. The change, in this case, is clearly a late-stage merger; *WISE* colours could be dominated by a SF galaxy (maybe the larger of the three in the merger) while AGNs could come from any of these sources.

Galaxies 5249547 and 5155115, in Figures 5.21 and 5.22, respectively, are two examples of a clear disagreement between optical and mid-IR classifications. While the optical lines present them as AGNs without ambiguity, the two galaxies sit exactly on the *WISE* SF main sequence, Equation 5.1. Furthermore, the SED confirms star formation as the dominant activity. Generally, the galaxies in this category are relatively nearby, with the optical and the mid-IR giving evidence of AGN and SF activity, respectively. We could argue that the galaxies here have strong enough AGN to be picked up by the optical wavelengths, but with continuum (and mid-IR) emission dominated by the star formation of the host. The narrow optical fibres may see only the centre, while *WISE* integrates the flux over the entire galaxy. It could also be that the AGN has recently turned off or shut down. Generally, once the AGN turns off, the BLR, X-rays, and mid-IR shut down within a few decades, while the NLR

could last thousands of years (Sartori et al. 2018). This might be a plausible justification for some narrow-line optical AGNs being classified as *WISE* SF galaxies. Note that as can be seen in Figure 5.21 (5249547, $\log L[\text{O III}] = 41.19 \text{ erg s}^{-1}$), a substantial number of the oAGN (mSF) present high luminosities (see Figure 5.10b), generally indicative of the presence of an AGN. The $[\text{O III}]$ lines in these cases could originate from other processes different from AGN activity. Possible explanations for this scenario are proposed in the discussion below.

5.3.4 Optical Non-AGNs, IR AGNs

In this subsection we address galaxies with no AGN characteristic emission lines in the optical waveband, but classified as either an AGN or warm in the mid-IR (the orange circles and squares in figure 5.10), named non-oAGN(mAGN) and non-oAGN(mWarm), respectively.

In our study, the tension between the optical vs IR classification is mainly caused by two factors. The first is due to tightly blended galaxies that the *WISE* image alone cannot separate, but that are clearly distinguishable in the deep KiDS r-band image. By comparing the KiDS vs *WISE* images in Figures 5.23, 5.24 and 5.27, we can see that multiple sources are mistakenly being considered as single (in *WISE*) owing to their angular proximity at the given redshift with mean redshift $z = 0.2$ (among the most distant galaxies of the study sample), while the optical (GAMA), which uses the KiDS galaxies location, is only targeting the central galaxy. The outcome of the classification in the mid-IR will depend on the components of the merging system. A composition of several AGNs will probably lead to a higher W1-W2 colour, while the opposite could instead lead to a decrease. The system presented in Figure 5.27 (CATAID: 5204947) is an extreme case where apparently more than three galaxies seem to be merging. As we can see from these three examples (i.e., Figures 5.23, 5.24, and 5.27), 5204947, which lies below the AGN region, is still the only one presented as an AGN by the SED.

The second cause of opposing classifications is related to the BL measurement. It has been noted several times that for broad $\text{H}\alpha$ lines, it is sometimes challenging to distinguish between the $[\text{N II}]$ and $\text{H}\alpha$ to get the correct line ratios. In any case, broad $\text{H}\alpha$ and $\text{H}\beta$ lines are already enough for the galaxy to be classified as an AGN. Using the line ratio here leads to an underestimation of $[\text{N II}]/\text{H}\alpha$, therefore classifying the galaxy as non-oAGN. This picture is seen in Figures 5.25 and 5.26 where the BL galaxies are correctly classified

as AGNs, both using the *WISE* colour-colour diagram and the SED fitting, though they lie in the composite area of the optical BPT.

The last case study, 5135645 (Figure 5.28), represents a blended system classified as an optical SF and IR SF, but located at the extreme limit between the AGN and SF zone. We suspect the second galaxy to be an AGN, justifying the high W1-W2 colour (0.74 mag, very warm) or related to the fact that the interaction is triggering AGN activity. The extreme $W2-W3 > 5.04$ mag is not unlike the class of HyperLIRGS that *WISE* has recently uncovered (Tsai et al. 2015) consisting of extremely dusty SF-AGN systems at high redshift. The SED template fit using the famous starburst-AGN hybrid system NGC3690 gives a glimpse of the probable internal processes taking place. These cases will be part of our next study, which will introduce radio data from SKA pathfinders ASKAP/EMU and MeerKAT already in the reduction phase.

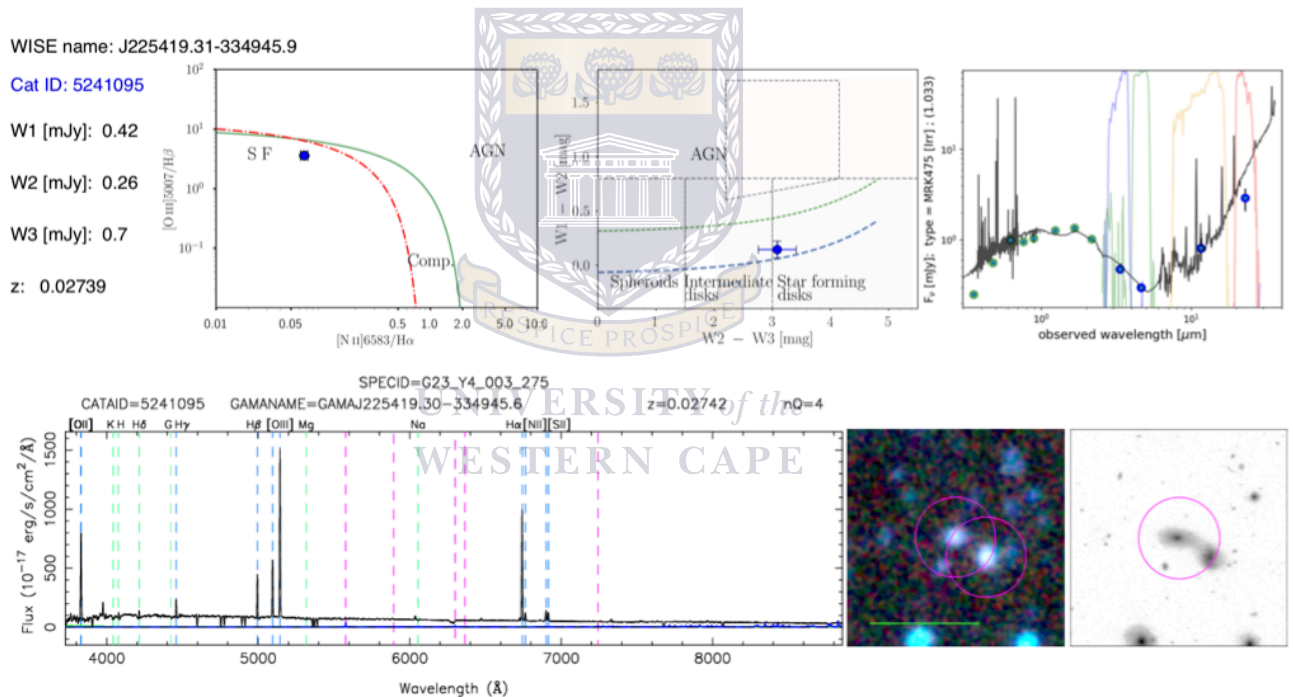


Figure 5.13: Classification of the galaxy (GAMA ID: 5241095) based on its optical (GAMA) and mid-IR (*WISE*) properties. The first row, from left to right shows the BPT diagram, the *WISE* colour-colour diagram and the photometric SED (with best-fit template). The second row shows the spectrum, the *WISE* RGB stamp (2 arcmin, the horizontal green line represents 1 arcmin) and the KiDS stamp (2 arcmin). A zoomed-in KiDS stamp (30 arcsec) is given to show a detailed picture of the galaxy and its nearby environment. This galaxy is an example of a tidal-interacting galaxy, which is classified as SF by both the optical (BPT) and the mid-IR (*WISE* colours). The classification is also confirmed by the shape of the SED, but the galaxy exhibits an uncommonly high $[O III]$ luminosity ($10^{41.14}$ erg s^{-1}) that could be related to interaction with its neighbours (see next figure).

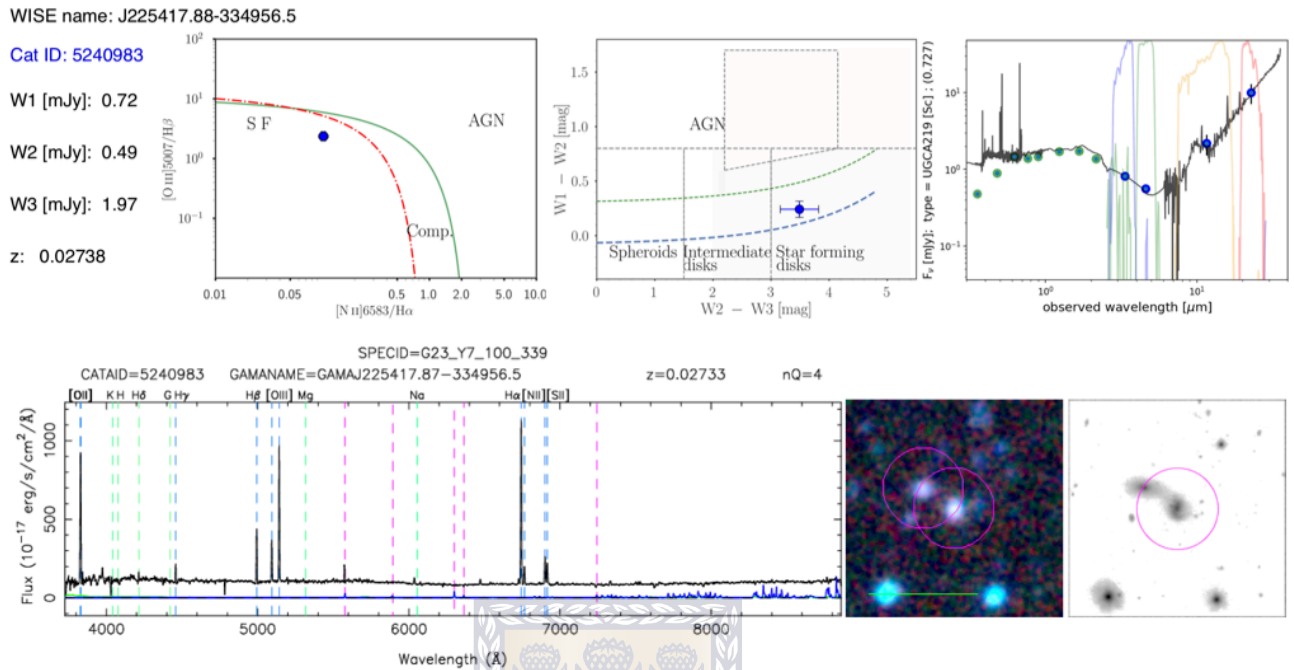


Figure 5.14: Galaxy 5240983. Classified as SF (blue). See also Figure 5.13, the companion galaxy.

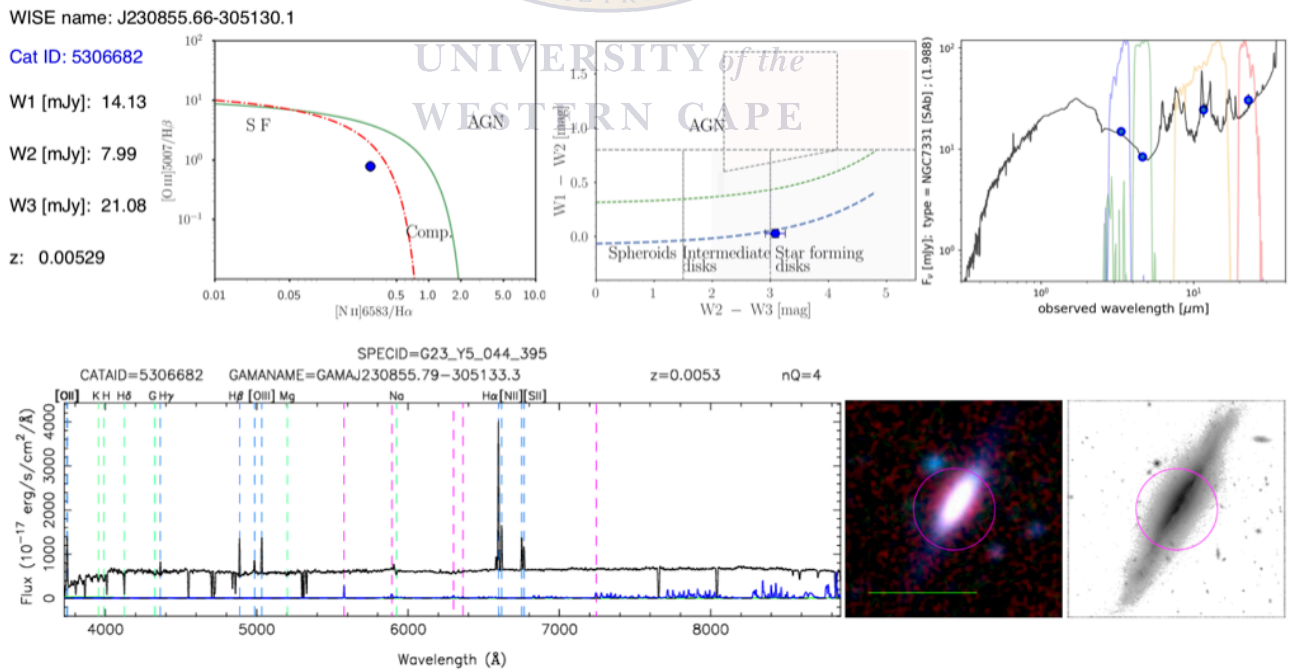


Figure 5.15: Galaxy 5306682. Classified as SF (blue).

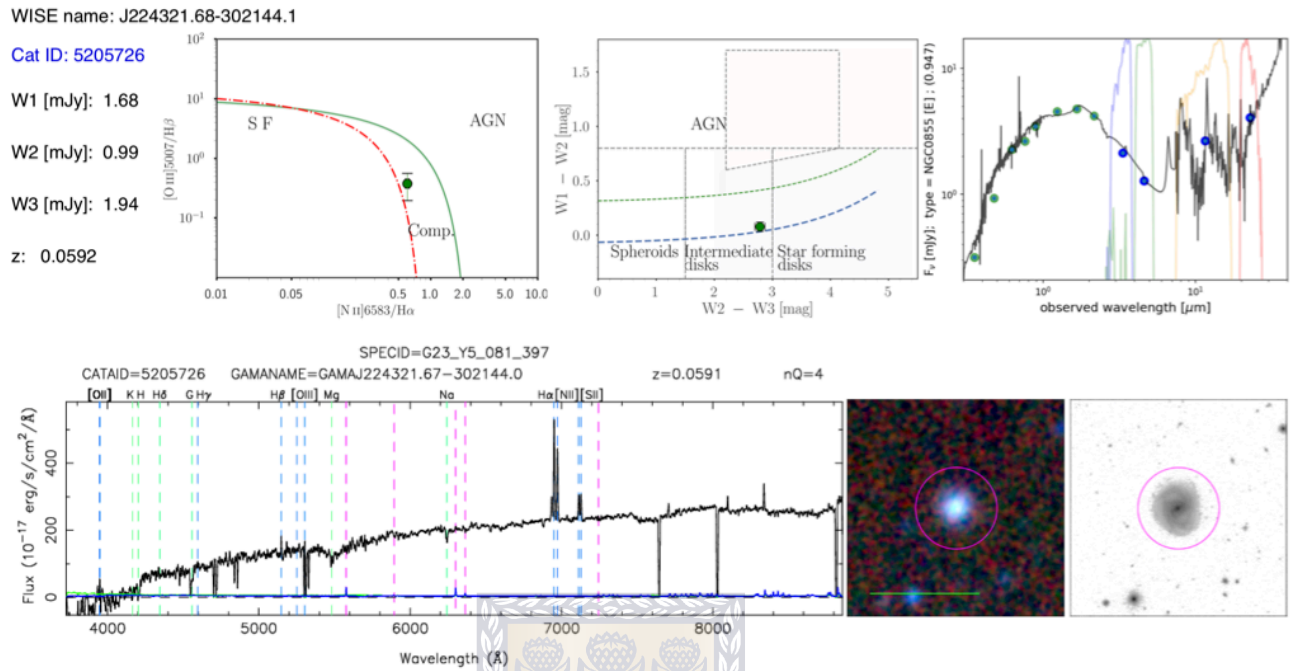


Figure 5.16: Galaxy 5205726. Classified as composite (green).

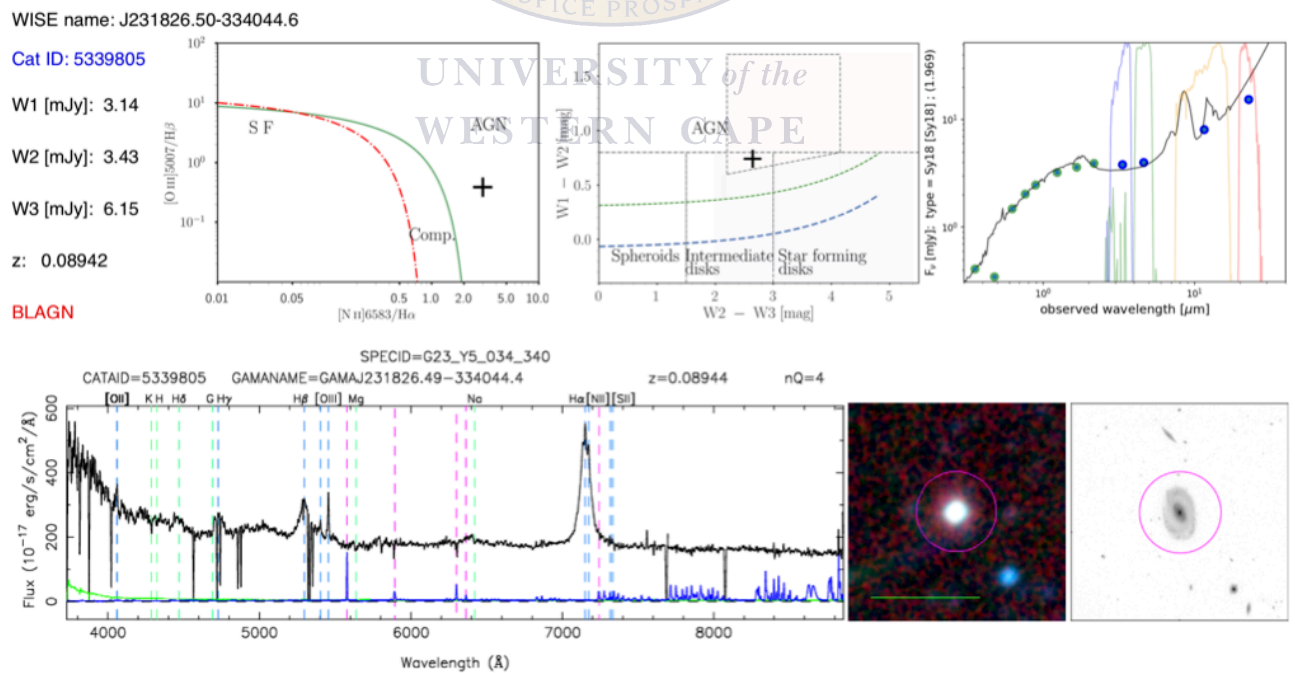


Figure 5.17: Galaxy 5339805. A BLAGN classified as oAGN (mAGN).

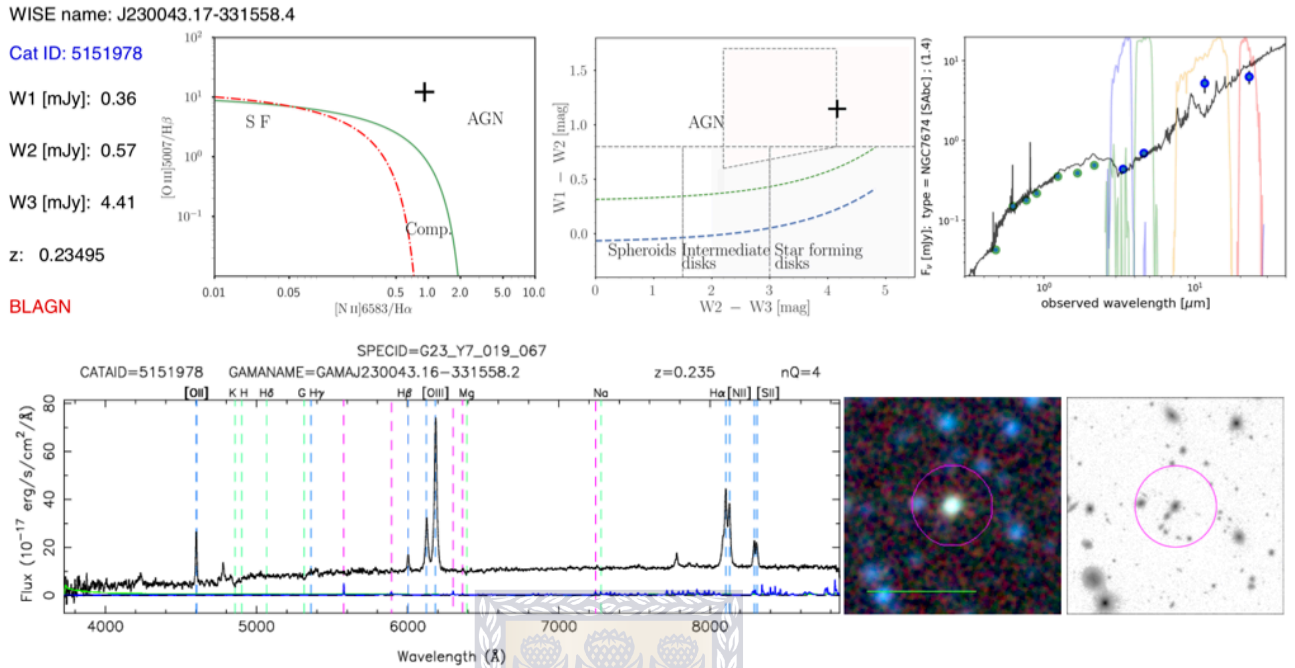


Figure 5.18: Galaxy 5151978. A BLAGN classified as oAGN (mAGN).

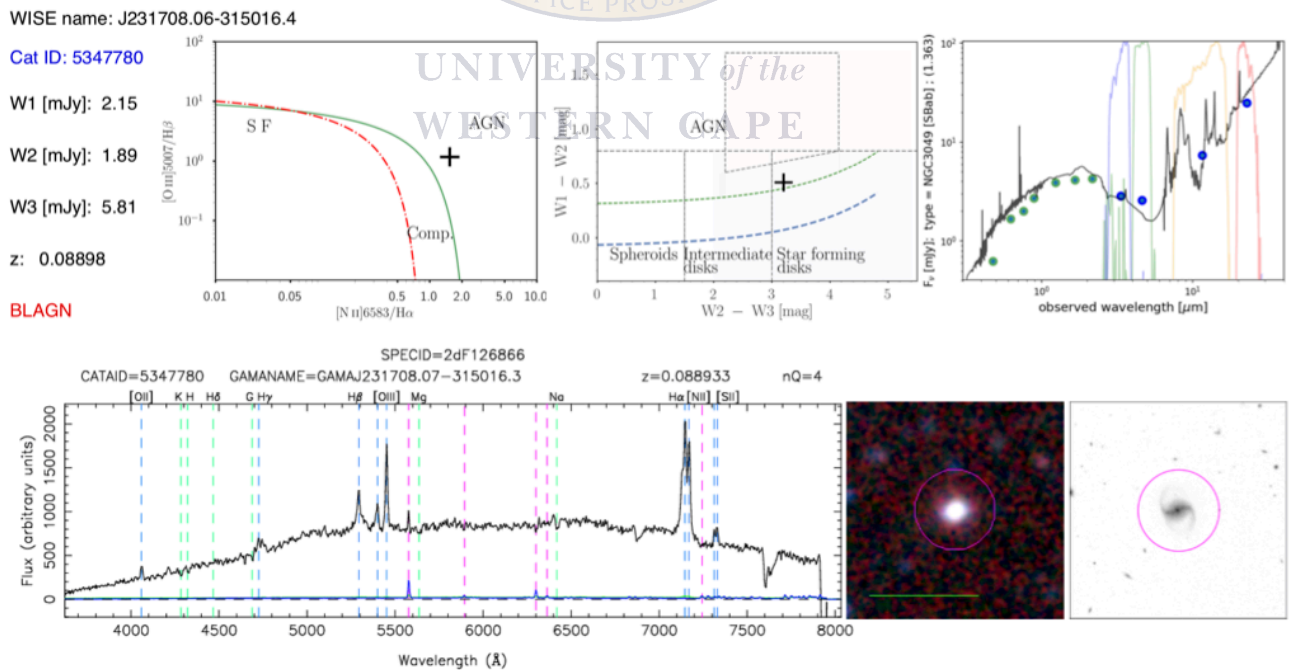


Figure 5.19: Galaxy 5347780. A BLAGN classified as oAGN (mWarm).

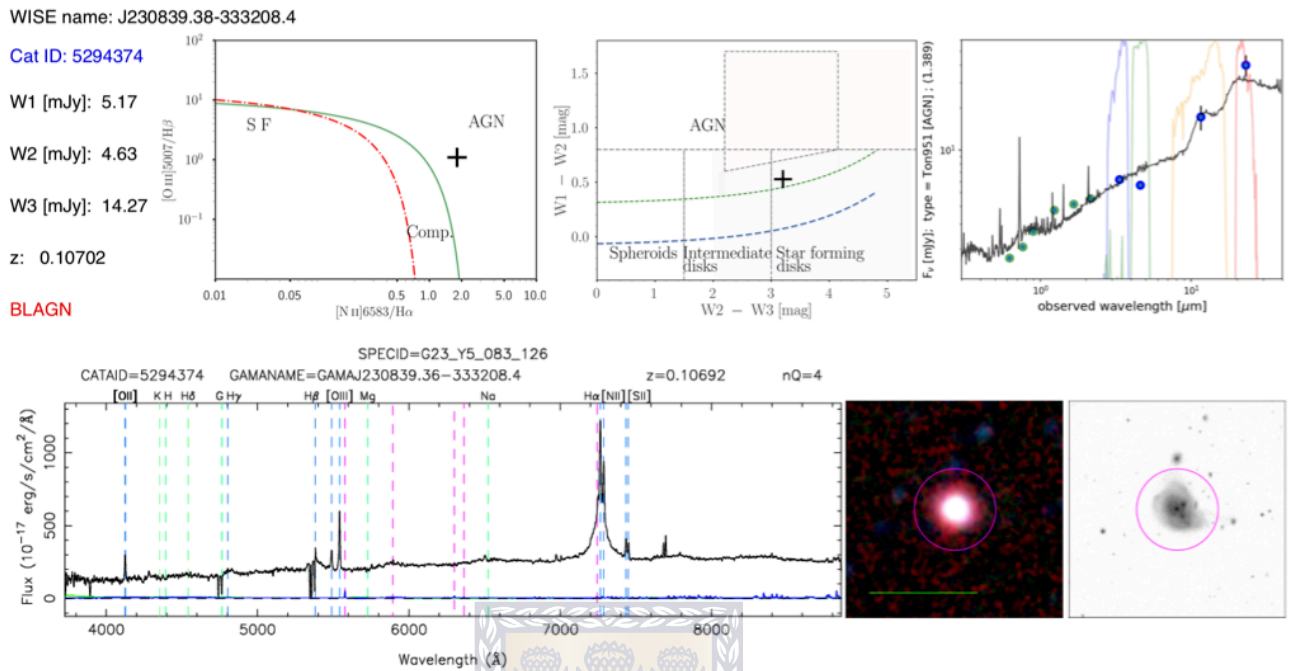


Figure 5.20: Galaxy 5294374. A BLAGN classified as oAGN (mWarm).

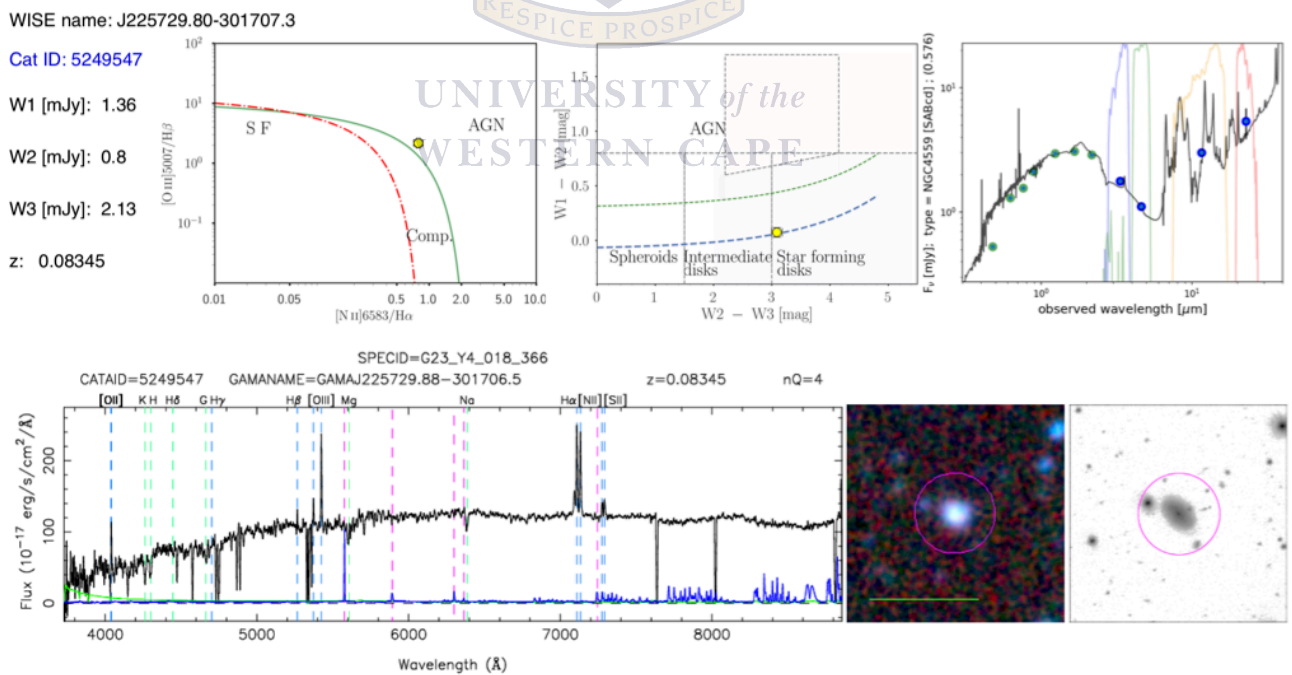


Figure 5.21: Galaxy 5249547. Classified as oAGN (mSF) (yellow, an example of a discordant classification).

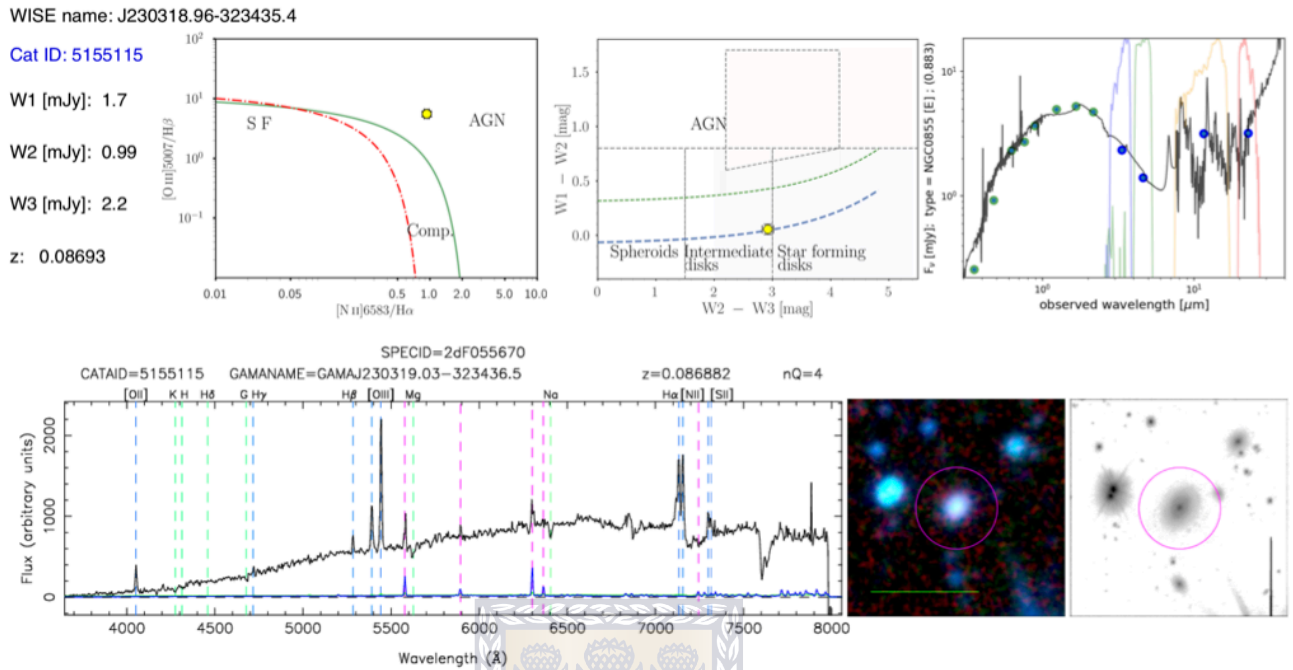


Figure 5.22: Galaxy 5155115. Classified as oAGN (mSF) (yellow).

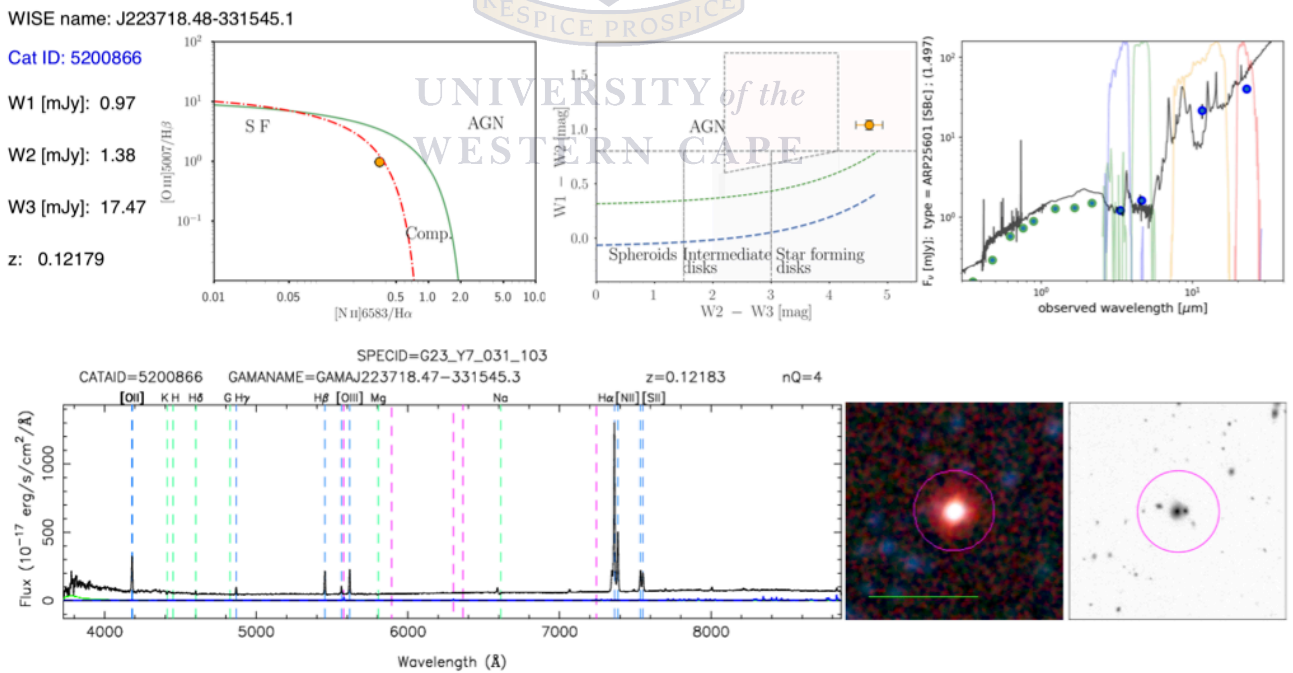


Figure 5.23: Galaxy 5200866. Classified as non-oAGN (mAGN) (orange, example of a discordant classification).

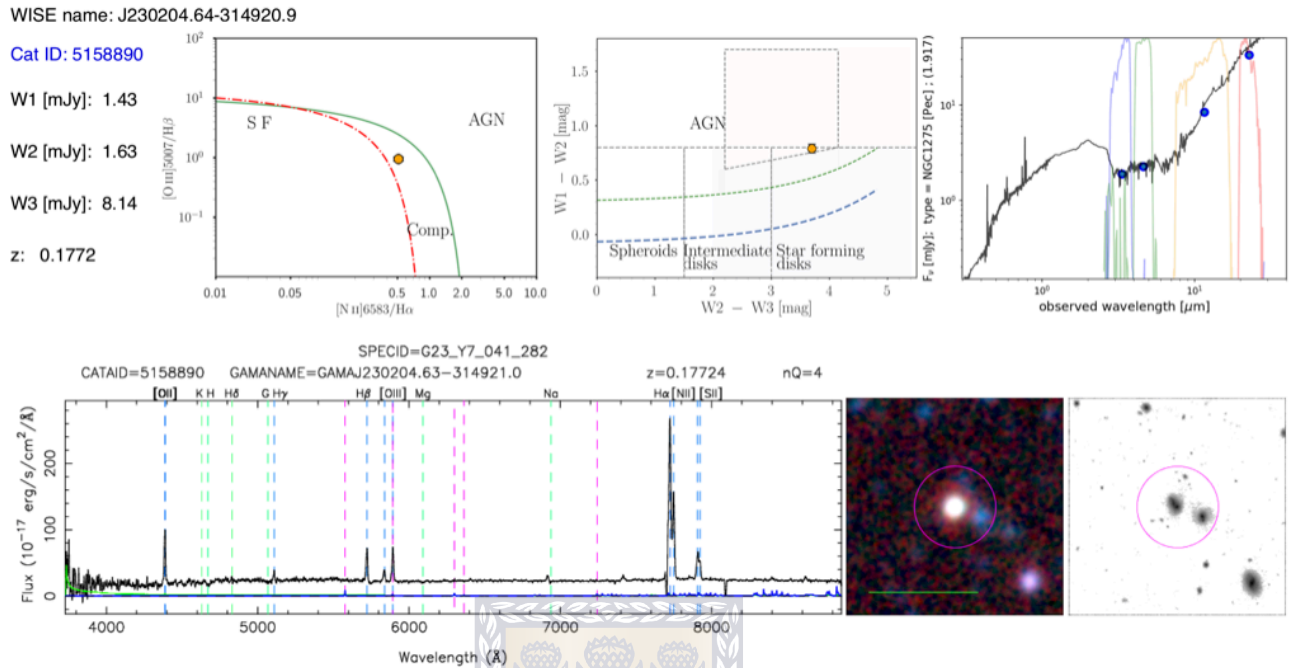


Figure 5.24: Galaxy 5158890. Classified as non-oAGN (mAGN) (orange).

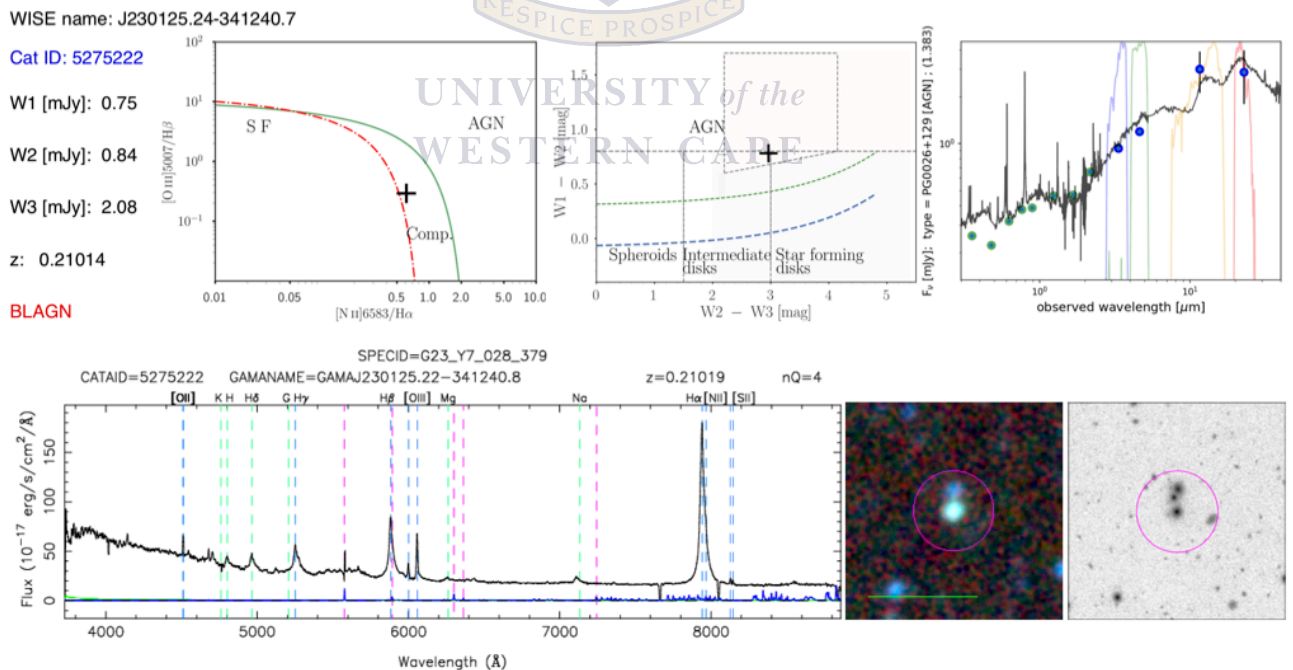


Figure 5.25: Galaxy 5275222. A BLAGN classified as non-oAGN (mAGN). Note the [N II] line cannot be distinguished from H α .

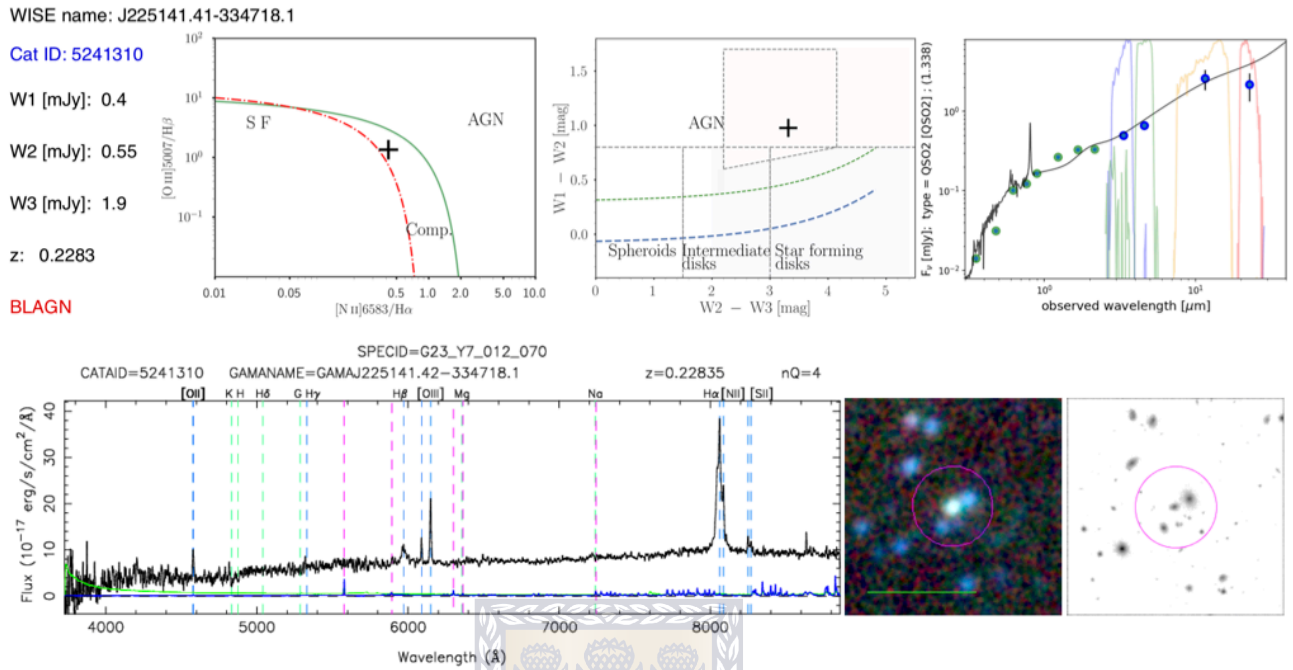


Figure 5.26: Galaxy 5241310. A broad-line AGN classified as a non-oAGN (mAGN).

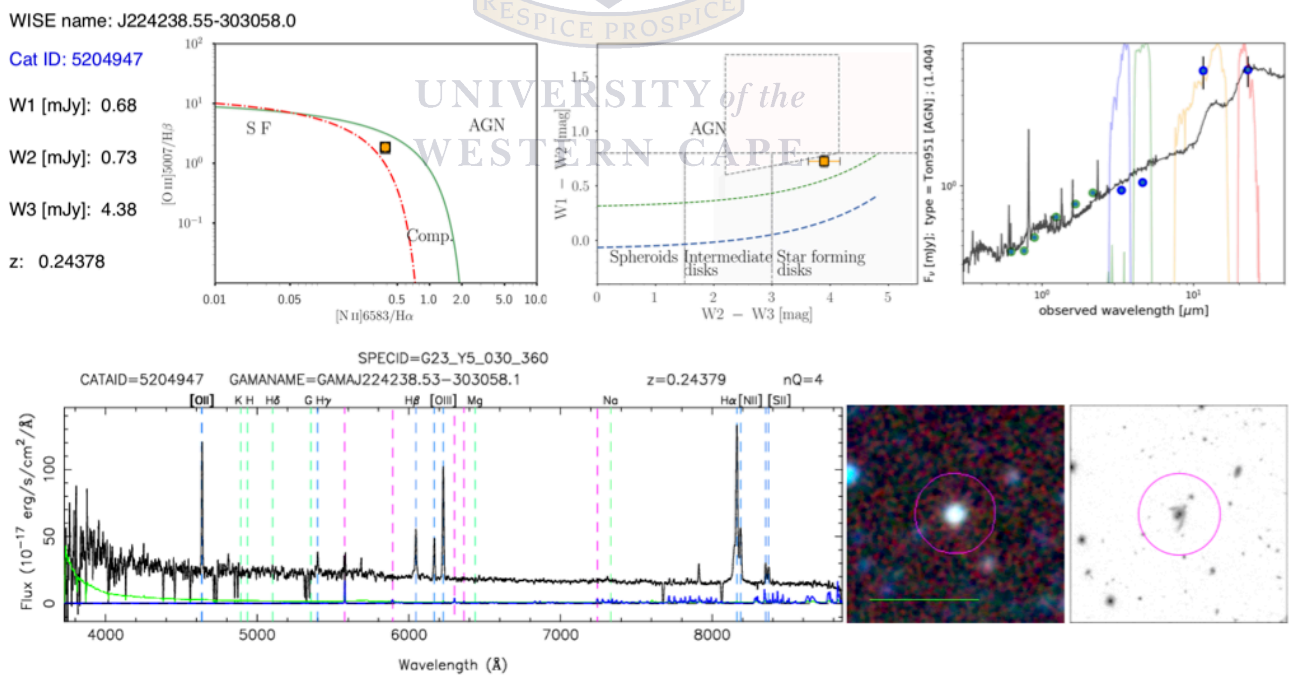


Figure 5.27: Galaxy 5204947. Classified as non-oAGN (mWarm) (orange). Blended system seen as a single in *WISE* 3-band colour.

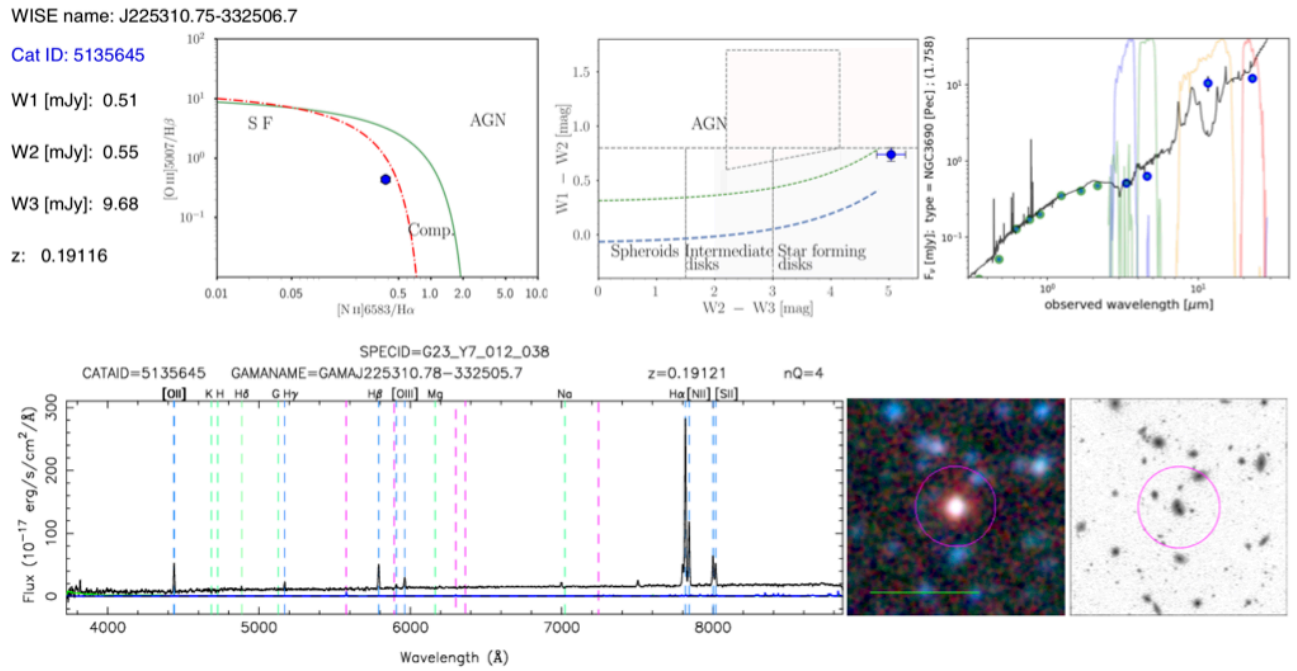


Figure 5.28: Galaxy 5135645. Classified as SF (blue). Extreme colours in *WISE*.

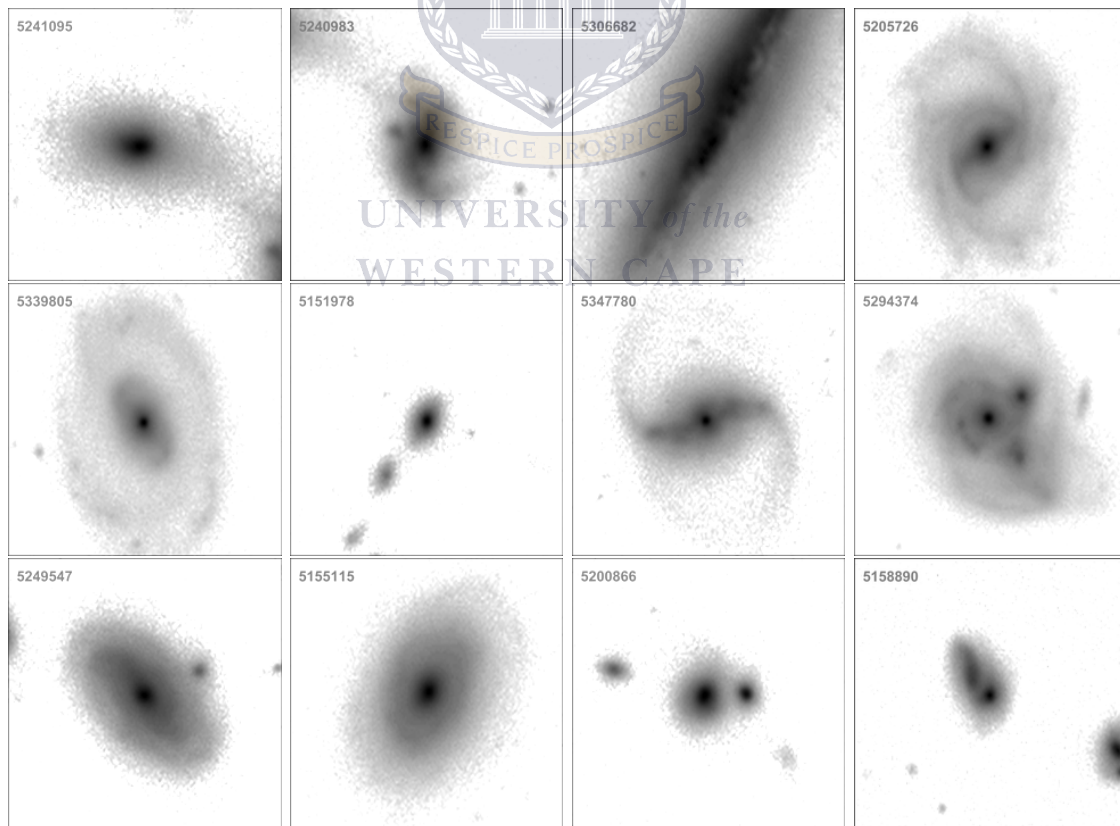


Figure 5.29: Individual KiDS r-band images of the galaxies selected from Figures 5.13 to 5.28. The GAMA names are in the upper left corner. All panels are 2 by 2 arcminutes.

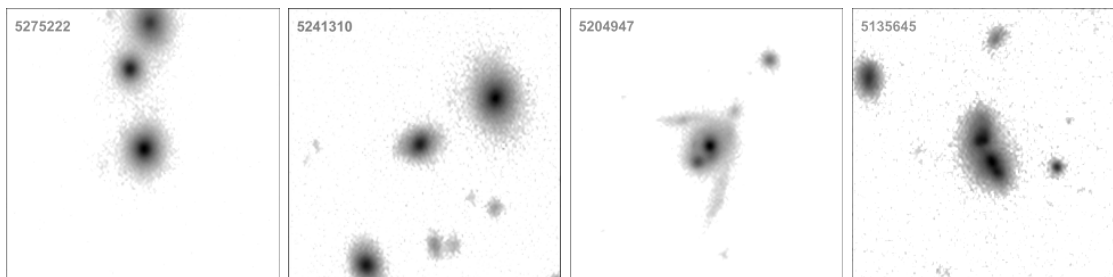


Figure 5.29: continued.

5.4 The New Diagnostic: $[W1-W2]$ vs $[N II]/H\alpha$

Based on the optical emission lines and the mid-IR colours, we now attempt to combine them into one diagnostic, where we choose the best parameters for each, namely the strongest emission lines: $[N II]/H\alpha$, and the highest-S/N and most-AGN-sensitive colours: W1-W2.

In Figure 5.30, we present our new classification scheme combining both the BPT and the *WISE* colour-colour diagrams. Figure 5.30a is a modified version of Figure 5.10, where the ratio $[O III]/H\beta$ is replaced by the W1-W2 colour, thus avoiding these emission lines that can be difficult to measure. Indeed, the BPT is typically limited by the low S/N of the $H\beta$ line (and sometimes the oxygen line as well), which represents a strong and significant bias for a *WISE*-selected sample. The dashed gray line, crossing the $[N II]/H\alpha$ line ratio, empirically represents the best separation between AGNs (upper region) and non-AGNs, with the latter divided into SF and mixed galaxy regions by the vertical gray line at $[N II]/H\alpha = 0.5$. The mixed division is motivated by the large number of composites, SFs, and oAGNs that inhabit relatively low (blue) W1-W2 colours. The Seyferts found in the SF region are the few SF galaxies that are found on the AGN side of the BPT, as presented in Figure 5.7. As both optical diagnostics agree generally, these few outliers at the boundary are unavoidable and inherent to any empirical method. However, the optical AGNs found at low *WISE* colours (in the SF or mixed zone) are interesting cases that need further investigation either in radio (see Chapter) or X-rays. The BL and Type-1 AGNs generally lie at $[N II]/H\alpha > 1$. The study sample does not include low-mass galaxies with AGNs (a type of low-luminosity AGN), and furthermore, is drawn from the local universe ($z < 0.3$). Therefore, our work is relevant to $z < 0.3$ and the limit boundaries here will require adjusting at higher redshift, especially when the impact of the metallicity on the BPT ($[N II]/H\alpha$) lines becomes more significant.

$W1-W2 < 0.5$ mag and the dashed gray line enclose all the SF and more than half of the composite galaxies. The mixed region delimited by $[N II]/H\alpha > 0.5$ and the dashed gray line described by Equation (5.3) is a mixture of oAGN(mSF) and composite galaxies and importantly, contains some strong [O III] emitters (see also Figure 5.10b).

$$Y = -0.24 \times \log(X) + 0.35 \quad (5.3)$$

where $Y = W1-W2$ mag, $X = [N II]/H\alpha$.

The remaining classes of galaxies are above the dashed gray line and represent the optical-IR AGNs, which makes this new classification scheme an efficient way of disentangling pure SF from galaxies having AGN activity. It allows us to get the best from both methods, and the use of the $W1-W2$ colour rejects far fewer galaxies than $[O III]/H\beta$. In Figure 5.30b the constraints on the [O III] (flux > 0) and $H\beta$ (flux > 0) are removed, leading to more classified galaxies. From the initial number of 1 154 classified galaxies in (a), 4 035 galaxies are now classified in (b) where the $W1-W2$ is used instead of $[O III]/H\beta$ hence nearly 400 % increase.

The galaxies from Figure 5.30b are presented by the *WISE* colour-colour diagram in Figure 5.31. It shows the position of the galaxies classified by the new diagram (Figure 5.30b) on the $W1-W2$ vs $W2-W3$ colour diagram with their associated fraction in blue (SF), green (mixed), and red (AGN). The new rendering of the colour-colour diagram may be directly compared with the relatively sparse results in Figure 5.8. More than 99 % of the SF and mixed galaxies from the new classification diagram are found in the SF region of the colour-colour diagram. About 75 % of the AGNs are either mWarm or mAGNs while 25 % are in the mSF zone. The galaxies in the latter case are, in general, close to the mWarm zone (at $W1-W2 = 0.4$ mag) and have a high value of $W2-W3 > 3.3$ mag (i.e., red, dusty). Hence, most of AGNs are found in “warm” zone of the *WISE* colour diagram. In rare cases of extremely broad $H\alpha$ or where the [N II] is stronger than the $H\alpha$ line, the AGNs from the new diagram are classified as mSFs. The galaxies with strong [O III] emission are highlighted by the black circles (see Figure 5.10). They seem to be distributed throughout the diagram but arguably represent a higher proportion of the AGN (37 %) in comparison to the SF (2 %) and mixed (5 %) galaxies.

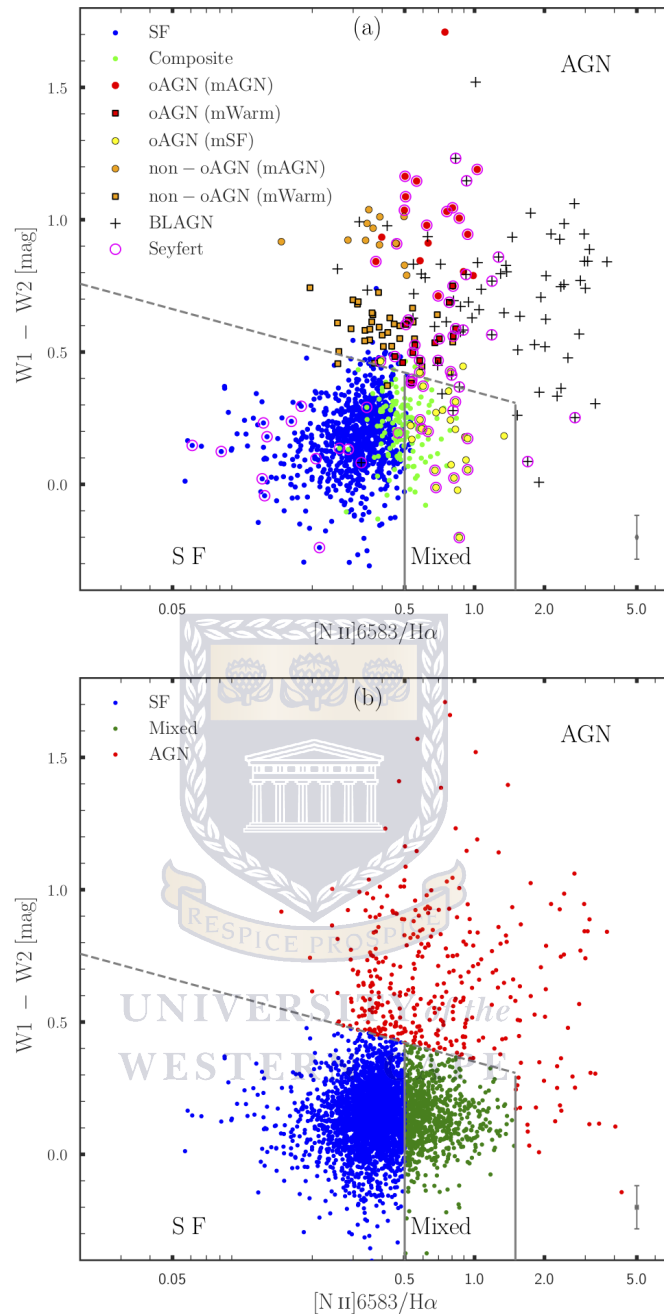


Figure 5.30: Optical-IR SF-AGN diagnostic plot. The new method used to classify galaxies based on both the optical BPT and the (*WISE*) colour-colour diagrams. In (a), we reproduce the classification of Figure 5.10, keeping the same galaxy groups with their assigned colours; all the optical lines in emission ($[O III]$, $[N II]$, $H\beta$ and $H\alpha$ lines are all positive), and replacing the $[O III]/H\beta$ by the $W1-W2$ colour. The mixed region (delimited by the solid and dashed gray lines) is a mixture of composites and oAGN (mSF). The mean $[N II]/H\alpha$ and $W1-W2$ uncertainties with the error bars are plotted in the lower right-hand corner. (b) is similar to (a), but only the fluxes of $[N II]$ and $H\alpha$ are required to be positive (emission lines). The $H\beta$ line could be either in emission or absorption. The statistic increases from 893 SF, 87 mixed, and 171 AGNs in (a) to 2818 SFs, 853 mixed, and 344 AGNs in panel (b). The mean $[N II]/H\alpha$ and $W2-W3$ uncertainties with the error bars are plotted in the lower right-hand corner.

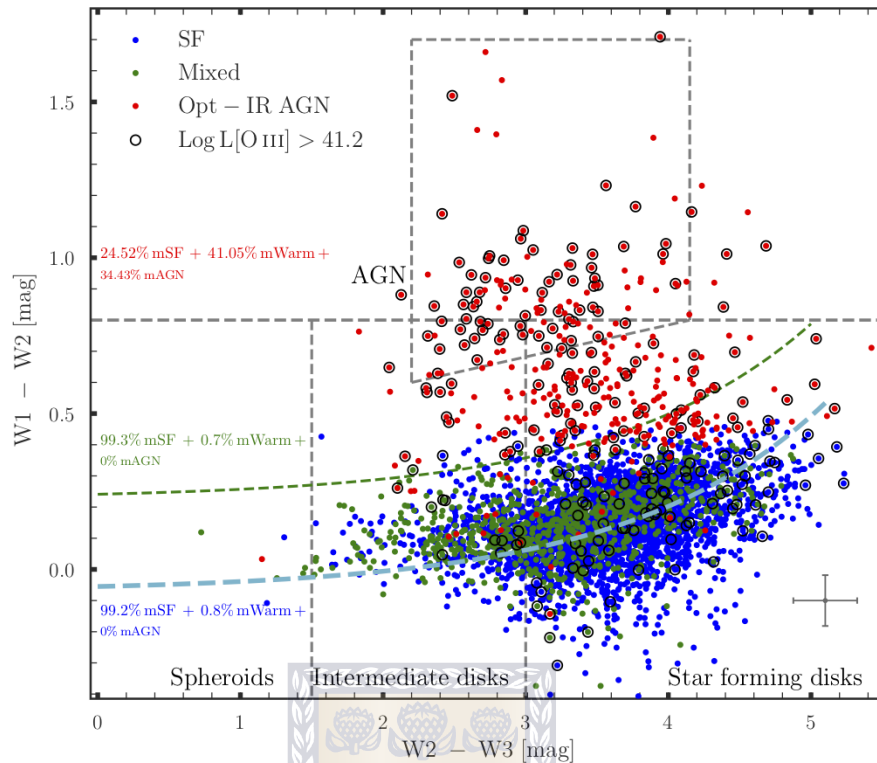


Figure 5.31: The *WISE* colour-colour representation of the galaxies classified in Figure 5.30b using the same key. The AGNs are well delimited by the 2σ offset line up to $W2-W3 \sim 3.8$ mag, where their $W1-W2$ colour tends to be slightly below the 2σ offset line. The different galaxy groups (derived in Figure 5.30b) are presented with their relative proportions, to the left. The strong $[O\text{III}]$ emitters (see Figure 5.10) are highlighted with black circles. We also plot the mean $W1-W2$ and $W2-W3$ uncertainties with the error bars in the lower-right corner.

5.5 Discussion

UNIVERSITY of the
WESTERN CAPE

We have conducted a careful analysis of the correspondence between an optically defined host and nuclear activity (using the BPT diagnostic) and mid-IR colours. There is wide agreement between optical and mid-IR classification, but real differences that highlight the limitations and strengths of each, while also suggesting that a synergy of combinations should provide new information.

Agostino et al. (2019) found a similar fraction of Seyferts and LINERs in their X-ray AGN sample. We find the opposite trend (BPT using $[S\text{II}]$ line), where very few galaxies are classified as LINERs in comparison to Seyferts. Generally, the LINERs from our sample are classified as mid-IR SF galaxies. A large majority are also classified as optical SF using the BPT based on the $[N\text{II}]$ line. This might be partly due to the very small number of LINERs (five in total) found in our sample. It is possible that the emission in these LINERs is not driven by AGNs (Yan & Blanton 2012; Belfiore et al. 2016) or they

could simply be LINERs with low-luminosity AGN (Filho et al. 2006; Flohic et al. 2006; Gonzalez-Martin et al. 2009). Additionally, strong shocks can significantly contribute to the AGN emission in these objects, creating the LINER-like emission lines (Dopita et al. 1996, 1997; Molina et al. 2018).

Using the KiDS r-band images, we found that a large number of the non-oAGN (mAGN) have more than one galaxy in the aperture, some of which may be interacting or galaxy pairs close enough to be seen as a single galaxy in *WISE*. As in this case *WISE* cannot distinguish the two galaxies, the companion of the targeted galaxy might have some AGN activity. It may also be that an interaction has triggered the AGN activity, as suggested by Ellison et al. (2019). Using the Canada France Imaging Survey images, the authors found that more than 60% of mid-IR AGNs are interacting systems and concluded that the interaction might play an important role in the nuclear feeding process.

The non-oAGN (mAGN) galaxies occasionally have their optical flux ratios underestimated because of the presence of broad H α lines, but there are still a few galaxies for which only the obscuration of the torus could explain their classification as non-AGNs in the optical wavelength regime. Compton-thick clouds such as those associated with galaxy mergers (Ricci et al. 2017; Satyapal et al. 2017) can prevent the optical lines from being detected.

Our study shows that about 21% of optical AGNs are located in the *WISE* SF zone. The simplest explanation is that they are low-power AGNs in which the starlight from the host dominates the AGN. This could be verified through the [O III] line luminosity generally thought to be correlated to the AGN strength (Bassani et al. 1999; Heckman et al. 2005). Unfortunately, not all the optical fluxes in the GAMA catalogue are calibrated to be used directly to determine luminosities (see section 3.1.1.1). Nevertheless, the available ones range from luminosity = 10^{41} to $10^{42.8}$ erg s $^{-1}$, which appears to be high and AGN-like, notably for those with luminosity $> 10^{42}$ erg s $^{-1}$ (see Reyes et al. 2008; Yan et al. 2019). The oAGN (mSF) galaxies with corresponding low [O III] luminosity thus fall in the category described above, where the starlight dominates the host galaxy emission. On the other hand, an oAGN (mSF) presenting high [O III] luminosity could be the consequence of a recent change in nuclear emission. This implies that the accretion disk has shut down and stopped emitting in the IR, but not enough time has passed to stop the NLR's emission, which corresponds to thousands of years (Sartori et al. 2016; Keel et al. 2017; D. Stern and R. Assef, private communication). This seems to be the case for galaxy 5249547 (see the case study and Figure 5.21), which has a strong [O III] luminosity of $10^{41.19}$ erg s $^{-1}$, but

whose AGN activity is invisible in *WISE* ($W1-W2 \sim 0$ mag).

An alternative explanation could be that the accretion disk is not powerful enough to generate winds that produce BL regions (BLRs) or alternatively the [O III] lines are coming from non-nuclear shocks rather than from the central AGN. Berney et al. (2015) found a weak correlation of the hard X-ray fluxes with the fluxes of high-ionisation narrow lines such as [O III], [Ne III], [He II], etc. not caused by factors such as obscuration or slit size. This begs the question of whether the [O III] lines are always related to the central AGN. Indeed, several studies have shown that while the optical line diagnostics can reasonably well separate AGNs and SFs, they are unable to differentiate between line emission arising from non-nuclear shocked gas and that of the AGN (Monreal-Ibero et al. 2013; Rich et al. 2015; D’Agostino et al. 2019; P. Väisänen, private communication).

These alternative scenarios may be investigated using X-ray data to check the presence of a torus and using long-slit spectroscopy to map the [O III] distribution, notably in the circumnuclear SF rings. It will also be useful to understand their radio properties using radio continuum data.

Few BLAGNs are found in the *WISE* SF zone. An investigation revealed them to be part of the rare cases where the $W1-W2$ colour drops (becomes bluer) after the k-correction, examples of where the limited templates (notably for AGN) fit to the apparent fluxes poorly.

The comparison of the *WISE* and the BPT diagrams revealed $W1-W2$ vs $[N II]/H\alpha$ to be a good diagnostic to separate SF galaxies from AGN. Our study shows the importance of the oAGN (mSF) class, which could provide crucial information about AGN activity in galaxies. Fortunately, the oAGN (mSF) can be reliably found in the mixed region (Figure 5.30a) that encompasses about 90 % of their total number. They generally have low $W1-W2$ colour, high $[N II]/H\alpha$ ratios and are separated from the rest of AGNs by the dashed line (in Figure 5.30) described by the equation (5.3). This new method does not require the $H\beta$ and [O III], thus allowing classification of galaxies with the [O III] and/or the $H\beta$ lines either absent (low S/N) or in absorption, which is not otherwise possible using the BPT. Figure 5.30b shows three times more classified galaxies than Figure 5.30a. Using this new method, we have separated our larger line-emission sample into over 4000 SF and AGN galaxies (see Figure 5.31, a 400 % improvement over the traditional BPT). As mentioned earlier, the accuracy of the *WISE* colour-colour and the BPT (using $[N II]/H\alpha$) classifications are potentially affected by the presence of dwarf galaxies and metallicity, respectively. This study has been conducted on safe ground where those two caveats have been avoided by using intermediate to high mass galaxies $\text{Log}M_{\text{stellar}} > 9 M_{\odot}$ and a sample with a redshift

limit of $z < 0.3$. A larger sample combining several GAMA fields could be used in future with radio data to update our new diagnostic method. New and deeper spectroscopic surveys will be useful to extend the study to higher redshift where the $[\text{N II}]/\text{H}\alpha$ line ratio is more susceptible to evolutionary effects.

5.6 Conclusion

We investigated the optical emission-line properties of galaxies in GAMA G23 using mid-IR (*WISE*) photometry. Unlike most preceding studies of the kind, special care was taken in extracting the nearby extended galaxies using our customised extended emission pipeline (see Section 3.3.2). The photometry was derived accordingly. A magnitude cut was applied to select the cleanest and highest-S/N galaxies, leading to a high-quality dataset of about 9800 galaxies. These were cross-matched to the emission-line catalogue and the resulting sample (1154 galaxies) was used for a comparison between the commonly used BPT and *WISE* colour-colour diagrams. Additional visual inspection of all the spectra and the high-resolution KiDS r-band image of each of the classified galaxies was carried out, with examples presented in Figure 5.13 to 5.28. The derived dataset and findings are presented as follows:

- The first *WISE* galaxy catalogue in the GAMA G23 field has been created including nearby galaxies extracted using the resolved pipeline.
- Visual checking of the spectra revealed the BPT based on the $[\text{N II}]/\text{H}\alpha$ vs $[\text{O III}]/\text{H}\beta$ to be more reliable than the one using $[\text{S II}]/\text{H}\alpha$ vs $[\text{O III}]/\text{H}\beta$. Most of the strong $[\text{S II}]$ detections are artifacts. This mostly affects galaxies classified as LINERS.
- Galaxies were classified based on their mid-IR and optical properties in Figure 5.8 and Figure 5.10a. There is good agreement between the two methods in classifying the non-AGN galaxies. Only 4% of the mid-IR SFs are classified as optical AGNs and 5% of the optical SFs are classified as mid-IR AGNs. However, 29% of the optical AGNs are non-mid-IR AGNs, while 33% (if we consider the mWarms as mid-IR mAGNs) of the mid-IR AGNs are not optical AGNs. The optical composites share similar properties to the optical SF galaxies in the *WISE* colour-colour diagram, but more than 60% of the non-oAGN(mAGN) are optical composites.

- Optical AGNs are well selected by high $[\text{O III}]/\text{H}\beta$ ratios, while the $[\text{N II}]/\text{H}\alpha$ ratios are generally < 1 . Visual inspection of the spectra revealed the AGN with $[\text{N II}]/\text{H}\alpha$ ratio > 1 in Figure 5.10a to be overestimated due to the BL feature of the $\text{H}\alpha$.
- A detailed study of the different groups of galaxies shows a scenario in which SF galaxies have the lowest redshifts, followed by the oAGNs(mSF), which have a combination of AGN and SF activity. *WISE* is often blind to these AGNs, sometimes leading to very low W1-W2 colours indicative of host galaxy emission. For these galaxies relatively nearby, the spectroscopic fibre might be capturing only the central part while *WISE* is sampling the flux over the entire galaxy dominated by SF activity. At higher redshifts are the oAGN(mAGN) and the non-oAGN(mAGN). The latter group is made up of galaxies with an underestimated $[\text{N II}]/\text{H}\alpha$ ratio (broad $\text{H}\alpha$ line) and by blended systems that are proximal-close and small enough to be seen as a single source by *WISE*. We were able to identify them using the high-resolution images provided by KiDS.
- We created a new diagnostic diagram that combines the optical lines and the *WISE* colour in the form of W1-W2 vs $[\text{N II}]/\text{H}\alpha$. The W1-W2 colour, which is sensitive to the AGN emission, can reliably replace the $[\text{O III}]/\text{H}\beta$ ratio (in the BPT diagram), which is limited by $\text{H}\beta$ and $[\text{O III}]$ detection. It has the distinct advantage of increasing the number of classified galaxies more than three or four times.

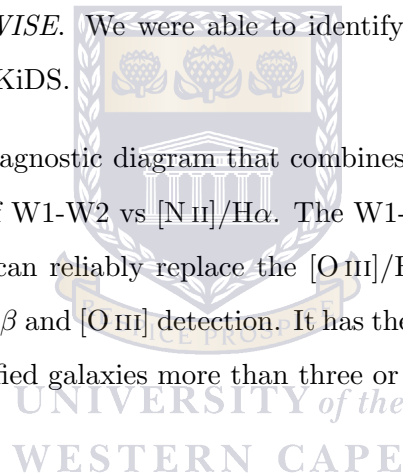


Table 5.3: Measured properties of a representative sample of the galaxies from each activity group. The fluxes are k-corrected and the rest-frame fluxes in W1, W2, and W3 are given in mJy. W1-W2 and W2-W3 are rest-frame colours and the GAMA redshifts are also presented. The selected galaxies for case study in the next section are designated by a star next to their GAMA ID (ex 5241095*: for the first selected galaxy in the SF group, etc.) and the BLAGN by a plus sign (ex 5340595+: a BLAGN in the oAGN (mAGN) group, etc.). The colours used for the different groups as presented in Figure 5.9 are added for clarity.

CATAID	z_{spec}	W1 (mJy)	W2 (mJy)	W3 _{PAH} (mJy)	W1-W2 (mag)	W2-W3 (mag)	[O III]/H β	[N II]/H α
SF (blue circles)								
5241095*	0.0274	0.42 \pm 0.01	0.26 \pm 0.02	0.7 \pm 0.2	0.14 \pm 0.08	3.08 \pm 0.33	3.6 \pm 0.09	0.07 \pm 0.01
5240983*	0.0274	0.72 \pm 0.02	0.49 \pm 0.03	1.97 \pm 0.59	0.24 \pm 0.07	3.49 \pm 0.33	2.37 \pm 0.08	0.1 \pm 0.0
5306682*	0.0053	14.13 \pm 0.16	7.99 \pm 0.15	21.08 \pm 3.24	0.03 \pm 0.04	3.08 \pm 0.17	0.78 \pm 0.03	0.28 \pm 0.01
5135645*	0.1912	0.51 \pm 0.01	0.55 \pm 0.02	9.68 \pm 2.16	0.74 \pm 0.06	5.04 \pm 0.25	0.44 \pm 0.04	0.38 \pm 0.01
5325430	0.0648	0.59 \pm 0.01	0.34 \pm 0.02	1.93 \pm 0.15	0.06 \pm 0.07	3.86 \pm 0.11	0.29 \pm 0.06	0.33 \pm 0.01
5327563	0.0652	0.4 \pm 0.01	0.27 \pm 0.02	1.11 \pm 0.43	0.22 \pm 0.09	3.54 \pm 0.43	1.01 \pm 0.14	0.25 \pm 0.03
5325339	0.1247	0.66 \pm 0.01	0.44 \pm 0.02	1.71 \pm 0.1	0.2 \pm 0.07	3.46 \pm 0.09	0.37 \pm 0.09	0.38 \pm 0.03
5123445	0.0795	0.4 \pm 0.01	0.29 \pm 0.02	1.19 \pm 0.18	0.28 \pm 0.09	3.53 \pm 0.19	0.41 \pm 0.12	0.38 \pm 0.03
5138489	0.0852	0.24 \pm 0.01	0.15 \pm 0.02	0.7 \pm 0.17	0.15 \pm 0.13	3.63 \pm 0.29	0.42 \pm 0.15	0.35 \pm 0.03
5153375	0.0807	0.39 \pm 0.01	0.28 \pm 0.01	1.36 \pm 0.16	0.28 \pm 0.06	3.71 \pm 0.14	0.67 \pm 0.15	0.3 \pm 0.02
5261290	0.0834	1.16 \pm 0.02	0.79 \pm 0.03	5.57 \pm 1.25	0.23 \pm 0.05	4.08 \pm 0.25	0.16 \pm 0.04	0.4 \pm 0.02
5187670	0.1067	0.27 \pm 0.01	0.16 \pm 0.02	0.78 \pm 0.12	0.08 \pm 0.15	3.72 \pm 0.23	0.18 \pm 0.06	0.31 \pm 0.04
5281879	0.0286	2.89 \pm 0.03	1.75 \pm 0.04	6.64 \pm 0.16	0.1 \pm 0.04	3.44 \pm 0.05	0.26 \pm 0.03	0.41 \pm 0.01
5281521	0.0288	0.35 \pm 0.01	0.18 \pm 0.02	0.45 \pm 0.17	-0.06 \pm 0.11	3.03 \pm 0.43	1.6 \pm 0.14	0.14 \pm 0.01
5305483	0.086	0.46 \pm 0.01	0.33 \pm 0.02	1.68 \pm 0.43	0.28 \pm 0.07	3.74 \pm 0.29	0.36 \pm 0.03	0.31 \pm 0.01
5222747	0.2084	0.22 \pm 0.01	0.15 \pm 0.01	0.56 \pm 0.09	0.24 \pm 0.07	3.4 \pm 0.18	0.55 \pm 0.15	0.37 \pm 0.04
5266202	0.0844	0.74 \pm 0.02	0.49 \pm 0.03	3.09 \pm 0.15	0.19 \pm 0.07	3.97 \pm 0.09	0.18 \pm 0.06	0.36 \pm 0.01
5185570	0.0594	0.53 \pm 0.02	0.31 \pm 0.02	0.3 \pm 0.12	0.08 \pm 0.09	2.15 \pm 0.45	0.31 \pm 0.04	0.31 \pm 0.02
5256068	0.223	0.67 \pm 0.01	0.6 \pm 0.01	6.5 \pm 0.11	0.54 \pm 0.04	4.52 \pm 0.04	0.82 \pm 0.1	0.36 \pm 0.01
Composites (green circles)								
5205726*	0.0592	1.68 \pm 0.02	0.99 \pm 0.02	1.94 \pm 0.14	0.08 \pm 0.04	2.78 \pm 0.09	0.38 \pm 0.18	0.6 \pm 0.02
5322507	0.0608	1.38 \pm 0.02	0.81 \pm 0.03	1.05 \pm 0.16	0.07 \pm 0.05	2.41 \pm 0.17	0.55 \pm 0.11	0.76 \pm 0.05
5246049	0.1064	0.87 \pm 0.01	0.64 \pm 0.02	5.13 \pm 1.16	0.32 \pm 0.05	4.2 \pm 0.25	0.29 \pm 0.05	0.53 \pm 0.01
5277048	0.1088	0.21 \pm 0.01	0.16 \pm 0.02	1.31 \pm 0.18	0.34 \pm 0.12	4.25 \pm 0.19	1.62 \pm 0.28	0.36 \pm 0.09
5251443	0.2361	0.21 \pm 0.01	0.11 \pm 0.01	0.37 \pm 0.13	-0.08 \pm 0.09	3.37 \pm 0.39	0.41 \pm 0.13	0.62 \pm 0.04
5279625	0.0842	0.63 \pm 0.01	0.42 \pm 0.02	2.61 \pm 0.61	0.19 \pm 0.06	3.96 \pm 0.26	0.57 \pm 0.1	0.46 \pm 0.01
5285888	0.2012	0.46 \pm 0.01	0.32 \pm 0.02	3.11 \pm 0.77	0.25 \pm 0.07	4.41 \pm 0.28	1.36 \pm 0.27	0.52 \pm 0.06
5159722	0.0656	1.84 \pm 0.02	1.2 \pm 0.04	7.04 \pm 0.21	0.18 \pm 0.05	3.88 \pm 0.06	0.62 \pm 0.11	0.46 \pm 0.02
5154601	0.0789	0.33 \pm 0.01	0.18 \pm 0.01	0.67 \pm 0.13	-0.04 \pm 0.08	3.46 \pm 0.22	0.8 \pm 0.15	0.42 \pm 0.03
5264991	0.1897	0.3 \pm 0.01	0.25 \pm 0.01	2.09 \pm 0.14	0.44 \pm 0.07	4.24 \pm 0.1	1.16 \pm 0.34	0.55 \pm 0.08

...

Table 5.3 – continued

CATAID	z_{spec}	W1 (mJy)	W2 (mJy)	W3 _{PAH} (mJy)	W1-W2 (mag)	W2-W3 (mag)	[O III]/H β	[N II]/H α
5364072	0.0955	0.2 ± 0.01	0.1 ± 0.01	0.55 ± 0.12	-0.13 ± 0.14	3.84 ± 0.28	1.09 ± 0.3	0.38 ± 0.04
5249313	0.0799	0.9 ± 0.01	0.54 ± 0.02	0.86 ± 0.17	0.08 ± 0.06	2.61 ± 0.22	0.25 ± 0.04	0.61 ± 0.02
5280475	0.0675	0.45 ± 0.01	0.27 ± 0.02	3.5 ± 0.95	0.1 ± 0.08	4.72 ± 0.3	1.35 ± 0.06	0.37 ± 0.01
5154381	0.0832	0.4 ± 0.02	0.25 ± 0.01	0.87 ± 0.13	0.15 ± 0.08	3.34 ± 0.18	1.16 ± 0.28	0.4 ± 0.04
oAGN (mAGN) (red circles)								
5339805* ⁺	0.0894	3.14 ± 0.04	3.43 ± 0.07	6.15 ± 0.14	0.74 ± 0.04	2.64 ± 0.05	0.39 ± 0.03	3.0 ± 0.09
5151978* ⁺	0.2349	0.36 ± 0.01	0.57 ± 0.02	4.41 ± 1.08	1.15 ± 0.06	4.16 ± 0.27	12.17 ± 0.73	0.92 ± 0.02
5145801	0.1975	0.7 ± 0.01	0.8 ± 0.03	2.9 ± 0.76	0.79 ± 0.05	3.37 ± 0.29	2.96 ± 0.07	0.99 ± 0.06
5252110	0.1309	1.86 ± 0.03	2.53 ± 0.06	8.6 ± 1.89	0.98 ± 0.04	3.29 ± 0.24	3.89 ± 0.28	0.62 ± 0.02
5237160	0.0604	0.59 ± 0.01	0.93 ± 0.03	10.49 ± 2.26	1.15 ± 0.05	4.56 ± 0.24	8.9 ± 0.46	0.56 ± 0.02
5340595 ⁺	0.1882	1.2 ± 0.02	1.44 ± 0.04	4.67 ± 1.05	0.84 ± 0.04	3.24 ± 0.25	0.69 ± 0.02	2.97 ± 0.14
5286102 ⁺	0.2425	1.24 ± 0.02	1.37 ± 0.03	3.01 ± 0.76	0.76 ± 0.04	2.84 ± 0.28	0.51 ± 0.05	2.43 ± 0.12
5108709	0.1528	0.44 ± 0.01	0.63 ± 0.02	3.13 ± 0.16	1.04 ± 0.05	3.69 ± 0.07	3.41 ± 0.12	0.5 ± 0.01
5369226	0.1367	1.28 ± 0.02	1.84 ± 0.05	12.08 ± 2.58	1.04 ± 0.04	3.98 ± 0.23	5.51 ± 0.83	0.8 ± 0.03
5162821 ⁺	0.2459	0.34 ± 0.01	0.42 ± 0.01	0.76 ± 0.11	0.86 ± 0.05	2.66 ± 0.17	4.71 ± 0.5	1.27 ± 0.08
5233898	0.2039	0.82 ± 0.01	1.05 ± 0.03	4.38 ± 1.02	0.91 ± 0.05	3.51 ± 0.26	3.81 ± 0.63	0.63 ± 0.06
5197408 ⁺	0.2086	0.36 ± 0.01	0.41 ± 0.01	0.81 ± 0.13	0.79 ± 0.05	2.73 ± 0.17	2.81 ± 0.12	2.03 ± 0.08
5312967 ⁺	0.1963	0.27 ± 0.01	0.31 ± 0.01	0.53 ± 0.14	0.8 ± 0.06	2.58 ± 0.28	6.63 ± 0.63	0.9 ± 0.07
5305653 ⁺	0.2124	0.69 ± 0.01	0.71 ± 0.01	1.29 ± 0.11	0.67 ± 0.04	2.66 ± 0.1	2.74 ± 0.28	0.87 ± 0.04
5216684 ⁺	0.2096	1.13 ± 0.02	1.94 ± 0.05	8.59 ± 1.86	1.23 ± 0.04	3.56 ± 0.24	8.23 ± 0.36	0.83 ± 0.01
5342686 ⁺	0.1861	2.98 ± 0.03	4.1 ± 0.08	9.12 ± 1.93	0.99 ± 0.04	2.85 ± 0.23	4.95 ± 0.15	0.32 ± 0.02
5213139 ⁺	0.1228	2.43 ± 0.03	2.86 ± 0.06	9.16 ± 2.0	0.83 ± 0.04	3.23 ± 0.24	1.72 ± 0.06	1.37 ± 0.03
5155308 ⁺	0.209	4.63 ± 0.03	5.99 ± 0.03	21.22 ± 4.44	0.93 ± 0.03	3.33 ± 0.23	1.71 ± 0.08	2.33 ± 0.04
5240292 ⁺	0.2238	0.5 ± 0.01	0.66 ± 0.03	2.69 ± 0.7	0.93 ± 0.06	3.48 ± 0.29	0.43 ± 0.02	1.45 ± 0.03
oAGN (mWarm) (red squares)								
5347780* ⁺	0.089	2.15 ± 0.03	1.89 ± 0.05	5.81 ± 0.14	0.51 ± 0.04	3.2 ± 0.05	1.17 ± 0.05	1.53 ± 0.07
5294374* ⁺	0.107	5.17 ± 0.06	4.63 ± 0.1	14.27 ± 2.81	0.53 ± 0.04	3.2 ± 0.22	1.09 ± 0.04	1.81 ± 0.03
5112784 ⁺	0.0578	1.74 ± 0.02	1.49 ± 0.04	2.31 ± 0.62	0.48 ± 0.04	2.52 ± 0.3	0.96 ± 0.18	2.52 ± 0.38
5153772	0.189	0.44 ± 0.01	0.48 ± 0.02	4.79 ± 1.15	0.75 ± 0.06	4.43 ± 0.27	7.62 ± 0.4	0.8 ± 0.06
5351862 ⁺	0.1103	0.75 ± 0.01	0.7 ± 0.02	3.62 ± 0.89	0.56 ± 0.05	3.74 ± 0.27	3.43 ± 0.17	1.19 ± 0.06
5369229	0.1402	0.53 ± 0.02	0.48 ± 0.02	2.97 ± 0.17	0.55 ± 0.06	3.92 ± 0.08	7.45 ± 0.52	0.71 ± 0.06
5346487 ⁺	0.1898	0.45 ± 0.01	0.44 ± 0.02	3.46 ± 0.88	0.64 ± 0.06	4.17 ± 0.28	0.99 ± 0.04	1.57 ± 0.04
5110547 ⁺	0.0889	0.96 ± 0.01	0.78 ± 0.02	2.46 ± 0.65	0.41 ± 0.04	3.24 ± 0.29	6.17 ± 0.32	0.8 ± 0.02
5180136	0.1056	0.61 ± 0.01	0.52 ± 0.02	1.76 ± 0.18	0.47 ± 0.05	3.32 ± 0.12	7.12 ± 0.67	0.7 ± 0.02
5137338 ⁺	0.2597	0.45 ± 0.01	0.43 ± 0.02	0.65 ± 0.14	0.6 ± 0.06	2.48 ± 0.24	1.77 ± 0.31	0.67 ± 0.04

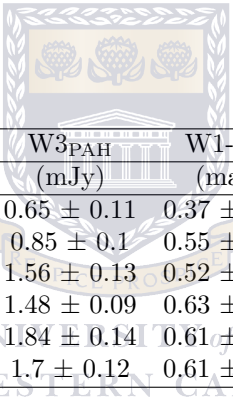
...

Table 5.3 – continued

CATAID	z_{spec}	W1 (mJy)	W2 (mJy)	W3 _{PAH} (mJy)	W1-W2 (mag)	W2-W3 (mag)	[O III]/H β	[N II]/H α
5196019	0.1258	0.69 \pm 0.01	0.72 \pm 0.03	5.65 \pm 1.31	0.69 \pm 0.05	4.18 \pm 0.26	6.96 \pm 0.68	0.78 \pm 0.02
5211450	0.2535	0.36 \pm 0.01	0.34 \pm 0.01	1.32 \pm 0.41	0.6 \pm 0.06	3.43 \pm 0.34	8.64 \pm 1.51	0.51 \pm 0.05
5367800 ⁺	0.2627	0.43 \pm 0.01	0.43 \pm 0.02	0.41 \pm 0.08	0.65 \pm 0.06	2.04 \pm 0.22	1.19 \pm 0.1	1.34 \pm 0.14
oAGN (mSF) (yellow circles)								
5249547*	0.0834	1.36 \pm 0.02	0.8 \pm 0.02	2.13 \pm 0.16	0.07 \pm 0.04	3.09 \pm 0.09	2.17 \pm 0.21	0.79 \pm 0.03
5155115*	0.0869	1.7 \pm 0.02	0.99 \pm 0.03	2.2 \pm 0.18	0.06 \pm 0.05	2.92 \pm 0.1	5.56 \pm 0.57	0.93 \pm 0.05
5163580 ⁺	0.1228	0.51 \pm 0.01	0.36 \pm 0.02	0.39 \pm 0.1	0.25 \pm 0.06	2.22 \pm 0.29	2.54 \pm 0.2	2.71 \pm 0.19
5368644	0.1194	0.43 \pm 0.01	0.34 \pm 0.01	1.18 \pm 0.13	0.37 \pm 0.06	3.35 \pm 0.13	2.55 \pm 0.3	0.6 \pm 0.08
5278828	0.1388	0.22 \pm 0.01	0.18 \pm 0.01	1.15 \pm 0.13	0.42 \pm 0.1	3.97 \pm 0.15	2.7 \pm 0.46	0.59 \pm 0.02
5139540 ⁺	0.2323	0.36 \pm 0.01	0.2 \pm 0.01	0.59 \pm 0.13	0.01 \pm 0.07	3.18 \pm 0.25	0.49 \pm 0.09	1.89 \pm 0.15
5305775	0.133	0.63 \pm 0.01	0.41 \pm 0.02	2.32 \pm 0.59	0.17 \pm 0.06	3.86 \pm 0.28	2.35 \pm 0.34	0.54 \pm 0.03
5355371 ⁺	0.2006	0.25 \pm 0.01	0.2 \pm 0.01	0.92 \pm 0.1	0.42 \pm 0.06	3.62 \pm 0.13	8.12 \pm 0.28	0.58 \pm 0.01
5188449 ⁺	0.1169	0.2 \pm 0.01	0.11 \pm 0.01	0.24 \pm 0.1	-0.01 \pm 0.14	2.95 \pm 0.46	3.32 \pm 0.2	0.68 \pm 0.04
5427366	0.0881	0.45 \pm 0.01	0.32 \pm 0.01	0.87 \pm 0.11	0.27 \pm 0.05	3.11 \pm 0.15	1.84 \pm 0.17	0.68 \pm 0.04
5163246	0.2064	0.37 \pm 0.01	0.25 \pm 0.01	0.3 \pm 0.07	0.2 \pm 0.06	2.34 \pm 0.26	4.53 \pm 0.32	0.63 \pm 0.02
5258350	0.0768	0.89 \pm 0.01	0.6 \pm 0.01	1.94 \pm 0.17	0.21 \pm 0.04	3.28 \pm 0.1	3.07 \pm 0.16	0.59 \pm 0.01
5154519	0.2123	0.21 \pm 0.01	0.17 \pm 0.01	0.95 \pm 0.12	0.43 \pm 0.08	3.83 \pm 0.15	3.61 \pm 0.73	0.79 \pm 0.05
5271798	0.152	0.36 \pm 0.01	0.29 \pm 0.01	3.34 \pm 0.81	0.4 \pm 0.06	4.61 \pm 0.27	4.59 \pm 0.16	0.54 \pm 0.01
non-oAGN (mAGN) (orange circles)								
5200866*	0.1218	0.97 \pm 0.01	1.38 \pm 0.04	17.47 \pm 3.64	1.04 \pm 0.04	4.68 \pm 0.23	0.97 \pm 0.02	0.35 \pm 0.0
5158890*	0.1772	1.43 \pm 0.02	1.63 \pm 0.04	8.14 \pm 0.15	0.79 \pm 0.04	3.7 \pm 0.04	0.95 \pm 0.07	0.51 \pm 0.01
5275222* ⁺	0.2101	0.75 \pm 0.01	0.84 \pm 0.03	2.08 \pm 0.62	0.78 \pm 0.06	2.96 \pm 0.33	0.29 \pm 0.01	0.61 \pm 0.01
5241310* ⁺	0.2283	0.4 \pm 0.01	0.55 \pm 0.04	1.9 \pm 0.54	0.98 \pm 0.09	3.31 \pm 0.32	1.35 \pm 0.1	0.42 \pm 0.02
5362108	0.1669	0.36 \pm 0.01	0.46 \pm 0.02	3.47 \pm 0.84	0.92 \pm 0.06	4.13 \pm 0.27	0.93 \pm 0.23	0.28 \pm 0.05
5154472	0.1107	0.25 \pm 0.01	0.31 \pm 0.01	1.59 \pm 0.12	0.91 \pm 0.07	3.71 \pm 0.1	0.45 \pm 0.15	0.39 \pm 0.03
5129662	0.2045	0.44 \pm 0.01	0.52 \pm 0.02	2.18 \pm 0.56	0.83 \pm 0.06	3.51 \pm 0.28	1.73 \pm 0.1	0.5 \pm 0.01
5246095 ⁺	0.2184	0.7 \pm 0.01	0.84 \pm 0.03	3.08 \pm 0.73	0.83 \pm 0.05	3.38 \pm 0.26	0.78 \pm 0.04	0.71 \pm 0.01
5119859	0.1865	0.2 \pm 0.01	0.25 \pm 0.01	1.41 \pm 0.14	0.92 \pm 0.08	3.81 \pm 0.13	0.2 \pm 0.06	0.34 \pm 0.03
5317117 ⁺	0.2038	0.79 \pm 0.01	0.92 \pm 0.01	2.35 \pm 0.12	0.81 \pm 0.04	3.0 \pm 0.07	0.57 \pm 0.02	0.26 \pm 0.01
5247018 ⁺	0.209	0.22 \pm 0.01	0.49 \pm 0.03	0.78 \pm 0.21	1.52 \pm 0.07	2.48 \pm 0.3	0.3 \pm 0.02	1.01 \pm 0.05
non-oAGN (mWarm) (orange squares)								
5204947*	0.2438	0.68 \pm 0.01	0.73 \pm 0.03	4.38 \pm 1.08	0.72 \pm 0.05	3.9 \pm 0.27	1.86 \pm 0.4	0.39 \pm 0.01
5219936	0.0935	0.63 \pm 0.01	0.66 \pm 0.03	6.72 \pm 1.51	0.7 \pm 0.06	4.47 \pm 0.25	1.02 \pm 0.06	0.3 \pm 0.01
5282867	0.0846	0.25 \pm 0.01	0.21 \pm 0.01	0.85 \pm 0.15	0.46 \pm 0.09	3.49 \pm 0.2	0.71 \pm 0.14	0.26 \pm 0.02
5310140	0.2038	0.26 \pm 0.01	0.23 \pm 0.01	1.41 \pm 0.12	0.54 \pm 0.07	3.9 \pm 0.11	0.84 \pm 0.16	0.34 \pm 0.02

...

Table 5.3 – continued



CATAID	z_{spec}	W1 (mJy)	W2 (mJy)	W3 _{PAH} (mJy)	W1-W2 (mag)	W2-W3 (mag)	[O III]/H β	[N II]/H α
5100400	0.2733	0.52 ± 0.01	0.41 ± 0.02	0.65 ± 0.11	0.37 ± 0.06	2.57 ± 0.19	0.11 ± 0.04	0.42 ± 0.02
5115102	0.2989	0.22 ± 0.01	0.2 ± 0.01	0.85 ± 0.1	0.55 ± 0.08	3.55 ± 0.15	0.61 ± 0.13	0.48 ± 0.03
5154420	0.1993	0.28 ± 0.01	0.25 ± 0.01	1.56 ± 0.13	0.52 ± 0.07	3.96 ± 0.11	0.3 ± 0.09	0.4 ± 0.02
5228724 ⁺	0.2367	0.44 ± 0.01	0.43 ± 0.01	1.48 ± 0.09	0.63 ± 0.04	3.3 ± 0.08	1.36 ± 0.14	0.54 ± 0.02
5350683	0.2508	0.27 ± 0.01	0.26 ± 0.01	1.84 ± 0.14	0.61 ± 0.06	4.06 ± 0.1	0.68 ± 0.15	0.54 ± 0.03
5133213	0.2059	0.29 ± 0.01	0.28 ± 0.01	1.7 ± 0.12	0.61 ± 0.07	3.92 ± 0.09	0.24 ± 0.07	0.45 ± 0.02

Table 5.4: Derived properties of a representative sample of the galaxies from each activity group. The stellar masses are derived based on the M/L ratio from Cluver et al. (2014). The star formation rate ($\text{SFR}_{12\mu\text{m}}$) are derived using the $\nu\text{L}\nu(12\mu\text{m})$ and the calibration from Cluver et al. (2017).

	$\text{Log}M_{\text{stellar}} [M_{\odot}]$ (M_{\odot})	$\text{SFR}_{12\mu\text{m}}$ ($M_{\odot}\text{yr}^{-1}$)	$\text{Log} (L[\text{O III}])$ (erg s^{-1})	$\text{Log} (\text{sSFR})$ (yr^{-1})
SF (blue circles)				
5241095*	9.05 ± 0.20	0.2 ± 0.09	41.14 ± 0.0	-9.75 ± 0.27
5240983*	9.14 ± 0.19	0.49 ± 0.21	40.94 ± 0.01	-9.45 ± 0.27
5306682*	9.43 ± 0.10	0.21 ± 0.08	39.44 ± 0.01	-10.11 ± 0.19
5135645*	10.78 ± 0.16	73.44 ± 29.20	41.25 ± 0.03	-8.91 ± 0.23
5325430	10.19 ± 0.18	2.3 ± 0.81	40.23 ± 0.08	-9.83 ± 0.24
5327563	9.66 ± 0.24	1.43 ± 0.69	–	-9.51 ± 0.32
5325339	10.48 ± 0.17	7.0 ± 2.45	–	-9.64 ± 0.23
5123445	9.85 ± 0.23	2.2 ± 0.82	–	-9.51 ± 0.28
5138489	9.82 ± 0.33	1.57 ± 0.64	40.23 ± 0.14	-9.62 ± 0.38
5153375	9.85 ± 0.16	2.53 ± 0.91	40.29 ± 0.08	-9.44 ± 0.23
5261290	10.35 ± 0.13	9.29 ± 3.70	40.35 ± 0.11	-9.39 ± 0.22
5187670	10.25 ± 0.38	2.63 ± 0.98	39.94 ± 0.13	-9.83 ± 0.42
5281879	10.04 ± 0.11	1.54 ± 0.54	39.87 ± 0.05	-9.85 ± 0.19
5281521	9.51 ± 0.28	0.15 ± 0.07	40.01 ± 0.02	-10.35 ± 0.35
5305483	9.98 ± 0.19	3.42 ± 1.42	40.54 ± 0.04	-9.45 ± 0.26
5222747	10.50 ± 0.18	7.13 ± 2.65	40.76 ± 0.11	-9.65 ± 0.24
5266202	10.20 ± 0.18	5.67 ± 1.98	40.09 ± 0.14	-9.44 ± 0.24
5185570	10.01 ± 0.23	0.38 ± 0.19	39.86 ± 0.05	-10.43 ± 0.31
5256068	11.05 ± 0.10	70.22 ± 24.32	41.47 ± 0.04	-9.2 ± 0.18
Composites (green circles)				
5205726*	10.51 ± 0.11	1.94 ± 0.68	40.29 ± 0.21	-10.22 ± 0.19
5322507	10.47 ± 0.13	1.19 ± 0.44	–	-10.39 ± 0.2
5246049	10.45 ± 0.14	13.63 ± 5.44	40.57 ± 0.07	-9.32 ± 0.22
5277048	9.85 ± 0.31	4.27 ± 1.56	–	-9.22 ± 0.35
5251443	11.23 ± 0.24	6.3 ± 2.90	40.62 ± 0.13	-10.43 ± 0.31
5279625	10.11 ± 0.15	4.86 ± 1.95	40.32 ± 0.06	-9.43 ± 0.23
5285888	10.78 ± 0.17	29.91 ± 12.21	41.5 ± 0.07	-9.31 ± 0.25
5159722	10.37 ± 0.13	7.32 ± 2.54	40.64 ± 0.07	-9.51 ± 0.20
5154601	10.37 ± 0.21	1.31 ± 0.50	40.18 ± 0.07	-10.25 ± 0.27
5264991	10.55 ± 0.19	18.81 ± 6.60	41.2 ± 0.07	-9.27 ± 0.24
5364072	10.35 ± 0.35	1.55 ± 0.62	40.56 ± 0.08	-10.16 ± 0.39
5249313	10.50 ± 0.14	1.66 ± 0.64	40.01 ± 0.07	-10.28 ± 0.22
5280475	9.99 ± 0.21	4.17 ± 1.75	40.54 ± 0.02	-9.38 ± 0.28
5154381	10.01 ± 0.20	1.8 ± 0.67	40.64 ± 0.1	-9.75 ± 0.26
oAGN (mAGN) (red circles)				
5339805* +	10.85 ± 0.10	11.54 ± 4.00	41.4 ± 0.03	-9.79 ± 0.18
5151978* +	10.83 ± 0.14	55.33 ± 22.54	42.37 ± 0.0	-9.08 ± 0.23
5145801	10.95 ± 0.13	27.1 ± 11.27	–	-9.51 ± 0.22
5252110	10.97 ± 0.11	31.75 ± 12.57	–	-9.48 ± 0.20
5237160	9.76 ± 0.13	8.9 ± 3.51	–	-8.81 ± 0.21
5340595 +	11.13 ± 0.11	37.46 ± 14.92	–	-9.56 ± 0.21
5286102 +	11.40 ± 0.11	42.13 ± 17.32	41.63 ± 0.04	-9.77 ± 0.21
5108709	10.50 ± 0.13	17.61 ± 6.15	42.11 ± 0.01	-9.25 ± 0.20
5369226	10.85 ± 0.11	46.57 ± 18.33	41.73 ± 0.02	-9.19 ± 0.20
5162821 +	10.85 ± 0.12	12.99 ± 4.80	41.89 ± 0.03	-9.74 ± 0.20
5233898	11.05 ± 0.12	41.49 ± 16.68	42.15 ± 0.02	-9.43 ± 0.21
5197408 +	10.71 ± 0.14	9.86 ± 3.67	41.97 ± 0.01	-9.72 ± 0.21
5312967 +	10.53 ± 0.16	6.06 ± 2.50	41.68 ± 0.01	-9.75 ± 0.24
5305653 +	11.01 ± 0.11	15.34 ± 5.42	41.92 ± 0.01	-9.83 ± 0.19
5216684 +	11.21 ± 0.11	79.31 ± 31.31	42.99 ± 0.0	-9.31 ± 0.20
5342686 +	11.52 ± 0.10	66.05 ± 25.95	42.78 ± 0.0	-9.70 ± 0.20
5213139 +	11.03 ± 0.10	29.78 ± 11.78	42.17 ± 0.01	-9.56 ± 0.20
5155308 +	11.82 ± 0.08	174.43 ± 68.32	42.13 ± 0.01	-9.58 ± 0.19
...				

Table 5.4 – continued

	LogM _{stellar} [M _⊙] (M _⊙)	SFR _{12μm} (M _⊙ yr ⁻¹)	Log (L[O III]) (erg s ⁻¹)	Log (sSFR) (yr ⁻¹)
5240292 +	10.93 ± 0.15	32.53 ± 13.51	41.52 ± 0.01	-9.41 ± 0.24
oAGN (mWarm) (red squares)				
5347780* +	10.68 ± 0.11	10.86 ± 3.77	–	-9.64 ± 0.19
5294374* +	11.23 ± 0.10	33.8 ± 13.08	42.0 ± 0.01	-9.7 ± 0.2
5112784 +	10.19 ± 0.11	2.17 ± 0.91	–	-9.86 ± 0.21
5153772	10.70 ± 0.15	38.63 ± 15.66	–	-9.12 ± 0.23
5351862 +	10.42 ± 0.13	10.73 ± 4.37	–	-9.39 ± 0.22
5369229	10.50 ± 0.16	14.24 ± 4.98	–	-9.34 ± 0.22
5346487 +	10.71 ± 0.15	29.29 ± 12.05	41.71 ± 0.01	-9.25 ± 0.23
5110547 +	10.33 ± 0.11	5.11 ± 2.13	41.7 ± 0.01	-9.62 ± 0.21
5180136	10.29 ± 0.12	5.25 ± 1.88	41.75 ± 0.01	-9.57 ± 0.2
5137338 +	11.03 ± 0.15	12.56 ± 4.96	41.51 ± 0.04	-9.93 ± 0.23
5196019	10.51 ± 0.13	20.38 ± 8.18	41.68 ± 0.01	-9.2 ± 0.22
5211450	10.90 ± 0.15	22.25 ± 9.79	42.56 ± 0.01	-9.55 ± 0.24
5367800 +	11.01 ± 0.14	8.59 ± 3.32	41.8 ± 0.03	-10.08 ± 0.22
oAGN (mSF) (yellow circles)				
5249547*	10.74 ± 0.11	3.99 ± 1.40	41.19 ± 0.02	-10.14 ± 0.19
5155115*	10.92 ± 0.12	4.44 ± 1.57	–	-10.28 ± 0.19
5163580 +	10.36 ± 0.16	1.85 ± 0.77	–	-10.09 ± 0.24
5368644	10.26 ± 0.15	4.66 ± 1.67	–	-9.59 ± 0.22
5278828	10.11 ± 0.25	6.08 ± 2.18	41.0 ± 0.07	-9.33 ± 0.29
5139540 +	11.31 ± 0.18	9.17 ± 3.65	41.15 ± 0.07	-10.35 ± 0.25
5305775	10.60 ± 0.15	10.37 ± 4.28	41.35 ± 0.06	-9.59 ± 0.23
5355371 +	10.51 ± 0.16	10.19 ± 3.67	42.5 ± 0.0	-9.5 ± 0.22
5188449 +	10.44 ± 0.35	1.12 ± 0.55	40.99 ± 0.02	-10.39 ± 0.41
5427366	9.99 ± 0.13	2.01 ± 0.73	–	-9.69 ± 0.21
5163246	10.71 ± 0.15	4.06 ± 1.63	42.42 ± 0.01	-10.11 ± 0.23
5258350	10.16 ± 0.10	3.15 ± 1.12	41.24 ± 0.01	-9.66 ± 0.19
5154519	10.49 ± 0.20	11.78 ± 4.28	41.87 ± 0.02	-9.42 ± 0.26
5271798	10.41 ± 0.16	18.45 ± 7.49	42.1 ± 0.0	-9.14 ± 0.24
non-oAGN (mAGN) (orange circles)				
5200866*	10.63 ± 0.11	51.72 ± 20.24	41.69 ± 0.01	-8.91 ± 0.2
5158890*	11.15 ± 0.11	54.4 ± 18.85	41.75 ± 0.02	-9.42 ± 0.19
5275222* +	11.04 ± 0.14	22.92 ± 9.91	41.78 ± 0.01	-9.68 ± 0.24
5241310* +	10.85 ± 0.22	24.95 ± 10.65	41.39 ± 0.02	-9.45 ± 0.29
5362108	10.49 ± 0.16	22.85 ± 9.29	–	-9.14 ± 0.24
5154472	9.94 ± 0.17	5.25 ± 1.85	40.42 ± 0.13	-9.22 ± 0.23
5129662	10.78 ± 0.15	22.59 ± 9.33	41.87 ± 0.01	-9.43 ± 0.24
5246095 +	11.05 ± 0.13	34.86 ± 14.10	41.68 ± 0.02	-9.51 ± 0.22
5119859	10.34 ± 0.19	12.84 ± 4.59	40.56 ± 0.12	-9.23 ± 0.25
5317117 +	11.03 ± 0.09	23.98 ± 8.37	41.89 ± 0.01	-9.65 ± 0.18
5247018 +	10.49 ± 0.18	9.58 ± 4.03	41.4 ± 0.03	-9.51 ± 0.26
non-oAGN (mWarm) (orange squares)				
5204947*	11.14 ± 0.14	59.25 ± 24.19	42.19 ± 0.07	-9.37 ± 0.22
5219936	10.19 ± 0.14	13.57 ± 5.41	41.36 ± 0.02	-9.06 ± 0.22
5282867	9.70 ± 0.22	1.84 ± 0.70	40.28 ± 0.07	-9.44 ± 0.27
5310140	10.54 ± 0.19	15.28 ± 5.42	41.19 ± 0.06	-9.36 ± 0.24
5100400	11.14 ± 0.15	13.99 ± 5.27	40.77 ± 0.14	-9.99 ± 0.22
5115102	10.84 ± 0.22	21.03 ± 7.63	41.0 ± 0.07	-9.52 ± 0.27
5154420	10.55 ± 0.17	16.05 ± 5.67	40.57 ± 0.13	-9.35 ± 0.23
5228724 +	10.92 ± 0.12	21.46 ± 7.52	41.47 ± 0.03	-9.59 ± 0.19
5350683	10.77 ± 0.15	29.26 ± 10.31	41.02 ± 0.09	-9.3 ± 0.22
5133213	10.60 ± 0.16	18.44 ± 6.48	40.78 ± 0.11	-9.34 ± 0.22

Chapter 6

Expanding the Analysis: Radio Continuum from MeerKAT

In our quest to exploit the large electromagnetic spectrum for a better understanding of AGNs and SF galaxy activities, we combined the optical and the IR data in the preceding chapter (Chap. 5). We now add the radio continuum data from the MeerKAT interferometer telescope in this chapter. We compare IR versus radio luminosity, looking for radio excess that could be related to the presence of AGN activity. The radio data were acquired via the MeerKAT call for proposal in 2019, which allocated 16.5 hours of observation time (details are available in Chap. 4) and is the basis of the MeerHOGS Pilot program (Józsa, Jarrett, P.I.).

6.1 Assessing the Photometric and Astrometric Quality

We used *ProFound* for source detection and extraction (see preceding chapter 4.4). For the point-source data, we used a sky cut (S/N) of 3 and a tolerance of 1 (see Section 4.1.2 for more information about these parameters). These parameters can be adjusted slightly for the resolved galaxies, which are extracted individually.

The astrometric offset between the galaxies detected by the MeerHOGS 20-cm and *WISE* 3.4 μm are shown in Figure 6.1 for a position cross-match of 5'' (more than 70 % of the galaxies are found within 3''). The comparison of the positions of the newly built instrument MeerKAT to *WISE* (already well-established survey) shows only a negligible average offset

of $0.126''$ in RA and $0.0202''$ in Dec, respectively. A more detailed picture is shown in Figure 6.2, where all the tiles (small regions) are inspected. We see some variations in the median Δ RA and median Δ Dec across the tiles, but all are small in magnitude. The lower part of the figure (for $RA < -35^\circ$) is outside the GAMA footprint; there are no redshifts for the galaxies in this area. Overall, MeerKAT shows good pointing and astrometric quality.

The photometric quality of the data tested against the NVSS is equally good. The fluxes measured in the two surveys generally agree within 10% error (see Figure 4.15 in Section 4.4).

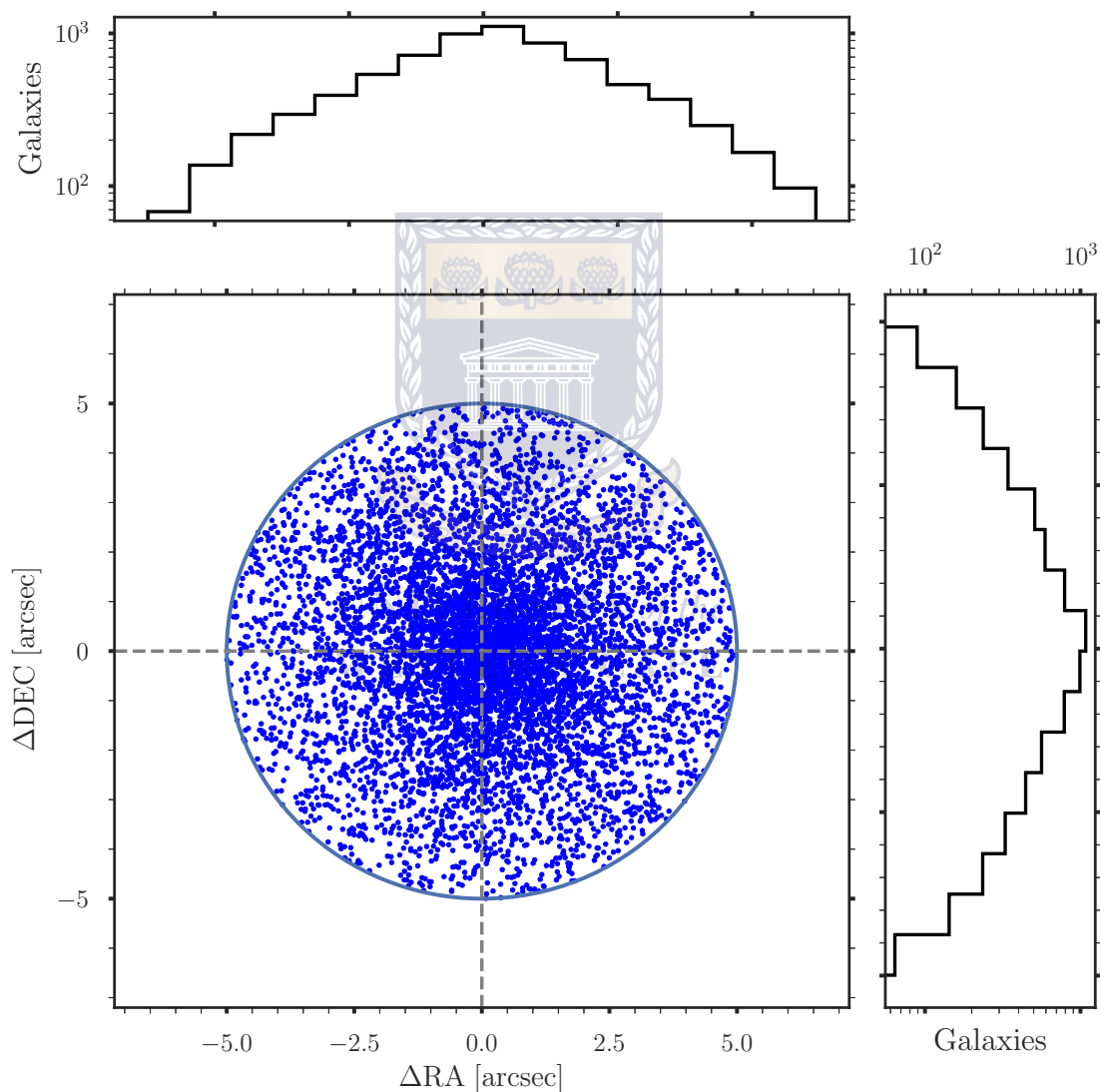


Figure 6.1: Average position offset between MeerHOGS (M) and *WISE* (W). The average (median) $RA (M) - RA (W) = 0.1268$ (0.1441) and $Dec (M) - Dec (W) = 0.0202$ (0.0305) arcsec, which confirms good astrometry for the MeerKAT instruments.

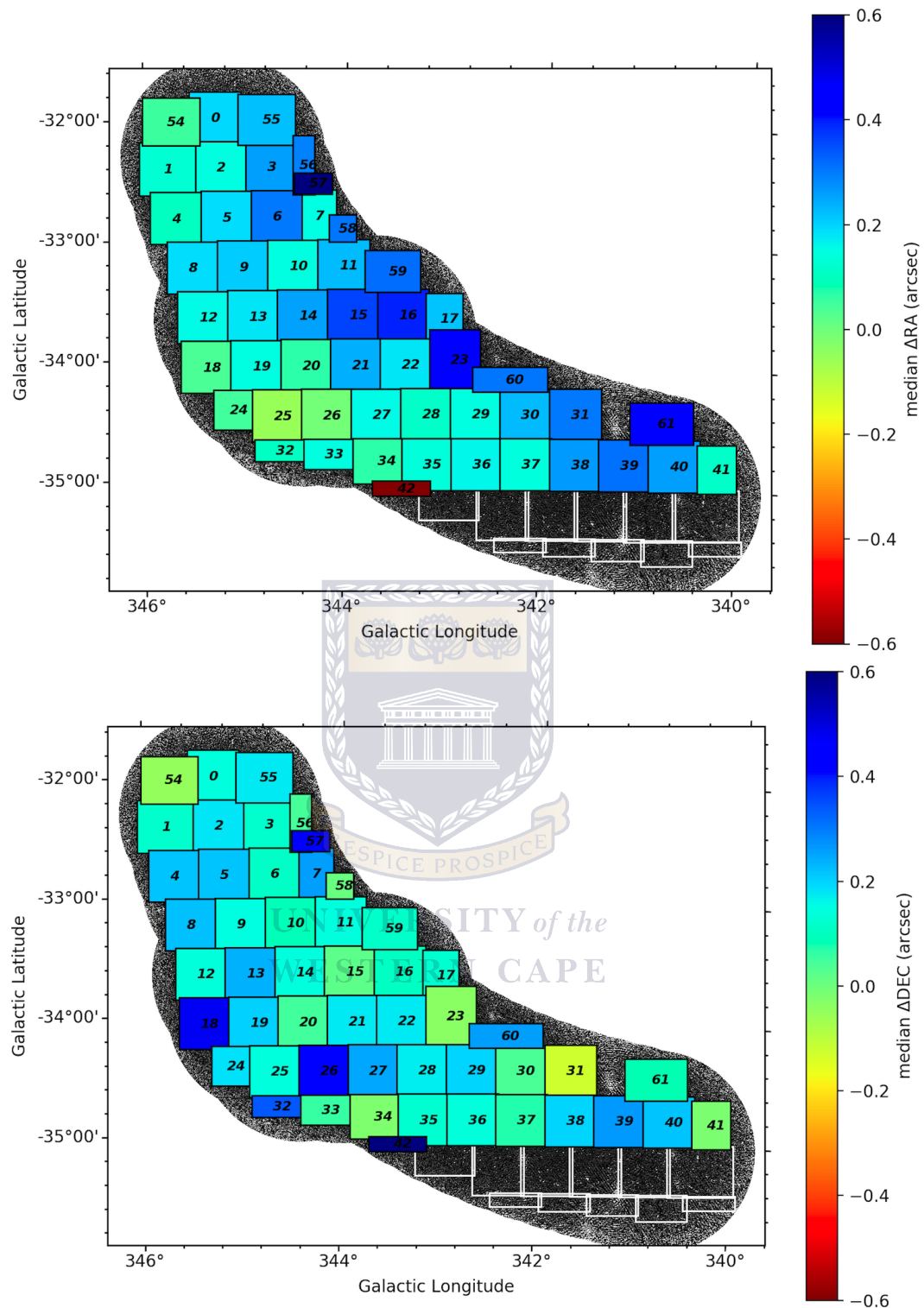


Figure 6.2: Offsets of the 1.4 GHz MeerHOGS positions from the *WISE* positions for sources detected in both surveys. Upper panel: Right ascension (MeerHOGS) - Right ascension (*WISE*). Lower panel: Declination (MeerHOGS) - Declination (*WISE*). There are small offsets (subarcsecs) visible in each tile along the observation’s footprint. However, these are negligible in comparison to the cross-match radius of about $5''$. The numbers on the images are just used to identify the different tiles.

6.2 Radio Catalogue

This section describes the radio galaxies (observation area of $\sim 10 \text{ deg}^2$). The sources are extracted with *ProFound* (Robotham et al. 2018) using a 3σ threshold, resulting in about 18 000 galaxies (a source density of $\sim 1 800 \text{ galaxies/deg}^2$). Visual inspection shows about 170 galaxies to be resolved (galaxies at least larger than twice the circular synthesised beam of $13.''5$). The radio sample within GAMA footprint ($\sim 8 \text{ deg}^2$), cross-matched with the *WISE*-GAMA catalogue used in Chapter 5, gives $\sim 1 800$ galaxies. The position cross-match was done using a $5''$ search radius between the radio and the *WISE* galaxies having a redshift in GAMA.

6.2.1 Resolved Sources in the Field

We extracted approximately 18 000 radio galaxies from the MeerHOGS data. The majority are point sources with few resolved galaxies (~ 170 resolved galaxies). The resolved multicomponents and the most interesting single component galaxies are presented in Figure 6.3). This list of multicomponent objects (also resolved) was made based solely on a visual inspection and may not in fact be physically associated. We looked for objects that are visibly larger than common point-like sources (dimensions at least larger than twice the circular beam size of $13.''5$). Note that apart from obvious cases of FRII such as MH4, MH8 or MH18 (see Figure 6.3), some of these may be just a chance superposition.

The resolved galaxies are triple components, probably some FRIIs for which the central AGN is still visible, as much as the lobes and some complex systems with three radio components. The FRII sources for which the central part is faint, or no longer visible constitute the majority of the double components. Some present one very bright lobe in comparison to the other. It is probably the result of an orientation effect boosting the jet pointing toward us at a low angle. This effect might be exacerbated when the angle is close to zero. Indeed, many single components and extremely bright galaxies in radio (about 50 cases; e.g., MH19 and MH20) seem not to have a counterpart in *WISE*, which means that they are emitting weakly in IR or are distant galaxies whose directly pointing jets are Doppler-boosted. They are intriguing galaxies that will need further attention with deeper and more intense spectroscopic coverage. A selection of some elements among the radio resolved galaxies is presented in Figure 6.3 and their fluxes are given in Table 6.1. There are some galaxies with abnormal morphology, such as MH6 showing a bent shape probably

caused by an interaction of the jet with its surrounding environment or maybe a galaxy merger. MH3 has a faint horizontal radio emission perpendicular to the main jet, but could just be two sources next to each other. Galaxy MH12 has a single radio component with a noticeable tail, which may be a result of a post-merger of two radio-emitting galaxies. Although the KiDS r-band image does not show any sign of interaction for these galaxies (MH3, MH6, and MH12) in the optical. MH22 looks like FRI whose jets have almost completely faded away or could be a background jet-like emission. We can only speculate about

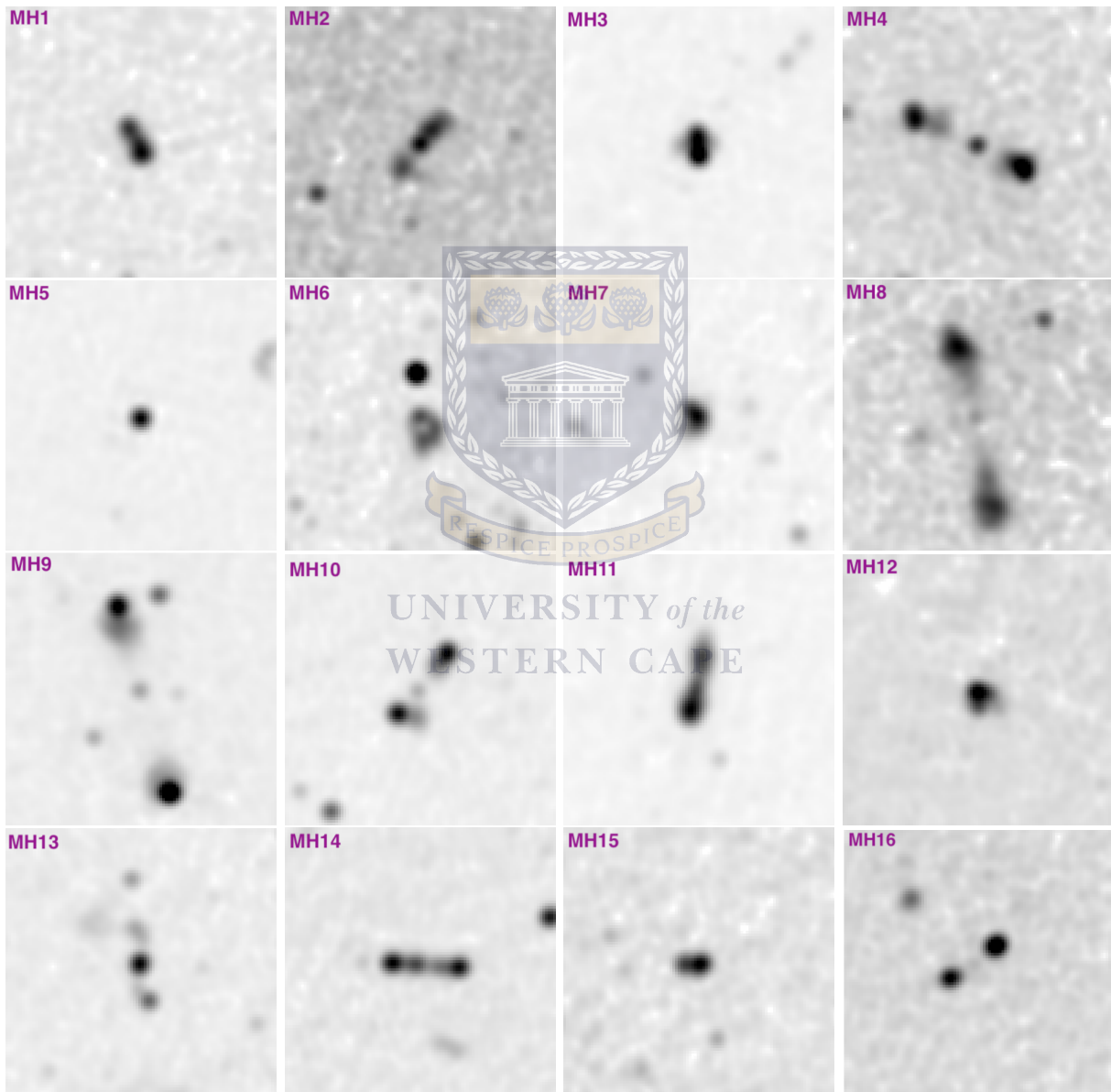


Figure 6.3: List of some resolved representative galaxies in MeerHOGS (the central images). Each stamp is 5×5 arcmin except MH17, which is 7×7 arcmin, and the beam size is 13.5 arcsecs. See Table 6.1 for measurements. MH17 is a known giant radio galaxy (GRG), which will be discussed in the text.

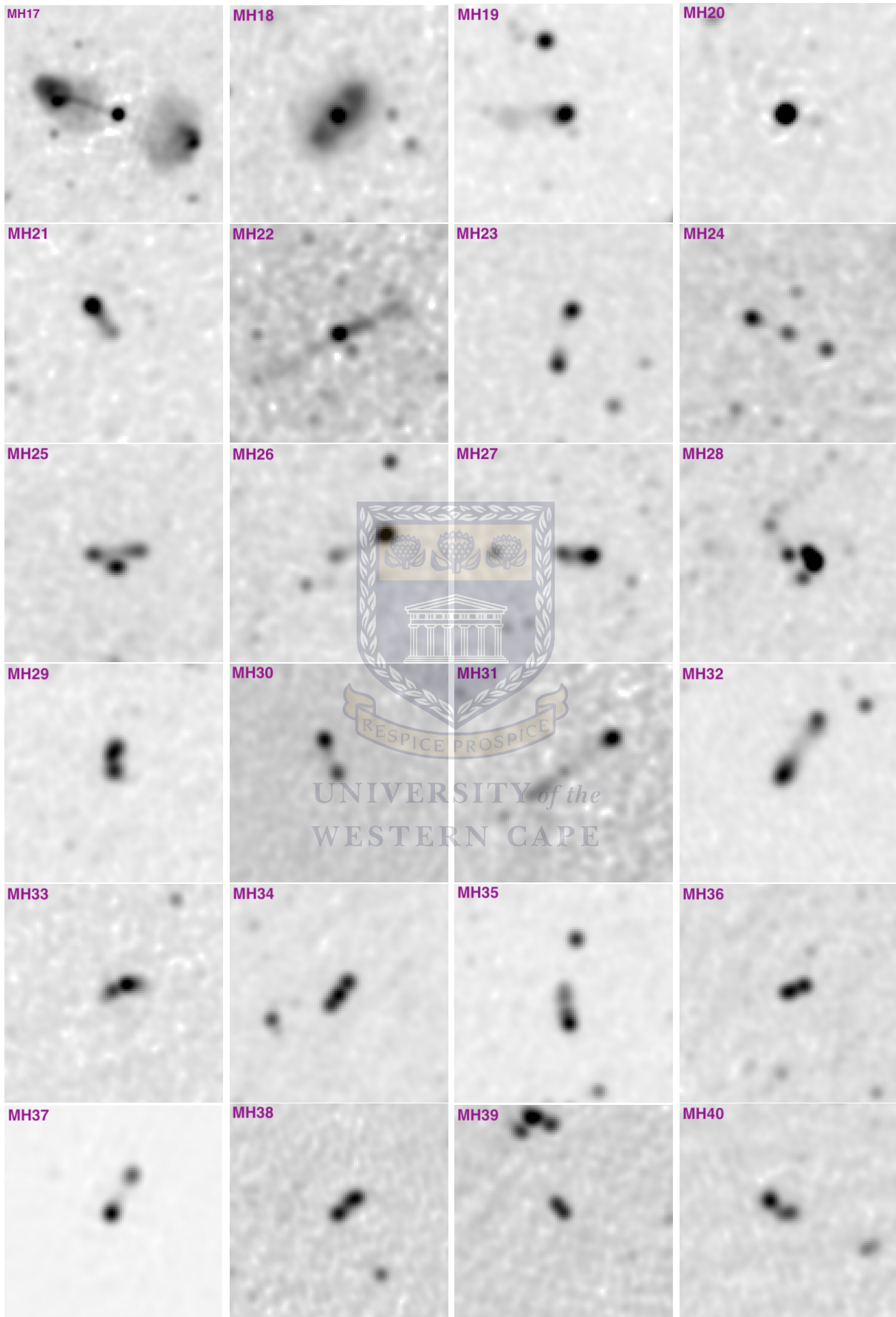


Figure 6.3: continued.

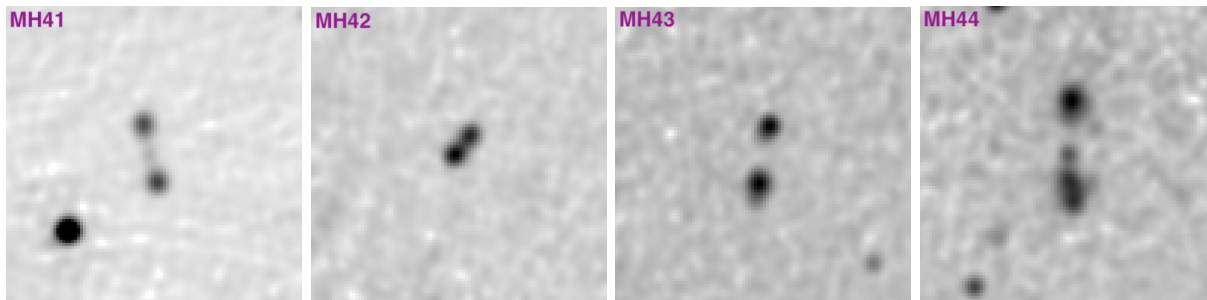


Figure 6.3: continued.

the true nature of these radio galaxies. A much longer observation time or a combination of more antennas (i.e., SKA-1) will reveal more details.

The most interesting specimen is MH18, known as IC5271, which is a SF galaxy largely resolved ($118'' \times 70''$) in radio and similarly in *WISE* (a *WISE* 3-colour image is presented in Figure 6.22). Such galaxies, resolved and large enough to do a pixel-by-pixel study, are very rare, and MH18 is the only one in our entire sample. Following a similar idea as Murphy et al. (2011b), local q_{TIR} could be determined within the galaxy to see how it evolves from the central to the outer side of the galaxy. This galaxy is one of the example cases used throughout the chapter, noted in diagnostic plots.

It is followed by MH17, the famous PKS 2250–351, a radio giant galaxy for which flux measurements are available in several works (Brown et al. 1991; Condon et al. 1998; Intema et al. 2009; Seymour et al. 2020). We found a total flux of $\sim 318.6 \pm 0.6$ mJy, which is comparable to that found by the NVSS (285 ± 29 mJy) within the errors. ProFound generates segments that enclose the flux of the galaxies. For resolved FR II galaxies like MH17, a visual inspection of the segmentation map is needed to add up the different flux contribution from the lobes and the central galaxy together for the total flux of the galaxy (see an example of segmentation map in Figure 3 of Robotham et al. 2018). The jets of MH17 extend across ~ 350 arcsecs (1.25 Mpc) from end to end. Some of the measurements compiled by Seymour et al. (2020) are presented in Table 6.2. The fluxes from Table 6.2 are plotted in Figure 6.4. Consistent with steep-spectrum synchrotron emission, we see a rapid decrease of the flux in the two lobes West (red) and East (blue) from ~ 200 mJy at 675 MHz to ~ 10 mJy at 9.5 GHz, while the emission from the core remains roughly constant (from 45 to 66 mJy). MH17 (PKS 2250–351) is also used as an example case in the analysis to follow.

Based on visual inspection, we found 15 three-component objects of which 11 are FR IIs.

The remaining four (MH24, MH25, MH28, and MH34) look like chance superpositions of

Table 6.1: Radio flux densities of the components of the resolved galaxies selected in Fig 6.3. It is an ensemble of interesting single and multicomponent radio emitters found in the observed area. The galaxies MH25 and MH28 were classified as three components although they are different from the conventional FR II. MH24 may be a fortunate alignment of emissions coming from three non-connected galaxies.

Galaxy id.	RA (deg)	Dec (deg)	N.comp.	Left.comp. (mJy)	central.comp. (mJy)	Right.comp. (mJy)	Total flux (mJy)
MH1	345.16548	-31.96997	2	10.41	N/A	14.99	25.41
MH2	345.76627	-32.54131	3	2.25	2.62	3.83	8.70
MH3	345.29553	-32.30024	1	N/A	138.17	N/A	138.17
MH4	344.22943	-32.70342	3	12.34	3.96	16.50	32.80
MH5	343.76173	-33.30183	1	N/A	43.72	N/A	43.72
MH6	344.28134	-33.59379	1	N/A	8.01	N/A	8.01
MH7	344.39038	-33.76065	1	N/A	33.31	N/A	33.31
MH8	342.81942	-33.82685	3	13.08	0.96	11.93	25.97
MH9	345.29649	-33.93349	3	77.13	4.21	104.34	185.68
MH10	344.30609	-34.54677	3	34.30	3.33	38.82	76.45
MH11	342.83231	-34.35561	2	82.77	N/A	49.95	132.71
MH12	341.65759	-34.43136	1	N/A	24.39	N/A	24.39
MH13	341.85518	-34.60437	3	3.83	11.68	4.22	19.74
MH14	343.93365	-34.68008	3	14.11	10.62	16.38	41.11
MH15	342.72356	-34.88700	1	N/A	8.25	N/A	8.25
MH16	343.73528	-33.10917	2	9.38	N/A	15.96	25.34
MH17	343.40012	-34.92519	3	151.47	45.00	122.10	318.57
MH18	344.50777	-33.74226	1	N/A	22.74	N/A	22.74
MH19	345.21566	-34.02112	1	N/A	33.38	N/A	33.38
MH20	345.4142	-33.26196	1	N/A	62.39	N/A	62.39
MH21	345.5588	-32.16678	2	0.44	NA	0.07	0.50
MH22	344.81651	-32.2304	1	NA	4.70	NA	4.70
MH23	345.84269	-32.89788	2	15.25	NA	17.23	32.48
MH24	345.2202	-32.84014	3	2.37	0.95	1.07	4.39
MH25	345.53025	-33.36734	3	6.95	11.47	6.29	24.71
MH26	345.20294	-33.14328	2	1.58	NA	7.24	8.83
MH27	345.0538	-33.0967	2	2.90	NA	7.27	10.16
MH28	344.57336	-32.97658	3	3.24	19.98	2.28	25.50
MH29	344.252	-33.37644	2	NA	11.54	NA	11.54
MH30	343.64585	-33.09938	2	8.01	NA	4.29	12.30
MH31	342.9438	-33.33359	3	7.57	2.58	18.11	28.26
MH32	345.17558	-34.08114	2	30.50	NA	15.04	45.54
MH33	343.06187	-33.92648	2	4.04	NA	7.72	11.76
MH34	343.02919	-34.206	3	10.40	NA	5.67	16.07
MH35	343.21541	-34.31053	2	5.56	NA	13.15	18.71
MH36	342.74987	-34.36203	2	4.36	NA	3.33	7.69
MH37	341.66499	-34.32315	2	236.18	NA	96.11	332.30
MH38	344.07075	-34.76574	2	6.02	NA	6.54	12.56
MH39	341.3357	-34.77133	3	NA	3.76	NA	3.76
MH40	342.6264	-35.2621	2	9.67	NA	6.43	16.10
MH41	341.13076	-35.21164	3	3.13	0.52	3.39	7.05
MH42	342.01801	-35.4946	2	5.61	NA	4.16	9.77
MH43	345.80901	-31.67244	2	9.64	NA	13.42	23.07
MH44	345.09855	-31.69654	3	1.63	3.93	4.21	9.774

Table 6.2: Radio flux densities of the components of MH17 (PKS 2250–351). Some of the measurements compiled by Seymour et al. (2020) are presented along with our own measurements using MeerKAT (64 dishes).

Telescope	Survey	Frequency (GHz)	East Lobe (mJy)	Core (mJy)	West Lobe (mJy)	Total (mJy)
ATCA	Green Time	9.5	22.1 ± 1.2	66.2 ± 3.3	10.7 ± 0.6	96.6 ± 3.4
ATCA	Green Time	5.5	38.7 ± 2.1	71.4 ± 3.6	23.6 ± 1.4	134 ± 49
VLA	NVSS	1.4	135 ± 5	50.0 ± 2.2	100.1 ± 3.8	285 ± 29
MeerKAT	MeerHOGS	1.4	151.5 ± 0.1	45.00 ± 0.1	122.1 ± 0.4	318.6 ± 0.6
ASKAP	EMU	0.888	193 ± 26	N/A	145 ± 17	> 338
MOST	SUMSS	0.843	175.1 ± 5.8	64 ± 5.6	153.8 ± 7.5	393 ± 41
uGMRT	GLASS	0.675	237 ± 17	45 ± 3	182 ± 12	464 ± 29

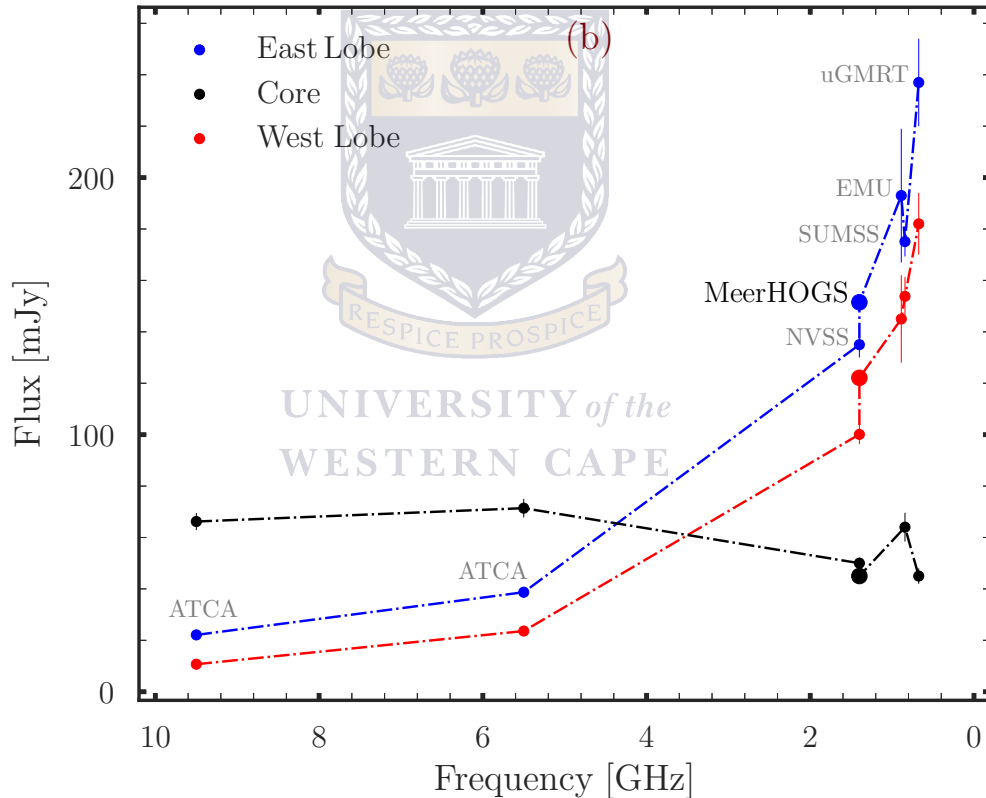


Figure 6.4: The variation of flux in the different components (East lobe, Core, West lobe) of MH17 (PKS 2250–351) as presented in table 6.2. The three components of the galaxy are measured in all the surveys except for EMU, where there is no measurement for the core. The flux density in the core remains flat, while it decreases in the lobes with higher frequencies. It shows a steep synchrotron signature. Given the large size of MH17, we can consider multiple shocks during the expansion of the jets as a potential cause of the steep spectrum as suggested by Gopal-Krishna & Wiita (1990).

emission, interacting systems, or emission from sources next to each other. We also found about 18 two-component objects which could contain some FR II too faint to be identified. We did not see many compelling FR I, but they may be hiding among the single-component sources and require higher sensitivity to be seen and discerned. This list is not exhaustive and has to be used with caution as many more FR II and FR I from our radio catalogue are probably too faint to be visually identified, which is a common issue when dealing with radio morphology classification.

6.2.2 MeerHOGS Cross-matched with the *WISE*-GAMA Sample

The MeerHOGS survey covers an area of roughly 10 deg^2 . However, as can be seen in Figure 6.2a and b, the survey goes slightly below $\text{Dec} = -35 \text{ deg}$, which is beyond the GAMA G23 footprint. Accounting for the galaxies lost at the edges, there are about 8 deg^2 to be effectively cross-matched with *WISE*-GAMA. Using a 5 arcsec search radius resulted in 1 841 radio galaxies having a *WISE* counterpart and a redshift available in GAMA (here referred to as the “MeerHOGS–GAMA–*WISE* sample”). Yao et al. (2020) devised a new classification diagram to classify AGNs combining optical lines ($[\text{N II}]$ and $\text{H}\alpha$) and the $\text{W1} - \text{W2}$ colour (detailed in Chapter 5, Section 5.4). The main criteria for this classification are $[\text{N II}]$ and $\text{H}\alpha$ lines in emission with $\text{S/N} > 3$, $\text{S/N}(\text{W1}) > 5$, and $\text{S/N}(\text{W2}) > 5$, respectively. Four hundred and seventy-eight galaxies from the MeerHOGS–GAMA–*WISE* sample follow these conditions and the different classifications provided by this new diagram will be represented throughout this radio study.

The redshift distribution of the radio samples is presented in Figure 6.5. The total sample (black) is distributed from $z \sim 0$ up to $z \sim 0.8$, but no more than 2% of the galaxies are found beyond $z = 0.5$ and 76% have $z < 0.3$. A redshift limit of 0.3 was used to establish the new diagram (see details in Chapter 5). The SF and mixed galaxies in the new diagram have a flat distribution between the redshift of 0 and 0.3, but the AGNs seem to be more concentrated at $z \sim 0.25$. The AGNs classified by the method of Jarrett et al. (2011), which are generally very luminous in mid-IR are found up to a redshift of 0.4 (note that GAMA, generally selected against QSOs, and hence are rare in the GAMA catalogue).

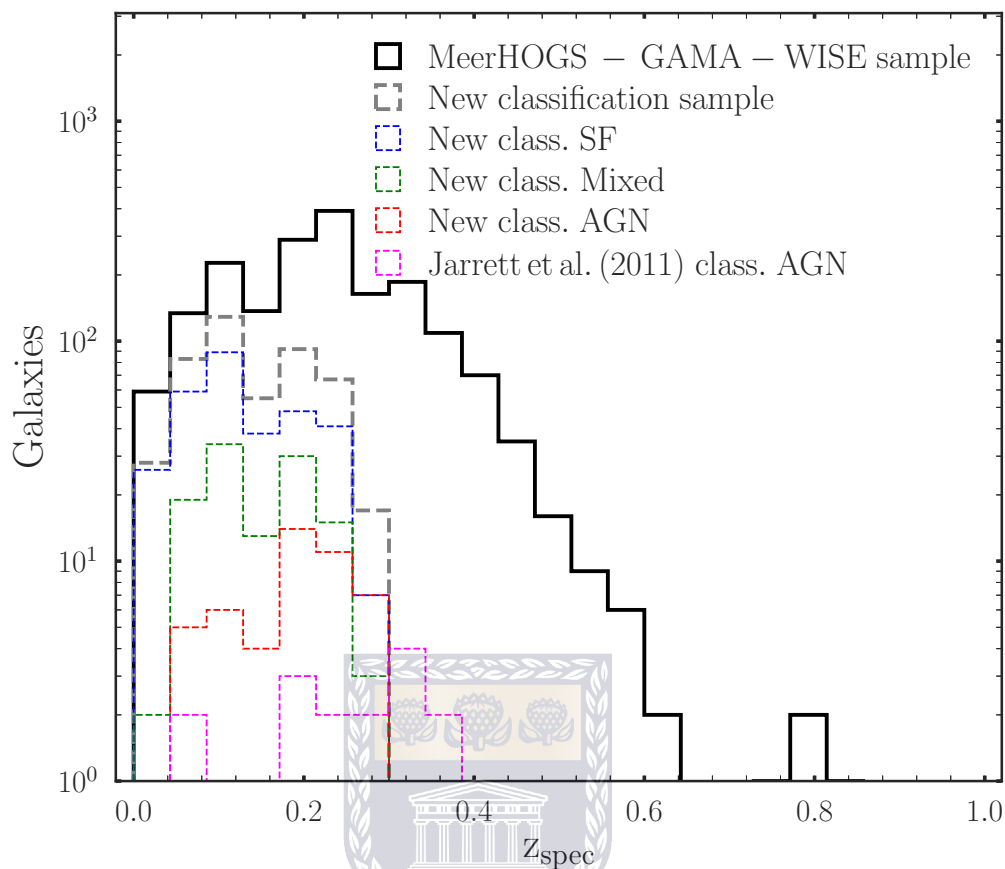


Figure 6.5: The redshift distribution of the radio galaxies in MeerHOGS. The total Optical–IR–Radio sample is represented in black. We can see radio galaxies all the way to redshift $z \sim 0.6$, but the bulk ($>75\%$) of the distribution is at $z < 0.3$, which corresponds to the redshift limit applied to the GAMA-*WISE* study in Chapter 5. The distributions of the galaxies classified by our new classification diagnostic are also presented, along with the AGNs classified using the *WISE* colour method by Jarrett et al. (2011). All the classifications from the new diagram are based on the GAMA-*WISE* sample. They are thus limited to $z < 0.3$.

6.3 Optical–IR–Radio Study of AGN vs SF

In this section, the MeerHOGS–GAMA–*WISE* sample is used to study the properties of AGNs and SF galaxies. Parameters such as the stellar mass and the $\text{SFR}_{12\mu\text{m}}$ are already available from our previous *WISE*-GAMA catalogue (see Chap. 5.1.2). The spectroscopic redshifts from GAMA are used to derive the radio luminosities. Seven galaxies among the resolved ones presented in Figure 6.3 have spectroscopic redshift in GAMA and their radio luminosities range from $\log L_{1.4\text{GHz}} = 24.4$ W/Hz (MH6) to 25.6 W/Hz (MH17). Some interesting specimens from Chapter 5 will be highlighted in this section.

6.3.1 The Infrared-to-Radio Luminosity Ratio: q_{TIR}

In Section 2.4.2, we described the correlation between the radio continuum that traces synchrotron emission and the IR emission in SF galaxies (see Helou et al. 1985). The TIR/radio ratio represented by the q_{TIR} helps to classify galaxies as starbursts or AGNs based on the excess IR or radio emission, respectively.

Here we compare the total IR (TIR) versus radio luminosity looking for an excess that could be attributed to AGN activity. The luminosity from the W3 band can be converted to the total IR luminosity using the formula derived by Cluver et al. (2017). Indeed, Cluver et al. (2017) found a tight correlation between the two parameters given by Equation 6.1. We characterise the TIR/radio correlation by the logarithmic ratio between the luminosities represented by q_{TIR} (Equation 6.2; Helou et al. 1985):

$$\log L_{\text{TIR}}(L_{\odot}) (M_{\odot}\text{yr}^{-1}) = (0.889 \pm 0.018)\log L_{12\mu\text{m}}(L_{\odot}) + (2.21 \pm 0.15) \quad (6.1)$$

$$q_{\text{TIR}} = \log\left(\frac{L_{\text{TIR}}}{3.75 \times 10^{12}\text{Hz}}\right) - \log\left(\frac{L_{1.4\text{GHz}}}{W \text{ Hz}}\right) \quad (6.2)$$

Figure 6.6a shows the q_{TIR} versus the W1-W2 colour. There is the expected flat distribution for high q_{TIR} values which is also seen in Figure 6.6b showing q_{TIR} versus W2-W3, indicative of the global SF activity. However, the distribution has a q_{TIR} tail along the

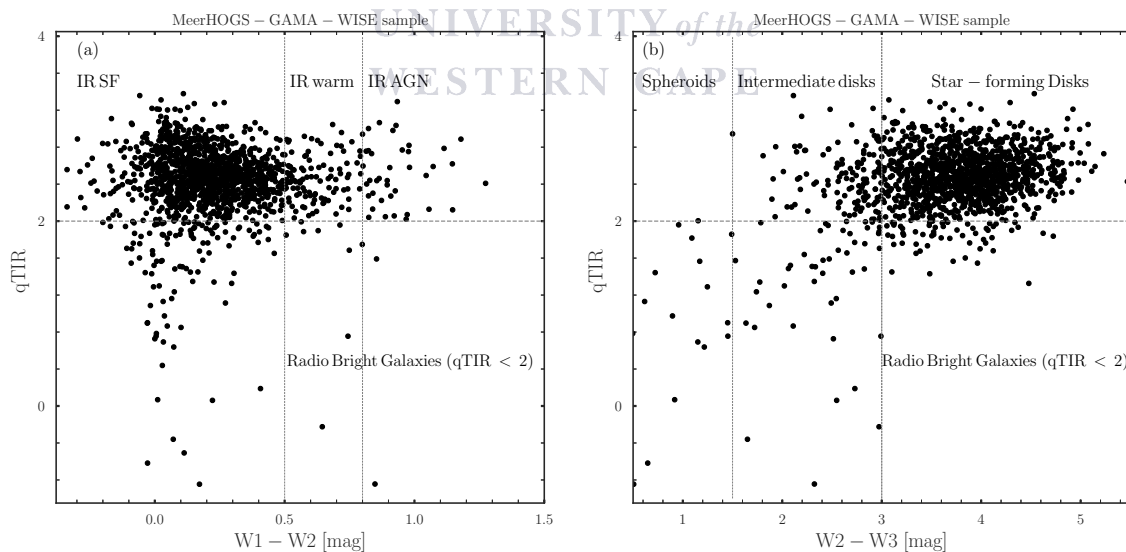


Figure 6.6: q_{TIR} vs W1-W2 (a) and q_{TIR} vs W2 - W3 (b) for the MeerHOGS-*WISE*-GAMA sample of galaxies (spectroscopic redshift available). The mean q_{TIR} for the galaxies with W2-W3 colour > 3 is 2.5. The radio bright galaxies are seen as a tail in the distribution showing radio excess at low W1-W2 and W2-W3 colours. They will be represented with cyan colour in the following figures.

y-axis for $W1-W2$ values close to 0. These galaxies with q_{TIR} values lower than 2 and hence anomalously high radio luminosity relative to the IR, will be referred to as “radio bright galaxies” throughout the document.

The average value using only the SF galaxies represented by the distribution between $W2-W3 > 3$ and $q_{\text{TIR}} > 2$ is about 2.5 ± 0.22 (median ~ 2.5). In comparison, a similar result was found by Ocran et al. (2020) using data from the Giant Metrewave Radio Telescope (GMRT). They observed an evolution of the q_{TIR} with redshift in which the average q_{TIR} value at low redshift would be ≈ 2.8 . In a sample of 162 SF galaxies, Bell (2003) found a median $q_{\text{TIR}} 2.64 \pm 0.02$. The median $q_{\text{TIR}} \sim 2.5 \pm 0.22$ in this work is also close to their result but with large scatter.

6.3.2 Evolution of some Parameters with the Radio Power

The radio flux is shown compared to the radio luminosity in Figure 6.7a and b. Figure 6.7a represents the total sample and Figure 6.7b shows the detail of the different groups of galaxies and their locations. The blue, green and red represent, respectively, the SFs, the composites and the AGNs as classified by our new diagram (see Section 5.4). The magenta circles are galaxies classified as AGNs by Jarrett et al. (2011). These are generally powerful AGNs such as quasars because of the conservatively high selection limit for $W1-W2$ ($W1-W2 > 0.8$ from Stern et al. 2012). The AGNs selected by Jarrett et al. (2011) should normally be a subgroup of the AGNs in the New diagram, except those with $[\text{N II}]$ and $\text{H}\alpha$ lines in absorption. The new diagram, which is a combination of optical BPT and the *WISE* colour-colour diagrams can only classify galaxies with $[\text{N II}]$ and $\text{H}\alpha$ lines in absorption. On the other hand, the New classification can detect significantly more low-power AGNs not taken into account by the Jarrett et al. (2011) classification. The New diagram selection, the Jarrett et al. (2011) selected AGNs and the radio selection methods (presented in this section) should be used as complementary methods for a better separation of the different class of galaxies.

Different layers are seen in the distribution where SF galaxies and composites are generally less luminous. The AGNs from the new classification diagram are mixed with the SFs ones, but, have a higher average luminosity. This is due to the fact that the new diagram takes into account the low-power AGNs for which the emission from the hosts are very significant. The AGNs by Jarrett et al. (2011) also by Stern et al. (2012) and Assef et al. (2013), are

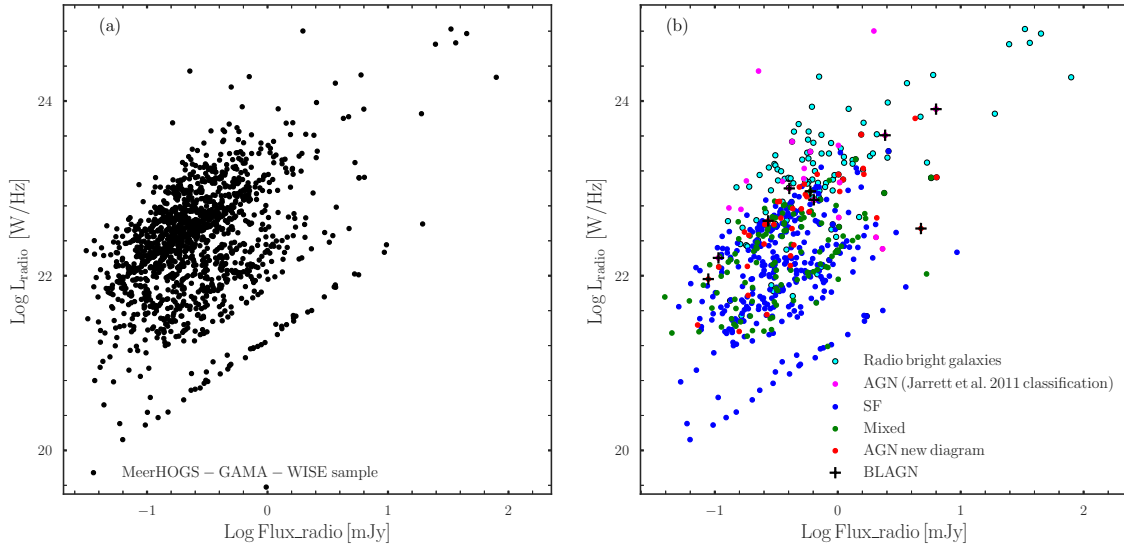


Figure 6.7: Radio flux as a function of radio luminosity for the total sample (a). The different categories of galaxies using the new classification diagram are represented in (b). The obscured AGNs as defined by Jarrett et al. (2011) and Stern et al. (2012) (the quasar mode) are also represented along with the radio bright galaxies. One can see different layers, with AGNs similar to radio bright galaxies having the highest luminosity at constant radio flux. This diagram is used as a consistency check for our radio fluxes. It also shows radio similarities between the AGNs and these radio bright galaxies, which are generally not seen at IR or optical wavelengths. More details about the radio bright galaxies will be presented in the text and the following figures.

among the brightest in the radio sharing the same luminosity space with the radio bright galaxies. The few BLs (BLAGN) from our sample also have similar properties. This figure is more about a consistency check of the radio fluxes, as it confirms that each group is found where expected.

The $\text{SFR}_{12\mu\text{m}}$ is represented versus the radio luminosity in Figure 6.8 using only the SF galaxies from our new diagram classification with $9 < \log M_{\text{stellar}} < 11 M_{\odot}$. The lower mass limit is required for the classification using our new diagram to avoid metallicity and colour degeneracies in low mass galaxies. As the presence of AGNs generally leads to overestimated stellar masses, we used the upper limit of $\log M_{\text{stellar}} < 11 M_{\odot}$ to ensure the more pristine SF sample. We included the best fit from Brown et al. (2017), Davies et al. (2017), and Murphy et al. (2011b). The data shows the expected increase in the radio luminosity with the $\text{SFR}_{12\mu\text{m}}$. The best fit is given by the relation in Equation 6.3.

$$\log \text{SFR}_{12\mu\text{m}} (M_{\odot} \text{yr}^{-1}) = (0.79 \pm 0.021) \times \log L_{1.4\text{GHz}} (\text{W Hz}^{-1}) - (16.77 \pm 0.46) \quad (6.3)$$

Our best fit is slightly steeper than the fit of Davies and much closer to that of Brown. The

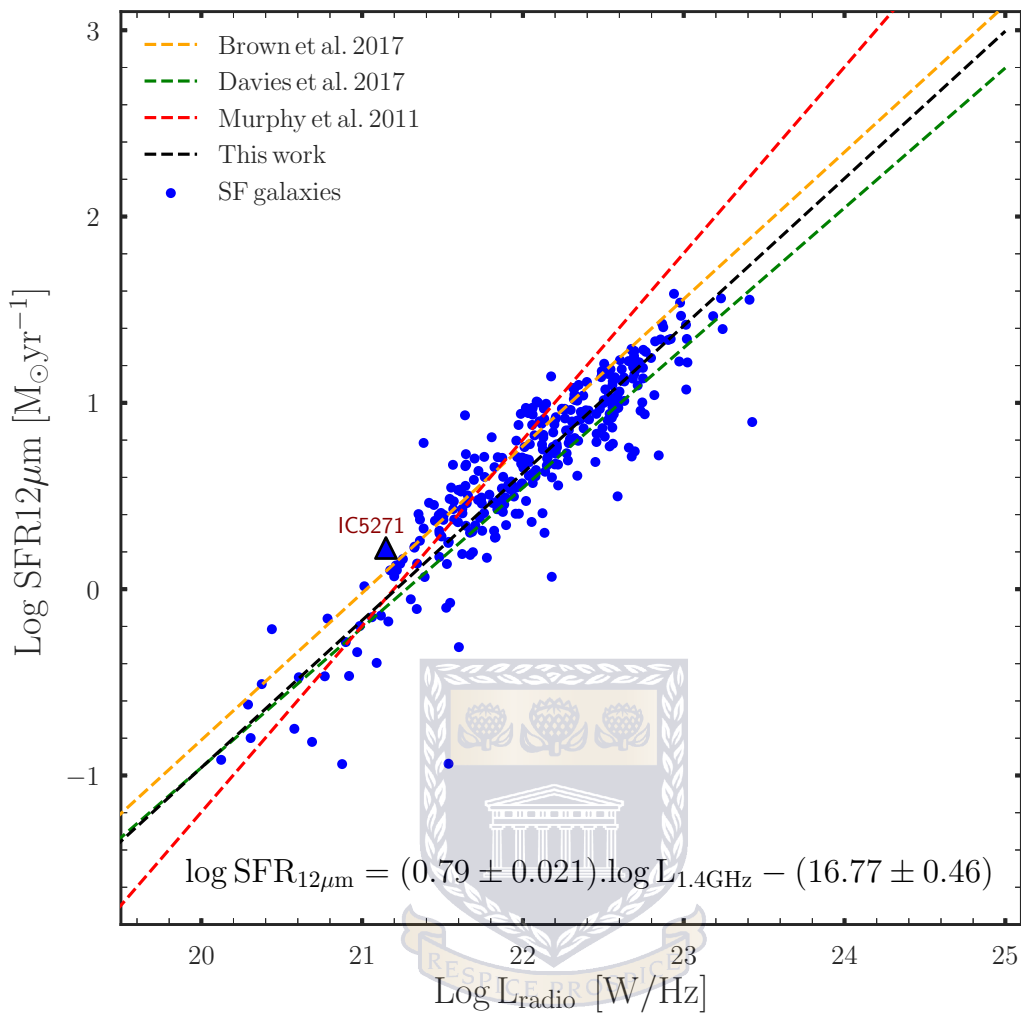


Figure 6.8: The radio luminosity as a function of $\text{SFR}_{12\mu\text{m}}$ for SF galaxies (classified using our new diagram, Yao et al. 2020) with $9 < \log M_{\text{stellar}} < 11 M_{\odot}$. The best fit from Brown et al. (2017), Davies et al. (2017) and Murphy et al. (2011b, radio) have been added. The best fit of our data is given by the equation on the figure and is slightly steeper than that of Davies, with a very similar slope to that of Brown. The radio SFR by Murphy predicts the highest radio values. We will use our best fit to derive the radio SFR presented in Figure 6.17b. The blue triangle is the low- z (0.00636), high S/N galaxy IC5271 represented as an example for comparison. It is the largest ($118'' \times 70''$) radio galaxy in our field and is also well resolved in IR. The radio and IR images are presented in Figure 6.3 (MH18) and Figure 6.22, respectively.

difference in Murphy’s much steeper relation is probably due to their data and method: their relation is derived using H α data from diverse SF regions in a single galaxy as opposed to global flux in a wider range of galaxies used in the other studies, including ours.

As many studies focused on the evolution of the q_{TIR} with redshifts (Magnelli et al. 2015; Calistro Rivera et al. 2017; Ocran et al. 2020), we investigated its variation with the radio luminosity in the local universe. Figure 6.9 shows a decreasing trend in the q_{TIR} with increasing radio luminosity. This trend, which is yet to be understood, was also observed

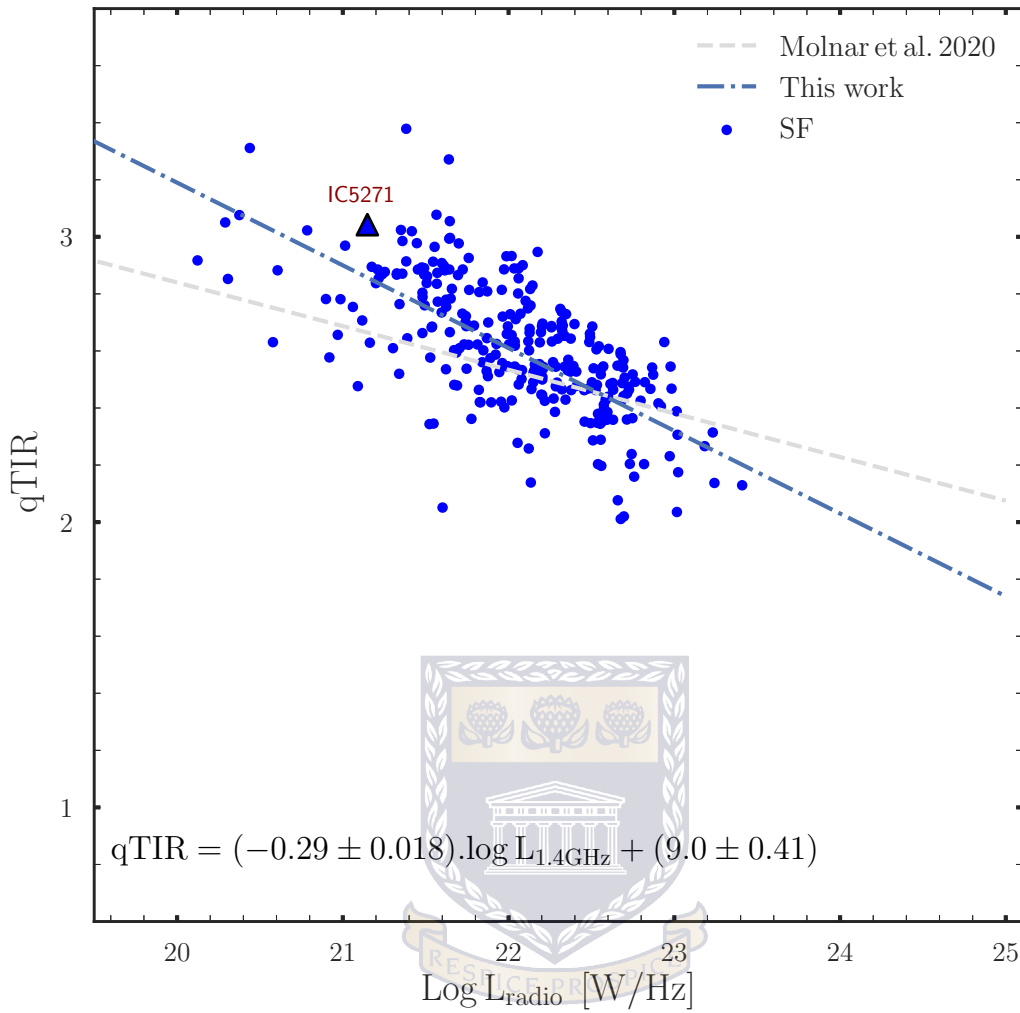


Figure 6.9: The radio luminosity as a function of q_{TIR} for SF galaxies with $9 < \log M_{\text{stellar}} < 11$. We used the IR radio luminosity relation as defined by Helou et al. (1985). In this relation, the total IR luminosity (L_{TIR}) is derived using the equation from Cluver et al. (2017). The relation derived by Molnar et al. (2020) is added for comparison. Our best fit is represented by the blue line (see the equation in the figure). Our fit is slightly steeper than that of Molnar, which is likely because *ProFound* captures more light from the galaxies. The best fit is obtained also using SF galaxies as classified by our new diagram. The blue triangle is Galaxy IC5271, which has the largest radio disk in our sample. It is an active SF galaxy with $\text{SFR}_{12\mu\text{m}} \sim 1.7 M_{\odot}\text{yr}^{-1}$.

by Molnar et al. (2020), with a less steep slope (in Figure 6.9). It seems to suggest that we are seeing excess radio power relative to the IR SF activity. The best fit is given by Equation 6.4.

$$q_{\text{TIR}} = (-0.29 \pm 0.018) \times \log L_{1.4\text{GHz}} (\text{W Hz}^{-1}) + (9 \pm 0.41); \quad (6.4)$$

this applies to low z ($z < 0.3$) galaxies.

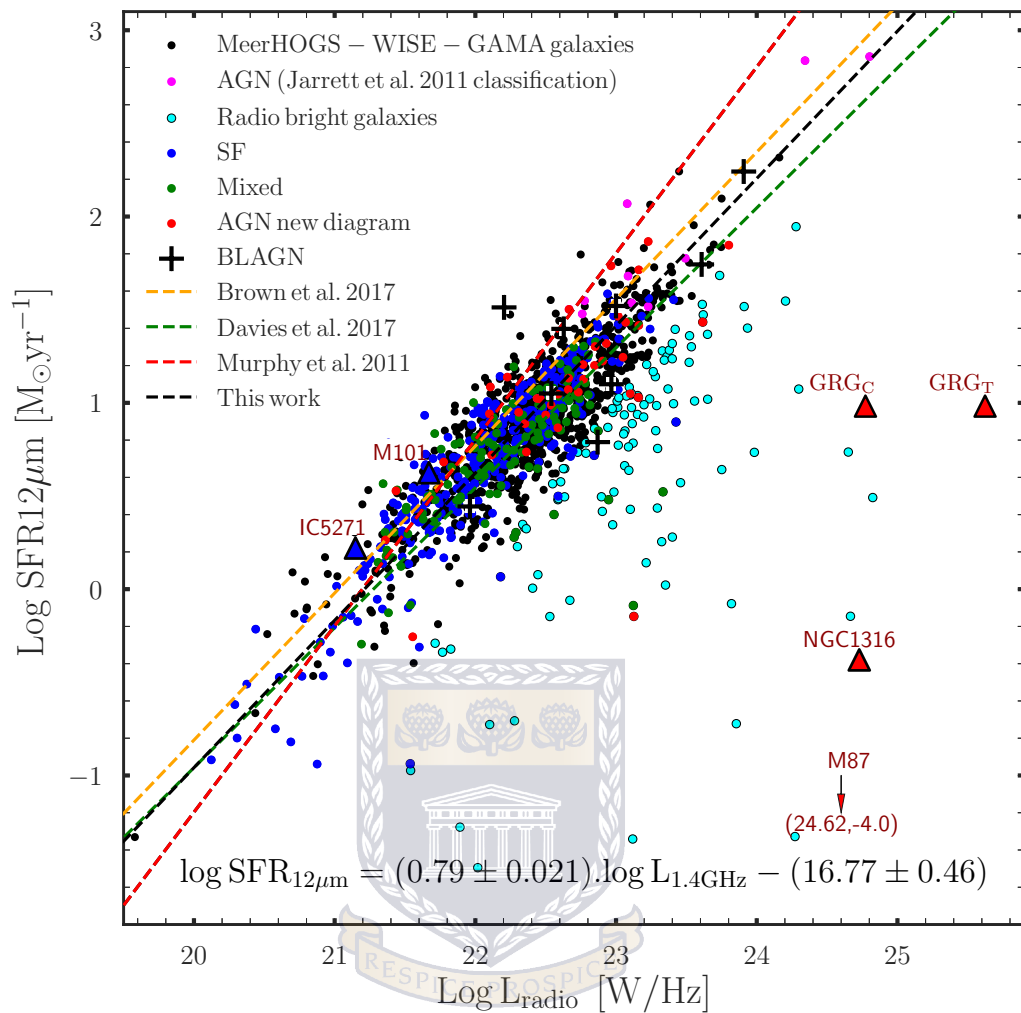


Figure 6.10: Figure 6.8 is reproduced adding the remaining group of galaxies as classified using our new diagram (see Figure 5.30). The blue, green, and red points are SFs, composites, and AGNs, respectively. The obscured AGNs identified according to Jarrett et al. (2011) are represented in magenta colour and the cyan are radio bright galaxies ($qTIR < 2$). The same colour scheme will be used throughout the document, except where clearly stated otherwise. GRG_C and GRG_T represent the central and total flux of the giant radio galaxy (GRG; see Figure 6.23) PK2250–351, respectively.

Figure 6.10 confirms the peculiarity of the galaxies classified as radio bright (cyan points). This figure is similar to Figure 6.8. Here the SFs, composites and AGNs are represented.

For comparison, we added case examples of SF galaxies and AGNs. IC5271 is a nearby active SF spiral galaxy with a $SFR_{12\mu m}$ of $1.66 M_{\odot} yr^{-1}$. It has by far the largest ($118'' \times 70''$) radio disk in our entire sample (see Figure 6.22). The second example SF galaxy (M101) is a well-known nearby spiral with an active $SFR_{12\mu m}$ of $3.9 M_{\odot} yr^{-1}$. Both follow the distribution of the SF galaxies well. M87 and NGC1316 are two well-known AGNs with massive hosts (Jarrett et al. 2019) from nearby galaxy clusters. They have radio fluxes

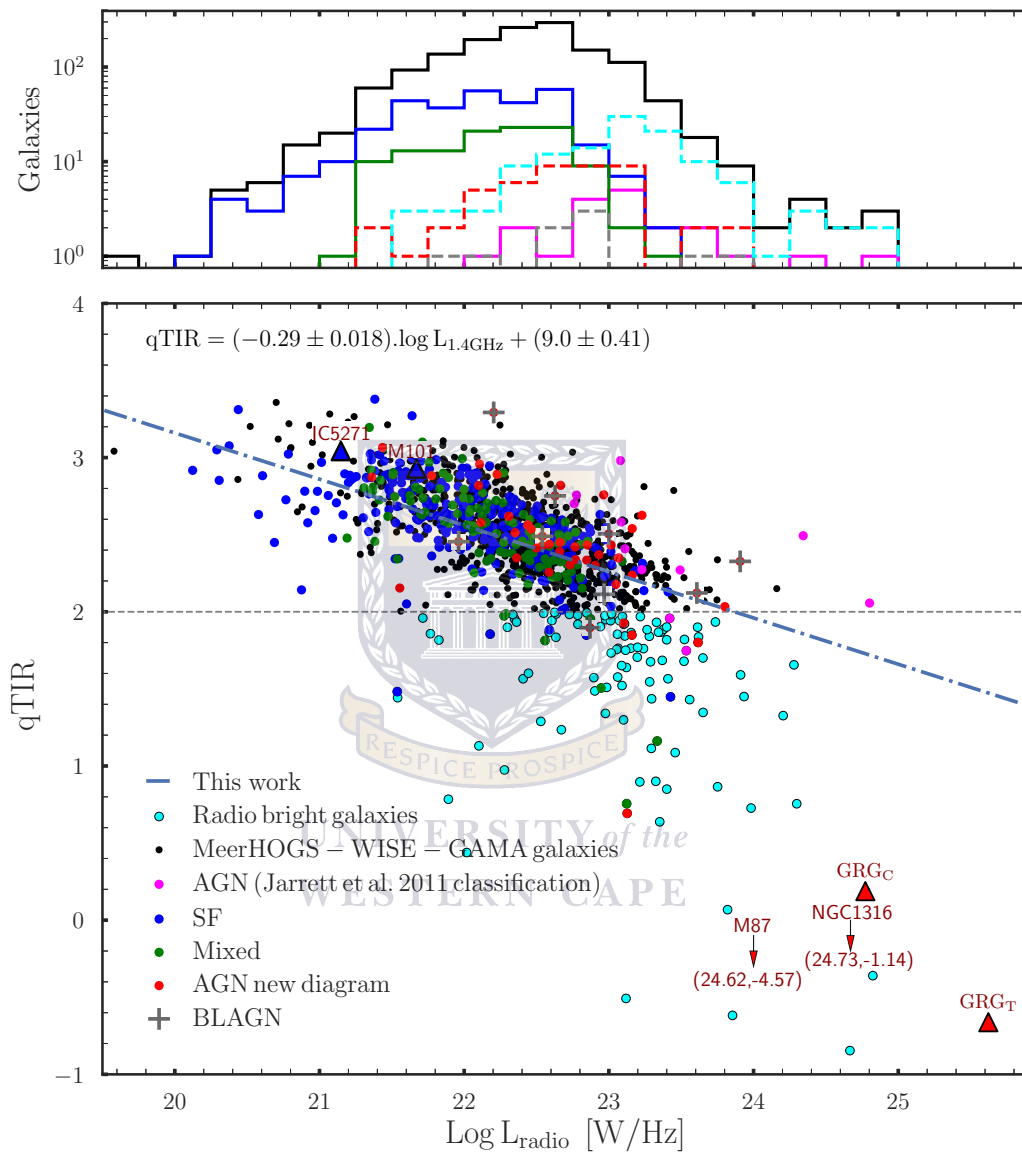


Figure 6.11: Figure 6.9 is reproduced adding the remaining group of galaxies as classified using our new diagram. The blue, green, and red points are SFs, composites, and AGNs, respectively. The obscured AGNs and QSOs are represented in magenta colour and the cyan are radio bright galaxies ($qTIR < 2$). The same colour scheme will be used throughout the document, except where clearly stated otherwise.

of 138.487 Jy and 125 Jy, respectively. These radio fluxes are extremely high, but their $\text{SFR}_{12\mu\text{m}}$ show that they are passive galaxies, which have stopped forming new stars. GRG_C and GRG_T represent the giant radio galaxy from our sample, using only the flux from the core and the total flux, respectively. The particularity of these AGNs is their high radio luminosities, which classify them as radio bright galaxies. These are classic examples of radio galaxies whose emission derives from the central SMBH engine. More photometric and physical details about these examples are presented from Figure 6.22 to Figure 6.26.

Both categories of AGNs, including the BLAGNs, seem to follow the relation. However, it is a scenario where the galaxies have similar flux both in the radio and IR such that although their $\text{SFR}_{12\mu\text{m}}$ is overestimated because of the flux contamination from the AGN, they are still aligned with the trend. The radio bright galaxies (cyan points) express another picture whereby the radio flux is much stronger than that emitted in the IR. These galaxies fall systematically on the right side of the figure. It could be interpreted as an underestimation of the $\text{SFR}_{12\mu\text{m}}$ with regard to the radio luminosity. However, as will be shown later, everything indicates that the observed radio luminosity is coming from the central AGN rather than being generated by the evolving stars in the galaxy.

Figure 6.11 adds more details to Figure 6.9b by showing the different categories of galaxies as described previously. For similar reasons evoked previously, the AGNs also follow the decreasing trend well. The effect is more pronounced with the radio bright galaxies for which the radio luminosities abruptly decrease, as also seen from simulated data by SIMBA (Thomas et al. 2020) for $L_{1.4\text{GHz}} > 10^{23} \text{ W Hz}^{-1}$.

6.3.3 Relationship between the q_{TIR} and *WISE* Colours

All the different galaxy classifications seem to have comparable q_{TIR} values, as presented in Figure 6.12. Even the AGNs selected using the conservative limit or the BLAGN from our sample have similar q_{TIR} compared to the mixed and SF group of galaxies. A few galaxies among the radio bright ones are classified by the new optical-IR diagram (see blue and red points below $q_{\text{TIR}} = 2$). These represent galaxies whose IR emission is still significant enough to be classified as either SFs or AGNs in *WISE*, but with much stronger radio emission than what is expected from the radio-IR correlation (see Eq. 6.2).

In Chapter 5 we presented the galaxies classified as AGN in the optical (BPT) and SF in the IR (*WISE*) “oAGN(mSF)” as an interesting class of galaxies to be followed up in radio. The aim is to understand why they show strong emission lines characteristic of AGN in

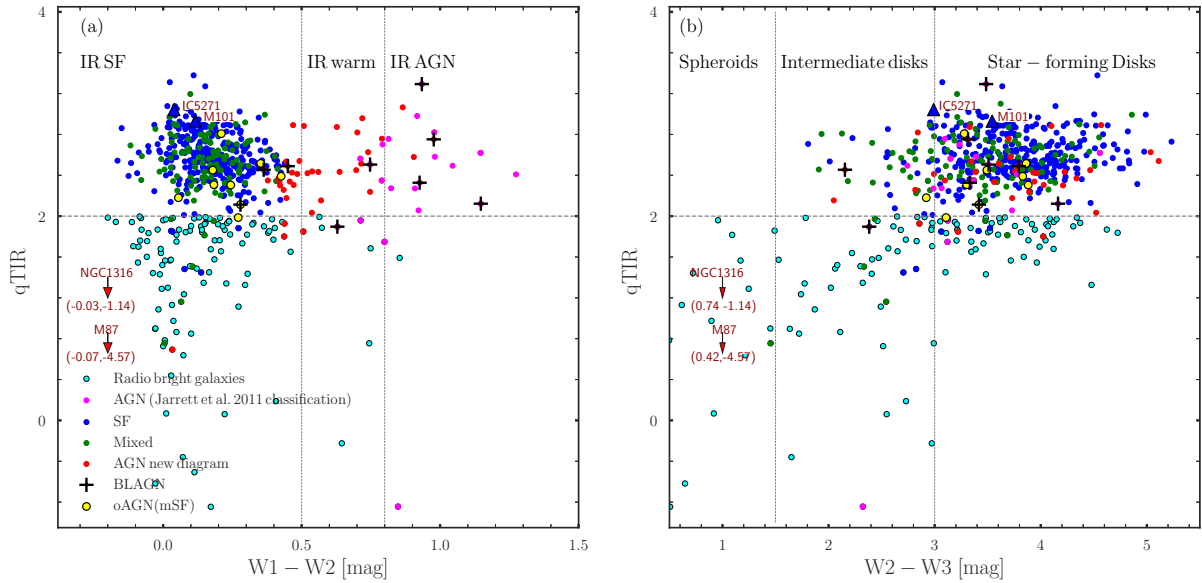


Figure 6.12: q_{TIR} versus *WISE* colours. It is similar to Figure 6.6 with the different galaxy groups represented. The q_{TIR} range for SF galaxies is from 2 to 3.4, but more typical values of 2.5 ± 0.22 , and the radio bright AGNs are found for q_{TIR} values < 2 . The yellow circles represent the galaxies classified as oAGN(mSF) in Chapter 5 (see Figure 5.9) with a radio counterpart. They show similar radio properties ($2 \leq q_{\text{TIR}} \leq 3$) to normal SF galaxies.

optical, but low values of $W1 - W2$ colours. Nine galaxies from the original IR-optical sample of oAGN(mSF) (see Table 5.2) have radio counterparts. Among which detailed measurements of the galaxies 5427366, 5155115, 5258350, and 5154519 are provided in Tables 5.3 and 5.4. The *WISE* and KiDS *r*-band images for the galaxy 5155115 can be visualised in Figure 5.22. Figure 6.12 shows these specimens (yellow) and they all have q_{TIR} values between two and three, sharing a similar IR/radio luminosity ratio with normal SF galaxies. With their additional characteristic in radio, we could think of the discordant classification between the IR and the optical of these galaxies being caused by the dominant emission from the host. We could also question the origin of the optical lines mostly the [O III] lines that can be generated by shocks rather than central AGNs (see Berney et al 2015).

In Figure 6.13 the q_{TIR} is represented vs the $W1 - W2$ colour and includes the stellar mass (in colour coding). The galaxies with high stellar masses commonly have a low $W1 - W2$ colour and as it can be seen, the radio bright ones are in this category. Some high-mass galaxies can be found in the IR AGN region (high $W1 - W2$ colour), but for this case, the M_{stellar} of the AGNs is for the most part overestimated, probably because of the additional (non-stellar) flux coming from the central accretion disk.

In Figure 6.14 the *WISE* colour-colour diagram is colour-coded by the q_{TIR} . The

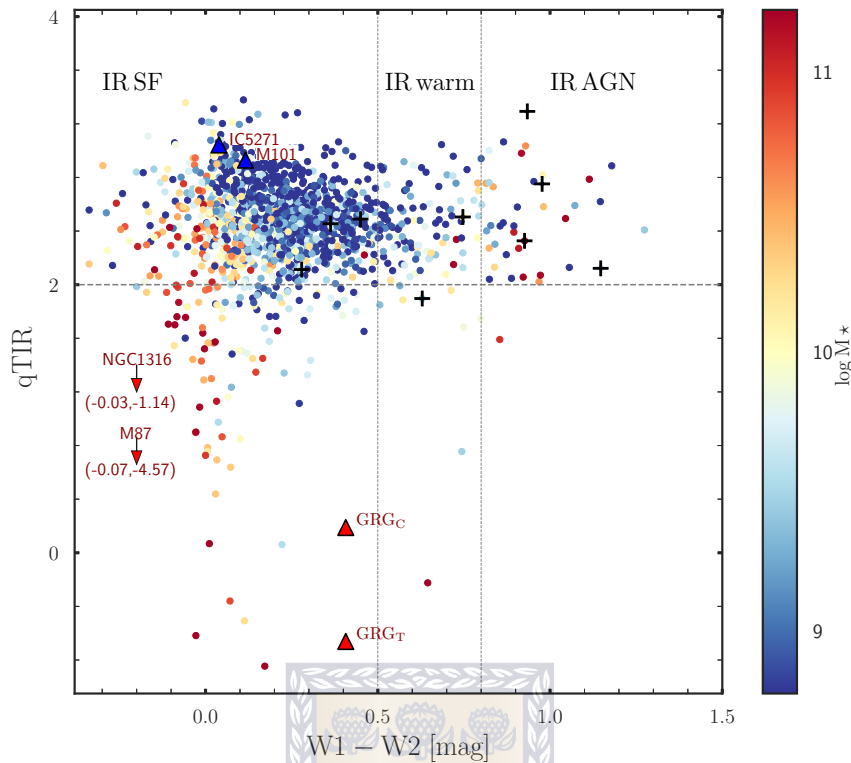


Figure 6.13: The q_{TIR} vs $W1-W2$ for the MeerHOGS-*WISE*-GAMA sample colour-coded as a function of stellar mass (M_{stellar}). The tail, seen in both $W1-W2$ and $W2-W3$ colours in the preceding figure (Figure 6.12), appears to be made of high-mass galaxies. The majority of the highest masses are seen at very low $W1-W2$ and few cases at high $W1-W2$ colour where the IR AGNs (including BL specimens) reside. The triangles are galaxies used as examples for comparison. The arrows are used for the galaxies with extreme (upper limit) values. Their names and positions are given.

spheroids region is where massive ellipticals are believed to have exhausted their reservoirs of cold gas, and are seen as inactive giant galaxies. The q_{TIR} reveals a different picture in which although the galaxies seem quiescent in IR (star-dominated colours), they are much more active in radio with a very strong radio emission. The radio emission is probably coming exclusively from the central SMBH. M87 (see Figure 6.25) is a typical example in which the first-ever image of a black hole was recently captured (Event Horizon Telescope Collaboration 2019). The GRG (MH17), classified as AGN in the literature (Seymour et al. 2020), is in the *WISE* warm zone of the colour-colour diagram (see Yao et al. 2020) and is also powered by its central engine. It can be seen as part of those radio bright AGNs for which the IR emission is strong, but the radio luminosity is very high (see the GRG's luminosity in Figure 6.10), hence the low q_{TIR} such that both the *WISE* colour-colour diagram and the q_{TIR} classify them as AGNs. Details about the GRG are

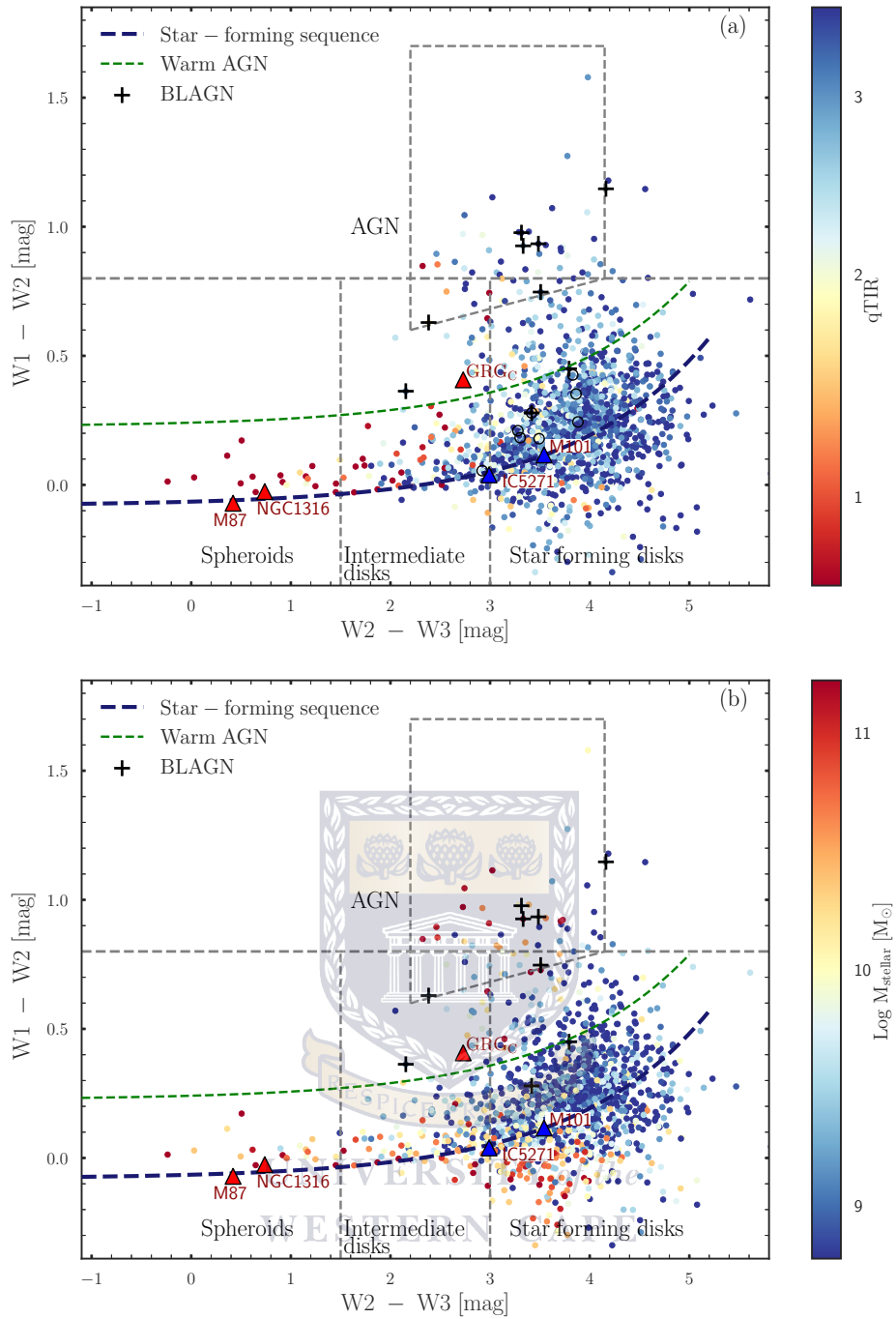


Figure 6.14: The *WISE* colour-colour diagram colour-coded by the q_{TIR} and the stellar mass in (a) and (b), respectively. We can see the galaxies with the lowest q_{TIR} either in the spheroids or the intermediate disk region. It is quite interesting to see how the galaxies in this area of the *WISE* colour-colour diagram appear to be very active in radio. Since star formation is mostly associated with dust, not having a dust signature (very low SFR) in *WISE* means that the radio flux is probably coming exclusively from the central AGN. This comes as a complementary finding in our quest to identify all forms of AGN through multiwavelength study. Note that the host galaxy (M087) from which the first-ever picture of a black hole was taken in 2019 is part of this group of AGNs found in the spheroid zone. GRG_C represents the core (45 mJy) of the giant radio galaxy (PKS 2250–351) from our sample (MH17). The blue and green dashed sequences' relations were first introduced in Fig 5.8. The galaxies between the green dashed line and the AGN box are classified as *WISE* warm galaxies and are believed to be AGNs (Yao et al. 2020). However, their q_{TIR} looks similar to that of normal SF galaxies.

available in Table 6.1 and Figure 6.23.

The massive and radio bright (loud, or luminous) galaxies located at low W2-W3 (<

2 mag) with very low or imperceptible star formation activity ($SFR \ll 1$) in *WISE* are a category of AGNs that can only be seen using a combination of radio and IR emissions. This comes as an interesting result in a grander picture of trying to identify and study the properties of AGN and SF galaxies using multiwavelength, which is the main aim of this thesis. The galaxies in the *WISE* warm zone like the QSOs and obscured AGNs, show the same q_{TIR} range ($2 < q_{TIR} < 3.4$) as the normal SF galaxies. This shows that *WISE* is more efficient in picking up the thermal change in the galaxy characteristic of AGN activity in comparison to q_{TIR} which relies on relative radio excess. These classification methods therefore appear to be complementary.

The q_{TIR} vs the stellar mass is shown in Figure 6.15a and Figure 6.15b for the total sample and the different groups, respectively. There is no visible trend in the data distribution for $q_{TIR} > 2$. The SFs and AGNs seem to have similar distributions. Once more,

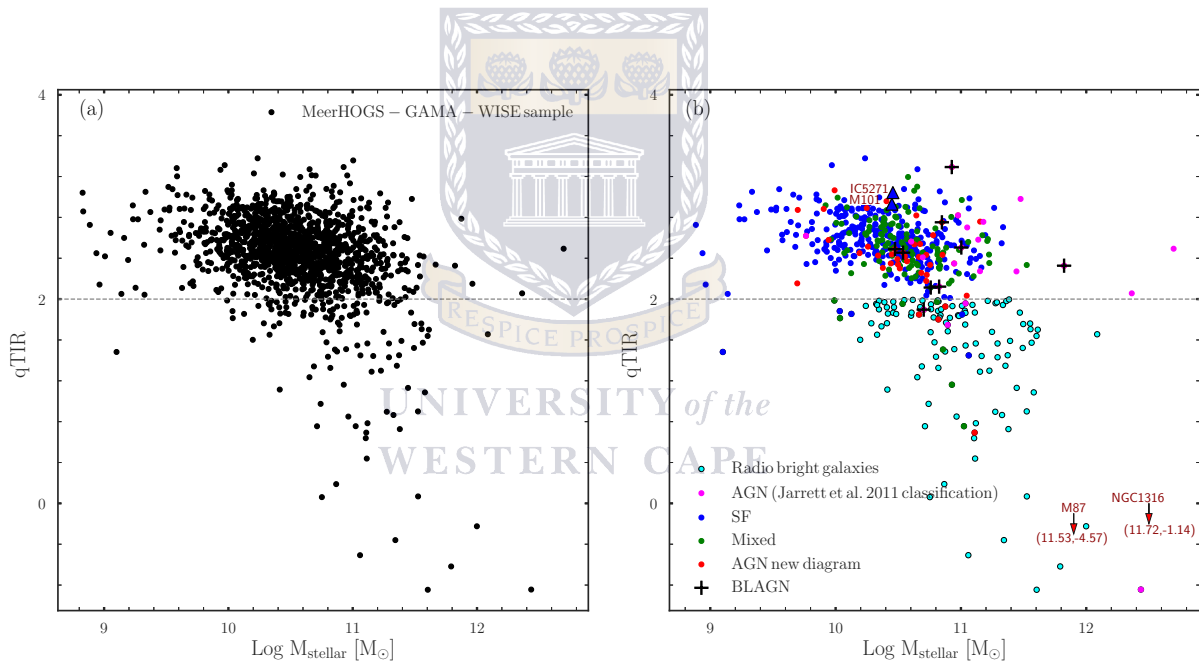


Figure 6.15: Variation of the q_{TIR} as a function of stellar mass. In (a) the total sample is represented and in (b) their subdivisions per group (same classification as in the preceding diagrams). There is an abrupt decrease in the q_{TIR} with stellar mass particularly for $\log M_{\text{stellar}} > 11 M_{\odot}$. This seems to show dominance of the radio emission over IR as galaxies grow larger, eventually depleting their gas reservoirs.

the radio brights show a steep decrease with a large scatter for stellar mass $\log M_{\text{stellar}} > 10.5 M_{\odot}$. The massive cluster central galaxies M87 and NGC1316 among the example cases can be seen further down in this decreasing trend. They both have $\log M_{\text{stellar}} [M_{\odot}] > 11.5$,

which is consistent with the trend that low q_{TIR} values being found in massive SF-quenched galaxies.

6.3.4 HERGs and LERGs

We plotted the HERG and LERG in the *WISE* colour-colour diagram in Figure 6.16 colour-coded by the q_{TIR} . In the literature, two different classes of AGNs exist, based on the accretion mode. One can be qualified as the “traditional” AGN with an accretion disk and

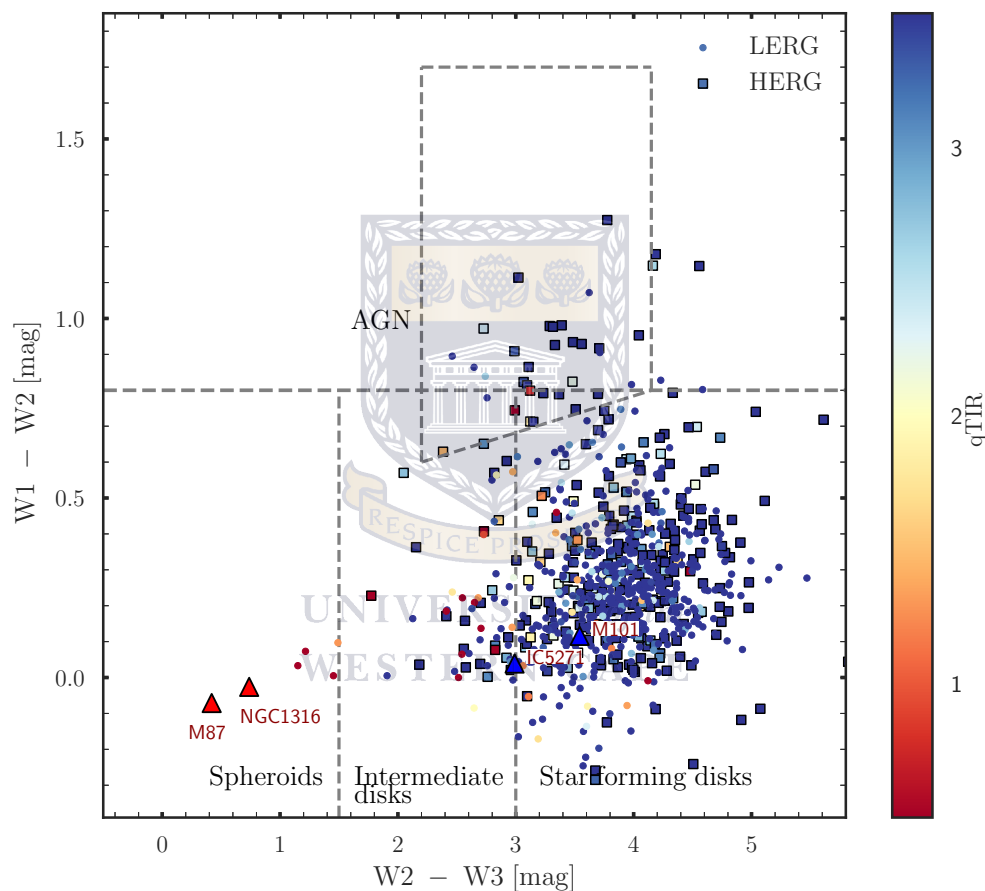


Figure 6.16: The *WISE* colour-colour diagram colour-coded as a function of q_{TIR} . There is no clear dichotomy between HERGs and LERGs, but there is an excess of LERGs among the radio bright galaxies located at low $W2 - W3$ colour. This gives a hint about the accretion mode of this category of AGNs (radio bright AGNs). Most AGNs from the Jarrett et al. (2011) or Stern et al. (2012) classification seem to be dominated by HERGs, on the other hand.

a dusty torus. The galaxies in this class are known as HERG and radiate efficiently across the whole electromagnetic spectrum. On the other hand, LERGs, lacking these structures (disk and dusty torus) emit most of their energy as powerful radio jets (Merloni & Heinz 2007; Hardcastle et al. 2009). Several methods exist to separate LERGs from HERGs

(Buttiglione et al. 2010; Fernandes et al. 2010). We adopted the most basic method, which classifies galaxies with [O III] line S/N > 3; and [O III] equivalent width < 5 Å as LERG and [O III] equivalent width > 5 Å as HERG. Figure 6.16 does not show a clear dichotomy between the two categories. We can nevertheless see that the few radio bright galaxies in the spheroids zone are LERGs. This partly explains why using IR and/or optical could not classify these galaxies as AGNs. They probably lack a disk from which most optical emissions from AGNs come, and in the absence of a dusty torus, almost no emission in the IR from the AGN will be possible (evolved stars with dusty shells can of course create IR signature in early-type galaxies). The radio is needed to reveal the “hot” accretion mode that is not visible in other wavebands (see review by Fabian 2012). The spheroid region in the *WISE* colour-colour diagram could henceforth be referred to as radio powerful AGNs zone or dust-free AGNs (as opposed to obscured AGNs). Alternatively, some of these galaxies could still have a torus and disk or even gas and dust due to minor merger, NGC1316 is a good example (Duah Asabere et al. 2016), but the massive host dominates these emissions (from the torus and disk) such that it is not detected in optical and IR. On the contrary, the emission from the central AGN would be very strong and visible at radio wavelengths.

6.3.5 Relation between $\text{SFR}_{\text{radio}}$ and Stellar Mass

We recall that the emission from SF-excited ISM can be detected in IR and hence used as a proxy for SFR (Cluver et al. 2017). The radio emission is a more complex process, driven by energised cosmic rays from Supernovae, which relies heavily on the tight and linear radio-IR correlation (Condon et al. 1991; Price & Duric 1992; Yun et al. 2001) in order to be used for the SFR estimation. As the q_{TIR} is the ratio between the IR and the radio emissions, a linear radio-IR correlation would have led to a constant value of q_{TIR} . However, Figure 6.9 shows a constant decrease in the q_{TIR} with increasing radio luminosity for SF galaxies. This means that the correlation between the radio and IR emissions is not as linear as we would expect. In this work we first correct for the non-linearity between the radio and IR flux emissions using Equation 6.2 and Equation 6.4. Next, we find the corrected relation between the L_{TIR} and the $L_{1.4\text{GHz}}$ in (a). The L_{TIR} in Equation 6.5 (see Equation 3 in Cluver et al. 2017) is replaced by $L_{1.4\text{GHz}}$ and the final equation (Equation

6.6) represents the corrected $\text{SFR}_{\text{radio}}$. This equation can be used as an

$$\text{SFR}(\text{M}_{\odot}\text{yr}^{-1}) = 2.8 \times 10^{-44} L_{\text{TIR}} (\text{erg s}^{-1}) \quad (6.5)$$

Combining Equation 6.4 and Equation 6.2 leads to the following relation with

$$q_{\text{TIR}} = -0.29 \times \log L_{1.4\text{GHz}} + 9 = \log \left(\frac{L_{\text{TIR}}}{3.75 \times 10^{12} \text{ Hz}} \right) - \log \left(\frac{L_{1.4\text{GHz}}}{\text{W Hz}} \right)$$

$$\log \left(\frac{L_{\text{TIR}}}{3.75 \times 10^{12} \text{ Hz}} \right) = (1 - 0.29) \times \log L_{1.4\text{GHz}} + 9$$

$$\log L_{\text{TIR}} = 0.71 \times \log L_{1.4\text{GHz}} (\text{W Hz}^{-1}) + 9 + \log (3.75 \times 10^{12})$$

$$\log L_{\text{TIR}} (\text{W}) = 0.71 \times \log L_{1.4\text{GHz}} (\text{W Hz}^{-1}) + 21.574 \quad (\text{a})$$

using Equation 6.5 \Rightarrow

$$\text{SFR}(\text{M}_{\odot}\text{yr}^{-1}) = 2.8 \times 10^{-37} L_{\text{TIR}} (\text{W}) \quad (\text{b})$$

(a) and (b) \Rightarrow

$$\log \text{SFR}_{\text{radio}}(\text{M}_{\odot}\text{yr}^{-1}) = 0.71 \times \log L_{1.4\text{GHz}} (\text{W Hz}^{-1}) + 21.574 - 36.553$$

$$\log \text{SFR}_{\text{radio}}(\text{M}_{\odot}\text{yr}^{-1}) = 0.71 \times \log L_{1.4\text{GHz}} (\text{W Hz}^{-1}) - 14.98 \quad (6.6)$$

alternative to determine the SFR of SF galaxies in the local universe ($z < 0.3$ in this study), mostly for future large radio surveys.

Figure 6.17 shows the $\text{SFR}_{12\mu\text{m}}$ and the $\text{SFR}_{\text{radio}}$ versus the stellar mass (using Equation 6.6), respectively in (a) and (b). The best fit in both cases (see Equation 6.7 and Equation 6.8)

$$\log \text{SFR}_{12\mu\text{m}} (\text{M}_{\odot}\text{yr}^{-1}) = (1.12 \pm 0.06) \times \log M_{\text{stellar}} (\text{M}_{\odot}) - (10.97 \pm 0.61) \quad (6.7)$$

$$\log \text{SFR}_{\text{radio}} (\text{M}_{\odot}\text{yr}^{-1}) = (0.93 \pm 0.05) \times \log M_{\text{stellar}} (\text{M}_{\odot}) - (8.95 \pm 0.54) \quad (6.8)$$

are represented and we can see a similar distribution with a slightly steeper slope for the IR. It must be noted that without taking into account the decrease of the q_{TIR} with $L_{1.4\text{GHz}}$, the $\text{SFR}_{\text{radio}}$ cases are systematically much higher (overestimated) than their counterparts in IR.

Both star formation rates, the IR and the newly calibrated $\text{SFR}_{\text{radio}}$ are used to represent all the categories of galaxy. For clarity, Figure 6.18 shows the SFs and the mixed

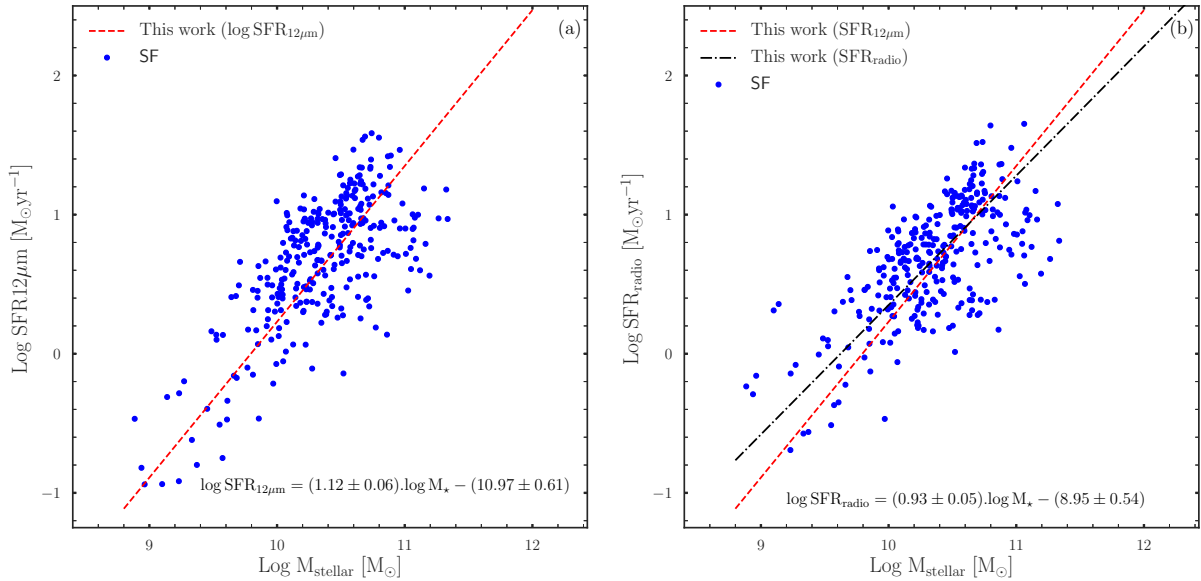


Figure 6.17: $\text{SFR}_{12\mu\text{m}}$ vs stellar mass (a) and $\text{SFR}_{\text{radio}}$ vs stellar mass (b). The $\text{SFR}_{\text{radio}}$ is derived based on the IR SFR. The best fits are represented by the dashed red and dash-dotted black lines for $\text{SFR}_{12\mu\text{m}}$ and $\text{SFR}_{\text{radio}}$ respectively. Both lines are represented in (b) for comparison. The expression of the $\text{SFR}_{\text{radio}}$ (black dash-dotted line) is given by Equation 6.6. This brings the new $\text{SFR}_{\text{radio}}$ close to that derived using the IR (W3 measurements). The $\text{SFR}_{\text{radio}}$ is therefore a hybrid; it includes the q_{TIR} for SF galaxies.

populations, while the AGNs and radio bright galaxies are presented in Figure 6.19. The mixed show no difference from the SFs distribution. They also follow the galaxy main sequence ($\log \text{SFR}$ vs $\log M_{\text{stellar}}$) well. As it would have been expected at this stage of our analysis, the galaxies standing out from the main sequence (Fig 6.19a) are the radio luminous galaxies. It explains that although these galaxies are massive and luminous in radio, they have stopped forming new stars. On the other hand, using the corrected $\text{SFR}_{\text{radio}}$ will lead to a higher SFR estimate, which is in fact an overestimation of the radio flux generated by star formation. We should recall that the correction applies only to the SF galaxies. It happens to work for the mixed (see Figure 6.11). This is not the case for the radio luminous galaxies with a much steeper decrease of the q_{TIR} with $L_{1.4\text{GHz}}$ as seen in the same figure (Figure 6.11).

With more radio data coming in from new and powerful surveys such as the MeerKAT, EMU, MIGHTEE all the way to the SKA, combined with IR data will be of great importance. It will be very challenging to calibrate the $\text{SFR}_{\text{radio}}$ for these galaxies that are very luminous in radio but have almost no activity in IR. The most important requirement will be our ability to identify them. The combination of radio and IR data seems to work quite well to this

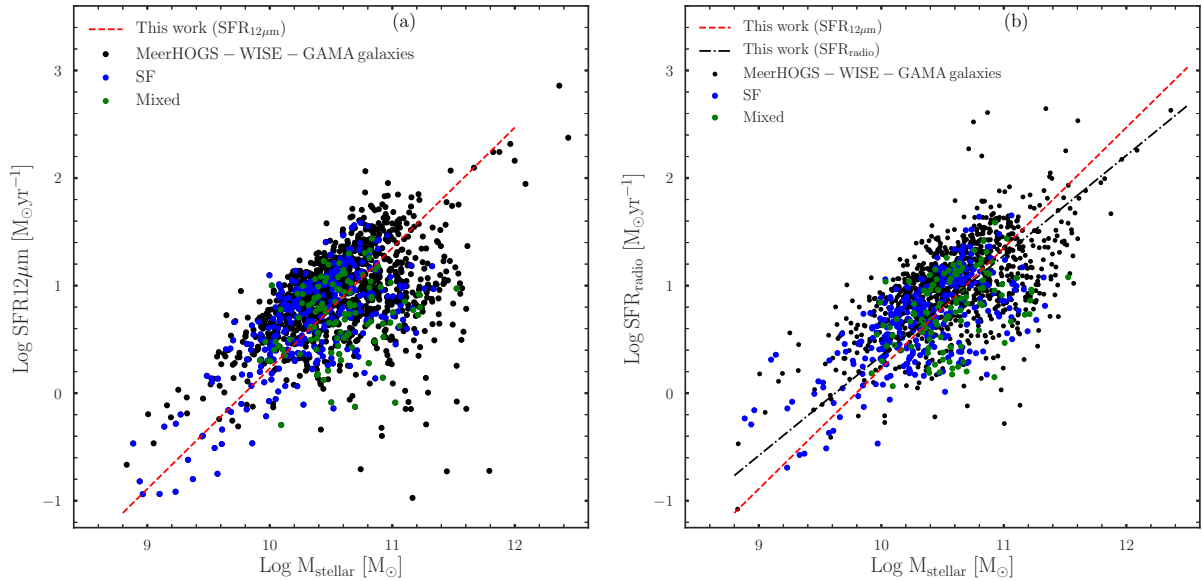


Figure 6.18: $SFR_{12\mu m}$ vs stellar mass (a) and SFR_{radio} vs stellar mass (b) similar to Figure 6.17. The total sample is shown in black. The non-classified galaxies (the visible black points in the background) did not meet the requirement to be classified using the new diagram ($[N II]$ and $H\alpha$ in absorption, lines with $S/N > 3$... see Section 5.4 for more details about the new classification diagram). The SF and composite galaxies are also presented. Both samples have the same distributions.

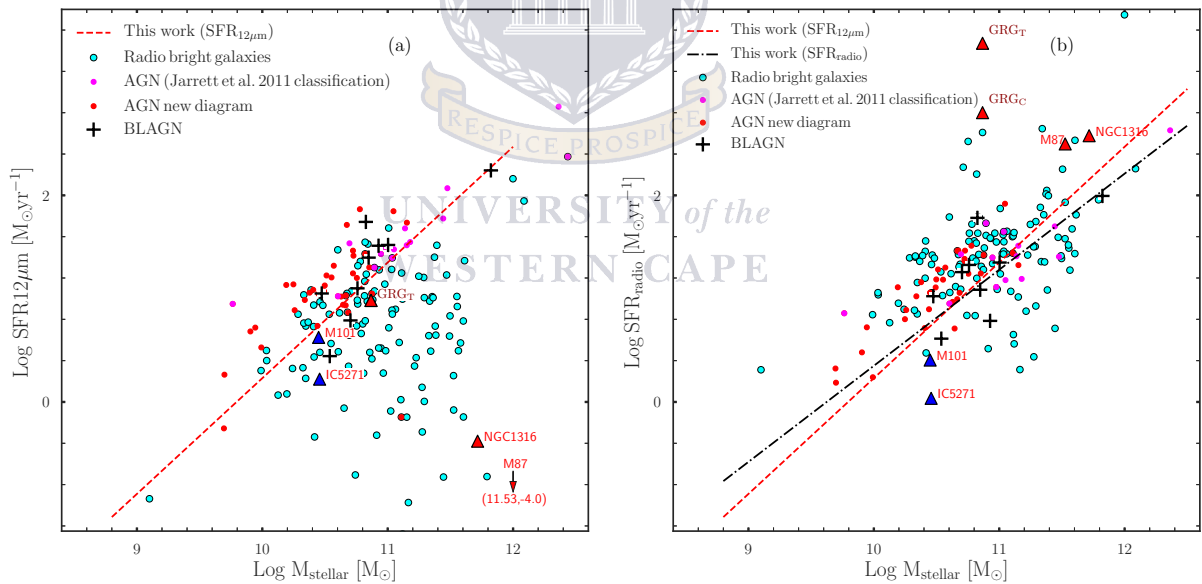


Figure 6.19: $SFR_{12\mu m}$ vs stellar mass (a) and SFR_{radio} vs stellar mass (b) similar to Figure 6.17. Here only the galaxies with AGN activity are represented. One can see the radio bright galaxies (cyan) below the main sequence in (a), while their SFRs are estimated to be high in radio (b). The radio cannot be reliably used to estimate the SFR of these galaxies, since the flux observed is coming mostly from the central AGN. All the galaxies selected as examples are represented (SFs and AGNs).

effect. Figure 6.20 shows that galaxies with the lowest q_{TIR} tend to be much further from the main sequence (Figure 6.20a). They have the most overestimated SFR using the radio

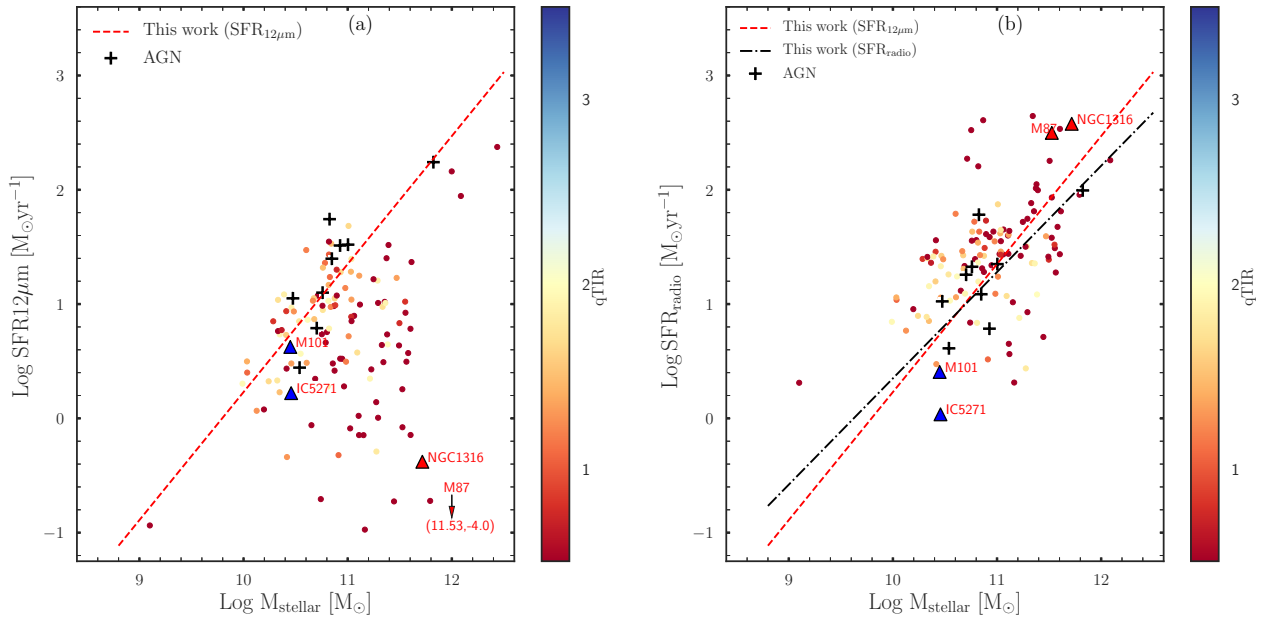


Figure 6.20: $\text{SFR}_{12\mu\text{m}}$ vs stellar mass (a) and $\text{SFR}_{\text{radio}}$ vs stellar mass (b). Here only the radio bright galaxies are represented and colour-coded as a function of q_{TIR} . The galaxies with the lowest q_{TIR} deviate more from the stellar mass SFR relation. This is not very surprising as it was shown earlier that the AGNs with the lowest q_{TIR} are massive galaxies with very low $\text{SFR}_{12\mu\text{m}}$ (see Figures 6.13 and 6.14). We also represented all the galaxies selected as examples (SFs and AGNs). *We emphasise that the SFR and M_{stellar} of an AGN derived using IR (or radio) luminosity are not reliable because of the flux contamination by the central AGN. These AGNs are presented in the two figures (Figure 6.19 and Figure 6.20) to show where they are likely to be found in case they are not properly removed from the SF galaxy samples*

calibration in Figure 6.20b (follow the positions of NGC1316 and M87 from one Figure to the other). Indeed since the radio bright galaxies are AGNs, their emissions come mostly from the central AGN and are not related to star formation activity as it can be seen in Figure 6.20a. However, deriving the SFR using the radio flux, in this case, will be a large overestimation. We conclude that the SFR of these radio bright galaxies can not be directly derived from the radio flux without a reliable extraction of the AGN's component.

6.4 Discussion

The ASKAP (Johnston et al. 2008) and the MeerKAT are two precursors of the SKA. During the commissioning phase of the ASKAP (McConnell et al. 2016), 12 of the antennas were used to observe the GAMA field G23 at both 936MHz and 1320 MHz (see Leahy et al. 2019) with synthesised beams of $32.''7 \times 17.''8$ and $15.''8 \times 12.''0$, respectively. Their observation covered a total area of 35 deg^2 in G23 for 10 hrs versus $\sim 10 \text{ deg}^2$ for 16 hrs with

MeerKAT at 1.4 GHz. The two observations have the best radio continuum data available to date in the field. Using the 64 antennas from MeerKAT (1.4 GHz) we found about 18 000 galaxies in a total area of $\sim 10 \text{ deg}^2$. This represents a source density of ~ 1800 galaxies/deg 2 .

We carried out the determination of the q_{TIR} for the SF galaxies at low z , which yielded

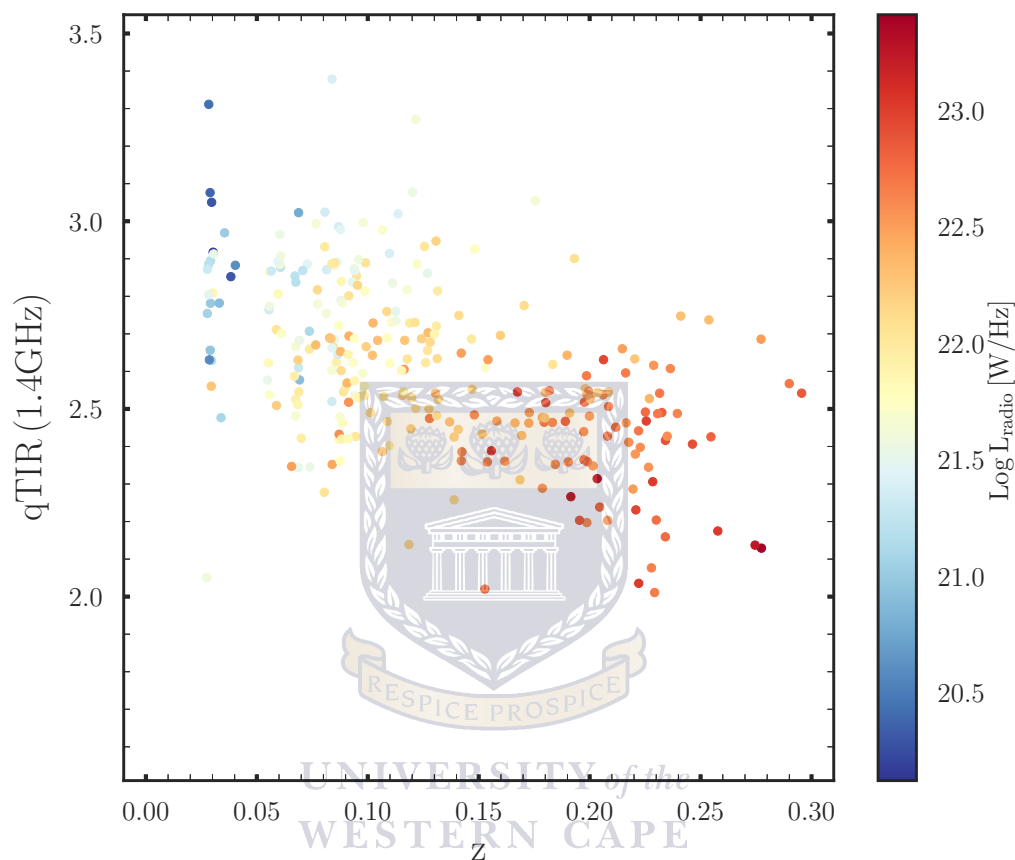


Figure 6.21: Evolution of the q_{TIR} with redshift colour-coded as a function of radio luminosity. The figure shows that the decrease of the q_{TIR} with the radio luminosity is related to its redshift evolution. We can see higher luminosities for galaxies located at high redshifts.

a range from 2 to 3.4 with an average value of 2.5 (rms = 2.54), similar to 2.64 ± 0.02 found by Bell (2003). The range of q_{TIR} from 2.10 to 3.11 in Bressan et al. (2002) using 26 compact ULIRGs is also in good agreement with our finding. The galaxies classified as AGNs in our sample are no different from the SF galaxies in terms of the q_{TIR} values. The AGN in these galaxies is definitely affecting the estimation of both luminosities (radio and IR) such that the q_{TIR} is still deceptively consistent with that of SF galaxies. AGNs will normally be found at $q_{\text{TIR}} < 2$ (Baan & Klockner 2006) when the galaxy is no longer forming stars.

Several studies in the literature (Magnelli et al. 2015; Delhaize et al. 2017; Calistro

Rivera et al. 2017; Ocran et al. 2020) have shown a variation of the q_{TIR} with redshift. We see a decrease of the q_{TIR} with the radio luminosity similar to the result found in Molnar et al. (2020). Although our study does not focus on the evolution of the FIR/radio luminosity with redshift, we placed it in context in Figure 6.21. The figure confirms that the decrease seen is related to the redshift. Indeed, as expected, the radio luminosities increase with redshift.

In our recent study, which combined carefully measured *WISE* photometry and optical data (Yao et al. 2020), we found some galaxies with optical lines characteristic of AGNs, but with very low W1-W2 mag values. These have been classified as “optical AGNs (*WISE* SF)” and are seen as interesting galaxies to be followed up in radio. Nine of these galaxies (GAMA ID: 5154519, 5155115, 5222053, 5234844, 5237886, 5240322, 5240366, 5258350, and 5427366) have radio counterparts in MeerHOGS. They do not show any excess in radio and have q_{TIR} values generally between 2 and 2.8. The host probably dominates the emission (see 5155115 in Figure 5.22) in which case both the radio and the IR luminosities are similarly affected. As Yao et al. 2020 pointed out in their study, maybe X-ray data will be able to provide more understanding about the nature of this class of galaxies.

On the other hand, radio excesses were seen in *WISE* SF galaxies, mainly among the spheroids and intermediate disk galaxies. The IR–X-ray study by Ting-Chi Huang et al. (2017) showed that building SEDs with data collected at several different frequency bands (combination of *WISE*, *spitzer* and *AKARI* that give a continuous IR coverage from 2 to 24 μm) helps reveal an important fraction of hidden AGNs in the *WISE* SF galaxy sample. Indeed, the four *WISE* bands are robust enough to identify AGNs, but are limited in cases where the power of the AGN is submerged by the star formation activity from the host. Another issue in the same regard is when there is not enough dusty material around the AGN to be clearly detected and delineated in the IR. These cases are frequent among AGNs with a “hot” accretion mode (see review by Fabian 2012) known as LERG, which emit almost exclusively in the form of powerful radio jets. They are seen in IR-radio analysis as galaxies having $q_{\text{TIR}} < 2$ and low $\text{SFR}_{12\mu\text{m}}$.

6.5 Conclusion

We processed the radio continuum data obtained with MeerKAT (64 dishes) at 1.4 GHz for a total area of $\sim 10 \text{ deg}^2$ in the southern region of GAMA (G23), known as the MeerHOGS

survey. Although the observation time was only 16.5 hours, we obtained very good image quality down to $20 \mu\text{Jy}$ because of the exceptional sensitivity of MeerKAT. We found several notable multicomponent objects presented in Figure 6.3. The radio sources were extracted and position cross-matched to *WISE* galaxies with GAMA counterparts. This IR-optical-radio catalogue was used as a follow-up to the preceding work in Chapter 5. We studied the IR/radio luminosity ratio. Our main findings are presented as follows:

- We found a tight correlation between the $\text{SFR}_{12\mu\text{m}}$ and the $L_{1.4\text{GHz}}$ for SF galaxies given by: $\log \text{SFR}_{12\mu\text{m}} = (0.79 \pm 0.021) \cdot \log L_{1.4\text{GHz}} - (16.77 \pm 0.46)$.
- The q_{TIR} decreases with $L_{1.4\text{GHz}}$ for the SF galaxies and its values range from 2 to 3.4 with an average of 2.5 ± 0.22 . The radio luminosity increases at a higher rate in comparison to the IR counterpart. It results in very high values of $\text{SFR}_{\text{radio}}$. This shows a need for radio luminosity calibration before using it to estimate the SFR. We therefore calibrated the $\text{SFR}_{\text{radio}}$ using the $\text{SFR}_{12\mu\text{m}}$ to account for the trend seen in Figure 6.9.
- The galaxies identified as spheroids in the *WISE* colour-colour diagram generally have low SFR and q_{TIR} values < 2 . These galaxies, considered to be inactive in IR are very powerful AGNs that probably emit most of their power at radio wavelengths.

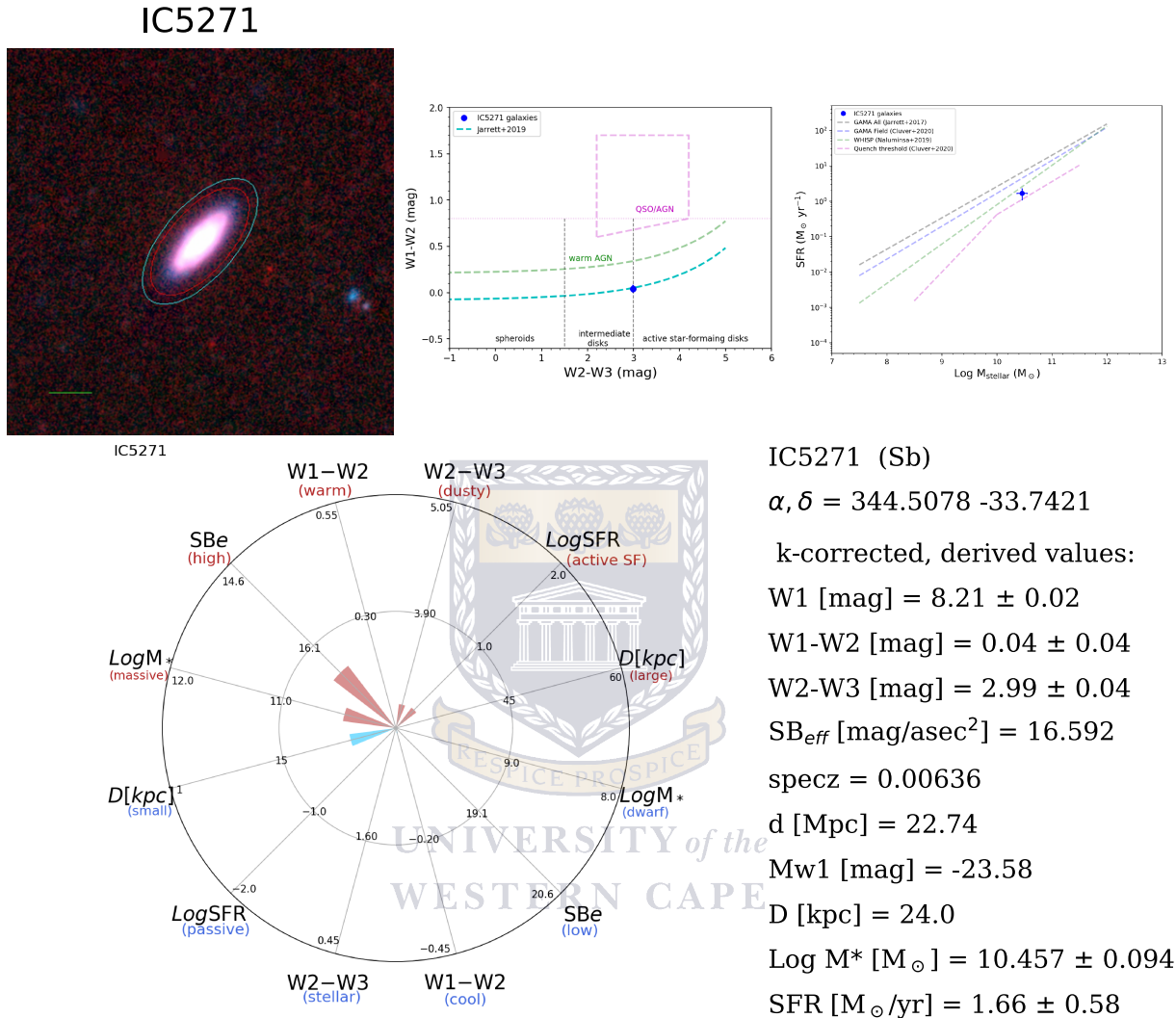


Figure 6.22: Physical properties of the galaxies selected as well-known cases. In the upper panel, from left to right, are presented Galaxy IC5271 (which is a notable member of the *WISE*-GAMA sample presented in this work), the *WISE* colour-colour diagram, and the SFR vs $\log M_{\text{stellar}}$ in the last diagram. The central diagram is described in Figure 9 of Yao et al. (2020). The SFR vs $\log M_{\text{stellar}}$ relation from Jarrett et al. (2017), Naluminisa et al. (2019), and Cluver et al. (2020) are presented. The lower panel shows a pinwheel diagram, which displays the physical properties of the galaxies (see Jarrett et al. 2019 for more details about the diagram). The values of the different parameters are also presented on the right. IC5271 (MH18) is classified as SF in *WISE* with a radio flux of 0.0227 Jy.

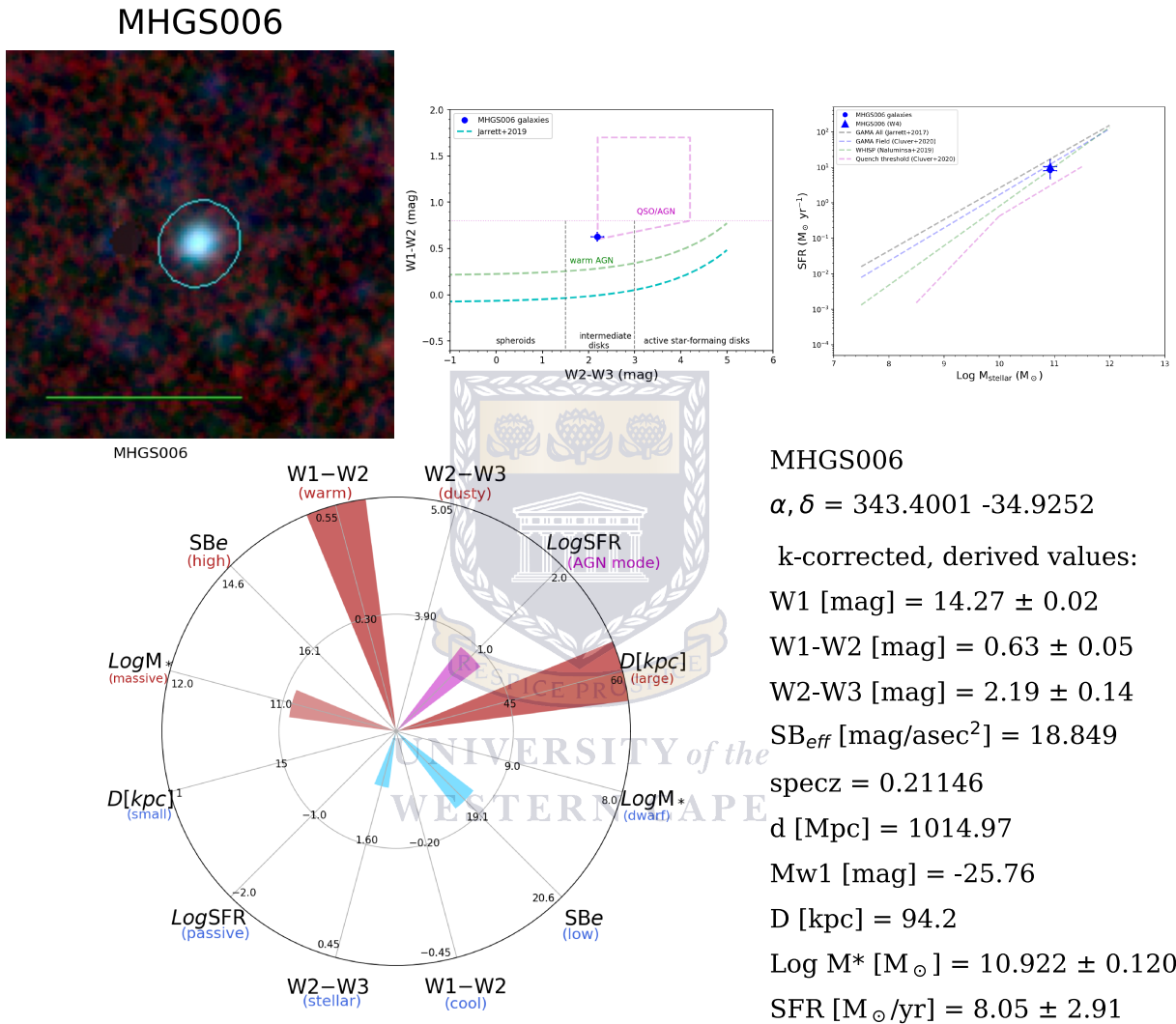


Figure 6.23: MHGS006 (radio image presented in Figure 6.3, MH17) is a giant radio galaxy (PKS 2250–351 in Abell 3936, Seymour et al. 2020) classified as SF in *WISE* with a radio flux of 0.318 Jy.

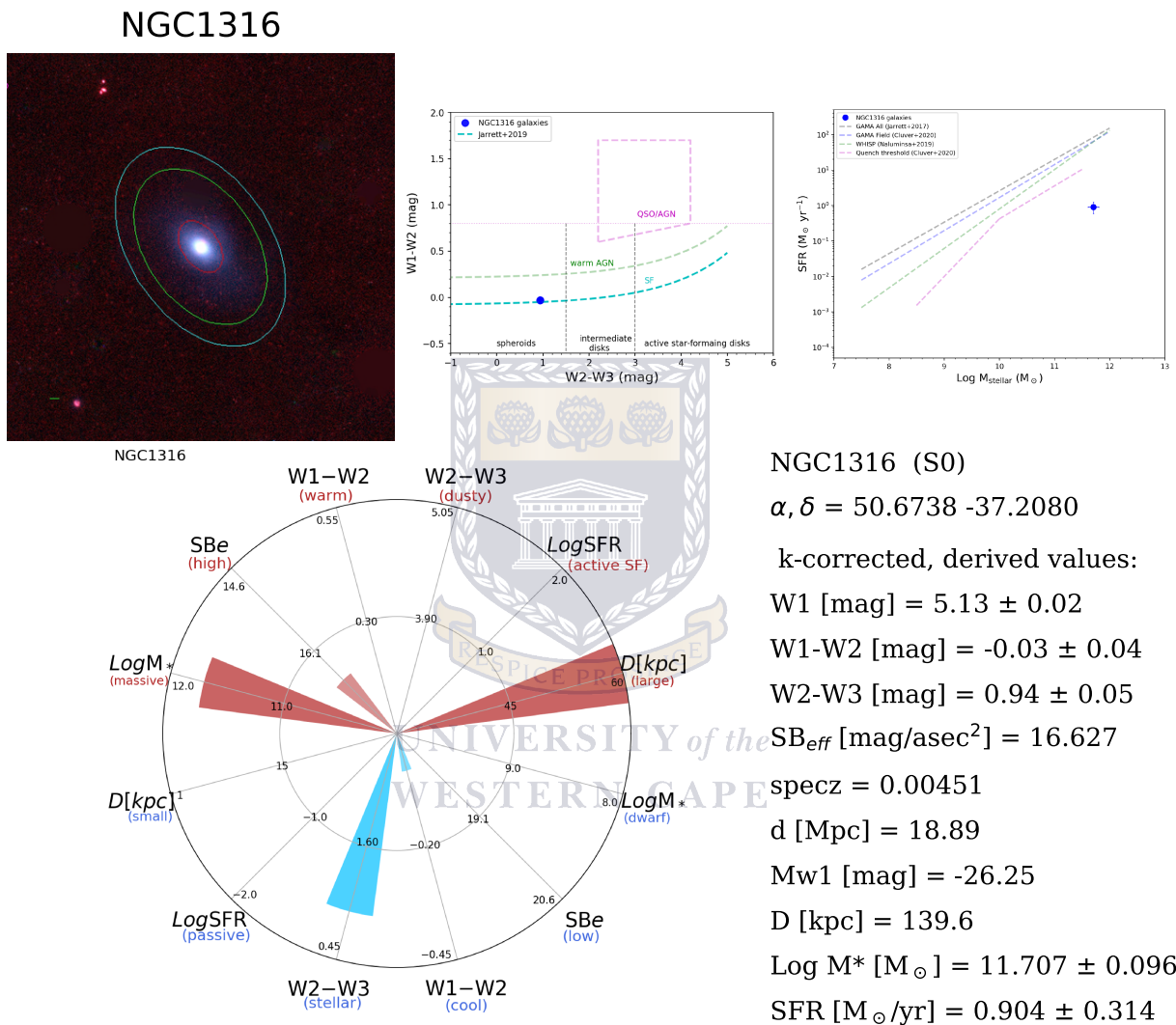


Figure 6.24: For comparison purposes, here is the massive Fornax Cluster galaxy, Fornax A (NGC1316), NGC1316 is classified as spheroid in *WISE* with a radio flux of 125 Jy.

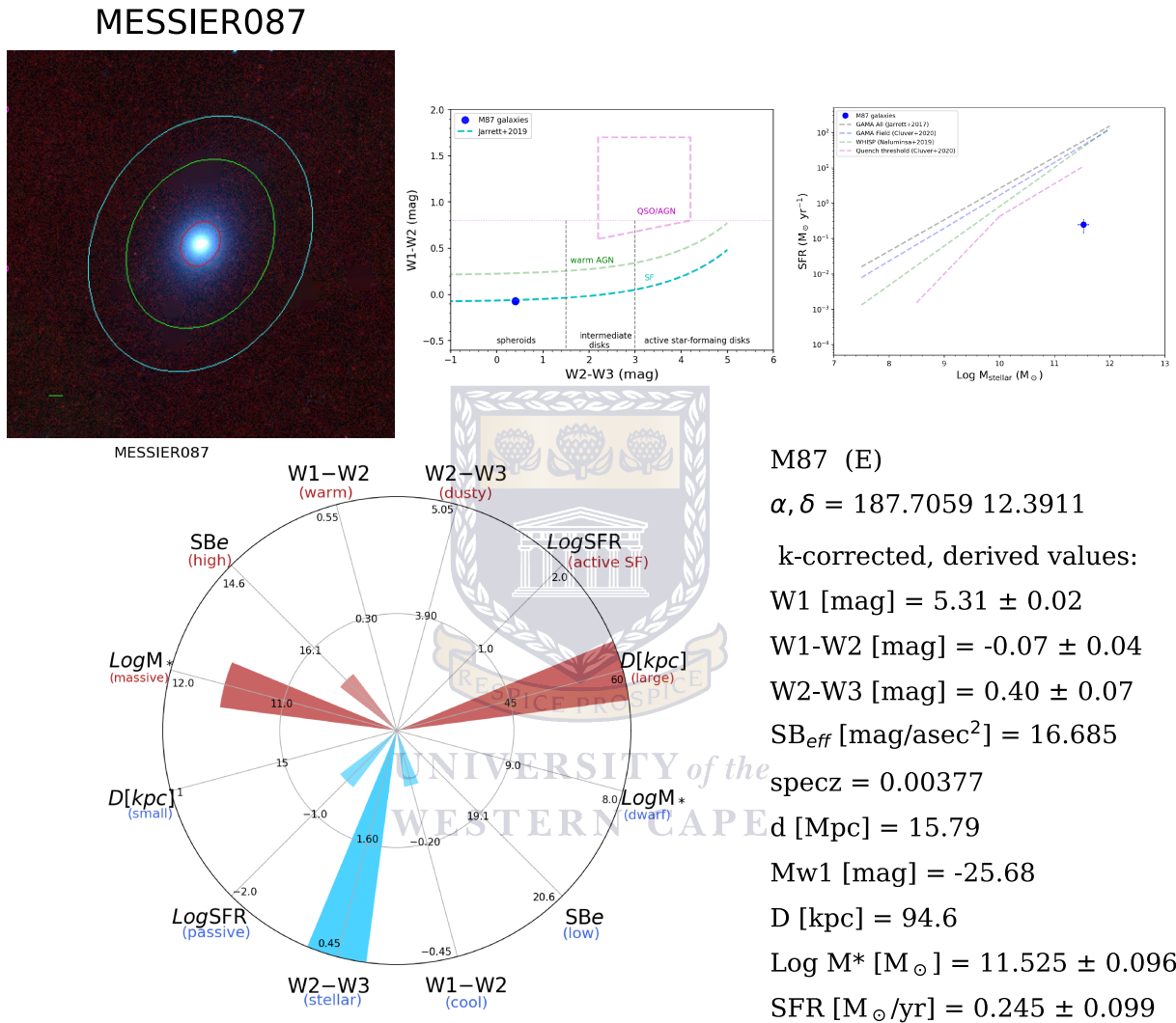
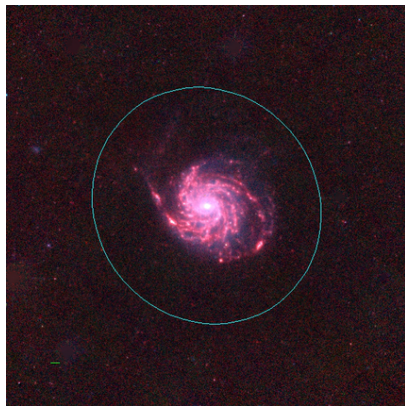
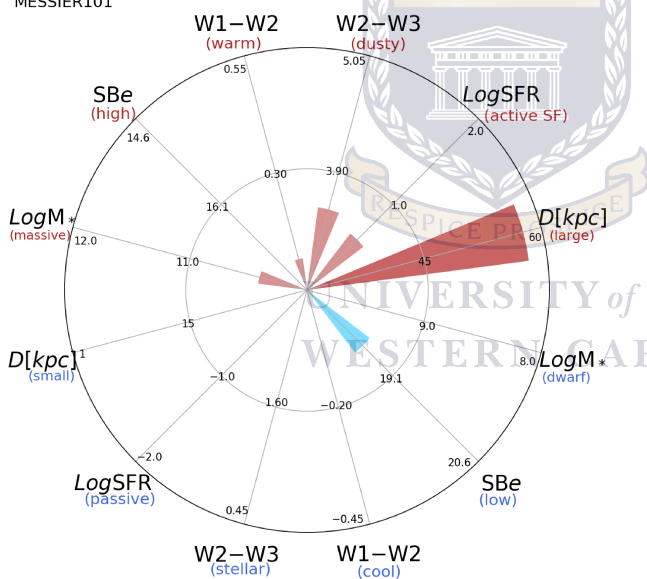
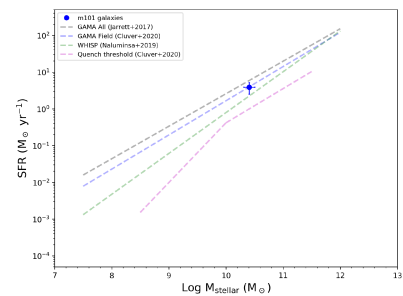
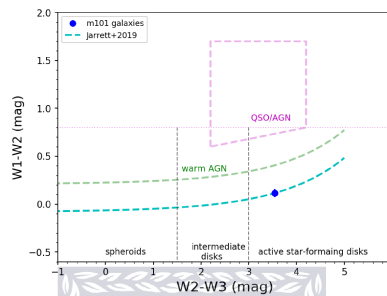


Figure 6.25: For comparison purposes, here is the massive Virgo Cluster galaxy, Virgo A (M87), M87 is classified as spheroid in *WISE* with a radio flux of 138.487 Jy. It has a super-massive black hole at the centre, which was pictured as the first ever real image of a black hole.

MESSIER101



MESSIER101



m101 (SABc)

$\alpha, \delta = 210.8022 \ 54.3489$

k-corrected, derived values:

W1 [mag] = 5.25 ± 0.02

W1-W2 [mag] = 0.12 ± 0.04

W2-W3 [mag] = 3.54 ± 0.04

SBeff [mag/asec²] = 18.574

specz = 0.00124

d [Mpc] = 6.87

Mw1 [mag] = -23.93

D [kpc] = 57.7

Log M* [M_{\odot}] = 10.406 ± 0.096

SFR [M_{\odot}/yr] = 3.85 ± 1.34

Figure 6.26: For comparison purposes, here is the nearby grand design spiral galaxy, M101, is classified as SF in *WISE* with a radio flux of 0.75 Jy.

Chapter 7

Concluding Remarks

Having presented and discussed our work in the preceding chapters, we summarise our findings and the scope for future work in this chapter.

AGN activity and its feedback mechanism is crucial to our understanding of galaxy growth over time. In AGNs the accretion process that conveys gas into the SMBH releases a tremendous amount of energy in the form of powerful jets and radiation that generate outflows (magnetohydrodynamic winds). The powerful winds and jets in return have the potential to quench the star formation and even starve the AGN itself by stopping the gas inflow or preventing the gas from cooling down. In some cases the outflows compress the ISM, leading to a boost in star formation (see Shin et al. 2019 and references therein). As a result, the properties of normal SF galaxies are affected by the presence of an AGN. This is the reason why, since their discovery (AGNs), techniques have been devised at different wavebands to more or less separate them from normal galaxies. However, there is clearly still room for improvement regarding the consistency of classification across methods.

Our project aimed to achieve better understanding of the existing problems and rather than using different diagnostics independently, combine them for a more meaningful analysis. The key data used are the mid-IR imaging and galaxy photometry from WISE, the optical spectra from GAMA, high-resolution KiDS r-band images for visualisation, and finally early science radio continuum data from MeerKAT. The KiDS r-band images are among the best available with subarcsecond resolution. These were of great help in looking for details about the galaxies and their immediate environment. Some intriguing results could be clarified only with the KiDS images that revealed closely blended systems appearing like single galaxies.

In such projects, the quality of the data used could be an impediment if not properly understood and used optimally. We recall that WISE is an all-sky survey that is publicly available. Although it has good data quality extensively used in astronomy, there are complications related to nearby resolved galaxies. The *WISE* survey was optimised for point-source detection, thus compromising the photometry of extended sources. Generally, one can avoid this problem when dealing with galaxies at moderate and high redshifts (where the galaxies are mostly seen as point sources). In contrast, the proportion of extended galaxies increases at low redshift. Therefore, it becomes imperative to assess the photometry of the resolved galaxies properly for studies in the local universe.

This is why we undertook to create a WISE catalogue including resolved galaxies with carefully measured photometry (see Section 3.3.2), which will be made available to the public through journal publication (e.g., Yao et al. 2020). It is a lengthy process requiring the reconstruction of images, determining which galaxies are probably resolved, and foreground cleaning of the extracted resolved galaxies. Followed by full source characterisation of photometric, colour, morphology, and surface brightness properties. Finally, k-correction of the fluxes to derive rest (zero redshift) values has to occur.

The optical lines, on the other hand, are automatically fitted with the IDL code “mpfitfun” (Markwardt 2009), which uses a Levenberg–Marquardt non-linear least squares minimisation to identify the best-fitting parameters (see Section 3.1.1.1 for more details) and could sometimes contain errors that only a visual inspection of the spectra can reveal, not to mention the complexity of BLs and how they may compromise the BPT ratios. Indeed, the broad $H\alpha$ λ 6563 and the close $[N\text{II}]\lambda$ 6583 lines next to it are often hardly deblended, thus affecting their flux measurement. In addition to the optical lines measurement tables, we fortunately have access to the GAMA spectra that were thus all visually inspected.

For the radio continuum data, we opted for a new extraction software (*ProFound*) with the potential to follow the real asymmetric light distribution of the galaxy, as opposed to the conventional (e.g., PyBDSF; AEGEAN) software, which extrapolate the light distribution using ellipses. This supposedly yields more accurate radio fluxes, notably for extended sources that exhibit “jet” features.

We also carried out an early processing and analysis of *WISE* using *ProFound* (Chapter 4), to assess the viability of using this software package to detect and characterise point-sources and resolved galaxies. Our analysis suggested that it was not nearly as robust and reliable as our custom software (which is well-vetted and established in the past decade), and we did not use it any further for *WISE* catalogues or source measurement. However,

for the case of radio continuum imaging from MeerKAT, *ProFound* was found to be a viable alternative to source extraction and basic photometric measurements, and deployed to derive radio luminosities (see Chapter 6).

7.1 Optical and Mid-IR View

Once we were satisfied with the quality of the optical and the IR data, these were combined to compare the galaxy classification methods at both wavelength regimes (Chapter 5). It confirmed the necessity of using properly measured photometries as a way to ease the tension between these two methods. The two methods yield similar results in the classification of non-AGN galaxies with only 4% disagreement. However, about 29% of the optical AGNs are non-mid-IR AGNs, while $\sim 33\%$ of the mid-IR AGNs are not optical AGNs (Figure 5.8). The main technical issues causing these discordant results are the blending of the broad $H\alpha$ and the $[N II]$ lines in optical, and blended systems seen as single sources by *WISE* (see Section 5.3 for more details). We were able to observe the latter thanks to the high-quality KiDS r-band images.

We furthermore designed an optical-IR diagram showing more accuracy in the classification of the different groups of galaxies. It is a combination of optical ($[N II]/H\alpha$) lines and the W1-W2 colour, which can classify four times more galaxies than the classic BPT diagram (see Section 5.4). Among the optical lines used in the BPT ($[O III]/H\beta$ vs $[N II]/H\alpha$), the $H\beta$ line often has the lowest S/N, significantly reducing the number of classifiable galaxies using this diagram. On the contrary, the W1 and W2 used as replacement for $[O III]/H\beta$ in the new diagram are detected with a high S/N, making the classification of more galaxies possible.

7.2 Folding in the Radio Continuum

It is currently widely accepted that nearly all galaxies possess a supermassive black hole at their centre. They are seen as AGNs when the black hole is actively accreting materials, leading to energy release at different wavelengths. The major challenge is being able to differentiate this particular radiation from the general emission coming from the entire galaxy. This is why we always push further in the hope of uncovering more hidden AGNs. The focus is not only on finding AGNs; better identification of the AGNs will implicitly lead

to a much cleaner SF galaxy sample as well. The radio associated with the WISE-GAMA sample can aid us to uncover the underlying activity and its link to galaxy evolution more broadly through the AGN feedback mechanism.

The radio continuum data used for this project was acquired during the MeerKAT (64 dishes) first call for proposal in 2019. We were part of the very few to have access to this early science data from such a powerful facility. The quality of the images obtained can be seen in Figure 6.3, where we present some resolved sources showing well-defined emissions down to a flux limit of $20 \mu\text{Jy}$.

Using the q_{TIR} , we were able to identify AGNs based on their radio excess (meaning low q_{TIR} values). We found the radio AGNs to be high-mass galaxies with low W1-W2 colour values (Figure 6.13). The most interesting fact is that these galaxies are generally located in the region of the WISE classification diagram (Figure 6.14) where they are considered inactive galaxies (i.e. no star formation or apparent AGN). Most of them do not have optical emission lines (but do have absorption lines), making them impossible to be classified in the optical BPT. However, the q_{TIR} cannot make a difference between the mid-IR (or optical) AGNs and the SF galaxies. The optical-IR seem to be showing us AGNs when galaxies are active and dust obscuration is significant, while the radio-IR is adept at identifying AGNs that dominate at the end of the galaxy's life. The WISE colour-colour diagram is one of the most frequently used methods to separate AGNs from SF galaxies. Taking into account these low q_{TIR} AGNs could greatly improve the reliability and AGN completeness of this diagram.

Furthermore, comparing the radio to the IR emissions revealed a decreasing trend in q_{TIR} with radio luminosity. This decrease can be understood as having much higher radio fluxes in comparison to the IR as the radio emission becomes more prominent. Using, in this case, the radio flux as a proxy for SFR leads to an overestimation relative to the well-understood dust-obscured star formation activity. In our study we first corrected for the slope of the q_{TIR} and then performed calibration of the radio SFR with $\text{SFR}_{12\mu\text{m}}$ (derived using WISE $12 \mu\text{m}$), sensitive to, and calibrated to the dust-obscured SF activity.

7.3 Future Prospects

Our current study makes use of bespoke WISE photometry for a cleaner comparison between the optical and the IR galaxy classification models. To achieve our goal, we went

through a meticulous and time-consuming process to extract and derive the appropriate photometry for the WISE resolved sources. The way forward is to be able to create a WISE galaxy catalogue including resolved sources on a much larger area in a reasonable time span. The existing pipeline is semi-automated and relies additionally on human supervision to ensure the best data quality. A machine learning algorithm like the convolutional neural network associated to our pipeline will be of great help in this regard, as it could progressively replace human intervention. This algorithm could learn from our already existing cleaned catalogues used as a training data set in order to perform tough deblending and foreground removal automatically.

Some case studies, especially galaxies classified as optical AGN (WISE SF) are likely to be better understood if observed in X-ray. The addition of X-ray data will be the natural next step. The new and powerful all-sky X-ray survey by eROSITA¹ (launched in 2019), which will target up to 3 million AGNs, will be suitable for this project. The X-ray emission generated by AGNs is very close to SMBH in comparison to the optical and IR emission, which makes them a more direct signature for AGN activity (see Section 2.3.1). X-ray data are very scarce and limited for Compton-thick AGNs (Li et al. 2019). However, having X-ray measurements for the different samples used in this study would help to clarify cases of discordant classification observed between the optical, the IR, and the radio. Galaxies in the spheroids region of the WISE colour-colour diagram are largely powerful radio AGNs. X-rays might bring their share of surprises, always deepening our understanding.

Using all the GAMA fields with already available WISE resolved catalogues created by our team will provide statistical robustness to our findings. Upcoming big surveys such as the EMU will observe the entire southern sky with greater sensitivity than most of the existing ones (respectively 40 and four times the sensitivity and the resolution of the NVSS). Note that the largest radio survey to date is the NVSS, located in the northern sky, with about 1.8 million sources compared to EMU, that will detect about 70 million galaxies. However, the effective usage of these powerful survey will require redshift information best found using spectroscopic data. Multi object spectrographs (MOS; see Smith 2016) have the ability to collect multiple spectra at the same time over a large area and are being deployed on most of the major ground based and space telescopes. The wealth of spectroscopic data, which will be available in the near future through this technique in combination with radio surveys like EMU (will provide both large and high-quality data) will considerably improve our radio analysis presented in Chapter 6.

¹<https://www.mpe.mpg.de/eROSITA>

Bibliography

- Abazajian, K. N., Adelman-McCarthy, J. K., Agüeros, M. A., et al. 2009, *ApJS* 182, 543.
doi:10.1088/0067-0049/182/2/543
- Adams, T. F. 1977, *ApJS*, 33, 19. doi:10.1086/190416
- Adelman-McCarthy, J. K., et al. 2008, *ApJS*, 175, 297. doi:10.1086/524984
- Agostino, C. J. and Salim, S., 2019, *ApJ*, 876, 12. doi:10.3847/1538-4357/ab1094
- Alexander, D. M., Brandt, W. N., Hornschemeier, A. E., et al. 2001, *AJ*, 122, 2156.
doi:10.1086/323540
- Allington-Smith, J. 2006, *Nature*, 50, 244. doi:10.1016/j.newar.2006.02.024
- Anders, P. & Fritze-v. Alvensleben, U. 2003, *AAp*, 401, 1063. doi:10.1051/0004-6361:20030151
- Antonucci, R. 1993, *ARAA*, 31, 473. doi:10.1146/annurev.aa.31.090193.002353
- Arnouts, S., Cristiani, S., Moscardini, L., et al. 1999, *MNRAS*, 310, 540. doi:10.1046/j.1365-8711.1999.02978.x
- Assef, R. J., Kochanek, C. S., Brodwin, M., et al. 2010, *ApJ*, 713, 970. doi:10.1088/0004-637X/713/2/970
- Assef, R. J., Stern, D., Kochanek, C. S., et al. 2013, *ApJ*, 772, 26. doi:10.1088/0004-637X/772/1/26
- Baade W., Minkowski R. (1954) On the Identification of Radio Sources. *Astrophys J* 119: 215-231. doi:10.1086/145813
- Baan, W. A. & Klöckner, H.-R. 2006, *A&A*, 449, 559. doi:10.1051/0004-6361:20042331

- Baldry, I. K., Robotham, A. S. G., Hill, D. T., et al. 2010, MNRAS, 404, 86.
doi:10.1111/j.1365-2966.2010.16282.x
- Baldry, I. K., Alpaslan, M., Bauer, A. E., et al. 2014, MNRAS, 441, 2440.
doi:10.1093/mnras/stu727
- Baldry, I. K., Liske, J., Brown, M. J. I., et al. 2018, MNRAS, 474, 3875.
doi:10.1093/mnras/stx3042
- Baldwin, J. A., Phillips, M. M., & Terlevich, R. 1981, PASP, 93, 5. doi:10.1086/130766
- Baldwin, C., McDermid, R. M., Kuntschner, H., et al. 2018, MNRAS, 473, 4698.
doi:10.1093/mnras/stx2502
- Baloković, M., Smolčić, V., Ivezić, Ž., et al. 2012, ApJ, 759, 30. doi:10.1088/0004-637X/759/1/30
- Barsanti, S., Owers, M. S., Brough, S., et al. 2018, ApJ, 857, 71. doi:10.3847/1538-4357
- Bassani, L., Dadina, M., Maiolino, R., et al. 1999, ApJS, 121, 473. doi:10.1086/313202
- Beckmann, V., & Shrader, C. 2012, Proceedings of “an INTEGRAL View of the High-energy Sky (the First 10 Years)” - 9th INTEGRAL Workshop and Celebration of the 10th Anniversary of the Launch (INTEGRAL 2012). 15-19 October 2012. Bibliotheque Nationale De France, 69
- Belfiore, F., Maiolino, R., Maraston, C., et al. 2016, MNRAS, 461, 3111.
doi:10.1093/mnras/stw1234
- Bell, A. R. 1978, MNRAS, 182, 443. doi:10.1093/mnras/182.3.443
- Bell, E.F., 2003, ApJ, 586, 794. doi:10.1086/367829
- Bellstedt, S., Driver, S. P., Robotham, A. S. G., et al. 2020, MNRAS, 496, 3235.
doi:10.1093/mnras/staa1466
- Berney, S., Koss, M., Trakhtenbrot, B., et al. 2015, MNRAS 454, 3622.
doi:10.1093/mnras/stv2181
- Berti, A. M., Coil, A. L., Hearin, A. P., et al. 2021, AJ, 161, 49. doi:10.3847/1538-3881/abcc6a

- Bertin, E., & Arnouts, S. 2010, SExtractor: Source Extractor, ascl:1010.064
- Best, P. N., Kauffmann, G., Heckman, T. M., et al. 2005, MNRAS, 362, 9. doi:10.1111/j.1365-2966.2005.09283.x
- Best, P. N., von der Linden, A., Kauffmann, G., et al. 2007, MNRAS, 379, 894. doi:10.1111/j.1365-2966.2007.11937.x
- Best, P. N., & Heckman, T. M. 2012, MNRAS, 421, 1569. doi:10.1111/j.1365-2966.2012.20414.x
- Betancort-Rijo, J., and López-Corredoira, M., ApJ 534, L117 (2000), arXiv:astro-ph/0003482 [astro-ph].
- Bilicki, M., Hoekstra, H., Brown, M. J. I., et al. 2018, AAp, 616, A69. doi:10.1051/0004-6361/201731942
- Blandford, R. D. & Ostriker, J. P. 1978, ApJL, 221, L29. doi:10.1086/182658
- Bond J. R., Kofman L., Pogosyan D., 1996, Nature, 380, 603. doi:10.1038/380603a0
- Bonzini, M., Padovani, P., Mainieri, V., et al. 2013, MNRAS, 436, 3759. doi:10.1093/mnras/stt1879
- Boroson, T. 2005, AJ, 130, 381. doi:10.1086/431722
- Bouché, N., Dekel, A., Genzel, R., et al. 2010, ApJ, 718, 1001. doi:10.1088/0004-637X/718/2/1001
- Bouchet, F. R., Juskiewicz, R., Colombi, S., et al. 1992, ApJL, 394, L5. doi:10.1086/186459
- Bouchet, F. R., Colombi, S., Hivon, E., and Juskiewicz, R., Astr. Astrophy. 296, 575 (1995), arXiv:astro-ph/9406013 [astro-ph].
- Bressan, A., Silva, L., & Granato, G. L. 2002, A&A, 392, 377. doi:10.1051/0004-6361:20020960
- Brinchmann, J. & Ellis, R. S. 2000, ApJL, 536, L77. doi:10.1086/312738
- Brown, D. L. & Burns, J. O. 1991, AJ, 102, 1917. doi:10.1086/116012
- Brown, M. J. I., Moustakas, J., Smith, J.-D. T., et al. 2014a, ApJS, 212, 18. doi:10.1088/0067-0049/212/2/18

- Brown, M. J. I., Jarrett, T. H., & Cluver, M. E. 2014b, *PASA*, 31, 49B.
doi:10.1017/pasa.2014.44
- Brown, M. J. I., Moustakas, J., Kennicutt, R. C., et al. 2017, *ApJ*, 847, 136.
doi:10.3847/1538-4357/aa8ad2
- Brown, M. J. I., Duncan, K. J., Landt, H., et al. 2019, *MNRAS*, 489, 3351.
doi:10.1093/mnras/stz2324
- Bruzual, G., & Charlot, S. 2003, *MNRAS*, 344, 1000. doi:10.1046/j.1365-8711.2003.06897.x
- Buchert, T. 1994, *MNRAS*, 267, 811. doi:10.1093/mnras/267.4.811
- Burns J. O., 1990, *AJ*, 99, 14
- Buttiglione, S., Capetti, A., Celotti, A., et al. 2010, *A&A*, 509, A6. doi:10.1051/0004-6361/200913290
- Calistro Rivera, G., Williams, W. L., Hardcastle, M. J., et al. 2017, *MNRAS*, 469, 3468.
doi:10.1093/mnras/stx1040
- Casasola, V., Hunt, L., Combes, F., et al. 2015, *AAp*, 577, A135. doi:10.1051/0004-6361
- Castro C. S., Dors O. L., Cardaci M. V., Hagele G. F., 2017, *MNRAS*, 467, 1507.
doi.org/10.1093/mnras/stx150
- Chen, H., Gao, Y., Braine, J., et al. 2015, *ApJ*, 810, 140. doi:10.1088/0004-637X/810/2/140
- Ching, J. H. Y., Sadler, E. M., Croom, S. M., et al. 2017, *MNRAS*, 464, 1306.
doi:10.1093/mnras/stw2396
- Cid Fernandes, R., Stasińska, G., Schlickmann, M. S., et al. 2010, *MNRAS*, 403, 1036.
doi:10.1111/j.1365-2966.2009.16185.x
- Cluver, M. E., Jarrett, T. H., Hopkins, A. M., et al. 2014, *ApJ*, 782, 90. doi:10.1088/0004-637X/782/2/90
- Cluver, M. E., Jarrett, T. H., Dale, D. A., et al. 2017, *ApJ*, 850, 68. doi:10.3847/1538-4357/aa92c7
- Cluver, M. E., Jarrett, T. H., Taylor, E. N., et al. 2020, *ApJ*, 898, 20. doi:10.3847/1538-4357/ab9cb8

- Colless, M., Dalton, G., Maddox, S., et al. 2001, MNRAS, 328, 1039. doi:10.1046/j.1365-8711.2001.04902.x
- Condon, J. J., Anderson, M. L., & Helou, G. 1991, ApJ, 376, 95. doi:10.1086/170258
- Condon, J. J. 1992, ARA&A, 30, 575. doi:10.1146/annurev.aa.30.090192.003043
- Condon, J. J., Cotton, W. D., Greisen, E. W., et al. 1998, AJ, 115, 1693. doi:10.1086/300337
- Contini M., 2019, MNRAS, 488, 4487. doi:10.1093/mnras/stz1972
- Coutinho, B. C., Hong, S., Albrecht, K., et al. 2016, arXiv:1604.03236
- Croton, D. J., Springel, V., White, S. D. M., et al. 2006, MNRAS, 365, 11. doi:10.1111/j.1365-2966.2005.09675.x
- Curtis, H. D. 1918, Publications of Lick Observatory, 13, 9
- Cutri, R. M., Wright, E. L., Conrow, T., et al. 2012, Explanatory Supplement to the *WISE* All-Sky Data Release Products, 1
- D'Agostino, J. J., Kewley, L. J., Groves, B. A., et al. 2019, MNRAS, 487, 4153. doi:10.1093/mnras/stz1611
- Davies, L. J. M., Huynh, M. T., Hopkins, A. M., et al. 2017, MNRAS, 466, 2312–2324, <https://doi.org/10.1093/mnras/stw3080>
- de Jong, J. T. A., Kuijken, K., Applegate, D., et al. 2013, The Messenger, 154, 44
- Delhaize, J., Smolčić, V., Delvecchio, I., et al. 2017, A&A, 602, A4. doi:10.1051/0004-6361/201629430
- Dickey, C. M., van Dokkum, P. G., Oesch, P. A., et al. 2016, ApJL, 828, L11. doi:10.3847/2041-8205/828/1/L11
- Dopita, M. A., Koratkar, A. P., Evans, I. N., et al. 1996, The Physics of Liners in View of Recent Observations, 103, 44
- Dopita, M. A., Koratkar, A. P., Allen, M. G., et al. 1997, ApJ, 490, 202. doi:10.1086/304862
- Dors, O. L., Arellano-Córdova, K. Z., Cardaci, M. V., et al. 2017, MNRAS, 468, L113. doi:10.1093/mnrasl/slx036
- Driver, S. P., Popescu, C. C., Tuffs, R. J., et al. 2008, ApJL, 678, L101. doi:10.1086/588582

- Driver, S. P., Norberg, P., Baldry, I. K., et al. 2009, *Astronomy and Geophysics*, 50, 050000. doi:10.1111/j.1468-4004.2009.50512.x
- Driver, S. P., Hill, D. T., Kelvin, L. S., et al. 2011, *MNRAS*, 413, 971. doi:10.1111/j.1365-2966.2010.18188.x
- Duah Asabere, B., Horellou, C., Jarrett, T. H., et al. 2016, *AAp*, 592, A20. doi:10.1051/0004-6361/201528047
- Eke, V. R., Frenk, C. S., Baugh, C. M., et al. 2004, *MNRAS*, 355, 769. doi:10.1111/j.1365-2966.2004.08354.x
- Elbaz, D., Daddi, E., Le Borgne, D., et al. 2007, *A&A*, 468, 33. doi:10.1051/0004-6361:20077525
- Ellison, S. L., Viswanathan, A., Patton, D. R., et al. 2019, *MNRAS*, 487, 2491. doi:10.1093/mnras/stz1431
- Elvis M., Wilkes B. J., McDowell J. C., et al. (1994). *Astrophys J Suppl* 95: 1-68. doi:10.1086/192093
- Event Horizon Telescope Collaboration, Akiyama, K., Alberdi, A., et al. 2019, *ApJL*, 875, L1. doi:10.3847/2041-8213/ab0ec7
- Fabian, A. C. 2012, *ARA&A*, 50, 455, doi: 10.1146/annurev-astro-081811-125521
- Fanaroff, B. L., & Riley, J. M. 1974, *MNRAS*, 167, 31P. doi:10.1093/mnras/167.1.31P
- Fath, E. A. 1909, *Lick Observatory Bulletin*, 149, 71. doi:10.5479/ADS/bib/1909LicOB.5.71F
- Ferrarese L., Merritt D., 2000, *ApJL*, 539, L9. doi:10.1086/312838
- Filho, M. E., Barthel, P. D., & Ho, L. C. 2006, *Astronomy & Astrophysics*, 451, 71. doi:10.1051/0004-6361:20054510
- Flohic, H. M. L. G., Eracleous, M., Chartas, G., et al. 2006, *ApJ*, 647, 140. doi:10.1086/505296
- González-Martín, O., Masegosa, J., Márquez, I., et al. 2009, *Astronomy & Astrophysics*, 506, 1107. doi:10.1051/0004-6361/200912288

- Gopal-Krishna, Wiita, P. J. 1990, *Astr. Astrophys.*, 236, 305.
- Gordon, Y. A., Owers, M. S., Pimbblet, K. A., et al. 2017, *MNRAS*, 465, 2671.
doi.org/10.1093/mnras/stw2925
- Graham, A. W., & Driver, S. P. 2005, *PASA*, 22, 118. doi:10.1071/AS05001
- Graham, A. W., & Scott, N. 2013, *ApJ*, 764, 151. doi:10.1088/0004-637X/764/2/151
- Graham, A. W. 2016, *Galactic Bulges*, 263. doi:10.1007/978-3-319-19378-6_11
- Graham, A. W., & Soria, R. 2019, *MNRAS*, 484, 794. doi:10.1093/mnras/sty3398
- Grootes, M. W., Tuffs, R. J., Popescu, C. C., et al. 2013, *ApJ*, 766, 59. doi:10.1088/0004-637X/766/1/59
- Groves, B. A., Heckman, T. M., & Kauffmann, G. 2006, *MNRAS*, 371, 1559.
doi:10.1111/j.1365-2966.2006.10812.x
- Gunawardhana, M. L. P., Hopkins, A. M., Sharp, R. G., et al. 2011, *MNRAS*, 415, 1647.
doi:10.1111/j.1365-2966.2011.18800.x
- Gunawardhana, M. L. P., Hopkins, A. M., Sharp, R. G., et al. 2013, *MNRAS*, 433, 2764.
doi:10.1093/mnras/stt890
- Gunn, J. E., & Gott, J. R., III 1972, *ApJ*, 176, 1. doi:10.1086/151605
- Haardt, F. & Maraschi, L. 1993, *ApJ*, 413, 507. doi:10.1086/173020
- Hada, K., Doi, A., Wajima, K., et al. 2018, *ApJ*, 860, 141, doi: 10.3847/1538-4357/aac49f
- Hahn, O., Angulo, R. E., & Abel, T. 2015, *MNRAS*, 454, 3920. doi:10.1093/mnras/stv2179
- Hainline, K. N., Hickox, R. C., Carroll, C. M., et al. 2014, *ApJ*, 795, 124. doi:10.1088/0004-637X/795/2/124
- Hainline, K. N., Reines, A. E., Greene, J. E., et al. 2016, *ApJ*, 832, 119. doi:10.3847/0004-637X/832/2/119
- Hale, C. L., Robotham, A. S. G., Davies, L. J. M., et al. 2019, *MNRAS*, 487, 3971.
doi:10.1093/mnras/stz1462
- Hardcastle M. J., Evans D. A., Croston J. H., 2006, *MNRAS*, 370, 1893. doi:10.1111/j.1365-2966.2006.10615.x

- Hardcastle M. J., Evans D. A., Croston J. H., 2009, MNRAS, 396, 1929. doi:10.1111/j.1365-2966.2009.14887.x
- Hardcastle, M. J., & Croston, J. H. 2020, NewAR, 88, 101539, doi: 10.1016/j.newar.2020.101539
- Harrison, C. M. (2014) Observational constraints on the influence of active galactic nuclei on the evolution of galaxies. PhD Thesis. doi:10.1007/978-3-319-28454-5
- Heckman, T. M. 1980, AAp, 500, 187
- Heckman, T. M., Ptak, A., Hornschemeier, A., & Kauffmann, G. 2005, ApJ, 634, 161. doi:10.1086/491665
- Helou, G., Soifer, B. T., & Rowan-Robinson, M. 1985, ApJL, 298, L7. doi:10.1086/184556
- Hill, D. T., Kelvin, L. S., Driver, S. P., et al. 2011, MNRAS, 412, 765. doi:10.1111/j.1365-2966.2010.17950.x
- Hirv, A., Pelt, J., Saar, E., et al. 2017, A&A, 599, A31. doi:10.1051/0004-6361/201629248
- Ho, L. C., Filippenko, A. V., & Sargent, W. L. W. 1997, ApJ, 487, 568. doi:10.1086/304638
- Hönig, S. F. 2019, arXiv e-prints, arXiv:1909.08639. doi:10.3847/1538-4357/ab4591
- Hopkins, A. M., Driver, S. P., Brough, S., et al. 2013, MNRAS, 430, 2047. doi:10.1093/mnras/stt030
- Huang, T.-C., Goto, T., Hashimoto, T., et al. 2017, MNRAS, 471, 4239. doi:10.1093/mnras/stx1947
- Hubble, E. P. 1920, Publications of the Yerkes Observatory, 4, 2.iii
- Hubble, E. 1929, Proceedings of the National Academy of Science, 15, 168
- Intema, H. T., van der Tol, S., Cotton, W. D., et al. 2009, A&A, 501, 1185. doi:10.1051/0004-6361/200811094
- Intema, H. T., Jagannathan, P., Mooley, K. P., et al. Astronomy and Astrophysics, 598:A78, February 2017
- Iverson, R. J., Magnelli, B., Ibar, E., et al. 2010, A&A, 518, L31. doi:10.1051/0004-6361/201014552

- Jana, A., Chatterjee, A., Kumari, N., et al. 2020, arXiv:2008.08033
- Jarrett, T. H., Chester, T., Cutri, R., et al. 2000, *AJ*, 119, 2498. doi:10.1086/301330
- Jarrett, T. H., Cohen, M., Masci, F., et al. 2011, *ApJ*, 735, 112. doi:10.1088/0004-637X/735/2/112
- Jarrett, T. H., Masci, F., Tsai, C. W., et al. 2012, *AJ*, 144, 68. doi:10.1088/0004-6256/144/2/68
- Jarrett, T. H., Masci, F., Tsai, C. W., et al. 2013, *AJ*, 145, 6. doi:10.1088/0004-6256/145/1/6
- Jarrett, T. H., Cluver, M. E., Magoulas, C., et al. 2017, *ApJ*, 836, 182. doi:10.3847/1538-4357/836/2/182
- Jarrett, T. H., Cluver, M. E., Brown, M. J. I., et al. 2019, *ApJS*, 245, 25. doi:10.3847/1538-4365/ab521a
- Jarvis, M. E., Harrison, C. M., Thomson, A. P., et al. 2019, *MNRAS*, 485, 2710. doi:10.1093/mnras/stz556
- Jonas, J., L. IEEE Proceedings, 97:1522–1530, August 2009. doi:10.1109/JPROC.2009.2020713
- Jonas, J., & MeerKAT Team. In Proceedings of MeerKAT Science: On the Pathway to the SKA. 25-27 May, 2016 Stellenbosch, South Africa (MeerKAT2016). Online at <https://pos.sissa.it/cgi-bin/reader/conf.cgi?confid=277;A;id.1>, page 1, 2016.
- Jones, D. H., Saunders, W., Colless, M., et al. 2004, *MNRAS*, 355, 747. doi:10.1111/j.1365-2966.2004.08353.x
- Jones, D. H., Read, M. A., Saunders, W., et al. 2010, *VizieR Online Data Catalog*, VII/259
- Johnston, S., Taylor, R., Bailes, M., et al. 2008, *Experimental Astronomy*, 22, 151. doi:10.1007/s10686-008-9124-7
- Józsa, G. I. G., White, S. V., Thorat, K., et al. 2020, in *ASP Conf. Ser.*, Vol. 527, ADASS XXIX, ed. R. Pizzo, E. Deul, J.-D. Mol, J. de Plaa, & H. Verkouter, San Francisco, 63–638/
- Kaiser, C. R. 2006, *MNRAS*, 367, 1083. doi:10.1111/j.1365-2966.2006.10030.x

- Kaneda, H., Onaka, T., Sakon, I., et al. 2008, *ApJ*, 684, 270. doi:10.1086/590243
- Kashino, D., Silverman, J. D., Rodighiero, G., et al., 2013, *The Astrophysical Journal Letters*, 777, L8. doi:10.1088/2041-8205/777/1/L8
- Kauffmann, G., & Haehnelt, M. 2000, *MNRAS*, 311, 576. doi:10.1046/j.1365-8711.2000.03077.x
- Kauffmann, G., Heckman, T. M., Tremonti, C., et al. 2003, *MNRAS*, 346, 1055. doi:10.1111/j.1365-2966.2003.07154.x
- Keel, W. C., Lintott, C. J., Maksym, W. P., et al. 2017, *ApJ*, 835, 256. doi:10.3847/1538-4357/835/2/256
- Kellermann, K. I., Sramek, R., Schmidt, M., et al. 1989, *AJ*, 98, 1195. doi:10.1086/115207
- Kennicutt Jr. R. C., 1998a, *ARA&A*, 36, 189. doi:10.1146/annurev.astro.36.1.189
- Kennicutt, R. C. 1998b, *ApJ*, 498, 541. doi:10.1086/305588
- Kenyon, J. S., Smirnov, O. M., Grobler, T. L., & Perkins, S. J. 2018, *MNRAS*, 478, 2399. doi:10.1093/mnras/sty1221
- Kettlety, T., Hesling, J., Phillipps, S., et al. 2018, *MNRAS*, 473, 776. doi:10.1093/mnras/stx2379
- Kewley, L. J., Dopita, M. A., Sutherland, R. S., Heisler, C. A., & Trevena, J. 2001a, *ApJ*, 556, 121. doi:10.1086/321545
- Kewley, L. J., Groves, B., Kauffmann, G., & Heckman, T. 2006, *MNRAS*, 372, 961. doi:10.1111/j.1365-2966.2006.10859.x
- Kewley, L. J., Maier, C., Yabe, K., et al. 2013, *ApJL*, 774, L10. doi:10.1088/2041-8205/774/1/L10
- Kewley, L. J., Nicholls, D. C., & Sutherland, R. S. 2019, *ARA&A*, 57, 511. doi:10.1146/annurev-astro-081817-051832
- Kitaura, F.-S. & Angulo, R. E. 2012, *MNRAS*, 425, 2443. doi:10.1111/j.1365-2966.2012.21614.x
- Kormendy J., Richstone D., 1995, *ARA&A*, 33, 581. doi:10.1146/annurev.aa.33.090195.003053

- Kraljic, K., Arnouts, S., Pichon, C., et al. 2018, MNRAS, 474, 547.
doi:10.1093/mnras/stx2638
- Kubota, A. & Done, C. 2018, MNRAS, 480, 1247. doi:10.1093/mnras/sty1890
- Kuijken, K., Heymans, C., Dvornik, A., et al. 2019, AAp, 625, A2. doi:10.1051/0004-6361/201834918
- Kurczynski, P., Gawiser, E., Acquaviva, V., et al. 2016, ApJL, 820, L1. doi:10.3847/2041-8205/820/1/L1
- Kuutma, T., Tamm, A., & Tempel, E. 2017, A&A, 600, L6. doi:10.1051/0004-6361/201730526
- Lacki, B. C. & Thompson, T. A. 2010, ApJ, 717, 196. doi:10.1088/0004-637X/717/1/196
- Lacy, M. & Sajina, A. 2020, Nature Astronomy, 4, 352. doi:10.1038/s41550-020-1071-x
- Laing R. A., Jenkins C. R., Wall J. V., Unger S. W., 1994, ASPC, 54, 201
- Lam, A., Wright, E., & Malkan, M. 2018, MNRAS, 480, 451. doi:10.1093/mnras/sty1844
- Larson, R. B., Tinsley, B. M., & Caldwell, C. N. 1980, ApJ, 237, 692
- Leahy, D. A., Hopkins, A. M., Norris, R. P., et al. 2019, PASA, 36, e024.
doi:10.1017/pasa.2019.16
- Leftley, J. H., Hönic, S. F., Asmus, D., et al. 2019, ApJ, 886, 55. doi:10.3847/1538-4357/ab4a0b
- Leitherer, C., Robert, C., & Heckman, T. M. 1995, Ap. J. Suppl, 99, 173.
doi:10.1086/192183
- Leslie, S. K., Kewley, L. J., Sanders, D. B., et al. 2016, MNRAS, 455, L82.
doi:10.1093/mnrasl/slv135
- Leslie, S. K., Schinnerer, E., Liu, D., et al. 2020, ApJ, 899, 58. doi:10.3847/1538-4357/aba044
- Li, J., Xue, Y., Sun, M., et al. 2019, ApJ, 877, 5. doi:10.3847/1538-4357/ab184b
- Lilly, S. J., Le Fevre, O., Hammer, F., et al. 1996, ApJL, 460, L1. doi:10.1086/309975

- Lim, S. & Mo, H. 2019, American Astronomical Society Meeting Abstracts #233. adsurl = <https://ui.adsabs.harvard.edu/abs/2019AAS...23312802L>
- Liske, J., Baldry, I.K., Driver, S.P., et al. 2015, MNRAS, 452, 2087. doi:10.1093/mnras/stv1436
- Liu, G., Zakamska, N. L., Greene, J. E., Nesvadba, N. P. H., & Liu, X. 2013, MNRAS, 436, 2576. doi:10.1093/mnras/stt1755
- Luo, B., Brandt, W. N., Alexander, D. M., et al. 2014, ApJ, 794, 70. doi:10.1088/0004-637X/794/1/70
- Madau, P., Ferguson, H. C., Dickinson, M. E., et al. 1996, MNRAS, 283, 1388. doi:10.1093/mnras/283.4.1388
- Magnelli, B., Ivison, R. J., Lutz, D., et al. 2015, A&A, 573, A45. doi:10.1051/0004-6361/201424937
- Magorrian J., Tremaine S., Richstone D., et al. 1998, AJ, 115, 2285. doi:10.1086/300353
- Makhathini, S. 2018, PhD thesis, Rhodes University, Drostdy Rd, Grahamstown, 6139, Eastern Cape, South Africa, available via <http://hdl.handle.net/10962/57348>
- Markwardt, C. B. 2009, Astronomical Data Analysis Software and Systems XVIII, 411, 251
- Masci, F. 2013, Astrophysics Source Code Library, ascl:1302.010
- Matthews, T. A. & Sandage, A. R. 1963, ApJ, 138, 30. doi:10.1086/147615
- McConnell, D., Allison, J. R., Bannister, K., et al. 2016, PASA, 33, e042. doi:10.1017/pasa.2016.37
- Meidt, S. E., Schinnerer, E., Knapen, J. H., et al. 2012, ApJ, 744, 17. doi:10.1088/0004-637X/744/1/17
- Merloni A., Heinz S., 2007, MNRAS, 381, 589. doi:10.1111/j.1365-2966.2007.12253.x
- Michałowski, M. J., Dunlop, J. S., Koprowski, M. P., et al. 2017, MNRAS, 469, 492. doi:10.1093/mnras/stx861
- Mignoli, M., Feltre, A., Bongiorno, A., et al. 2019, Astronomy and Astrophysics, 626, A9. doi:10.1051/0004-6361/201935062

- Miley, G. 1980, *ARAA*, 18, 165. doi:10.1146/annurev.aa.18.090180.001121
- Miraghaei, H., & Best, P. N. 2017, *MNRAS*, 466, 4346. doi:10.1093/mnras/stx007
- Molina, M., Eracleous, M., Barth, A. J., et al. 2018, *ApJ*, 864, 90. doi:10.3847/1538-4357/aad5ed
- Molnár, D. C., Sargent M. T., Leslie S., 2020, *MNRAS*, Submitted, 475
- Monreal-Ibero, A., Arribas, S., Colina, L., et al. 2010, *AAp*, 517, A28. doi:10.1051/0004-6361/200913239
- Murphy, E. J., Chary, R.-R., Dickinson, M., et al. 2011a, *ApJ*, 732, 126. doi:10.1088/0004-637X/732/2/126
- Murphy, E. J., Condon, J. J., Schinnerer, E., et al. 2011b, *ApJ*, 737, 67. doi:10.1088/0004-637X/737/2/67
- Murphy, E. J. 2013, *ApJ* 777, 58. doi:10.1088/0004-637X/777/1/58
- Nan, R., Li, D., Jin, C., et al. 2011, *International Journal of Modern Physics D*, 20, 989. doi:10.1142/S0218271811019335
- Netzer, H. 2015, *ARA&A*, 53, 365, doi: 10.1146/annurev-astro-082214-122302
- Noeske, K. G., Weiner, B. J., Faber, S. M., et al. 2007, *ApJL*, 660, L43. doi:10.1086/517926
- Ocran, E. F., Taylor, A. R., Vaccari, M., et al. 2020, *MNRAS*, 491, 5911. doi:10.1093/mnras/stz3401
- Offringa, A. R. 2010, *Astrophysics Source Code Library*, ascl:1010.017
- Offringa, A. R., McKinley, B., & Hurley-Walker, N. , et al. 2014, *MNRAS*, 444, 606. doi:10.1093/mnras/stu1368
- Ogawa, S., Ueda, Y., Tanimoto, A., et al. 2020, arXiv:2011.13931
- Ogle P., Whyson D., Antonucci R., 2006, *ApJ*, 647, 161. doi:10.1086/505337
- Oke, J. B. 1963, *Nature*, 197, 1040. doi:10.1038/1971040b0
- Osterbrock, D. E., & Koski, A. T. 1976, *MNRAS*, 176, 61P. doi:10.1093/mnras/176.1.61P
- Others S., 2012, *Journal of Interesting Stuff*, 17, 198

- Padovani, P. 2011, MNRAS, 411, 1547. doi:10.1111/j.1365-2966.2010.17789.x
- Padovani, P. 2016, AAPR, 24, 13. doi:10.1007/s00159-016-0098-6
- Padovani, P. 2017, Nature Astronomy, 1, 0194. doi:10.1038/s41550-017-0194
- Pahwa, I., Libeskind, N. I., Tempel, E., et al. 2016, MNRAS, 457, 695. doi:10.1093/mnras/stv2930
- Parkash, V., Brown, M. J. I., Jarrett, T. H., et al. 2018, ApJ, 864, 40. doi:10.3847/1538-4357/aad3b9
- Pearson, W. J., Wang, L., Hurley, P. D., et al. 2018, A&A, 615, A146. doi:10.1051/0004-6361/201832821
- Pérez-González, P. G., Rieke, G. H., Egami, E., et al. 2005, ApJ, 630, 82. doi:10.1086/431894
- Peterken, T., Merrifield, M., Aragón-Salamanca, A., et al. 2020, MNRAS, 495, 3387. doi:10.1093/mnras/staa1303
- Polletta, M., et al. 2006, ApJ, 642, 673. doi:10.1086/500821
- Polletta, M., et al. 2007, ApJ, 663, 81. doi:10.1086/518113
- Postman, M. & Geller, M. J. 1984, ApJ, 281, 95. doi:10.1086/162078
- Price, R. & Duric, N. 1992, ApJ, 401, 81. doi:10.1086/172040
- Pu, H.-Y., Nakamura, M., Hirotani, K., et al. 2015, ApJ, 801, 56, doi: 10.1088/0004-637X/801/1/56
- Querejeta, M., Meidt, S. E., Schinnerer, E., et al. 2015, ApJS, 219, 5. doi:10.1088/0067-0049/219/1/5
- Norris, R. P. 2017, Nature Astronomy, 1, 671. doi:10.1038/s41550-017-0233-y
- Reddy, N., Dickinson, M., Elbaz, D., et al. 2012, ApJ, 744, 154. doi:10.1088/0004-637x/744/2/154
- Reines, A. E., Nidever, D. L., Whelan, D. G., et al. 2010, ApJ, 708, 26. doi:10.1088/0004-637X/708/1/26

- Reyes, R., Zakamska, N. L., Strauss, M. A., et al. 2008, *Astronomical Journal*, 136, 2373.
doi:10.1088/0004-6256/136/6/2373
- Ricci, C., Bauer, F. E., Treister, E., et al. 2017, *MNRAS*, 468, 1273.
doi:10.1093/mnras/stx173
- Rich, J. A., Kewley, L. J., & Dopita, M. A. 2015, *ApJS*, 221, 28. doi:10.1088/0067-0049/221/2/28
- Richards, G. T., Hall, P. B., Vanden Berk, D. E., et al. 2003, *AJ*, 126, 1131.
doi:10.1086/377014
- Richards G. T., Lacy M., Storrie-Lombardi L. J., et al. (2006a) *Astrophys J Suppl* 166: 470-497. doi:10.1086/506525
- Riffel, R., Mallmann, N. D., Ilha, G. S., et al. 2020, *MNRAS*. doi:10.1093/mnras/staa3907
- Riffel, R. A., Dors, O. L., Armah, M., et al. 2021, *MNRAS*, 501, L54.
doi:10.1093/mnrasl/slaa194
- Robotham, A., Driver, S. P., Norberg, P., et al. 2010, *PASA*, 27, 76. doi:10.1071/AS09053
- Robotham, A. S. G., Norberg, P., Driver, S. P., et al. 2011, *MNRAS*, 416, 2640.
doi:10.1111/j.1365-2966.2011.19217.x
- Robotham, A. S. G., Taranu, D. S., Tobar, R., et al. 2017, *MNRAS*, 466, 1513.
doi:10.1093/mnras/stw3039
- Robotham, A. S. G., Davies, L. J. M., Driver, S. P., et al. 2018, *MNRAS*, 476, 3137.
doi:10.1093/mnras/sty440
- Rong, Y., Liu, Y., & Zhang, S.-N. 2016, *MNRAS*, 455, 2267. doi:10.1093/mnras/stv2516
- Sadowski, A., Narayan, R., Penna, R., & Zhu, Y. 2013, *MNRAS*, 436, 3856, doi: 10.1093/mnras/stt1881
- Sahu, N., Graham, A. W., & Davis, B. L. 2019, *ApJ*, 876, 155. doi:10.3847/1538-4357/ab0f32
- Salim, S., Boquien, M., & Lee, J. C. 2018, *ApJ*, 859, 11. doi:10.3847/1538-4357/aabf3c
- Sanders, D. B. & Mirabel, I. F. 1996, *ARAA*, 34, 749. doi:10.1146/annurev.astro.34.1.749

- Sarangi, A., Dwek, E., & Kazanas, D. 2019, arXiv e-prints, arXiv:1909.10426
- Sartori, L. F., Schawinski, K., Koss, M., et al. 2016, MNRAS, 457, 3629.
doi:10.1093/mnras/stw230
- Sartori, L. F., Schawinski, K., Koss, M. J., et al. 2018, MNRAS, 474, 2444.
doi:10.1093/mnras/stx2952
- Satyapal, S., Secrest, N. J., Ricci, C., et al. 2017, ApJ, 848, 126. doi:10.3847/1538-4357/aa88ca
- Schlegel, D. J., Finkbeiner, D. P., & Davis, M. 1998, ApJ, 500, 525. doi:10.1086/305772
- Schmidt, M. 1959, ApJ, 129, 243. doi:10.1086/146614
- Schmidt, M. 1970, ApJ, 162, 371. doi:10.1086/150668
- Scoville, N., Lee, N., Vanden Bout, P., et al. 2017, ApJ, 837, 150. doi:10.3847/1538-4357/aa61a0
- Serra, P., Westmeier, T., & Giese, N., et al. 2015, MNRAS, 448, 1922.
doi:10.1093/mnras/stv079
- Sersic, J. L., 1968, Atlas de galaxias Australes, <https://ui.adsabs.harvard.edu/abs/1968adga.book.....S>,
Provided by the SAO/NASA Astrophysics Data System
- Seyfert, C. K. 1943, ApJ, 97, 28. doi:10.1086/144488
- Seymour, N., Huynh, M., Shabala, S. S., et al. 2020, PASA, 37, e013.
doi:10.1017/pasa.2019.49
- Shakura, N. I., & Sunyaev, R. A. 1973, A&A, 500, 33
- Sharp, R. & Birchall, M. N. 2010, PASA, 27, 91. doi:10.1071/AS08001
- Shin, J., Woo, J.-H., Chung, A., et al. 2019, ApJ, 881, 147. doi:10.3847/1538-4357/ab2e72
- Silva, L., et al. 1998, ApJ, 509, 103. doi:10.1086/306476
- Silverman, J. D., Daddi, E., Rujopakarn, W., et al. 2018, ApJ, 868, 75. doi:10.3847/1538-4357/aae64b
- Smith, D. J. B. 2016, Multi-Object Spectroscopy in the Next Decade: Big Questions, Large Surveys, and Wide Fields, 507, 373

- Smolčić, V., Zamorani, G., Schinnerer, E., et al. 2009, *ApJ*, 696, 24. doi:10.1088/0004-637x/696/1/24
- Smolčić, V., Novak, M., Bondi, M., et al. 2017, *A&A*, 602, A1. doi:10.1051/0004-6361/201628704
- Song, H., Laigle, C., Hwang, H. S., et al. 2021, *MNRAS*, 501, 4635. doi:10.1093/mnras/staa3981
- Stern, D., Eisenhardt, P., Gorjian, V., et al. 2005, *ApJ*, 631, 163. doi:10.1086/432523
- Stern, D., Assef, R. J., Benford, D. J., et al. 2012, *ApJ*, 753, 30. doi:10.1088/0004-637X/753/1/30
- Tacchella, S., Dekel, A., Carollo, C. M., et al. 2016, *MNRAS*, 457, 2790. doi:10.1093/mnras/stw131
- Tan, Q.-H., Gao, Y., Zhang, Z.-Y., et al. 2018, *ApJ*, 860, 165. doi:10.3847/1538-4357/aac512
- Tanimoto, A., Ueda, Y., Odaka, H., et al. 2019, *ApJ*, 877, 95. doi:10.3847/1538-4357/ab1b20
- Taylor, E. N., Hopkins, A. M., Baldry, I. K., et al. 2011, *MNRAS*, 418, 1587. doi:10.1111/j.1365-2966.2011.19536.x
- Thomas, N., Dave, R., Jarvis, M. J., et al. 2020, arXiv:2010.11225
- Tempel, E. & Libeskind, N. I. 2013, *ApJ*, 775, L42. doi:10.1088/2041-8205/775/2/L42
- Teng, S. H., Brandt, W. N., Harrison, F. A., et al. 2014, *ApJ*, 785, 19. doi:10.1088/0004-637X/785/1/19
- Trimble, V. 1987, *ARA&A*, 25, 425. doi:10.1146/annurev.aa.25.090187.002233
- Tsai, C.W., et al. 2015, *ApJ*, 805, 90 Tsai, C.-W., Eisenhardt, P. R. M., Wu, J., et al. 2015, *ApJ*, 805, 90. doi:10.1088/0004-637X/805/2/90
- van der Kruit, P. C. 1971, *A&A*, 15, 110
- van de Weygaert, R. & Bond, J. R. 2008, *A Pan-Chromatic View of Clusters of Galaxies and the Large-Scale Structure*, 335. doi:10.1007/978-1-4020-6941-3_10
- Veilleux, S., & Osterbrock, D. E. 1987, *ApJS*, 63, 295. doi:10.1086/191166

- Voelk H. J., 1989, *A&A*, 218, 67
- Whitaker, K. E., van Dokkum, P. G., Brammer, G., et al. 2012, *ApJL*, 754, L29.
doi:10.1088/2041-8205/754/2/L29
- Whittam, I. H. 2020, IAU General Assembly. doi:10.1017/S1743921319003521
- Wickramasinghe, T. & Ukwatta T. N. 2010, *MNRAS*, 406, 548. doi:10.1111/j.1365-2966.2010.16686.x
- Wilson, A. S. & Colbert, E. J. M. 1995, *ApJ*, 438, 62. doi:10.1086/175054
- Wright, E. L., Eisenhardt, P. R. M., Mainzer, A. K., et al. 2010, *AJ*, 140, 1868.
doi:10.1088/0004-6256/140/6/1868
- Wright, A. H., Robotham, A. S. G., Bourne, N., et al. 2016, *MNRAS*, 460, 765.
doi:10.1093/mnras/stw832
- Wu, X.-B., Wang, F., Fan, X., et al. 2015, *nature*, 518, 512. doi:10.1038/nature14241
- Wu, Y.-Z., Zhang, S.-N., Zhao, Y.-H., et al. 2016, *MNRAS*, 457, 2929.
doi:10.1093/mnras/stw113
- Xue, Y. Q. 2017, *New Astron. Rev.*, 79, 59. doi:10.1016/j.newar.2017.09.002
- Yan, R., & Blanton, M. R. 2012, *ApJ*, 747, 61. doi:10.1088/0004-637X/747/1/61
- Yan, W., Hickox, R., Hainline, K., et al. 2019, *ApJ*, 870, 33. doi:10.3847/1538-4357/aaeed4
- Yao, H. F. M., Jarrett, T. H., Cluver, M. E., et al. 2020, *ApJ*, 903, 91, doi:10.3847/1538-4357/abba1a
- Yun, M. S., Reddy, N. A., & Condon, J. J. 2001, *ApJ*, 554, 803. doi:10.1086/323145
- Zwicky, F. 1933, *Helvetica Physica Acta*, 6, 110 (Republication of: The redshift of extragalactic nebulae)